Author:
Wise, Dan E

Title:
Rational phosphine design for cytotoxic Ru complexes, luminescent compounds and allylation catalysts

Rational phosphine design for cytotoxic Ru complexes, luminescent compounds and allylation catalysts

Dan E. Wise

February 2021

A thesis submitted to the University of Bristol in accordance with the requirements for award of the degree of Doctor of Philosophy in the Faculty of Science

Abstract

Chelating diphosphine ligands have been prepared for two main applications: cytotoxic Ru complexes and organopalladium alkylation catalysts. By applying rational design ideas to the ligand targets, the desired properties of the resulting metal complexes have been achieved.

Ruthenium diphosphine complexes derived from [RuCl(DMSO-*S*)$_2$(*cis*-tach)]Cl (**2.1**) have been synthesised and assessed as cytotoxic agents by physical inorganic measurements, *in vitro* assays, and imaging techniques. The structures of the diphosphine ligand backbone and metallacycle size both have a significant influence on cytotoxicity. Therefore, diphosphines have been specifically designed to be capable of interacting with DNA by intercalation. Complexes with flexible aliphatic backbones (**2.7**-**2.8**) or planar aromatic backbones (**2.17**-**2.19**) are the most active, and we have demonstrated cytotoxicity may be the result of multiple mechanisms.

The diphosphine bis((diphenylphosphino)methyl)glycine **L$_{3.1}$** is a versatile amide coupling partner with a variety of aryl and alkyl amines, producing fluorescent ligand conjugates. In addition, **L$_{3.1}$** forms a Ru chelate complex [RuCl(*cis*-tach)(**L$_{3.1}$**)]Cl (**3.1**) which serves as a Ru precursor to fluorescent complex conjugates by coupling of the carboxylic acid functional group. The photophysical properties of the resulting diphosphine ligands and Ru complex conjugates have been assessed, and the methodology has been applied to other fluorescent, therapeutic agents. The cytotoxicity of a pyrene complex conjugate [RuCl(*cis*-tach)(**L$_{3.2}$**)]Cl (**3.3**) has been investigated in collaboration with the University of York and compared to (*cis*-tach)Ru complexes **2.17**-**2.19**. Changing from an all-carbon backbone to a PCNCP backbone does not have a detrimental effect on cytotoxicity and provides a useful point of derivatisation for metal diphosphine drug conjugates.

A series of primary, secondary, and tertiary 1-pyrenylphosphines **L$_{4.1}$**-**L$_{4.3}$** has been synthesised. The luminescence and air stability properties of these ligands and their associated (arene)Ru complexes have been investigated and it was found that phosphine oxidation increases fluorescence quantum yield, whereas Ru coordination dramatically quenches emission. The resistance to air-oxidation of 1-pyrenylphosphines has been explored experimentally and by computational studies on the phosphine radical cations.

A series of aminophosphine pincer ligands **L$_{5.1}$**-**L$_{5.9}$** have been synthesised and their derived organopalladium complexes with both symmetric (5,5- and 6,6-) and non-symmetric (5,6-) metallacycles were prepared. The ligands that form non-symmetric metallacycles have been shown to have a dramatic impact on the Pd coordination chemistry. When applied as catalysts in allylic alkylation reactions, the larger 5,6- and 6,6-metallacycles show superior catalytic activity to the widely studied 5,5-metallacyclic systems. By optimising the reaction, we have found organopalladium catalysts that perform allylation of dimethylmalonate with high activity and excellent linear selectivity under mild conditions.

Declaration

I declare that the work in this dissertation was carried out in accordance with the requirements of the University's Regulations and Code of Practice for Research Degree Programmes and that it has not been submitted for any other academic award. Except where indicated by specific reference in the text, the work is the candidate's own work. Work done in collaboration with, or with the assistance of, others, is indicated as such. Any views expressed in the dissertation are those of the author.

Dan E. Wise

University of Bristol

February 2021

Acknowledgements

Firstly, I thank Paul for being such a dedicated supervisor and mentor. While teaching me so much about organophosphorus and transition metal chemistry, you have allowed me to develop independently as a researcher and shape the direction of my projects. I also thank Jason Lynam for his immense support on a biomedical collaboration. I am truly grateful for the opportunities afforded to me by my supervisory team.

My time in the Pringle group would not have been the same without my fantastic colleagues. To all Pringles – Charley Faradji, Louise Hazeland, Adam Gorman, Hubert Meissel, Lexy Miles-Hobbs, Ailis Chawick, Callum Branfoot, Rachel Doyle, Sarah Williams, Ashley King, Rachel Nuttall, Derek Durand and Daniel Good – thank you for everything! You have been a great group to go to the pub with, where invariably, we would end up (lunging) in La Rocca. Thank you for the Christmas party karaoke.

A special mention to the 2016 cohort of the Synthesis CDT – what a way to start a PhD! We definitely earned that title of 'the fun ones' and for many happy hours spent in the hub, (the pub), the beaches of Majorca, as well as always being on hand with chemicals to borrow – thank you.

Thanks to all the people that made my research possible. Emma, Mar, Laura, and Kev for making the CDT tick. A huge thank you to Hazel Sparkes and Natalie Pridmore in X-ray crystallography, Natalie Fey for computational chemistry, Paul Lawrence in NMR, and Tony Rodgers for his technical support and everything he does for the SCB. Thanks also to Karen and Jo for assistance during my trips to York.

A massive thank you to my family for all the support, both during my undergrad and PhD years in Bristol. It has been incredible.

Thank you to Emma.

Collaborator acknowledgements and publications

Chapter 2 is based on the publication 'Cytotoxic (*cis,cis*-1,3,5-triaminocyclohexane)ruthenium(II)–diphosphine complexes; evidence for covalent binding *and* intercalation with DNA,' D. E. Wise, A. J. Gamble, S.W. Arkawazi, P. H. Walton, M. C. Galan, M. P. O'Hagan, K. G. Hogg, J. L. Marrison, P. J. O'Toole, H. A. Sparkes, J. M. Lynam and P. G. Pringle. A significant amount of this chapter is reproduced from *Dalton Trans.*, **2020**, 49, 15219–15230.

Chapter 3 contains compounds prepared by the author and biological testing was carried out in collaboration with Dr. Karen Hogg and Dr. Joanne Marrison at University of York.

Chapter 4 contains compounds prepared by the author. The photophysical measurements and DFT calculations were carried out by the author, with guidance provided by Dr. Natalie Fey and Dr. Lee Higham.

The work described in Chapters 3-5 is yet unpublished and was performed by the author.

Chapter 6 describes the experimental and supporting information for Chapters 2-5.

Contents

Table of Contents

Abbreviations

General

AcO	acetyl
app.	apparent
Ar	aryl/aromatic
cod	cyclooctadiene
DBA	dibenylideneacetone
DCC	dicyclohexylcarbodiimide
DFT	Density Functional Theory
DIPEA	diisopropylethylamine
DMAP	4-dimethylaminopyridine
DMF	dimethylformamide
DMSO	dimethylsulfoxide
dppa	bis(diphenylphosphino)amine
dppb	1,4-bis(diphenylphosphino)butane
dppbz	1,2-bis(diphenylphosphino)benzene
dppe	1,2-bis(diphenylphosphino)ethane
dppm	1,1-bis(diphenylphosphino)methane
dppp	1,3-bis(diphenylphosphino)propane
eq	equivalents
Et	ethyl
Fc	ferrocenyl
FLP	Frustrated Lewis Pair
g	gram(s)
h	hour(s)
HATU	(1-[Bis(dimethylamino)methylene]-1H-1,2,3-triazolo[4,5-b]pyridinium 3-oxide hexafluorophosphate
HOMO	Highest Occupied Molecular Orbital
^{i}Pr	iso-propyl
K	Kelvin
L	ligand
LUMO	Lowest Unoccupied Molecular Orbital
M	metal
m	meta
Me	methyl
Mes	mesityl
min	minute(s)
mmol	millimole(s)
mol	mole(s)
^{n}Bu	normal-butyl
nm	nanometre(s)
Np	naphthyl
o	ortho
p	para
PeT	photoinduced electron transfer
Ph	phenyl
Pyr	pyrenyl
R	aryl or alkyl substituent
SOMO	Singly Occupied Molecular Orbital
^{t}Bu	tertiary-butyl
TFA	trifluoroacetic acid
TfO	trifluoromethanesulfonic
THF	tetrahydrofuran
tht	tetrahydrothiophene
TMS	trimethylsilyl
TsO	*p*-toluenesulfonic
UV	ultra-violet

Spectrochemical

{^{1}H}	proton decoupled
A	absorbance
br.	broad
d	doublet
dd	doublet of doublets
dt	doublet of triplets
EI	electron ionisation
Elem. Anal.	elemental analysis
ESI	electrospray ionisation
GC	gas chromatography
hept	heptet
HR-MS	high-resolution mass spectrometry
IR	infra-red
J	coupling constant
m	multiplet
M^{+}	molecular ion
m/z	mass/charge ratio
NMR	nuclear magnetic resonance
ppm	parts per million
q	quartet
quat.	quaternary
s	singlet
t	triplet
vt	virtual triplet
Φ	quantum yield
$\omega_{1/2}$	peak width at 50% intensity
δ	chemical shift
ν	stretching frequency

Chapter 1. Introduction

This thesis describes discoveries in the applications of metal-phosphine complexes in two quite different areas of research: chemotherapy and homogeneous catalysis. For this reason, this Introduction contains elements for both of these aspects to provide context for the experimental results given in subsequent chapters.

There is a consistent drive to improve the safety and efficacy of cancer treatments and make them available to as many patients as possible. In 2018, there were 17 million new cases of cancer worldwide, which is predicted to rise to 28 million per year by 2040.[1] To help address this issue, industry and academia are developing metal-based chemotherapeutics with various modes of action to overcome the problems associated with the toxic side effects and emerging resistance that are prevalent in cancer treatment today.

There is currently an imperative to develop sustainable production processes for bulk and fine chemicals and catalysis will undoubtably have a pivotal role to play in achieving this objective. For over half a century, phosphorus(III) ligands have been central to the development of metal complex catalysts for a plethora of chemical transformations. Four Nobel Prizes in chemistry have been awarded for innovations in which phosphorus(III) ligands have played a significant part in their success: in 2001 (Knowles and Noyori) for asymmetric hydrogenation;[2] in 2005 (Chauvin, Grubbs and Schrock) for olefin metathesis methods;[3,4] in 2010 (Heck, Negishi and Suzuki) for Pd-catalysed cross-coupling;[5,6] and in 2016 (Sauvage, Stoddart and Feringa) for molecular machines.[7,8] This impressive record of success is partly due to the tunability of phosphorus(III) ligands, whereby the stereoelectronic properties can be modulated to tailor the ligand by judicious choice of P-substituents.

There are important examples of metal complexes of P(III) ligands used in medicine including clinically approved pharmaceuticals (Figure 1.1). One of the most widely used radioisotopes in modern medicine is ^{99m}Tc, known as the "Workhorse of Diagnostic Nuclear Medicine".[9] Myoview is an important heart imaging agent, based on a [$^{99m}TcO_2$] core with two coordinated tetrafosmin diphosphine ligands. This bidentate P(III) ligand has been specifically selected to confer the required lipophilicity and bioavailability that makes Myoview so effective in myocardial perfusion imaging.[10]

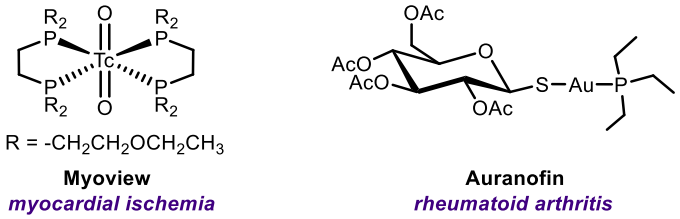

Figure 1.1. Chemical structures of phosphine containing pharmaceuticals.

Auranofin is a Au(I) compound that received FDA approval for the treatment of rheumatoid arthritis in 1985. Following the clinical success of auranofin, the development of Au–phosphine complexes for therapeutic applications, including anti-cancer agents, has accelerated. Auranofin is a key candidate for drug repurposing and has since been investigated for its activity against leukaemia, ovarian cancer, and microbial infections.[11]

1.1 Metals in medicine

1.1.1 Cytotoxic Pt complexes

Since its serendipitous discovery in 1965 by Rosenberg, cisplatin has become one of the most broadly administered chemotherapeutics.[12] Following the success of cisplatin, second and third generation Pt therapies (carboplatin and oxaliplatin respectively) have been developed with six derivatives in total gaining clinical approval worldwide (see Figure 1.2).[13–16] Around 50% of all cancer patients who require chemotherapy receive at least one form of Pt-based therapy.[17] Due to its consistent and widespread use, coupled with high toxicity (cisplatin cannot differentiate between cancerous cells and non-cancerous cells), Pt-based therapy can be considered a palliative treatment for many types of cancer, rather than a cure.[18] While the development of Pt-based therapies remains an active area of research, the continued use of these drugs is constrained by dose-limiting side effects, such as nephrotoxicity, neurotoxicity, and ototoxicity, due to a lack of selectivity for cancer cells.[19] For example, it has been reported that between 40–80% of all adults and 50% of children treated with cisplatin develop permanent hearing loss.[20] Another disadvantage for the persistent use of cisplatin is the propensity for cancers to mutate and acquire resistance.

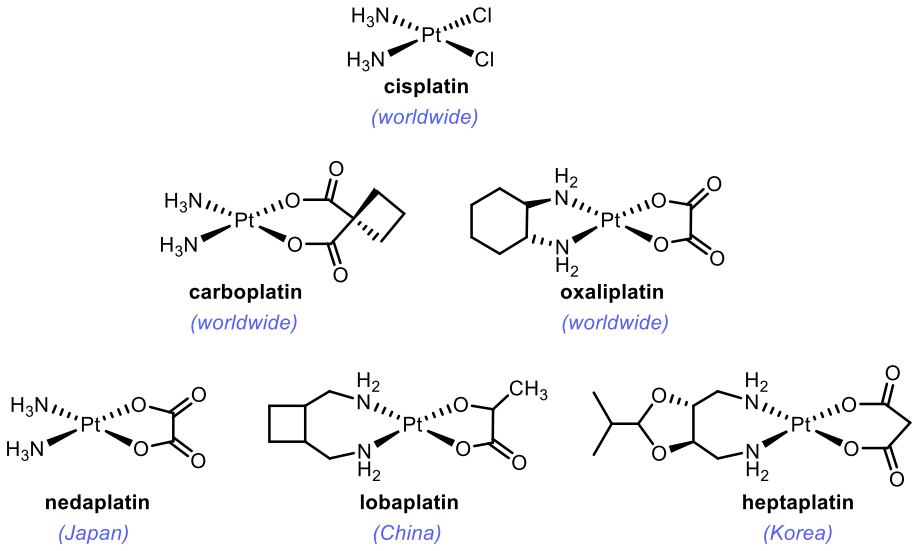

Figure 1.2. Chemical structures of clinically approved Pt complexes.

The mechanism of action for cisplatin is widely believed to be as follows (Figure 1.3).[21,22] First, introduction of cisplatin into the blood stream occurs via intravenous administration. The chloride concentration in the blood is high (100 mM) and hence aquation of the Pt–Cl bond is suppressed. It is then understood that cisplatin is transported into the cell by passive and facilitated diffusion. Once inside the cell, the lower chloride concentration (20 mM) allows aquation of one, or both Pt–Cl bonds. Deprotonation of the Pt–OH_2 complex to give the less reactive Pt–OH species can occur.[23] Another important deactivation mechanism involves *S*-coordination of glutathione (GSH), increased expression of which is associated with cisplatin resistance.[19] Overall, only a small percentage of the administered Pt reaches its target: the cell nucleus. Once inside the nucleus, the mono-aqua species *cis*-$[PtCl(NH_3)_2(OH_2)]^+$ is substituted at the site of the coordinated water ligand by a DNA base, primarily at the N7 site of guanine residues.[24] Once the DNA is platinated, substitution of the labile chloride ligand with a second DNA base forms the active Pt-DNA metallacycle, with intrastrand 1,2-d(GG) cross-linking predominating. Although duplex DNA platination is thought to be the primary mode of action, most of the Pt does not end up bound to DNA and the remainder are likely a major cause of the cytotoxicity through binding to other cellular targets.

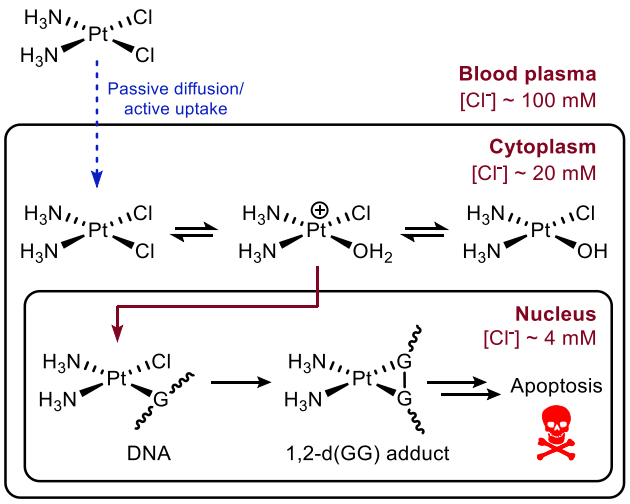

Figure 1.3. Primary mechanism of cell death by covalently binding to DNA via intrastrand 1,2-d(GG) cross-linking.

The emergence of Pt-resistant cancers has necessitated the development of alternative therapies. Generally, resistance mechanisms fall into one of two categories: (i) those that limit the formation of Pt-DNA adducts; or (ii) those that prevent cancer cell death following Pt-DNA adduct formation. For comprehensive reviews of metal based anticancer agents, see the work of Bonsignore, Capellá and McFarland.[25–27] The use of different metals will enable the development of anti-cancer agents that present alternative modes of action and diverse interactions with biomolecules, and therefore, may overcome the limitations of Pt-based therapy.[9] The next section details the most widely studied non-Pt, metal-based anticancer compounds: cytotoxic Ru complexes.

1.1.2 Cytotoxic Ru complexes

The first ruthenium complex tested for its anti-tumour properties was a ruthenium analogue of cisplatin, *fac*-[$RuCl_3(NH_3)_3$] (**1.1**, Figure 1.4).[28] The compound was found to inhibit cell division in *E. coli* which served as an initial proof-of-concept for the activity. Further development of this compound was halted due to its poor aqueous solubility and attention was directed towards ionic compounds with more halide ligands to improve aqueous solubility.[29]

The results of the initial phase I/II clinical trials of NAMI-A (**1.2**) were reported by Leijen *et al.* in 2015.[30] Following this, Keppler *et al.* published the synthesis and activity of indazolium *trans*-[tetrachloridobis(1*H*-indazole)ruthenate(III)] (KP1019, **1.3**) and the more aqueous-soluble sodium salt (NKP-1339, **1.4**).[31] The phase I clinical trials were successfully completed and noted very promising anticancer activities with low general toxicity and very limited adverse side effects. One useful feature of Ru(III) complexes **1.2-**

1.4 is that they are chemically inert and can be reduced to their more cytotoxic Ru(II) analogues in the hypoxic environment of tumour cells. This 'activation-by-reduction' approach has been exploited as a drug delivery method.[28,32]

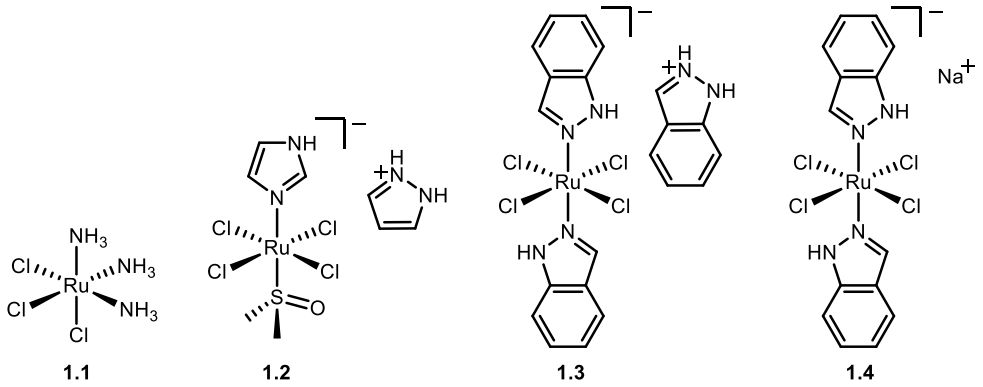

Figure 1.4. Chemical structures of early Ru anti-cancer agents.

Many studies have explored transport of Ru *in vivo*, thought to be facilitated by Fe transporters. Due to the similarities that Ru shares with Fe because of its position in the periodic table, Ru readily binds to nitrogen and sulfur donors and can therefore be transported by serum albumin and transferrin proteins. As the surface of cancer cells have a high concentration of transferrin receptors, Ru compounds target cancer cells and bypass non-cancer cells leading to a clear increase in selectivity and reduced toxicity.[31,33,34] The field of inorganic chemotherapeutics is constantly developing compounds with increased anti-tumour activity and reduced side-effects. Broadly, the cytotoxic Ru complexes that are under development today can be divided into three categories: (i) Ru–arene complexes; (ii) Ru half-sandwich complexes; (iii) Ru–polypyridyl complexes. All three of these categories of complexes are discussed below.

1.1.2.1 Ru–arene complexes

Organoruthenium complexes containing a facially capping arene ligand have been widely researched, notably by the groups of Sadler and Dyson, as well as many others.[35,36] In 2001, the first examples investigated for their anticancer activity by Dyson *et al.* contained an η^6-*p*-cymene ligand which provided a robust hydrophobic face to the molecule, and a 1,3,5-triaza-7-phospha-tricyclo-[3.3.1.1]decane (PTA) ligand to provide good aqueous solubility (**1.5**).[37] Due to their modular synthesis, many variants (>30) of these so-called RAPTA (Ruthenium-Arene-PTA) complexes **1.5** have been tested and they constitute one of the most promising classes of ruthenium anti-cancer drugs currently progressing through clinical trials.[33,38] Gasser *et al.* recently reported light-activated RAPTA derivatives bearing

azido ligands.[39] In aqueous conditions, the complexes are inert, but under irradiation (λ = 450 nm), slowly release the azido ligand, at which point an increase in toxicity in human cervical carcinoma (HeLa) cells under light exposure was observed.

Concurrently, Sadler *et al.* reported on the tumour growth inhibition by a series of ruthenium biphenyl complexes with a chelating diamine ligands, (RAen complexes, such as **1.6**, Figure 1.5).[40,41]

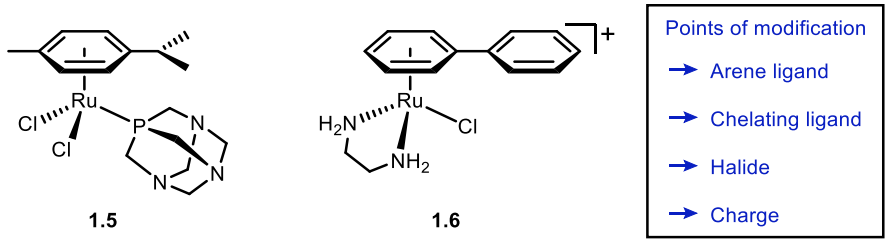

Figure 1.5. Original (arene)Ru complexes studied by Dyson and Sadler.

Loss of the arene ligand has been observed in some RAPTA complexes, although the contribution of this to the activity has not been elaborated.[33,42] While these complexes can covalently bind to DNA, studies have shown that the main mechanisms of cytotoxicity involve interactions with proteins, in a similar manner to NAMI-A (**1.2**).[38,43–45]

Larrosa and co-workers have recently investigated an (η^6-*p*-cymene)Ru arylation catalyst. It was shown that at elevated temperatures (80 °C) the bound η^6-arene ligand decoordinates rapidly and through a series of kinetics experiments it was found that free *p*-cymene inhibits the directed arylation catalysis.[46] This observation makes it feasible that η^6-arene dissociation at physiological temperature takes place to some degree.

1.1.2.2 Half-sandwich organoruthenium complexes

Based on the established cytotoxic properties of the above (arene)Ru complexes, Alessio *et al.* studied structure-activity relationships (SARs) to establish whether the η^6-arene ligand is essential for biological activity. They focused on complexes where the arene ligand was replaced with a neutral 6-electron donor such as 1,4,7-trithiacyclononane ([9]aneS3, **1.7**) and 1,4,7-triazacyclononane ([9]aneN3, **1.8**) (Figure 1.6). The compounds bearing a [9]aneS3 and chloride ligand **1.7** showed moderate activity *in vitro* against breast carcinoma (MDA-MB-231), for NN = 1,2-diaminoethane (IC_{50} = 80 μM) and NN = 1,2-diaminocyclohexane (IC_{50} = 124 μM). These *N*-ligand complexes were around 10 times less active than the analogous (arene)Ru complex (**1.6**, IC_{50} = 10 μM).[47,48]

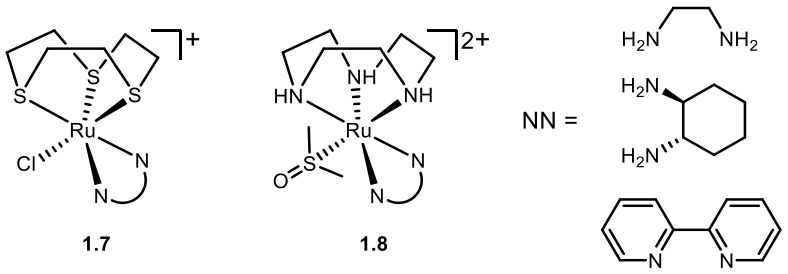

Figure 1.6. Chemical structures of representative Ru complexes of [9]aneS3 and [9]aneN3, Alessio *et al.*[48]

Despite this reduced activity compared to (arene)Ru complex **1.6**, it was argued that the features required for cytotoxicity are still present in some of these complexes: (i) a Ru–Cl bond that can undergo rapid aquation, and (ii) the ability for the chelating ligand NH_2 groups to form hydrogen bonds that could stabilise interactions with biomolecules. The complexes with [9]aneN3 that retained one DMSO ligand in the coordination sphere were found to be inactive up to the concentrations tested (IC_{50} > 300 μM).[48]

1.1.2.3 Ru–polypyridyl complexes

Cytotoxic Ru–polypyridyl complexes have been developed due to their favourable DNA binding and photophysical properties. The field has been the subject of many recent reviews.[18,26,49,50] Most studies on metal-based chemotherapeutics have concentrated on irreversible DNA binding (see Section 1.1.1). Many Ru–polypyridyl complexes are of interest due to their ability to reversibly bind DNA via three main mechanisms: (i) intercalation of the planar aromatic ligands in between DNA base pairs, (ii) binding of the complex within the major or minor groove of the DNA double helix, and (iii) external binding of positively charged drugs to the negatively charged phosphate backbone.[51]

Alessio *et al.* reported Ru–terpyridine complexes **1.9** that adopt a meridional configuration and found a correlation between lipophilicity and potency (Figure 1.7). The aquation rate constants for these complexes (2.0 – 9.7 $\times 10^{-3}$ s^{-1}) did not correlate with the Ru–Cl bond lengths, possibly indicating some degree of an associative interchange (I_a) pathway for aquation. This mechanism has also been suggested for $[(arene)RuCl(en)]^+$ complexes, such as **1.6**.[50] The rate constants for aquation of the Pt–Cl bonds in cisplatin are of the order of ~10^{-5} s^{-1}, notably slower than for **1.9**.[50,52] The (Ph-tpy)Ru complexes (**1.9**) can interact with DNA, both by covalent binding and by intercalation (Figure 1.8). For these derivatives, binding to calf thymus (CT)-DNA was found to be moderate to strong, as indicated by the binding constants determined (K_b ~ 10^3 – 10^5 M^{-1}).

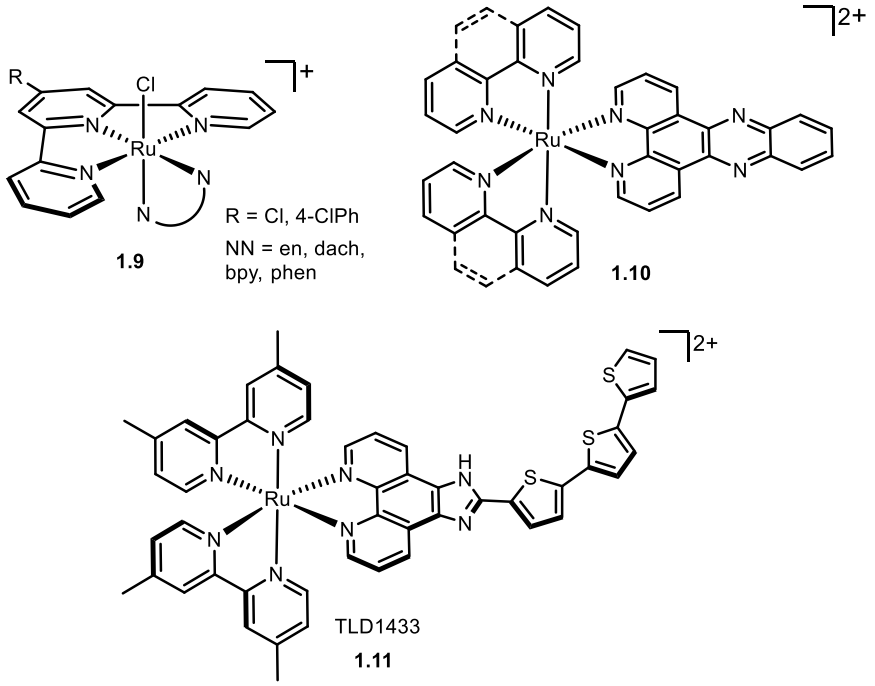

Figure 1.7. Chemical structures of representative Ru–polypyridyl complexes.

The main mode of action studied for polypyridyl complexes is DNA intercalation, which was initially reported by the groups of Barton and Sauvage for $[Ru(bpy)_2(DPPZ)]^{2+}$ (DPPZ = dipyrido[3,2-a:2',3'-c]phenazine).[53–55] Complexes of the type depicted in Figure 1.7 (**1.10**) were shown to have a high binding affinity for DNA (binding constants, $K_b \sim 10^6$ M^{-1}).[56,57] They also display luminescence upon addition of DNA due to the highly conjugated ligand structures. The increase in luminescence emission intensity from these complexes is only observed after DNA addition; thus, the term 'light-switch effect' was coined for complexes of this type. Ru–polypyridyl complexes have been developed for use in photodynamic therapy (PDT) and photochemotherapy (PCT).[26,58–63]

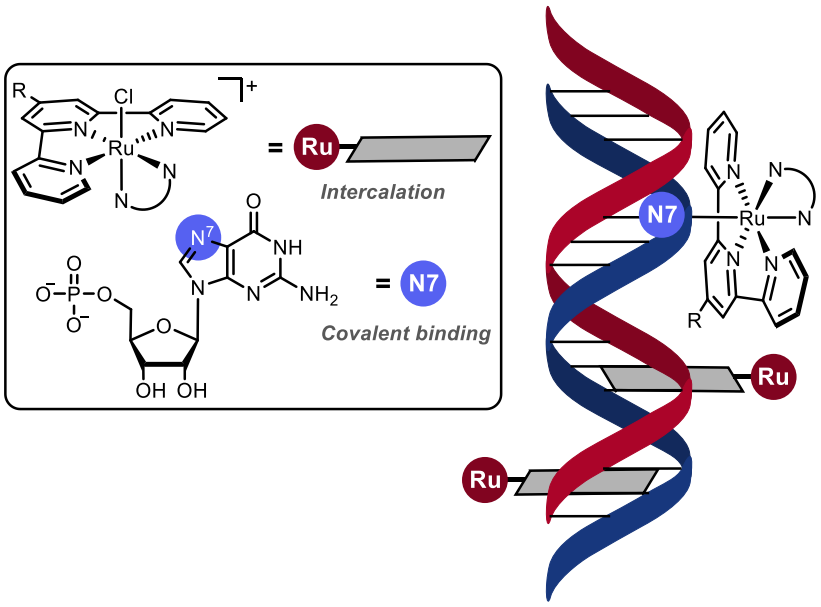

Figure 1.8. Representation of the different binding modes of **1.9** with DNA, adapted from reference 50.

The first of this class of compounds to enter human clinical trials was TLD1433 (**1.11**) which contains a terthienyl chromophore.[26] In 2020, the company that produce TLD1433, Theralase Technology, were granted FDA approval for a Fast-Track Phase II clinical trial in non-muscle invasive bladder cancer (NMIBC).[64] A Fast-Track Designation can lead to accelerated approval and priority review; therefore, if the trial meets the criteria, TLD1433 could become the first patient-specific Ru-based PDT to gain FDA approval. Moreover, it would be the first clinically approved Ru-based chemotherapy agent.

In a recent development, Theralase Technology have commenced research at the *in vitro*, preclinical stage, utilising Photodynamic Compounds (PDC), specifically TLD1433 for vaccine development against SARS-CoV-2.[65] If the initial *in vitro*, and subsequent small animal *in vivo* studies are successful, Theralase could commence human clinical studies in 2021, using TLD1433 to tackle coronavirus. This highlights the power of drug repurposing in the fight against infectious diseases. Complexes, such as TLD1433 (**1.12**), where the metal acts as a central scaffold to which active ligands are conjugated and ancillary ligands are used to modulate cellular uptake warrant further study.

1.2 Ruthenium *cis*-tach complexes

With most cytotoxic Ru drug candidates comprising either arene or polypyridyl ligands, there is a wide scope for investigating purely coordination, heteroleptic complexes. There is literature precedent for using the neutral tridentate ligand *cis,cis*-1,3,5-

triaminocyclohexane (*cis*-tach) as a facially capping ligand for various metal centres. There are three main reasons for using *cis*-tach as a facially capping ligand for biological applications: (i) the amine groups improve the water solubility of the metal complexes and may aid binding by forming hydrogen bonds with biomolecules; (ii) the amine groups are good σ-donors and therefore have a large trans effect; (iii) the cyclohexane ring provides a hydrophobic face to the complex, giving steric protection to the hydrophilic metal centre.

1.2.1 Synthesis of *cis*-tach complexes

The synthesis of *cis*-tach from *cis,cis*-1,3,5-cyclohexanetricarboxylic acid, originally reported by Brechbiel *et al.*, and later by Cronin and co-workers involves formation of the tris(benzylcarbamate) as the Curtius rearrangement product.[66,67] The carbamate groups are cleaved by hydrobromic acid to give *cis*-tach.3HBr. The free amine ligand is obtained as a hygroscopic, crystalline solid by treatment of *cis*-tach.3HBr with an anion exchange resin followed by purification by sublimation (Scheme 1.1).

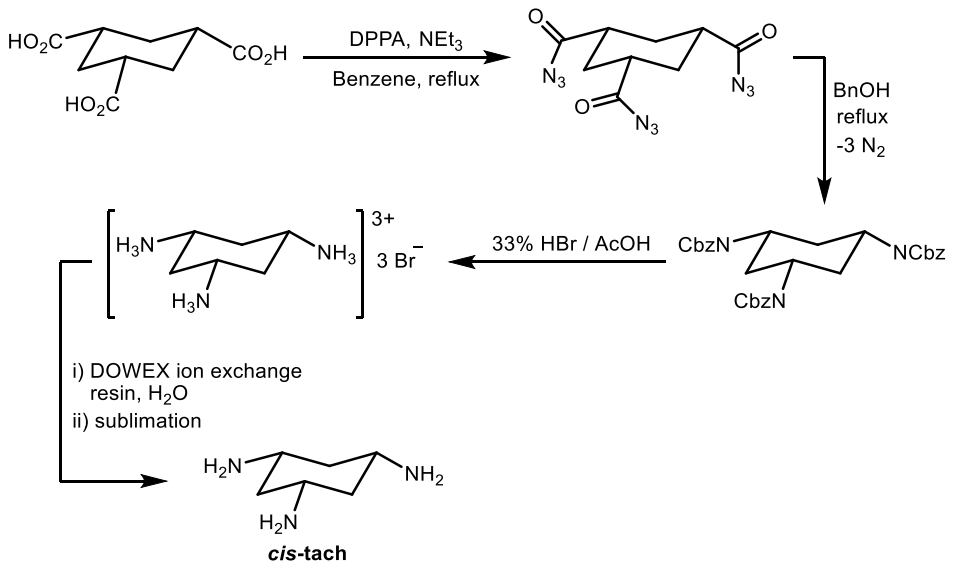

Scheme 1.1. Synthesis of *cis*-tach.[66,67]

When in solution, the cyclohexane ring of the *cis*-tach ligand adopts a conformation that makes all the amine substituents equatorial. When *cis*-tach is treated with suitable metal precursors, it can undergo a ring-flip, whereupon the amine substituents are all in an axial position and the metal centre becomes one of the vertices of an adamantane-type structure (Scheme 1.2). The *cis*-tach provides a robust platform for the synthesis of chemically diverse metallodrugs. A report has highlighted the lack of 3D complexity in pharmaceuticals (e.g., C(sp^3)-rich molecules).[68] Recently, a library of metal-based

fragments has been developed that cover a larger region of 3D chemical space than purely organic compounds.[69]

The amine groups of *cis*-tach are readily functionalised by condensation with aldehydes, resulting in tridentate imine ligands (Scheme 1.2).[70,71] The imine substituents can contain coordinating groups (such as pyridyl, see Scheme 1.3) generating a hexadentate ligand or the groups may be non-coordinating (see examples from Cronin and Walton, Figure 1.9).

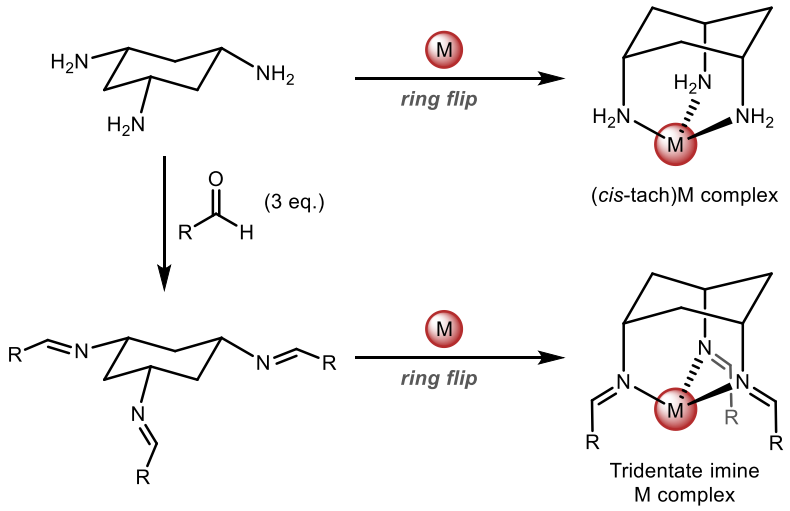

Scheme 1.2. Coordination of *cis*-tach to a metal centre and condensation with aldehydes to form a tridentate imine ligand.

1.2.2 Coordination chemistry of *cis*-tach

The versatility of *cis*-tach has enabled the synthesis of many mononuclear complexes containing different metal ions (Figure 1.9). The first metal *cis*-tach complexes took the form $[M(cis\text{-tach})_2]^{n+}$ (M = Ni, Co, Rh, **1.12**) and were analogues of organometallic sandwich complexes.[72] Following these initial discoveries, Erickson *et al.* reported a 6-coordinate Pt(IV) complex bearing a coordinated bipyridine and *cis*-tach ligand (**1.13**).[73] The acid dissociation properties of the NH_2 groups of the *cis*-tach ligand were studied but activity against cancer cells was not explored.

A Cu(I) complex bearing the unusual *cis,cis*-1,3,5-tris(2-fluoro-6-(trifluoromethyl)benzylideneamino)cyclohexane ligand (**1.14**) was reported by Wass *et al.* and was shown to reversibly bind ethylene under mild conditions.[74] Several Zn, Co and Cu complexes with cinnamaldehyde functionalised *cis*-tach ligands were reported by the Walton[75] (**1.15**) and Cronin[67] (**1.16**) groups. These complexes were investigated as a model system for carbonic anhydrase due to the similarities between the metal coordination environment and the active site of the enzyme.[67,75] The cytotoxicity of complexes **1.12-**

1.16 has not yet been reported. Fontaine and co-workers reported the synthesis and solid-state characterisation of Pt(II) complexes containing phosphine-substituted *cis*-tach ligands (**1.17**).[76]

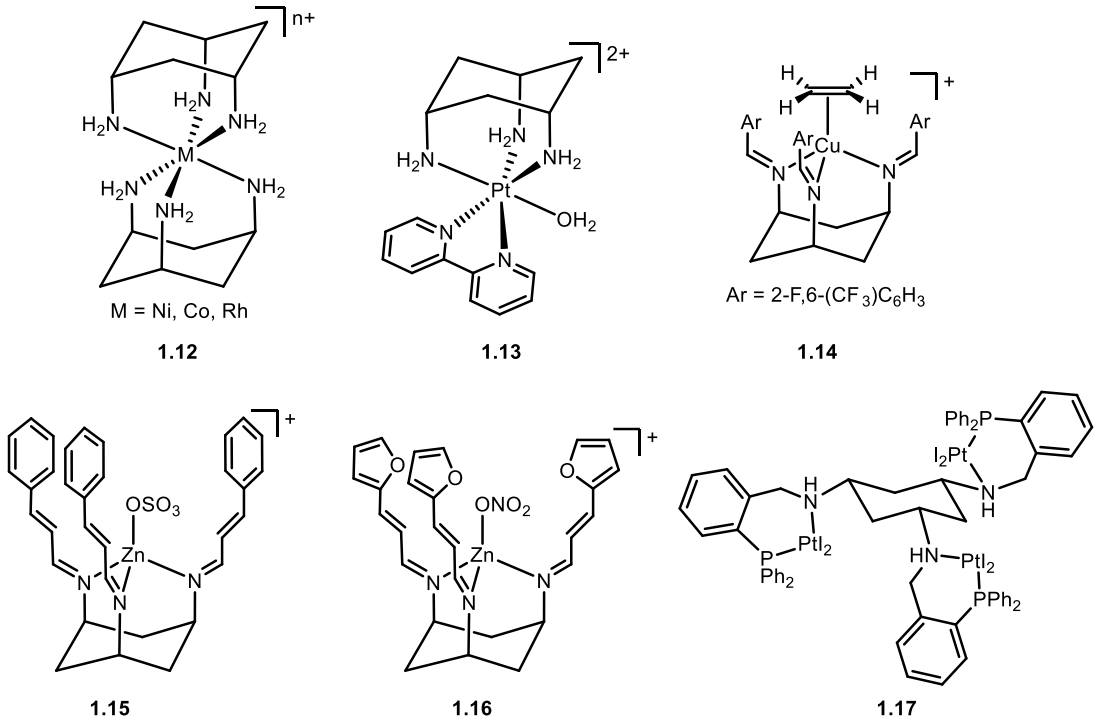

1.12 **1.13** **1.14**

1.15 **1.16** **1.17**

Figure 1.9. Chemical structures of previously reported metal *cis*-tach complexes, **1.12**-**1.17**.

1.2.3 Cytotoxicity of *cis*-tach complexes

Many *cis*-tach derivatives and other chelators are of interest for their cytotoxic properties.[77–81] The tachpyr ligand **1.18** (a 2-pyridylmethylene substituted *cis*-tach derivative) has been tested against MBT2 and T24 bladder cancers as well as A549 lung adenocarcinoma cells. The effectiveness of these compounds is attributed to the fact that rapidly growing cancer cells metabolise iron faster than non-cancerous cells, and the tachpyr ligand can efficiently bind Fe(II) ions (Scheme 1.3).[77,80] When the NH groups of tachpyr were substituted with methyl or ethyl groups, these derivatives could not bind Fe(II) ions and were found to be non-cytotoxic, consistent with iron depletion in tumour cells being involved in the mechanism of action.

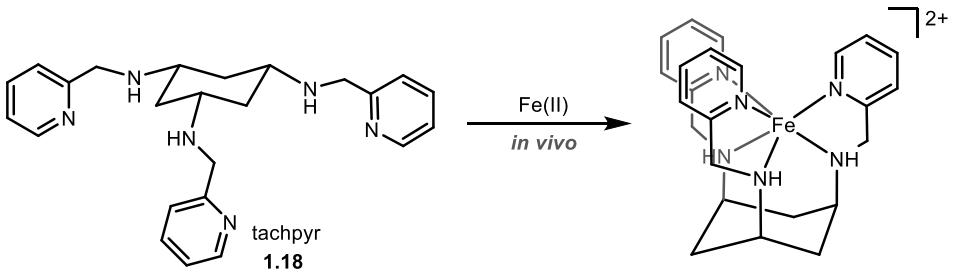

Scheme 1.3. Binding of tachpyr (**1.18**) to Fe(II) ions *in vivo*.

In 2013, Lynam *et al.* reported the synthesis of a new class of Ru half-sandwich complexes resulting from the reaction of *cis*-tach and *cis*-[$RuCl_2(DMSO)_4$] (Scheme 1.4). The labile complex [RuCl(DMSO-*S*)$_2$(*cis*-tach)]Cl (**1.19**) is the precursor to complexes with commercially available bidentate amine or phosphine ligands (Scheme 1.5).[82] Their study concerned the influence of the *cis*-tach and chelating ligands on features such as the Ru–Cl bond length, and compared these to the (arene)Ru analogues. It was demonstrated that *cis*-tach is a strong σ-donor, as would be expected due to the three nitrogen donors coordinated to the metal.

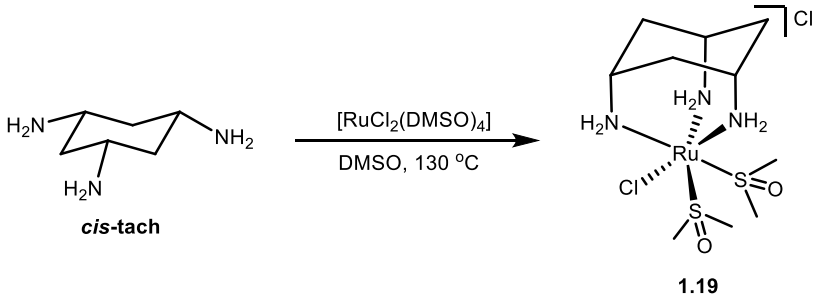

Scheme 1.4. Synthesis of [RuCl(DMSO-*S*)$_2$(*cis*-tach)]Cl (**1.19**).[82]

Interestingly, it was found that reaction of **1.19** with diamines yielded dicationic complexes retaining one DMSO ligand, whereas treatment of **1.19** with diphosphines gave complexes with a chloride ligand bound.[I] It was reasoned that the electron-rich Ru(*cis*-tach)(diphos) moiety may promote aquation of the Ru–Cl bond which might then result in enhanced *in vitro* activity.[81,83]

[I] A similar phenomenon is observed with the [9]aneS3 and [9]aneN3 derived complexes reported by Alessio *et al.* (see Figure 1.6).

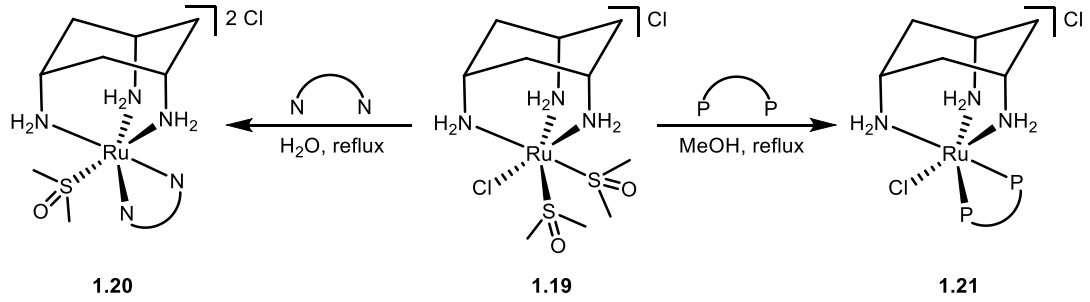

Scheme 1.5. Synthesis of *N,N*-chelate (**1.20**) and *P,P*-chelate complexes (**1.21**) previously reported (*N,N*- = bipyridine, phenanthroline, ethylenediamine; *P,P*- = dppm, dppe, dppp, dppb, dppv, dppbz).[82]

In recently published work, we have found that the *P,P*-chelate complexes (**1.21**) are cytotoxic, whereas the *N,N*-chelate complexes (**1.20**) are not.[84,85] For further details of the investigation of the anti-proliferative properties of (*cis*-tach)Ru complexes, see Chapter 2.

1.3 Metallodrug conjugates

1.3.1 Targeted therapy

It can be advantageous to covalently conjugate a metallodrug with a biomolecule that confers specific targeting functionality. Multitargeted complexes have been designed to overcome some of the main limitations associated with Pt-based therapy. For example, due to the Warburg effect, cancer cells rely much more heavily on anaerobic glycolysis than non-cancerous cells.[86–89] Therefore, many Pt(II) drugs conjugated with carbohydrates have been developed that target the glucose transporter (GLUT) membrane proteins which are overexpressed on the surface of cancer cells.[90] Several Pt(II) drugs conjugated with biomolecules have been developed that target receptors for testosterone, estrogen, folate, somatostatin, epidermal growth factor (EGFR), and integrins. These complexes, highlighted in the recent review by Marmion *et al.*,[87] have been specifically designed to overcome dose-limiting, toxic side effects and circumvent resistance, while increasing therapeutic efficacy. Many Pt(IV) prodrugs decorated with targeting groups are also known.[91–93]

The first targeted Ru-based chemotherapy agents were derivatives of the biologically active molecule staurosporin (**1.22**), reported by Meggers *et al.*[94] The Ru centre was not found to be biologically active and simply acted as an appropriate scaffold for the bioactive ligand. In another approach, the Keppler group developed Ru complexes with cyclin-dependent-kinase (CDK) inhibiting paullone ligands (**1.23**) that showed intercalative binding with DNA (Figure 1.10).[95] Following this, many of the subsequent

examples of targeted cytotoxic Ru agents were based on the heavily studied (arene)Ru complexes reported by Sadler and Dyson (see Section 1.1.2.1). Many proteins that are upregulated in cancer cells have been the targets of such complexes (see Marmion *et al.*[87]).

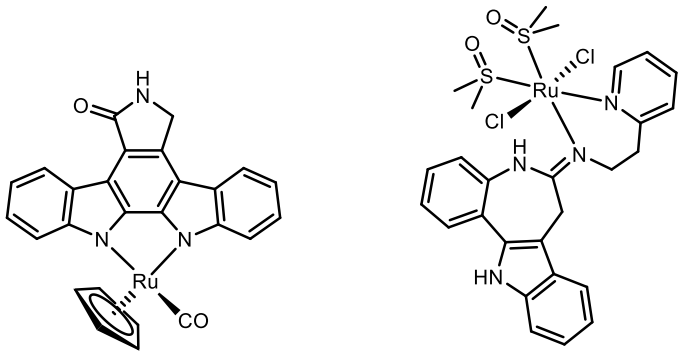

Figure 1.10. Chemical structures of Ru staurosporin derivative (R)-DW12 (**1.22**) and CDK-inhibiting Ru paullone derivative (**1.23**).

Targeted conjugates of Ru polypyridyl complexes have been reported. For example, TLD1433 (**1.11**) which contains a terthienyl chromophore has been shown to be an effective PDT agent and is progressing through Phase II clinical trials.[26,96] Recently, peptide-conjugated Ru(II) complexes featuring the [9]aneS3 facially capping ligand were reported by Metzler-Nolte *et al.* (Figure 1.11).[97] The hexapeptide sequence neurotensin (RRPYIL) was conjugated to a 2-(2'-pyridyl)pyrimidine-4-carboxylic acid (cppH) ligand via amide bond formation to give **1.24**. The stereochemical features of the complexes were investigated in aqueous and organic media, but unfortunately the compounds were found to be non-cytotoxic against colon adenocarcinoma (HT-29), breast cancer (MCF-7) and pancreatic cancer (PT-45) cells.

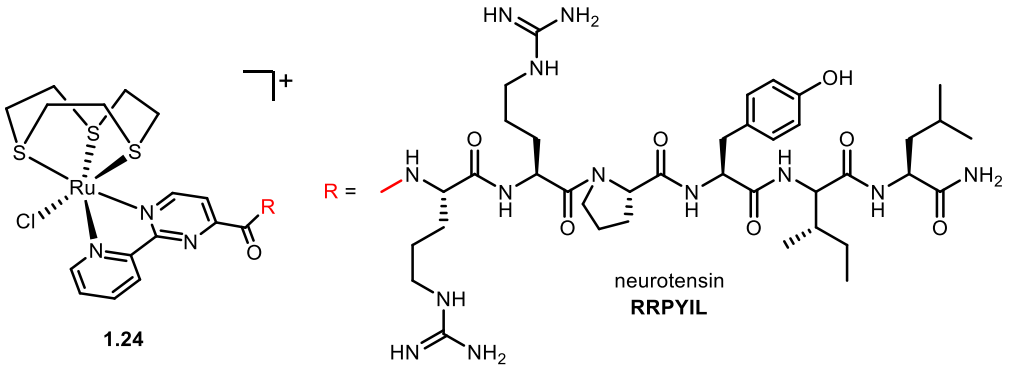

Figure 1.11. Chemical structure of $[([9]aneS3)RuCl(cppH\text{-}RRPYIL)]^+$ (**1.24**).[97]

The ability to chemically conjugate a chelating ligand, such as a diphosphine, with a biomolecule (or other small molecule) is desirable for applications in biological imaging,

therapy, and catalysis. By chemically modifying an ancillary ligand with an organic fluorophore, the resulting fluorescent complexes can lead to an understanding of the biological modes of action.[98,99] The following Section gives background to luminescence and selected examples pertinent to bioinorganic chemistry.

1.3.2 The role of luminescence in cancer diagnosis and therapy

Luminescence is the emission of light from an electronically excited state by radiative fluorescence or phosphorescence processes, which can be illustrated by a Jablonski diagram (Figure 1.12). Under typical conditions the molecule is in one of its ground states (S_0). Upon absorption of a photon ($h\nu_A$), one electron may be promoted to one of its excited states (e.g., $S_0 \rightarrow S_1$). For fluorescence to occur, in accordance with Kasha's Rule, the molecule relaxes to the lowest excited vibrational energy level through a non-radiative transition (which may include internal conversion, e.g., $S_2 \rightarrow S_1$) before emitting a photon at a longer wavelength ($h\nu_F$).[100] Electrons in the S_1 state can undergo intersystem crossing (ISC) to the first excited triplet state (T_1) which, after vibrational relaxation, will emit a photon via phosphorescence ($h\nu_P$), typically at a longer wavelength than fluorescence. The emission wavelength for a fluorescent molecule is invariably at longer wavelength (lower energy) than the absorption wavelength due to internal conversions that take the electron from the excited vibrational energy level to the lowest vibrational S_1 energy level.[100]

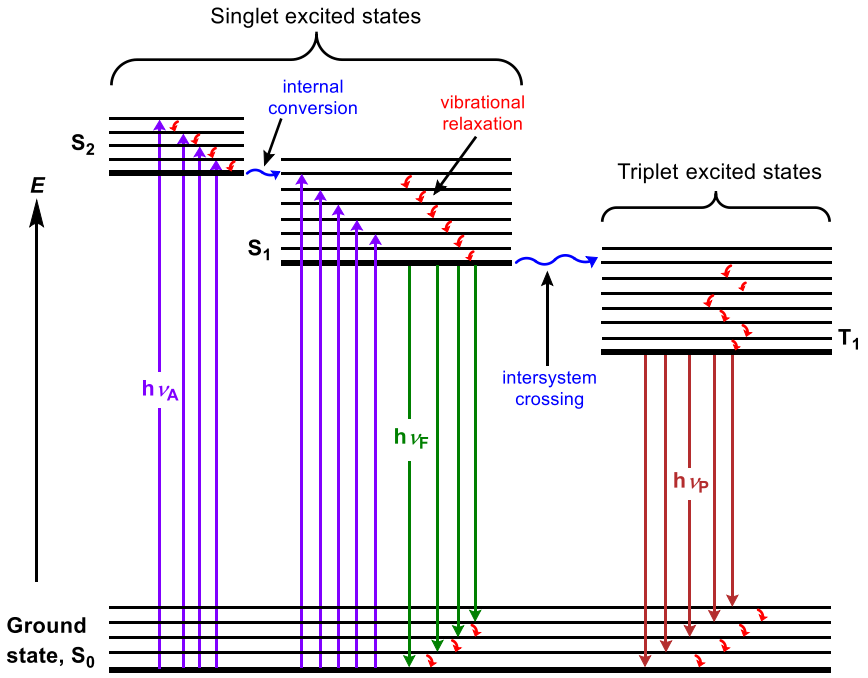

Figure 1.12. Jablonski diagram illustrating the main radiative decay processes following absorption ($h\nu_A$) from a ground state (S_0) to an electronically excited state (S_1 or S_2), followed by fluorescence ($h\nu_F$) or phosphorescence ($h\nu_P$).

The Stokes shift ($\Delta\nu_{st}$) is the energy gap between the maximum of the lowest energy absorption band and the energy of the emission maximum. It is particularly important as the excitation and emission energies for different molecular probes can be tuned to different biological applications.[101] The fluorescence quantum yield (Φ_F) is a measure of the efficiency of a fluorescent molecule comparing the ratio of photons absorbed to photons emitted. For a perfect fluorescent system where every photon that is absorbed gets emitted, the $\Phi_F = 1$.[II] In reality, many quenching processes are observed that erode the Φ_F value (see 1.3.2.1).

It should be noted that many biomolecules exhibit weak fluorescence known as autofluorescence.[102,103] Common sources of autofluorescence are nicotinamide adenine dinucleotide phosphate (NADPH), collagen and other proteins that are rich in tryptophan, tyrosine, and phenylalanine residues. To overcome background autofluorescence, fluorophores with specific emission properties are often required for biological imaging techniques.

1.3.2.1 Fluorescence quenching

Molecular oxygen (O_2) can quench fluorescence by colliding with the fluorescent molecule in solution, thus reducing the number of photons emitted from the S_1 state. Therefore, the solution phase Φ_F can be influenced by using either aerated or deaerated solvents. The concentration of a fluorescent sample can impact the Φ_F as, at higher concentrations, the probability of an excited molecule colliding with a ground state molecule is increased.[104]

An important quenching mechanism when considering fluorescent metal phosphine complexes is Photoinduced electron Transfer (PeT). A schematic for the PeT mechanism and a representative energy level diagram is shown in Figure 1.13. The PeT quenching mechanism is made possible by having an electron donating (or accepting) group in proximity to the fluorophore when it has been excited to its S_1 state.[105,106] It allows formation of a donor-acceptor complex (D^+A^-, Figure 1.13) which enables a non-radiative decay process, thus quenching emission from the S_1 state. The effect of engaging a phosphine lone pair (either by oxidation or metal coordination) can diminish the PeT quenching mechanism and result in a dramatic increase in the fluorescence quantum yield (Φ_F).[107]

[II] Φ_F values often quoted between 0–1, or between 0–100%.

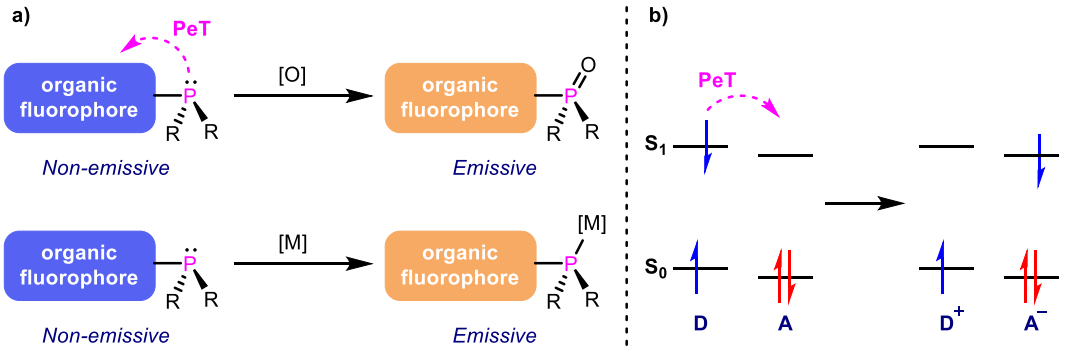

Figure 1.13. a) Representation of PeT quenching mechanism for organophosphines, and effect of oxidation and metal complexation. b) Energy level diagram for PeT process with electron transfer from donor (D) to acceptor (A).

Many examples of phosphines conjugated to electron acceptor moieties are now known to be sensitive detectors for hydroperoxides in aqueous environments (see Section 4.1.1, Chapter 4). More pertinent examples of fluorescent phosphines and their metal complex conjugates are discussed in Chapter 4.

1.3.2.2 Biological probes

Fluorescence spectroscopy and microscopy are non-destructive techniques for analysing drug interactions with biomolecules. Molecular probes, many of which are commercially available, can selectively label different proteins, nucleic acids, or sub-cellular components. These probes work because the biomolecule of interest usually has weak autofluorescence, well below the intensity of the probe molecule. Therefore, using spectrophotometry or microscopy, the labelled regions of interest are detectable well above the background autofluorescence. Figure 1.14 shows the structures of commonly used DNA probes, where the planar aromatic fragments can interact with base pairs through non-covalent π-π interactions.

The fluorescent dye ethidium bromide (EB) has been well-documented as a diagnostic technique for DNA intercalating small molecules.[108–110] EB is a planar, cationic dye that is a known carcinogen due to its ability to intercalate between the base pairs of double helical DNA. It is weakly fluorescent in water, but upon intercalation, the fluorescence intensity increases around 30-fold. Therefore, an EB competition assay with a DNA-interacting small molecule allows for the quantitative determination of binding constants by fluorescence spectroscopy.

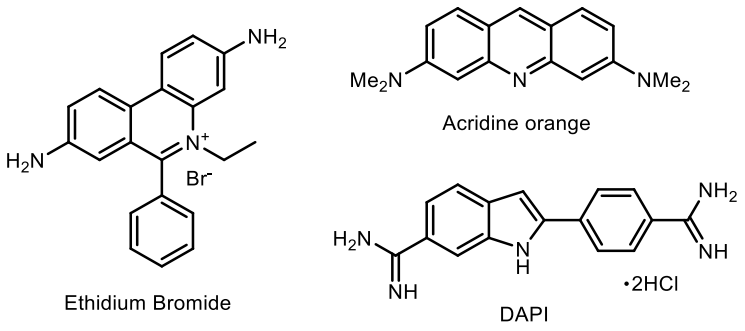

Figure 1.14. Chemical structures of commonly used fluorescent DNA probes.

Metal-ligand-complexes (MLCs), for example $[Ru(bpy)_3]^{2+}$, have been extensively used in solar energy conversion, photoredox catalysis and biomedicine.[88,111] Figure 1.15 shows a metal-to-ligand charge transfer (MLCT) transition for $[Ru(bpy)_3]^{2+}$ after excitation by a photon. The metal centre is oxidised, and an electron is excited to an MLCT state. After rapid intersystem crossing to the triplet MLCT state, the electron returns to the ground state and a photon is released (fluorescence). These spectral properties of MLCs have been exploited to study interactions with DNA, proteins, and other biomolecules (see Section 2.4.4, Chapter 2). The intensity of the emission from a fluorescent compound may increase or decrease when interacting with DNA. For example, for Ru–polypyridyl complexes (such as **1.10**, see Figure 1.7), fluorescence is quenched in polar solvents, thus an increase in fluorescence intensity indicates that polar solvent molecules cannot access the complex, for example, if it is bound within a hydrophobic pocket inside the DNA helix.

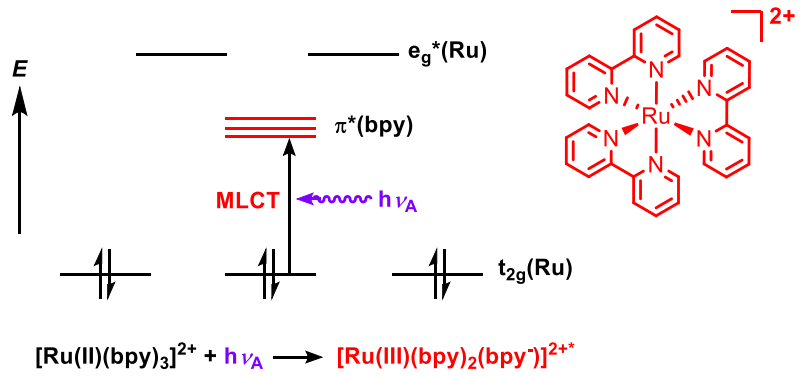

Figure 1.15. Energy level diagram for MLCT transition illustrated for $[Ru(bpy)_3]^{2+}$, modified from reference 100.

1.3.3 Fluorescent phosphine conjugates

There is increasing interest in tracking therapeutic agents via a tethered organic fluorophore (or probe) molecule. The advantage of these fluorescent conjugates is that tracking in living cells via fluorescence microscopy without an exogenous probe molecule

is possible. These so called theranostic (therapeutic plus diagnostic) agents have been extensively reviewed.[63,112,113] There are reported examples of phosphine ligands conjugated to many organic fluorophores that cover part of the UV-visible spectrum. Some examples containing pyrene, coumarin, BODIPY, fluorescein, and rhodamine are shown with their corresponding emission wavelengths (Figure 1.16a).[114–120] It is clear from a survey of these fluorescent phosphine conjugates that all of them contain fluorophores with emission maxima between 350–600 nm, (i.e., across the blue to yellow range of the visible spectrum). Many organic dyes that emit at longer wavelengths (i.e., the red to near-IR range of the spectrum) are commercially available (for example, see the Alexa Fluor series, Figure 1.16b).

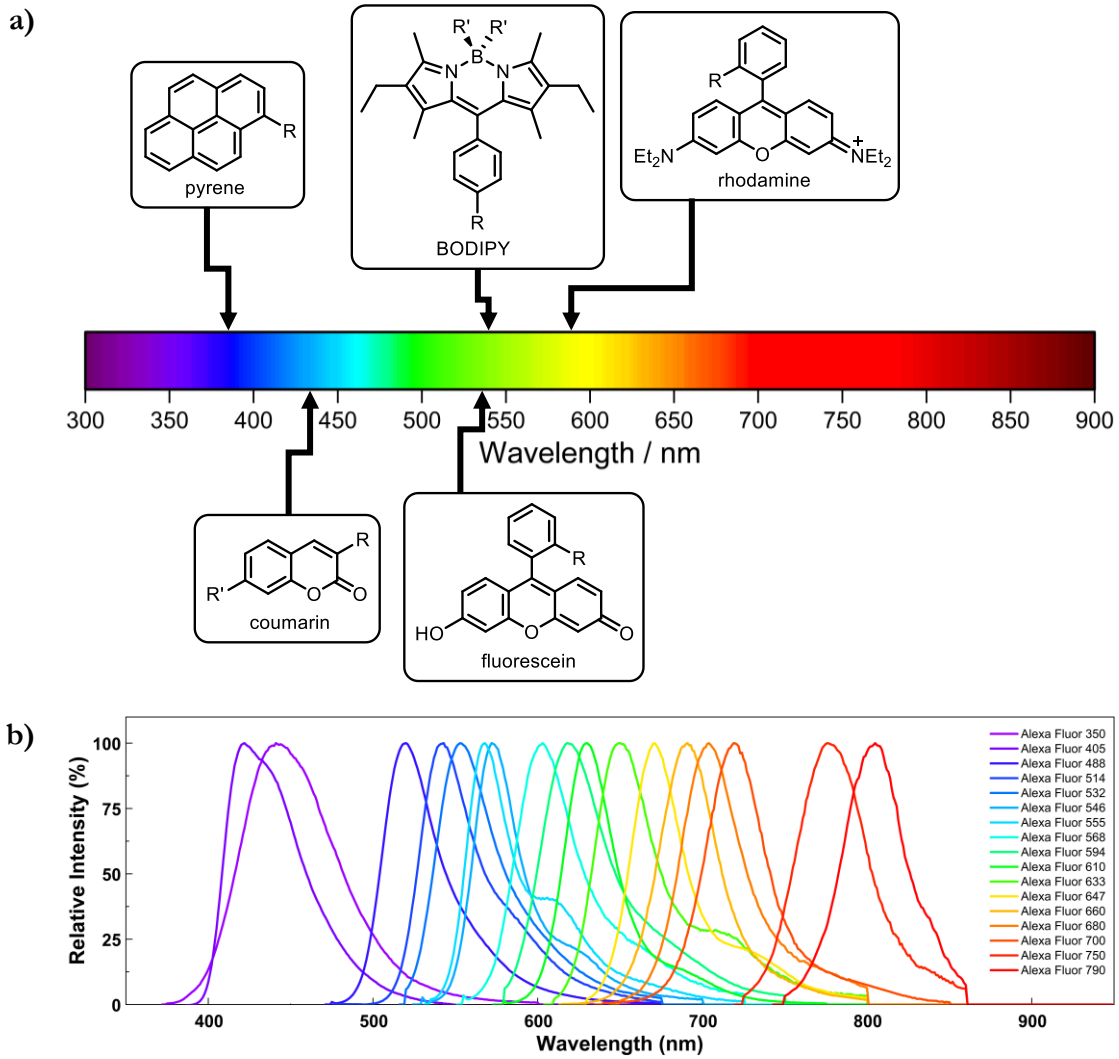

Figure 1.16. a) Fluorescence emission wavelengths of known fluorescent phosphine conjugates that cover part of the visible spectrum (~350–600 nm). R is a phosphine containing moiety, R' represents another substituent.[114–120] b) Fluorescence emission spectra of commercially available Alexa Fluor dyes, compiled from reference 121.

However, to the best of our knowledge, there are currently no examples of fluorescent phosphine conjugates with emission maxima >600 nm. Certain phosphorus-containing dyes with lower energy emission properties are known, but they are all based on polycyclic phosphine oxide and phosphinate P(V) materials.[122] Most Alexa Fluor dyes are constructed of a fluorescein or rhodamine core with several water solubilising groups, and therefore may be suitable conjugation partners for phosphines, useful for bioimaging techniques.

Jacquemin *et al.* reported a series of coumarin conjugated triarylphosphine derivatives **1.25** and the corresponding Ru(II), Os(II), and Au(I) complexes **1.27-1.28** (Scheme 1.6).[116] The fluorescence quantum yields for the free ligands were typically low (Φ_F = 0.03–0.05), primarily due to a PeT quenching mechanism with electron transfer from the phosphorus lone pair to the coumarin. Alkylation of the phosphine to form the methylphosphonium salts **1.26** significantly increased the fluorescence intensity (Φ_F = 0.91–0.98), as the lone pair is no longer accessible.

A similar observation was made for the Au(I) complexes (Φ_F = 0.83–0.95). In contrast, the Ru(II) and Os(II) complexes displayed significant fluorescence quenching compared to the Au(I) and phosphonium derivatives (Φ_F = 0.01–0.10) which was suggested to be due to triplet excited state deactivation pathways accessed via intersystem crossing. For many metal complexes, the presence of triplet metal-to-ligand-charge-transfer (^{3}MLCT) states can reduce the luminescence intensity via non-radiative deactivation pathways.[123]

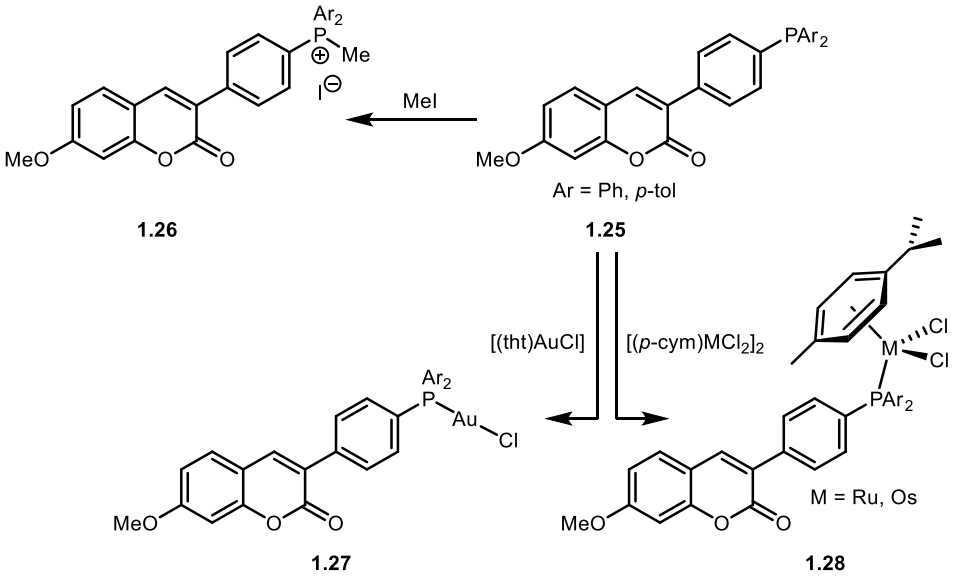

Scheme 1.6. Coumarin conjugated phosphines and complexes, Jacquemin *et al.*[116]

The cytotoxicity of the compounds **1.27-1.28** was assessed against four human cancer cell lines which determined that the Au(I) complexes were the most cytotoxic (IC_{50} ~ 25–50 μM). The authors suggested that the brightness ratios (complex luminescence : ligand luminescence) for only the Au(I) complexes **1.27** made them suitable compounds to use as theranostic agents, but experimental confirmatory results are yet to be reported.

1.4 Organometallic pincer complexes

PCP-pincer ligands are monoanionic, tridentate ligands that usually bind to metal centres in the meridional η^3-*PCP*-coordination mode. This rigid binding mode confers exceptional air-, temperature-, and moisture-stability, thus making pincer complexes robust catalysts under demanding conditions.[124] Most *PCP*-pincer complexes are derived from symmetric ligands with one linking atom between the aryl-carbon and the phosphine donors resulting in two fused 5-membered metallacycles (Figure 1.17). Due to the many points of derivatisation available, a plethora of catalysts with discrete structures and functions have been reported.[125] To date, one facet that has not received much attention, is metallacycle ring size. Very few examples of complexes with non-symmetric metallacycles (e.g., 5,6-) are known perhaps due to lengthy ligand syntheses or perceived lower stability of the organometallic complexes produced (Figure 1.17).[126,127]

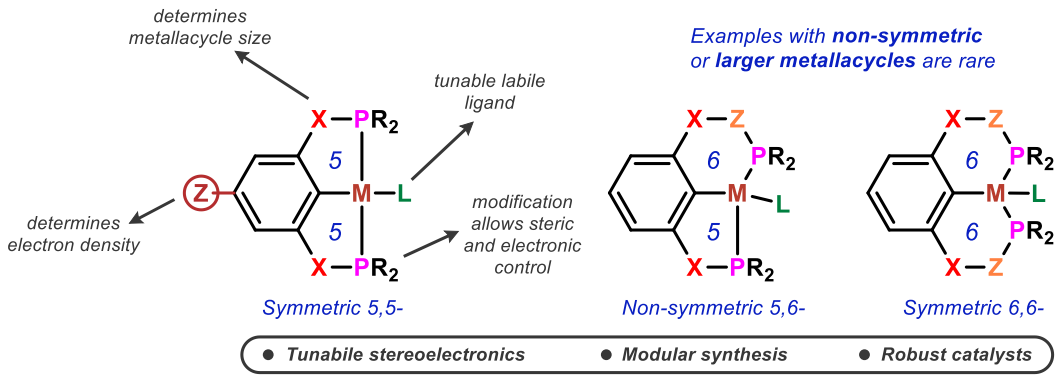

Figure 1.17. Schematic to show the properties and points of derivatisation for symmetric and non-symmetric *PCP*-pincer complexes.

Due to the rigid metallacycles that pincer ligands can form, they can enable otherwise labile ligands to remain firmly bound. The rigid structure has been extensively exploited in asymmetric catalysis by preventing the phosphorus donor substituents from rotating, thus holding them in a defined geometry that can direct the orientation of a substrate at the active site of the catalyst.[128–130] *PCP*-pincer complexes have been found to be active catalysts for many reactions, including transfer hydrogenation,[131] Suzuki-Miyaura cross-

coupling,[132–134] the Heck reaction,[135–137] and Sonogashira coupling,[138] as well as many asymmetric processes, such as hydrogenation and hydrophosphination.[129,130,139,140] For a review of the recent advances in the synthesis and applications of P-stereogenic pincer complexes, see Yang *et al.*[141]

The chemistry of pincer complexes containing metallacycles larger than conventional 5-membered metallacycles is discussed in Chapter 5.

1.4.1 Catalytic allylic alkylation

In 1965, Tsuji *et al.* reported the stoichiometric reaction between allylpalladium chloride dimer and the sodium salt of diethylmalonate which gave a mixture of the mono- and di-allylation products (Scheme 1.7).[142] The Trost group reported that PPh_3 was an essential additive for difficult to alkylate substrates. Following this discovery, a large family of phosphine ligands (Trost ligands) have become ubiquitous for the Tsuji-Trost allylic alkylation reaction, enabling fine-tuning of the stereoelectronic properties of the Pd catalyst.[143]

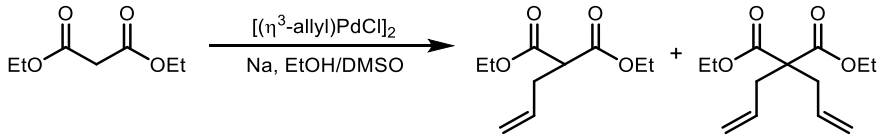

Scheme 1.7. Allylic alkylation of sodium diethylmalonate, reported by Tsuji *et al.*[142]

The field of allylic alkylation has continued to flourish with many transition metal complexes discovered as highly active (and selective) catalysts. Although catalysts based on Ni, Pt, W, and other metals are known, Pd-based systems – often employing optically-active ligands to effect an enantioselective transformation – have been unsurpassed in their utility.[143]

The Pd(0)-catalysed Tsuji-Trost reaction for allylic alkylation is proposed to proceed via the mechanism shown in Scheme 1.8: (i) the the alkene of the allylic electrophile coordinates to the Pd forming an η^2-propene-Pd(0) complex; (ii) oxidative addition to form an η^3-allyl-Pd(II) complex; (iii) nucleophilic attack at either terminus of the η^3-allyl-Pd(II) intermediate to regenerate one of two isomeric η^2-alkene-Pd(0) complexes; (iv) decomplexation from the Pd to give the linear or branched alkylation products and turn over the catalytic cycle. Nucleophilic attack is favoured at the least hindered terminus of the η^3-allyl-Pd(II) intermediate (indicated with a blue circle) which, in this case, would lead to preferential formation of the linear alkylation product.

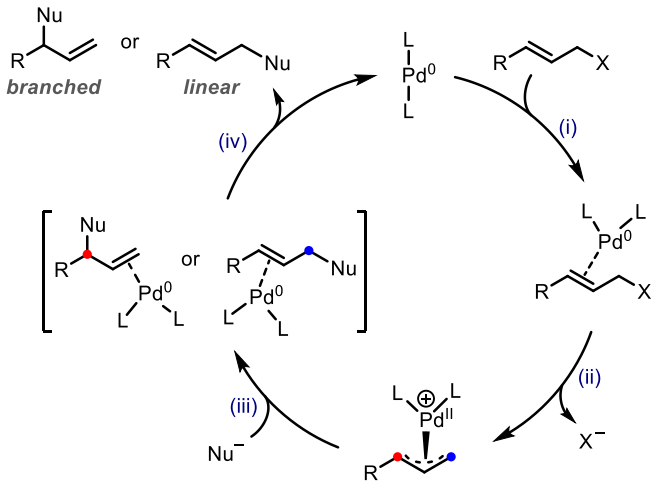

Scheme 1.8. Proposed mechanism for the Pd(0)-catalysed Tsuji-Trost allylic alkylation reaction.

PCP-pincer ligands have been applied to the Pd-catalysed allylic alkylation of cinnamyl acetate with sodium dimethylmalonate.[144] The mechanism of allylic alkylation catalysed by Pd(II) *PCP*-pincer complexes has not been conclusively established. One possible mechanism involves a Pd(0)/Pd(II) redox cycle where the Pd(II) pincer complex decomposes to give nanoparticulate heterogeneous Pd(0). This has been found to be the active catalyst in a range of cross-coupling reactions utilising pincer complexes.[145,146] Another possible mechanism involving a Pd(II)/Pd(IV) redox cycle could operate where the pincer ligand stabilises an octahedral Pd(IV) allyl intermediate, similar to the mechanisms for C–H acetoxylation and Heck-type cross-coupling with iodine(III) compounds, that have been previously reported.[146,147]

In Chapter 5, a series of Pd *PCP*-pincer complexes with symmetric and non-symmetric metallacycles are reported and applied as catalysts in allylic alkylation. The influence of metallacycle size on Pd coordination and catalytic activity and selectivity has been studied.

1.5 Objectives

The aims of the projects described in this thesis were to:

- Synthesise (*cis*-tach)Ru diphosphine complexes with planar aromatic backbones. The anti-proliferative properties of the novel derivatives would be investigated by a range of physical inorganic and biological experiments.

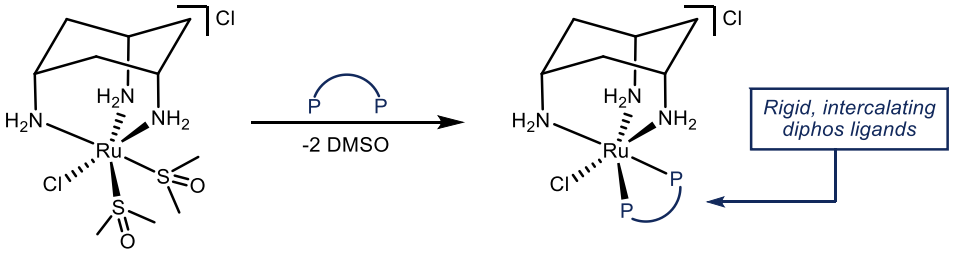

- Explore methods to chemically conjugate phosphine ligands with small organic fluorophores and study their coordination chemistry and luminescence properties.

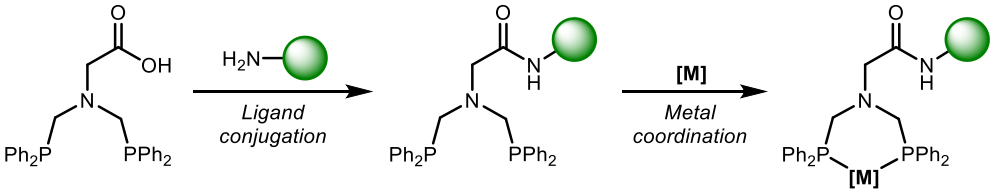

- Use a combination of spectroscopic and computational methods to rationalise the observed coordination, luminescence, and air-stability properties of novel pyrenylphosphines.

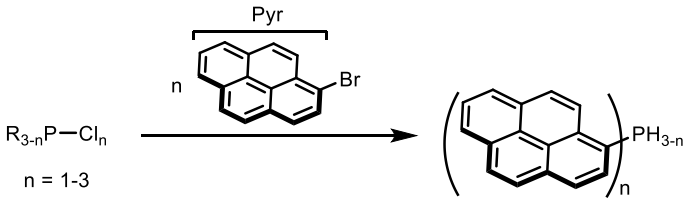

- Investigate the effect of metallacycle ring size on the coordination properties of a series of *PCP*-pincer ligands and apply the resulting Pd complexes to catalytic alkylation reactions.

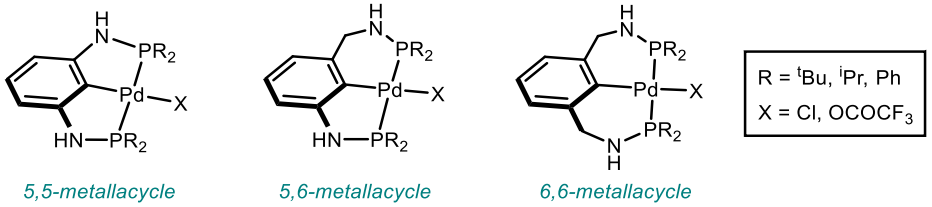

Chapter 2. Ru metallodrugs with DNA intercalating diphosphine ligands

This chapter is based on the publication 'Cytotoxic (*cis,cis*-1,3,5-triaminocyclohexane)ruthenium(II)–diphosphine complexes; evidence for covalent binding *and* intercalation with DNA', published in *Dalton Transactions*. The author of this thesis was the lead author of this paper and the co-authors were: A. J. Gamble, S.W. Arkawazi, P. H. Walton, M. C. Galan, M. P. O'Hagan, K. G. Hogg, J. L. Marrison, P. J. O'Toole, H. A. Sparkes, J. M. Lynam and P. G. Pringle. The project ideas originated at the University of York (P. H. Walton/J. M. Lynam) before the present author carried out further synthetic chemistry, analysis, and biological testing. A significant amount of this chapter is reproduced from *Dalton Trans.*, **2020**, 49, 15219–15230, however, additional compounds that were not evaluated as part of the publication are also included. All changes to the original manuscript are due to the present author.

2.1 Introduction

2.1.1 Cytotoxic Ru complexes

Ruthenium complexes have potential as alternatives to platinum-based chemotherapy in the treatment of cancers. Compounds **A-G** in Figure 2.1 show the structural diversity of Ru complexes whose anti-cancer activity has been investigated.[35] The ruthenium(III) complexes, NAMI-A (**A**) and KP1019 (**B**) have undergone clinical trials.[30,32,148–150] More recently, Sadler[151–155] and Dyson[18,33,37,44,156,157] have reported piano-stool (η^6-arene)ruthenium(II) compounds that are cytotoxic *in vitro* and *in vivo*. Notably, the chelate complex [RuCl(η^6-biphenyl)($H_2NCH_2CH_2NH_2$)]PF_6 (**C**) has been shown to target DNA directly, with the DNA-complex adduct stabilised by hydrogen bonds between the diamine ligand and the O6 of guanine.[158] It has been shown that [$RuCl_2$(*p*-cymene)(PTA)] (**D**) is active *in vivo* against secondary metastases.[156] In addition, due to their tunable photophysical properties, many Ru(II) polypyridyl complexes have been developed for use in photodynamic therapy (PDT) and photochemotherapy (PCT).[26,39,61,159] The first example of this class of complexes to have entered human clinical trials was TLD1433 (**E**), which contains a terthienyl chromophore.[26,58]

The seminal work on the anti-cancer properties of (η^6-arene)Ru complexes has spurred the investigation of many coordination complex analogues of organometallic piano-stool complexes. For example, Alessio *et al.* replaced the arene with [9]aneS_3 to give complex **F** with minimal loss of biological activity compared to its organometallic analogues.[47]

Furthermore, Ru-diphosphine complexes such as [(κ^3-tpm)RuCl(diphos)]PF_6 (**G**) showed activity *in vitro*.[160]

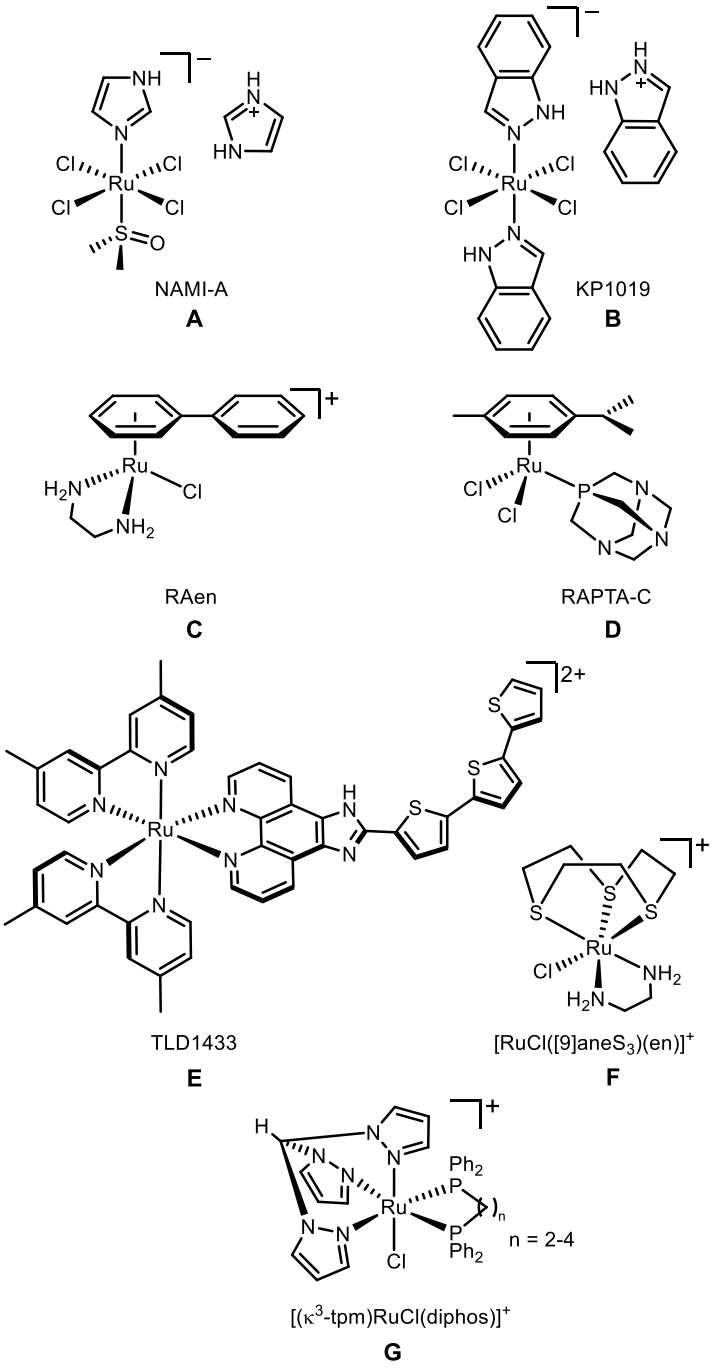

Figure 2.1. Chemical structures of cytotoxic Ru complexes.

However, despite the variety of facially capping ligands available that could be used to modulate activity, this aspect of the complexes has received far less attention than modification of the other ancillary ligands on the metal.[43,96,161] From a biological perspective, the narrow range of face-capping ligands that have been used limits the rate and extent of the substitution of the halido ligands by water. This rate is known to

correlate with *in vitro* activity,[152,162,163] and expanding its range is thus a critical factor in maximising the clinical potential of ruthenium complexes in the treatment of cancer.

The ligand *cis*-tach (*cis,cis*-1,3,5-triaminocyclohexane) forms face-capping complexes with many transition metals including ruthenium(II).[75,81,82,164,165] The labile complex [RuCl(DMSO-*S*)$_2$(*cis*-tach)]Cl (**2.1**) is the precursor to *N,N*-chelate complexes **2.2-2.4** and *P,P*-chelate complexes **2.5-2.10** (Scheme 2.1) that have been previously reported.[82] The influence of the *cis*-tach ligand was evaluated by comparison of the structural data with those for (η^6-arene)Ru complexes. It has previously been demonstrated[74,82] that *cis*-tach is a strong σ–donor, as would be expected due to the three nitrogen atoms coordinated to the metal. For instance, reaction of the DMSO complex **2.1** with diamines yields dicationic complexes in which one coordinated DMSO is retained, whereas reaction of **2.1** with diphosphines gave complexes with one chlorido ligand retained (Scheme 2.1). This difference in behaviour was rationalised on the basis of the different bonding characteristics of diamines and diphosphines. The electron-rich nature of the Ru created by the *cis*-tach, is augmented by the diamine σ–donors which leads to strong π–back-donation to the DMSO ligand, strengthening the Ru–S interaction. By contrast, diphosphines, which are better π–acceptors than DMSO, favour the coordination of chloride, which is presumed to be a π–donor. Importantly, for the use of these complexes as anti-cancer agents, it was reasoned that the Ru(*cis*-tach)(diphos) moiety may promote the rapid aquation of the Ru–Cl bond that might result in enhanced *in vitro* activity.[81,83]

The ruthenium(II) precursor [RuCl(DMSO-*S*)$_2$(*cis*-tach)]Cl (**2.1**) and the (*cis*-tach)Ru complexes containing *N,N*-chelates (**2.2-2.4**) and *P,P*-chelates (**2.5-2.10**) were synthesised by previously reported methods (Scheme 2.1).[82] Our initial biological investigations described herein focused on these complexes.

Notably, for the purposes of this study, the cationic Ru(II) *P,P*-chelates **2.5-2.10** are freely soluble in water up to millimolar concentrations, well in excess of that needed for therapy. The superior aqueous solubility of these complexes over traditional organometallic Ru complexes provides an advantage, in that biological studies can be performed without the addition of toxic, solubilising additives, such as DMSO.

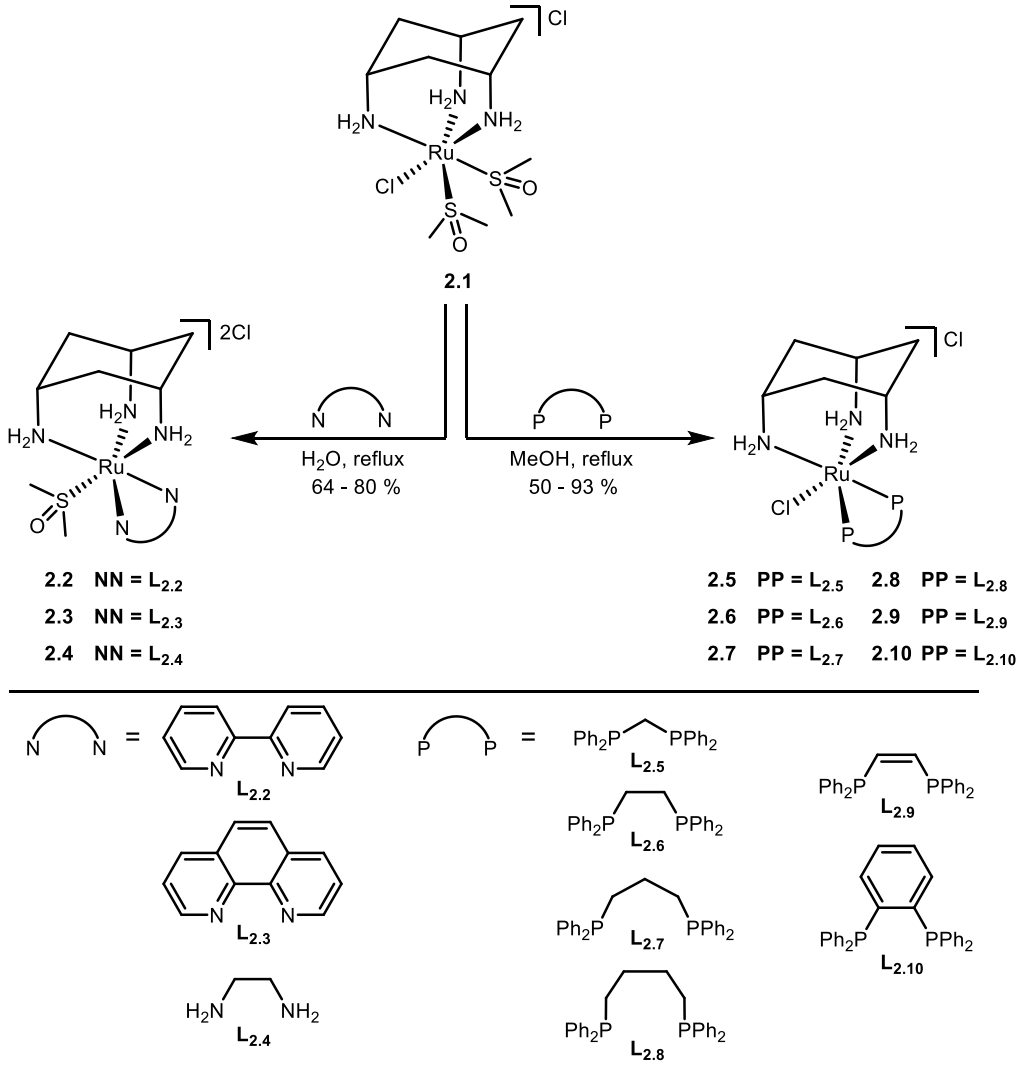

Scheme 2.1. Synthesis of complexes **2.2-2.10**.[82]

In addition to their potential as effective anti-cancer agents, Ru complexes of *cis*-tach have other features that make them attractive for medicinal chemistry. For instance, the cationic Ru *cis*-tach complexes are readily prepared as chloride salts, obviating the use of the toxic PF_6^- anion in potential pharmaceuticals.[166] The NH_2 groups of the *cis*-tach ligand enhance the water solubility of the complexes and, moreover, may strengthen any binding to DNA through hydrogen-bonding interactions, in a similar manner to the DNA binding with [RuCl(η^6-biphenyl)(en)]PF_6 (**C**).[152,153] Finally, the cyclohexane ring provides a hydrophobic face to the complex, giving steric protection to the hydrophilic metal centre.

It is in this context that a detailed investigation of the *in vitro* activity of ruthenium *cis*-tach complexes has been carried out and described in this Chapter. It has been shown that a range of diphosphine derivatives exhibit activity against three tumour cell lines, in some cases with potency exceeding that of cisplatin or established anti-cancer ruthenium

complexes. The extended aromatic backbones of the new diphosphines **L2.11-L2.13** (Figure 2.2) are shown to allow detailed insight into the nature of the biological interactions with their Ru-complexes via a range of physical inorganic and biological measurements including UV-visible, fluorescence and NMR spectroscopy as well as label-free cellular imaging techniques.

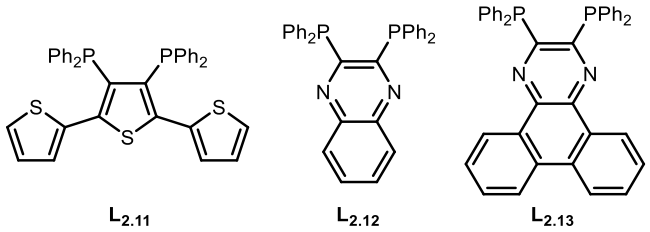

Figure 2.2. Chemical structures of **L2.11-L2.13** designed for this work.

2.1.2 Research aims

It was apparent from preliminary anti-proliferative studies on (*cis*-tach)Ru *P,P*-chelate complexes that they are highly cytotoxic. To study the nature of this biological activity further, we aimed to carry out the following:

- Design and structurally characterise diphosphine derivatives with planar aromatic backbones, capable of intercalative DNA binding interactions.
- Study the kinetics of aquation and compare this to organometallic derivatives.
- Assess the binding of the novel (*cis*-tach)Ru complexes to different DNA motifs and correlate this to the *in vitro* cytotoxicity observed by LiveCyte cell imaging techniques.

2.2 Ligand synthesis

The ligands **L2.11-L2.13** were made by the routes shown in the following schemes. The novel terthiophene diphosphine **L2.11** was prepared from 3',4'-dibromo-2,2':5',2''-terthiophene **2.11**, which has been reported by Yamaguchi and co-workers (Scheme 2.2).[167] It was necessary to install the diphenylphosphine groups in **L2.11** sequentially to avoid the formation of a complex mixture of products.

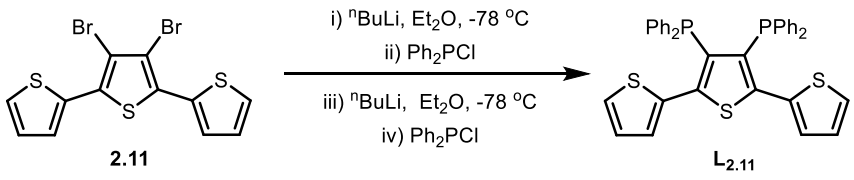

Scheme 2.2. Synthesis of **L2.11** via iterative lithiation/phosphination.

Crystals suitable for X-ray diffraction were grown by slow evaporation of a saturated CH_2Cl_2 solution of **L**$_{2.11}$ stored at room temperature (Figure 2.3).

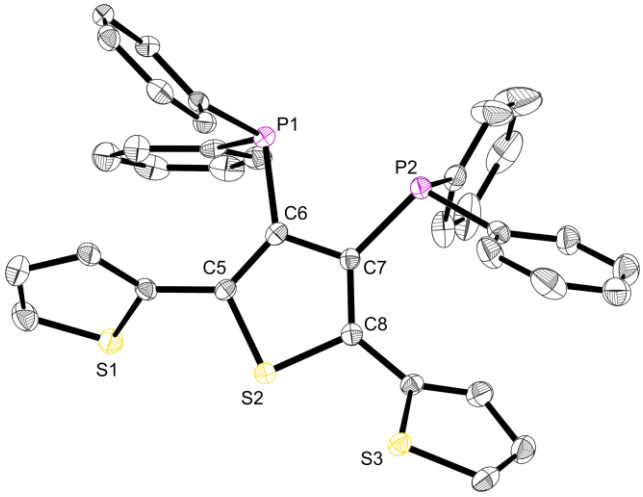

Figure 2.3. Single crystal X-ray crystallography structure of **L**$_{2.11}$. Hydrogen atoms have been omitted for clarity. Thermal ellipsoids at 50% probability level. Selected bond lengths (Å) and angles (°): P1–C6 1.846(2), P2–C7 1.837(2), C7–C6 1.448(3), C8–C7 1.384(3), C5–C6 1.375(3); C7–C6–P1 118.69(15), C5–C6–P1 128.43(15).

The P–C bonds between the diphenylphosphine groups and the central thiophene (1.846(2) and 1.837(2) Å) are within the normal range for previously reported thiophenyl phosphine ligands.[107] The dihedral angles between the central thiophene ring and the two flanking thiophenyl groups are ~53° and ~61°, thus **L**$_{2.11}$ crystallised with a twisted geometry. However, **L**$_{2.11}$ did not exhibit atropisomerism in solution as one sharp set of signals in the ^{1}H NMR spectrum was observed. If atropisomers were present, they would be enantiomers and therefore give one sharp singlet in the ^{31}P{^{1}H} NMR spectrum.

The quinoxaline diphosphine ligand, **L**$_{2.12}$ was prepared from 2,3-dichloroquinoxaline and lithium diphenylphosphide following a modified literature procedure (Scheme 2.3).[168]

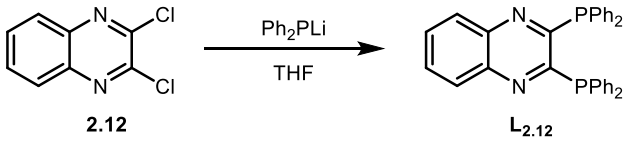

2.12 **L**$_{2.12}$

Scheme 2.3. Synthesis of **L**$_{2.12}$.

We sought to extend the aromatic surface area of quinoxaline diphosphine **L**$_{2.12}$ by addition of fused benzo groups in the [f,h] positions. Starting from phenanthrene-9,10-diamine **2.13**, the extended quinoxaline dibromide **2.15** has been previously reported and is obtained from treatment of 1,4-dihydrodibenzo[f,h]quinoxaline-2,3-dione **2.14** with PBr_3 in DMF (Scheme 2.4). Unfortunately, due to the highly insoluble nature of this

material, attempts to convert **2.15** to the desired diphosphine were unsuccessful. The most productive route to diphosphine ligand $\mathbf{L_{2.13}}$ was from its dichloro precursor (obtained from treatment of 1,4-dihydrodibenzo[f,h]quinoxaline-2,3-dione **2.13** with PCl_3 in DMF, Scheme 2.4).[169]

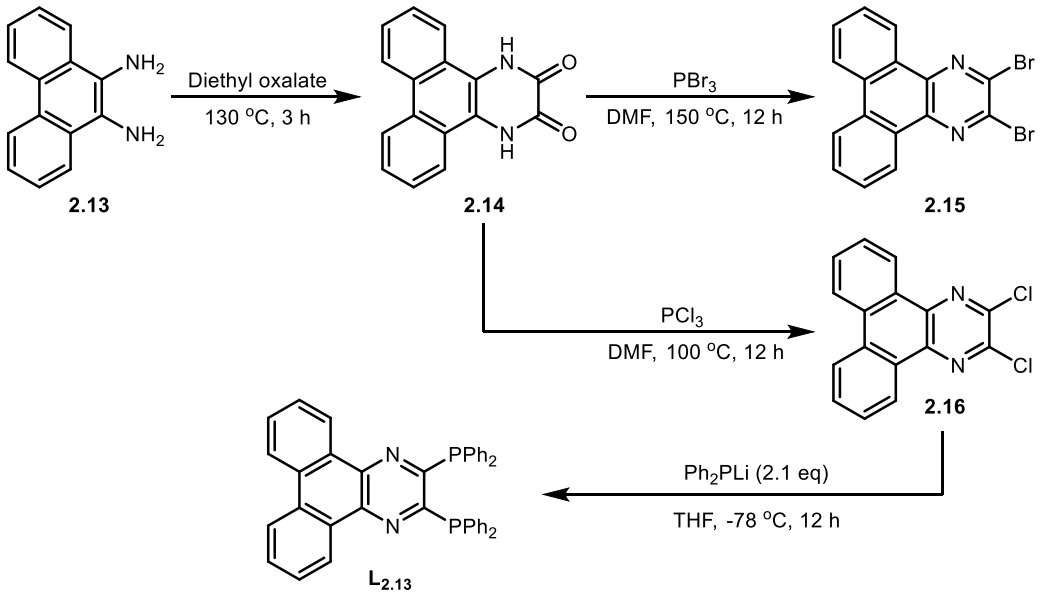

Scheme 2.4. Synthesis of $\mathbf{L_{2.13}}$.

2.3 Synthesis of cytotoxic complexes

The cationic Ru complexes **2.17-2.19** were prepared in an analogous way to **2.5-2.10** (Scheme 2.5). The two DMSO ligands were substituted with the chelating phosphines ($\mathbf{L_{2.11}}$-$\mathbf{L_{2.13}}$) by reaction of **2.1** with 1.8 equivalents of each of the ligands in alcohol solvent (MeOH or EtOH) heated under reflux. The formation of the desired complexes typically took between 18–48 h and was monitored by *in situ* $^{31}P\{^1H\}$ NMR spectroscopy.

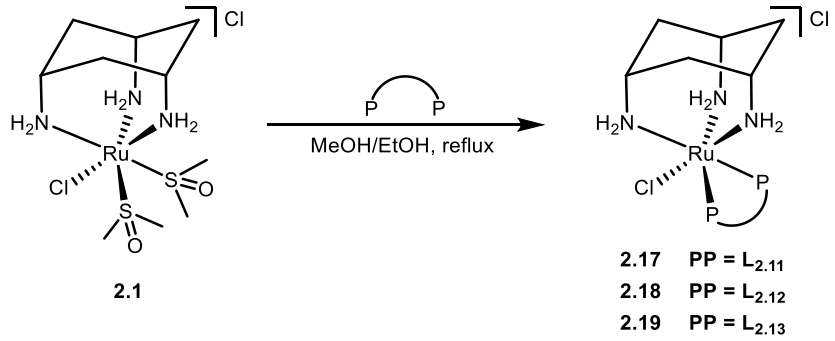

Scheme 2.5. Preparation of (*cis*-tach)Ru diphosphine complexes **2.17-2.19**.

Single crystals of a salt containing **2.18** were grown following anion metathesis with $NaPF_6$ in methanol followed by filtration (to remove NaCl) and slow evaporation of the saturated

solution at room temperature. The X-ray crystal structure of [**2.18**]PF_6 (Figure 2.4) demonstrates that the addition of the larger, planar aromatic quinoxaline diphosphine ligand $\mathbf{L}_{2.12}$ does not significantly alter the geometry of the (*cis*-tach)Ru complex, as shown by the overlap with the phenylene diphosphine (dppbenz) analogue (**2.10**) illustrated in Figure 2.4. The *cis*-tach ligand adopts the expected κ^3-coordination mode and there are intramolecular interactions detected between the $N(4)H_2$ and the centroids of the phenyl rings of the PPh_2 groups. In addition to the lipophilic cyclohexane ring, the PPh_2 groups provide further hydrophobicity to the complex and have the potential to interact with biomolecules (see below).

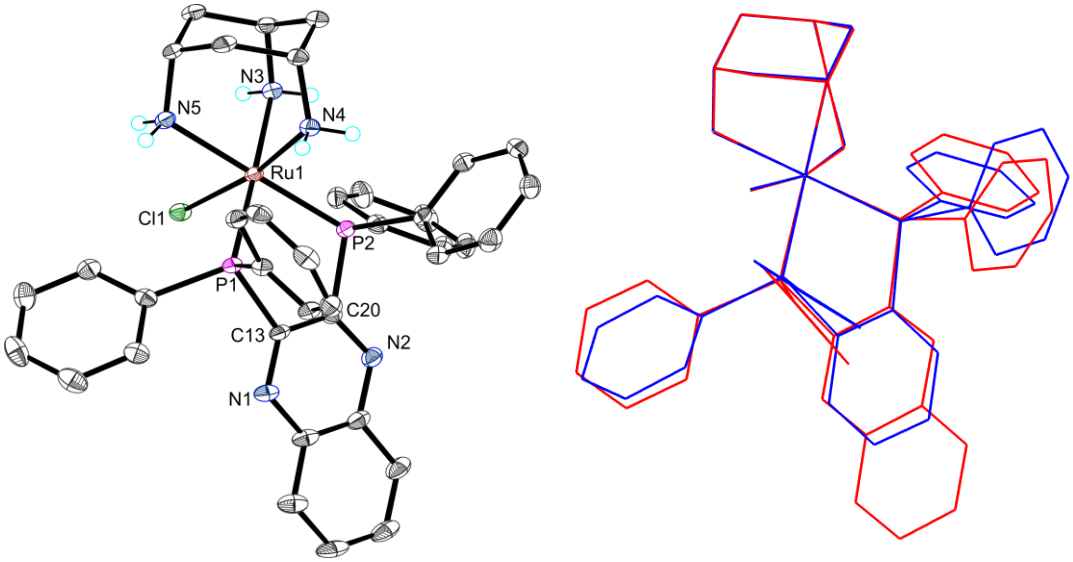

Figure 2.4. (left) Single crystal X-ray crystallography structure of [**2.18**]PF_6. Hydrogen atoms (except for the $–NH_2$ groups) and PF_6^- have been omitted for clarity. Thermal ellipsoids at 50% probability level. (right) Overlap of [**2.18**]PF_6 (red) with dppbenz derivative [**2.10**]PF_6 (blue). Selected bond lengths (Å) and angles (°): Ru1–Cl1 2.4335(6), Ru1–P1 2.2857(7), Ru1–P2 2.2654(6), Ru1–N3 2.179(2), Ru1–N4 2.130(2), Ru1–N5 2.182(2); P2–Ru1–P1 84.43(2), N4–Ru1–Cl1 170.90(6), P1–Ru1–Cl1 90.11(2), P2–Ru1–Cl1 93.92(2).

In addition to complexes **2.17-2.19** which possess diphosphine ligands with all-carbon backbones, (*cis*-tach)Ru complex **2.20** was prepared from **2.1** and bis(diphenylphosphino)amine $\mathbf{L}_{2.14}$ (Scheme 2.6). It was hypothesised that the additional N–H bond of this ligand could behave in a similar way to the *cis*-tach N–H bonds and allow formation of hydrogen bonding interactions with biomolecules. Ligands containing a reactive functional group that can be further functionalised are discussed in Chapter 3.

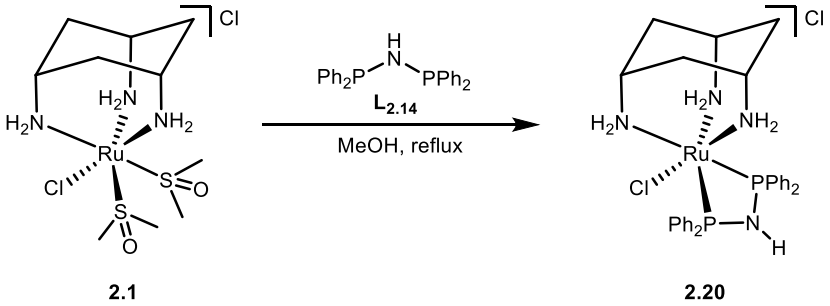

Scheme 2.6. Preparation of (*cis*-tach)Ru diphosphine complex **2.20**.

In the case of **2.20**, anion metathesis from chloride to hexafluorophosphate was not necessary and single crystals of **2.20** grew from evaporation of its concentrated solution in methanol at room temperature (Figure 2.5). The four-membered metallacycle has a diphosphine bite angle (69.6°) that is comparable, albeit slightly smaller, than the dppm derived (*cis*-tach)Ru complex **2.5** (72.3°).

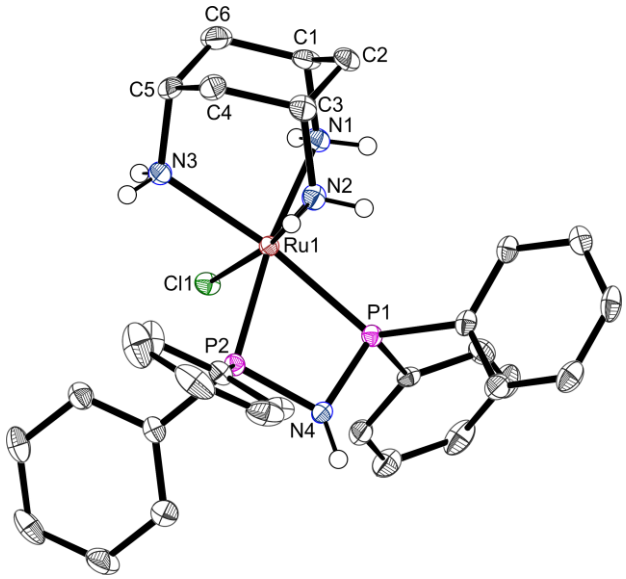

Figure 2.5. Single crystal X-ray crystallography structure of **2.20**. Hydrogen atoms (except for the $-NH_2$ groups) and Cl^- have been omitted for clarity. Thermal ellipsoids at 50% probability level. Selected bond lengths (Å) and angles (°): Ru1–Cl1 2.4269(6), Ru1–P1 2.2575(7), Ru1–P2 2.2437(7), P1–N4 1.686(2); P2–Ru1–P1 69.59(2), N2–Ru1–Cl1 171.91(7), P2–N4–P1 99.41(12).

To assess the ligand donor properties of **L**$_{2.11}$-**L**$_{2.13}$, dichloroplatinum(II) complexes were prepared by reaction of each ligand with one equivalent of [$PtCl_2$(cod)] (Scheme 2.7). The isolated complexes displayed characteristically large $^1J_{PPt}$ coupling constants consistent with *cis*-coordination of the diphosphine. Table 2.1 gives the chemical shifts, coordination chemical shifts and relevant coupling constants of Ru complexes **2.17-2.20** and Pt complexes **2.21-2.23**.

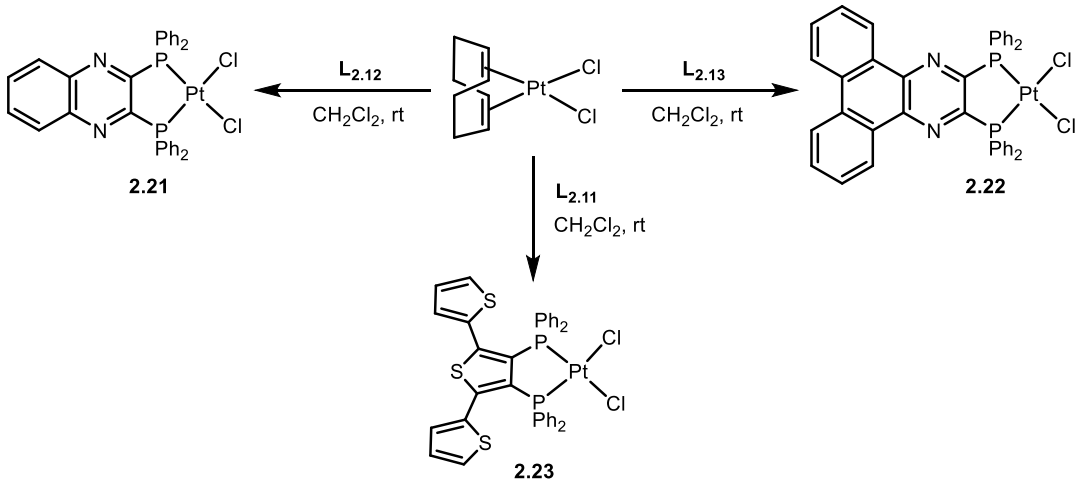

Scheme 2.7. Preparation of *cis*-[(PP)$PtCl_2$] complexes, **2.21-2.23**.

Table 2.1. Selected $^{31}P\{^1H\}$ NMR spectroscopy data for Ru complexes **2.17-2.20** and Pt complexes **2.21-2.23**.

Compound number	Ligand/Complex	δ_P / ppm[a]	$\Delta\delta_P$[b]	$^1J_{PPt}$ / Hz
$L_{2.11}$	Terthiophene (PP)	–17.3	–	–
2.17	[RuCl(*cis*-tach)(PP)]$^+$	56.2	+73.5	–
2.23	[$PtCl_2$(PP)]	11.8	+29.1	3580
$L_{2.12}$	Quinoxaline (PP)	–9.4	–	–
2.18	[RuCl(*cis*-tach)(PP)]$^+$	63.9	+73.3	–
2.21	[$PtCl_2$(PP)]	21.0	+30.4	3449
$L_{2.13}$	ExQuin (PP)	–10.2	–	–
2.19	[RuCl(*cis*-tach)(PP)]$^+$	63.3	+73.5	–
2.22	[$PtCl_2$(PP)]	21.4	+31.6	3500
$L_{2.14}$	$(Ph_2P)_2NH$ (PP)	43.0	–	–
2.20	[RuCl(*cis*-tach)(PP)]$^+$	64.3	+21.3	–

[a]Chemical shifts recorded in $CDCl_3$ and given in ppm. [b]Coordination chemical shifts ($\Delta\delta_P$) are relative to the free ligands in $CDCl_3$ ($\Delta\delta_P = \delta_P$(complex) – δ_P(ligand)).

In all cases, forming the 5-membered Ru metallacycles **2.17-2.19** resulted in a large $\Delta\delta_P$ of ~73 ppm consistent with the properties of previously reported Ru diphosphine complexes **2.9-2.10**.[82] The 4-membered Ru metallacycle **2.20** had a much smaller $\Delta\delta_P$ of ~21 ppm associated with the strained ring. This is similar to the 4-membered metallacycle derived from dppm (**$L_{2.5}$**) which, on forming the Ru complex **2.5**, gave a $\Delta\delta_P$ ~10 ppm.

The coordination of $\mathbf{L_{2.11}}$-$\mathbf{L_{2.13}}$ to [$PtCl_2$(cod)] to give 5-membered palladacycles induced smaller $\Delta\delta_P$ values than the Ru analogues (~30 ppm for **2.21-2.23**). The $^{31}P\{^1H\}$ NMR spectra for these complexes showed singlets with Pt satellites with $^1J_{PPt}$ values of 3580 Hz (**2.23**), 3449 Hz (**2.21**), and 3500 Hz (**2.22**).

Crystals of **2.21** and **2.22** were grown by slow evaporation of their saturated solutions in CH_2Cl_2 at room temperature and the structures determined by X-ray crystallography (Figure 2.6 and Figure 2.7).

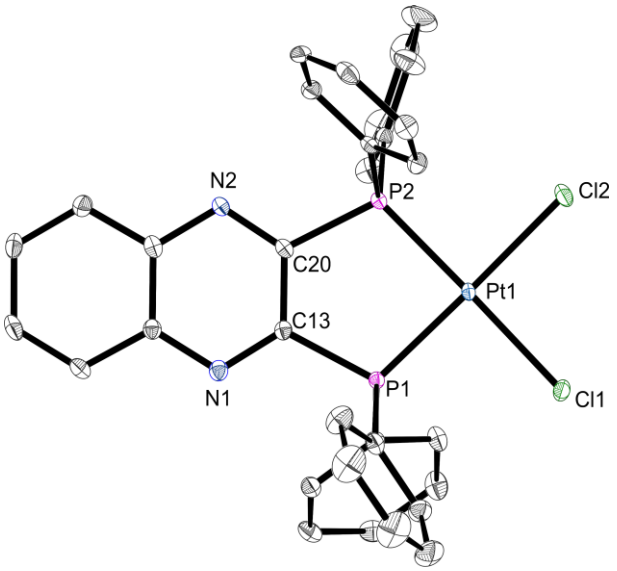

Figure 2.6. Single crystal X-ray crystallography structure of **2.21**. Hydrogen atoms have been omitted for clarity. Thermal ellipsoids at 50% probability level. Selected bond lengths (Å) and angles (°): Pt1–Cl1 2.3508(6), Pt1–Cl2 2.3576(6), Pt1–P1 2.2111(6), Pt1–P2 2.2122(6); Cl1–Pt1–Cl2 91.55(2), P1–Pt1–Cl1 89.69(2), P1–Pt1–P2 89.20(2).

The molecular structures of both complexes feature planar 5-membered PtPCCP metallacycles and show the expected square planar geometry. In the solid state, the complex with the larger ligand backbone (**2.22**) displays a twist (~17°) with respect to the $PtCl_2$ plane (Figure 2.7) which is not present in the parent quinoxaline complex **2.21**.

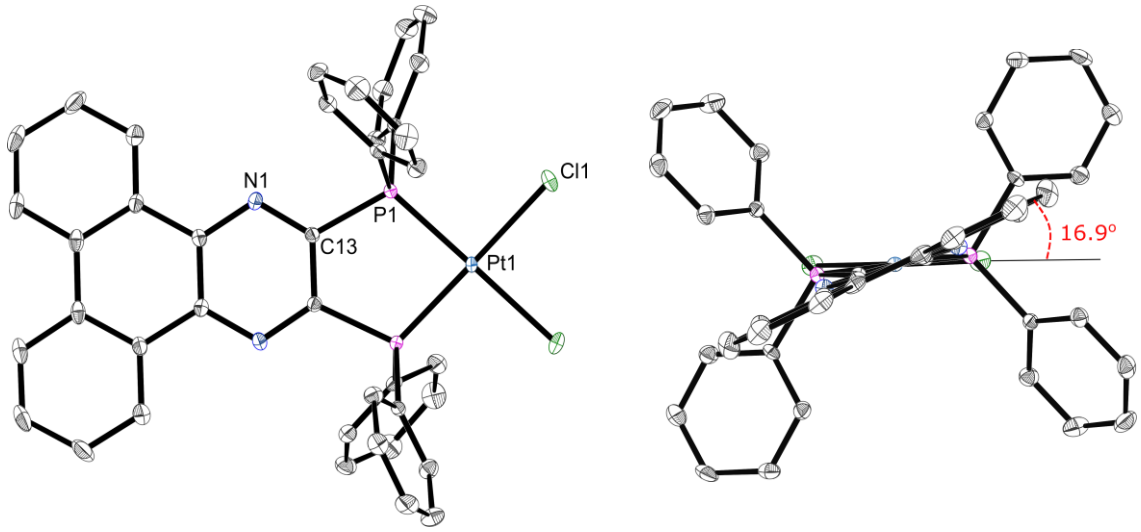

Figure 2.7. Single crystal X-ray crystallography structure of **2.22**. Hydrogen atoms have been omitted for clarity. Thermal ellipsoids at 50% probability level. Selected bond lengths (Å) and angles (°): Pt1–Cl1 2.3552(6), Pt1–P1 2.2078(6), P1–C13 1.828(2); P1–Pt1–Cl1 89.77(2), P1–Pt1–P1' 89.11(3).

2.4 Biophysical measurements

2.4.1 Inhibition of the proliferation of A549 and A2780 cancer cells

The *in vitro* growth inhibition was determined by MTT assay in two cell lines: A549 (human lung adenocarcinoma) and A2780 (human ovarian adenocarcinoma). The [Ru(DMSO)(*cis*-tach)($\mathbf{L}_{2.2}$)]$^+$ complex (**2.2**) in concentrations up to 300 μM, did not inhibit the growth of tumour cells and was therefore considered inactive.

Ruthenium mono-phosphine complexes containing an η^6-arene ligand have previously been shown to be active against cancer cells.[38,44,155,170–172] We have found clear antiproliferative activity with the *P,P*-chelates **2.5-2.10** (for structures see Scheme 2.1) as shown by the data given in Table 2.2 and Figure 2.8. The following trends can be discerned from the data. (1) The activity generally increases with increasing chelate ring size: **2.5** < **2.6** < **2.7** ≃ **2.8**; complexes **2.7** and **2.8** are over twice as active as cisplatin against the A549 cell line and are equipotent to cisplatin against the A2780 cell line. (2) Complex **2.6** is over twice as active as complex **2.9** against both cell lines, although both **2.6** and **2.9** are 5-membered chelates, the more active chelate **2.6** has a less rigid backbone. (3) Complex **2.10** is significantly more active (by factors of *ca.* 10 and 7 against the two cell lines) than the ostensibly similar complex **2.9**. Although both **2.9** and **2.10** are rigid, 5-membered chelates, the phenylene backbone in **2.10** will make the complex more lipophilic. It was also speculated that the intercalating potential of the planar aromatic backbone present in **2.10** may also be a contributing factor in its higher activity than **2.9**.

Table 2.2. Biological evaluation of compounds **2.1**, **2.2**, **2.5-2.10** and **2.17-2.19**.[a]

	IC_{50}[b] (μM)	
Compound	A549	A2780
cisplatin	2.70 (0.05)	0.43 (0.01)
2.1	> 300	> 300
2.2	> 300	> 300
2.5	41.7 (1.0)	12.4 (0.2)
2.9	25.1 (0.4)	7.47 (0.17)
2.6	9.88 (0.04)	3.39 (0.12)
2.7	1.02 (0.03)	0.35 (0.01)
2.8	1.15 (0.02)	0.39 (0.01)
2.10	2.73 (0.11)	1.14 (0.04)
2.17	1.83 ± 0.66[c]	–
2.18	11.81 ± 1.23[c]	–
2.19	5.06 ± 1.01[c]	–

[a]Antiproliferative activities were determined by MTT assay and dose response curves are given (Figure 2.9). The IC_{50} calculated as the concentration of drug required for 50% growth inhibition over 72 h. [b]Calculated as the average of triplicate experiments. [c]Subsequently determined to assess activity of the newly synthesised diphosphine ligand complexes, errors are calculated from 8 replicates. Standard deviations are given in parenthesis.

To explore this hypothesis further, the (*cis*-tach)Ru complexes **2.17-2.19** containing diphosphines with extended aromatic surfaces: terthiophenyl diphosphine (**L**$_{2.11}$), quinoxaline diphosphine (**L**$_{2.12}$) and dibenzo[f,h]quinoxaline diphosphine (**L**$_{2.13}$) (see Figure 2.2) were tested. It was postulated that these novel complexes might exhibit dual-function cytotoxicity by covalently binding to biomolecules and by intercalation with DNA in a similar way to the functioning of the cytotoxic Pt complex phenanthriplatin.[14,15] If this were the case, it was reasoned that **2.17-2.19** would be expected to show higher activity than the first-generation (*cis*-tach)Ru complexes **2.5-2.10**.

We assessed the antiproliferative activity of **2.17-2.19** against A549 cells by a 72 h MTT assay and found that the complexes were comparable in activity to the most active *P,P*-chelate complexes **2.7-2.8** with IC_{50} values of 1.83 ± 0.66 μM for **2.17**, 11.81 ± 1.23 μM for **2.18**, and 5.06 ± 1.01 μM for **2.19**. Considering the experimental errors inherent in the

MTT assays, the difference between the activity of **2.17** and **2.7-2.8** is not statistically significant.

Encouraged by the activities of these more lipophilic derivatives with planar aromatic backbones, we sought to understand their interactions with a variety of biomolecules and study their activity *in vitro*. The MTT data for complexes **2.17-2.19** (Table 2.2) demonstrated that their activity was comparable to the most active (*cis*-tach)Ru complexes. However, detailed time course studies using *in situ* cellular imaging revealed further details of the behaviour of the complexes and indicated that **2.17-2.19** are significantly more active against A549 and 293T cells when compared to cisplatin and **2.10** (see Section 2.5).

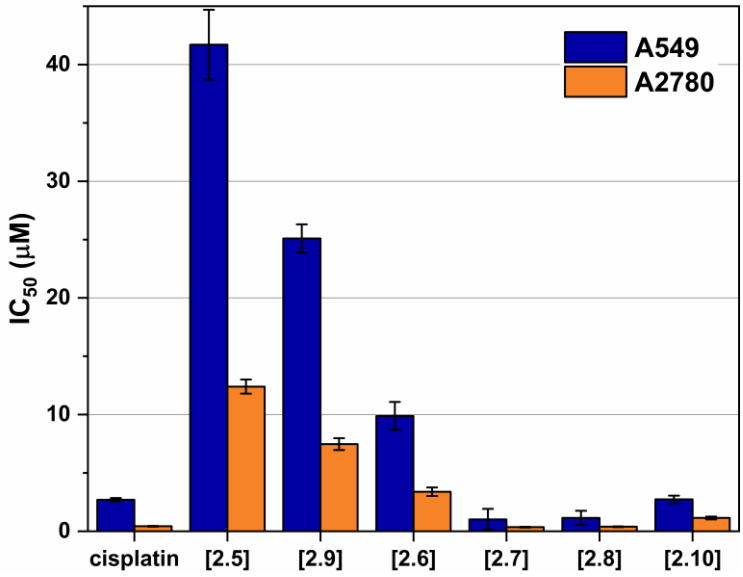

Figure 2.8. Cell viability data in A549 and A2780 cells treated with cisplatin and **2.5-2.10** to show influence of ligand backbone on cytotoxicity. Antiproliferative activities were determined by MTT assay and dose response curves are given in Figure 2.9. The IC_{50} calculated is the concentration of drug required for 50% growth inhibition over 72 h. The error bars represent one standard deviation from three independent experiments.

Two potential modes of action of the (*cis*-tach)Ru diphosphine complexes were investigated. First, aquation of the Ru–Cl bond to the labile Ru–OH_2 complex followed by covalent interactions with nucleosides; and second, the ability of the complexes to interact with DNA by non-covalent interactions.

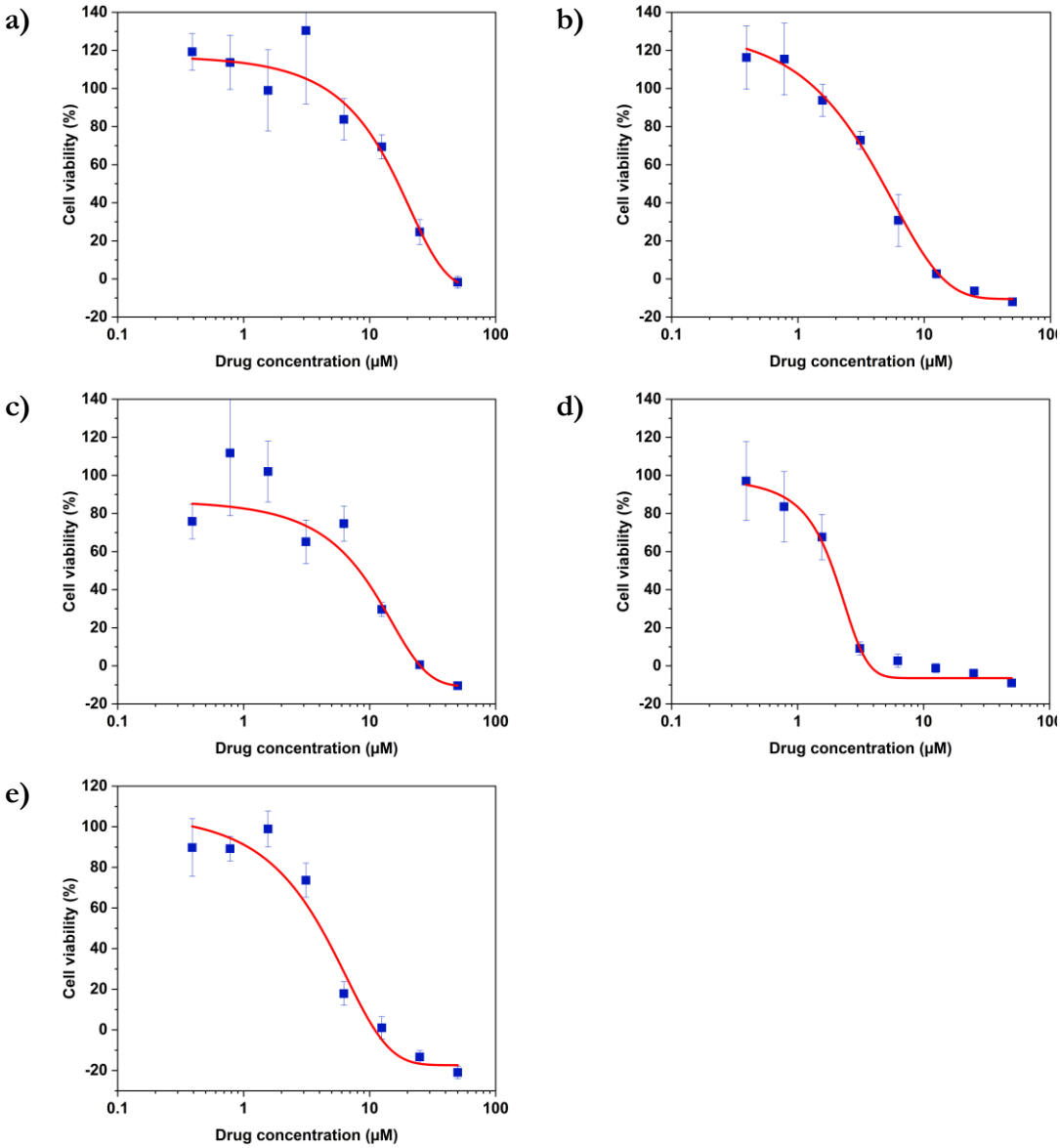

Figure 2.9. Representative dose response curves for A549 cells treated with a) cisplatin, b) **2.10**, c) **2.18**, d) **2.17**, e) **2.19**.

2.4.2 Aquation of Ru–Cl complexes

The aquation products of **2.6**, **2.7** and **2.18** were characterised by $^{31}P\{^{1}H\}$ NMR spectroscopy and ESI-MS. The $^{31}P\{^{1}H\}$ NMR spectra for complexes recorded in water at pH 7.4 consisted of two singlet resonances, with one corresponding to the starting chlorido complex, and the other to the aquated (water or hydroxo) complex (Scheme 2.8). The assignment of each resonance was made by monitoring the changes upon addition of sodium chloride to the aqueous solution. The high-resolution electrospray ionization mass spectrometry (HR-ESI-MS) data for **2.6**, **2.7** and **2.18** recorded in 75% H_2O/25% MeOH supported the formation of the aquated complexes with the molecular ion mass and isotope patterns corresponding to the ion $[Ru–Cl+OH]^+$ in all cases.

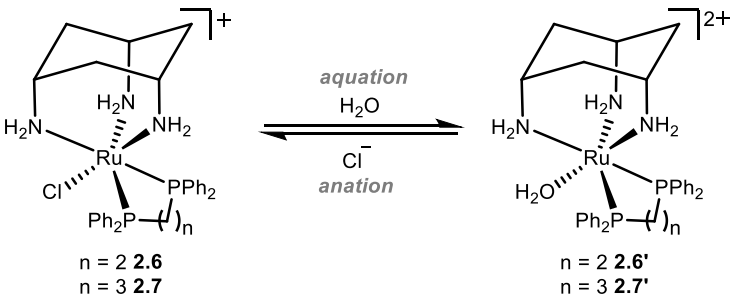

Scheme 2.8. Representative aquation/anation for **2.6** and **2.7** to give **2.6'** and **2.7'**.

2.4.3 Kinetics of aquation

The kinetics of aquation and anation of the (*cis*-tach)Ru complexes **2.6**, **2.10** and **2.18** were investigated by UV-visible spectroscopy and compared to $[RuCl(\eta^6\text{-bip})(en)]^+$ (**C** in Figure 2.1).[162] The time-evolution difference spectra (ΔA) for each complex are shown in Figure 2.10. The presence of isosbestic points in each spectrum suggests that the aquation process involves a single-step mechanism in the formation of the aqua derivative from the chlorido complex. The time dependence for the absorbance of each complex $(\Delta A)_{max}$ followed first order kinetics (Figure 2.11 and Table 2.3). The first order rate constants (k) are derived from fitting the data to a nonlinear exponential growth formula:

$$y = Ae^{\left(\frac{x}{t_1}\right)};$$

$$k = \frac{1}{t_1}$$

The rate of aquation of **2.6** at physiological temperature (310 K) corresponds to a half-life of 33 s. Therefore, the rate of aquation is not a significant factor in the *in vitro* activity of the complex as aquation occurs rapidly in comparison to cell proliferation (typically 24 h).

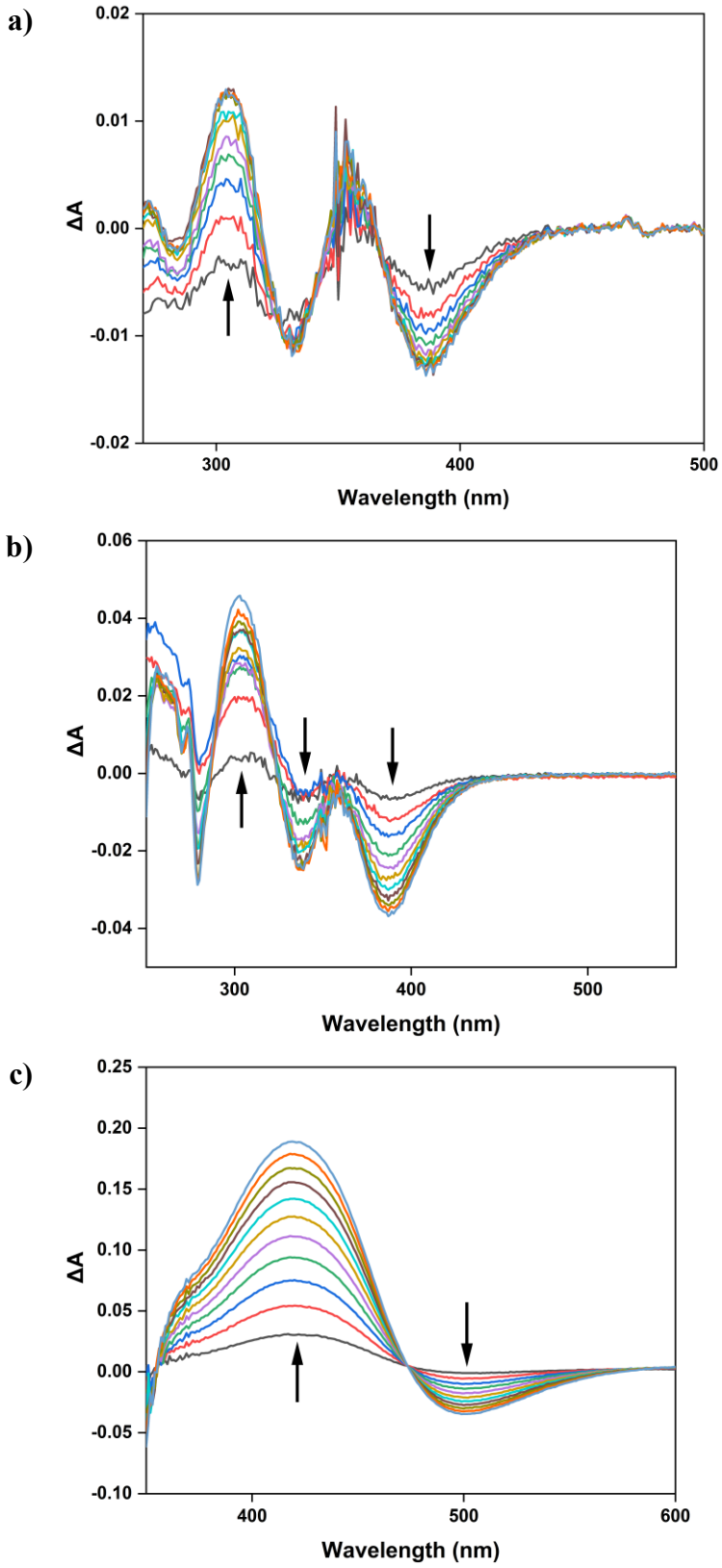

Figure 2.10. Time-evolution of UV-visible difference spectra for the aquation of 300 μM of a) **2.6**, b) **2.10**, c) **2.18** in aqueous solution buffered at pH 7.4 (10 mM sodium phosphate) with 1.6% MeOD at 298 K, $I \approx 25$ mM. Plots are given for minutes 1 to 9. $\Delta A = A_t - A_0$, where A_t = absorbance at time t and A_0 = A at t = 30 s.

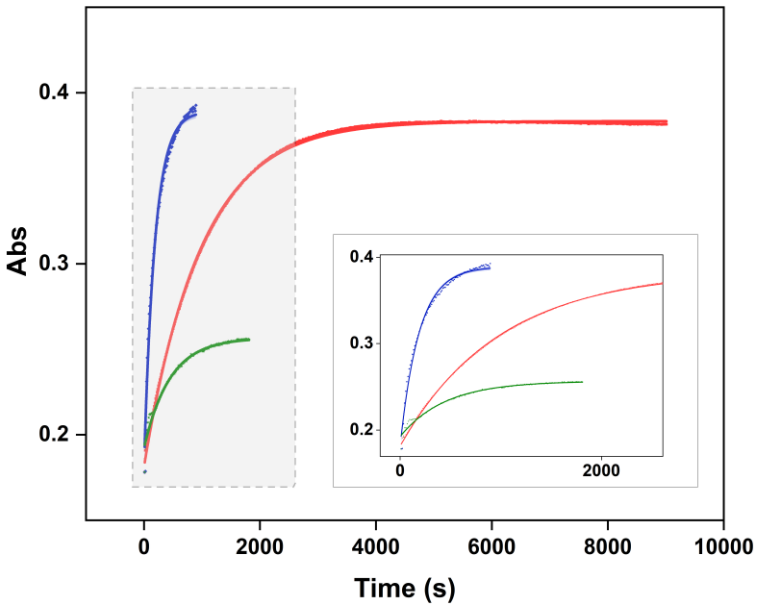

Figure 2.11. Time dependence of the absorbance (green **2.6**, blue **2.10**, red **2.18**, $(\Delta A)_{max}$ wavelength indicated by the up arrows in Figure 2.10) for each complex. Inset is an expansion to show the first 2000 s.

The rate constants for the aquation of **2.6** ($6.55 \pm 0.06 \times 10^{-3}$ s^{-1}) and **2.7** ($63.9 \pm 6.0 \times 10^{-3}$ s^{-1}) at 298 K are approximately 5 and 15 times faster than the η^6-biphenyl complex $[RuCl(\eta^6\text{-bip})(en)]^+$ (**C**) (1.28×10^{-3} s^{-1}) respectively. This difference could be attributed to a weakening of the Ru–Cl bond, as shown by its lengthening, observed in the crystal structures of **2.6** (2.4431(14) Å) and **2.7** (2.4404(4) Å)[82] when compared to RAen complex **C** (2.405(6) Å),[158] due to the *trans*-effect of the nitrogen donors in the *cis*-tach ligand.

Both **2.6** and **2.7** were found to be stable for the duration of a typical 72 h MTT assay experiment. Furthermore, over a two-week period at 37 °C, the ^{1}H NMR spectrum of **2.6** in 10% D_2O/90% H_2O did not change. Since the rate of aquation of the Ru–Cl is rapid, the biological activity is likely more dependent on the binding to biomolecules once this aquation step has taken place. Therefore, to test this hypothesis, a series of DNA binding experiments were carried out.

Table 2.3. First order rate constants and half-lives for the aquation of (*cis*-tach)Ru complexes at various temperatures, pH 7.4.

Complex	T (K)	k (10^{-3} s^{-1})[a]	$t_{½}$ (s)
2.6	288	2.09 ± 0.02	331 ± 3
2.6	293	3.60 ± 0.08	192 ± 5
2.6	298	6.55 ± 0.06	106 ± 1
2.6	303	10.7 ± 0.2	65 ± 1
2.6	310	21.0 ± 0.7	33 ± 1
2.7	298	63.9 ± 6.0	10 ± 2
2.10	298	2.23 ± 0.12	311 ± 17
2.18	298	1.02 ± 0.01	679 ± 3

[a]Measurements for the aquation of **2.6**, **2.7**, **2.10** and **2.18** (300 μM) in aqueous solution buffered at pH 7.4 (10 mM sodium phosphate).

Given the rapid rates of aquation, one likely method of causing antiproliferative effects is through coordination of a biomolecule to the complex at the coordination site initially occupied by the chloride ligand. The reported complexes share a structural feature with cisplatin – a nitrogen donor *trans*- to a chloride ligand – and thus have favourable aquation kinetics. As previously reported, the aquation kinetics for the Pt–Cl bonds of square planar Pt(II) d^8 complexes are on the order of ~10^{-5} s^{-1}, notably slower than the Ru–Cl bonds of octahedral Ru(II) d^6 complexes (~10^{-3} s^{-1}).[50] Additionally, the amine groups of the *cis*-tach ligand are located *cis*- to the chloride ligand and may have a role in strengthening interactions with a bound molecule through hydrogen bonding. With these considerations, the following DNA binding experiments were carried out.

2.4.4 Binding of Ru to CT-DNA

The intercalating fluorescent dye ethidium bromide (EB) was used in a competition assay with complexes **2.6**, **2.10**, **2.17**, **2.18**, **2.19** as well as the known DNA intercalator $[Ru(bpy)_2(DPPZ)]^{2+}$ (DPPZ = dipyrido[3,2-a:2',3'-c]phenazine) as a benchmark (Figure 2.12).[110] A solution of 50 μM calf thymus DNA (CT-DNA) and 5 μM EB ([CT-DNA]/[EB] = 10:1) was prepared and the EB-CT-DNA adduct was subjected to titration with Ru complexes.

The quenching constants (K_{SV}) were calculated according to the Stern-Volmer (SV) equation.[54,173,174]

$$\frac{I_0}{I} = 1 + K_{SV}[Q]$$

where I_0 and I are the emission intensity in the absence and presence of quencher complex respectively, K_{SV} is the Stern-Volmer quenching constant and [Q] is the quencher concentration.

From these plots, the apparent binding constants (K_{app}) were calculated using: K_{EB}[EB] = K_{app}[complex], where $K_{EB} = 1\times10^7$ M^{-1}, [EB] = 5 μM, and [complex] is the concentration of Ru complex that gave a 50% reduction of the initial emission intensity of EB.

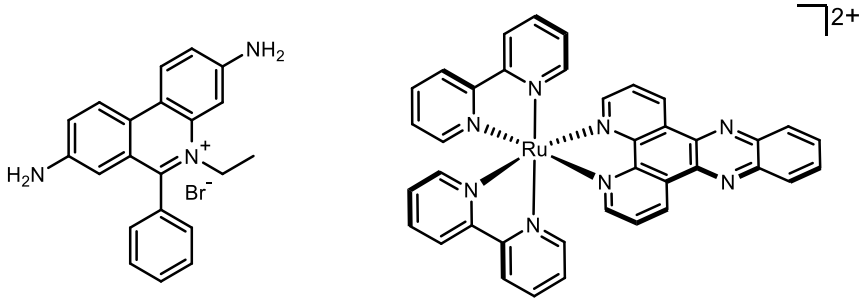

Ethidium bromide $[Ru(bpy)_2(DPPZ)]^{2+}$

Figure 2.12. Chemical structures of the DNA intercalating dye ethidium bromide (EB) and the known intercalating complex $[Ru(bpy)_2(DPPZ)]^{2+}$.

For titrations with complexes **2.17-2.19**, a gradual decrease in emission was observed (Figure 2.13 and Figure 2.14) implying that these complexes outcompete the EB to interact with DNA. The same titration was performed with **2.6** and **2.10**; however, no appreciable decrease in emission was observed for **2.6** indicating negligible intercalative interaction is present (Figure 2.15). For **2.10**, the decrease was so small that a binding constant could not be calculated and therefore intercalation is not considered a viable mode of action for this complex (Figure 2.15).

The binding constants (derived from $K_{app} = (K_{EB}[EB])/[complex]$) for **2.17**, **2.18** and **2.19** are $3.07 \pm 0.07 \times 10^5$ M^{-1}, $1.16 \pm 0.04 \times 10^5$ M^{-1} and $5.11 \pm 0.25 \times 10^5$ M^{-1} respectively (Figure 2.13 and Table 2.4), indicating that increasing the aromatic surface of the ligand backbone (**2.18** to **2.19**) gave a five-fold increase in binding affinity.

These binding constants are comparable, and in some cases superior to, rigid dinuclear (η^6-arene)Ru complexes previously reported.[175] The apparent binding constant of the

known DNA intercalator $[Ru(bpy)_2(DPPZ)]^{2+}$ was calculated as 1.75 ± 0.02 $\times 10^6$ M^{-1}, only one order of magnitude higher than the (*cis*-tach)Ru complexes **2.17-2.19**.

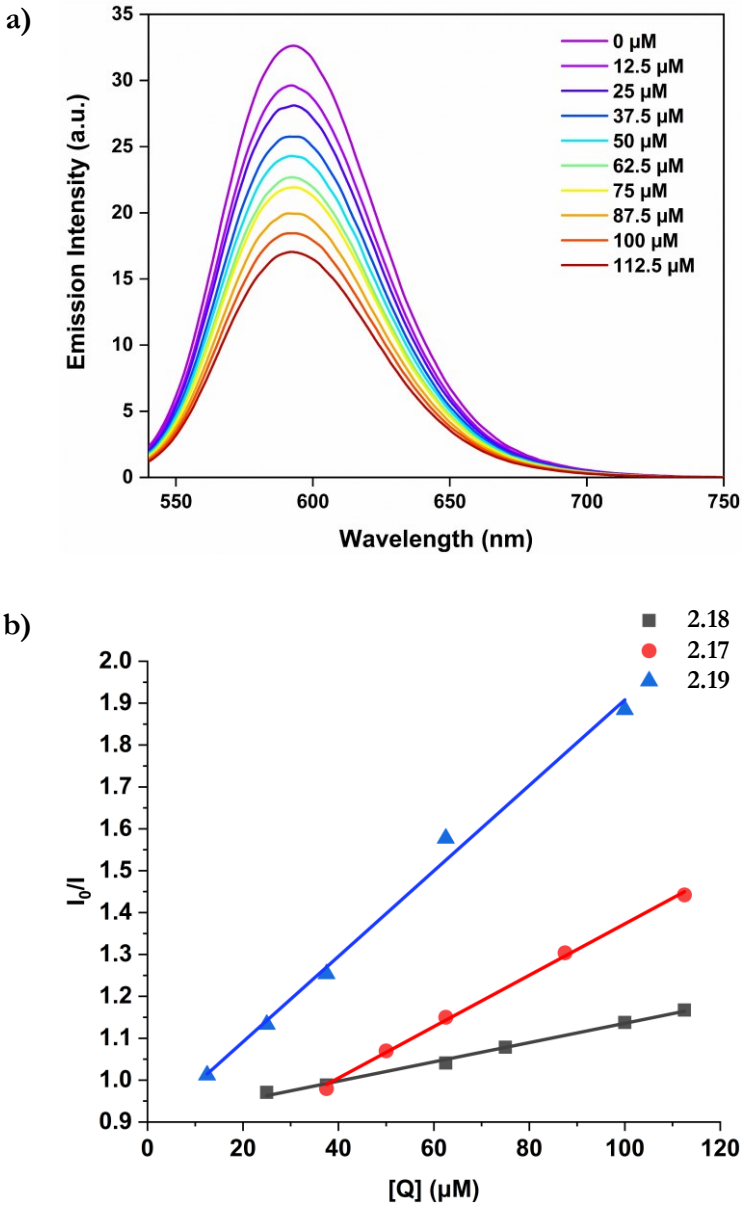

Figure 2.13. a) Emission spectra of CT-DNA (50 µM) and EB (5 µM) competition assay with **2.18** (0–112.5 µM). b) Stern-Volmer plots EB-CT-DNA vs. [Q] where Q = (*cis*-tach)Ru complexes **2.17-2.19**.

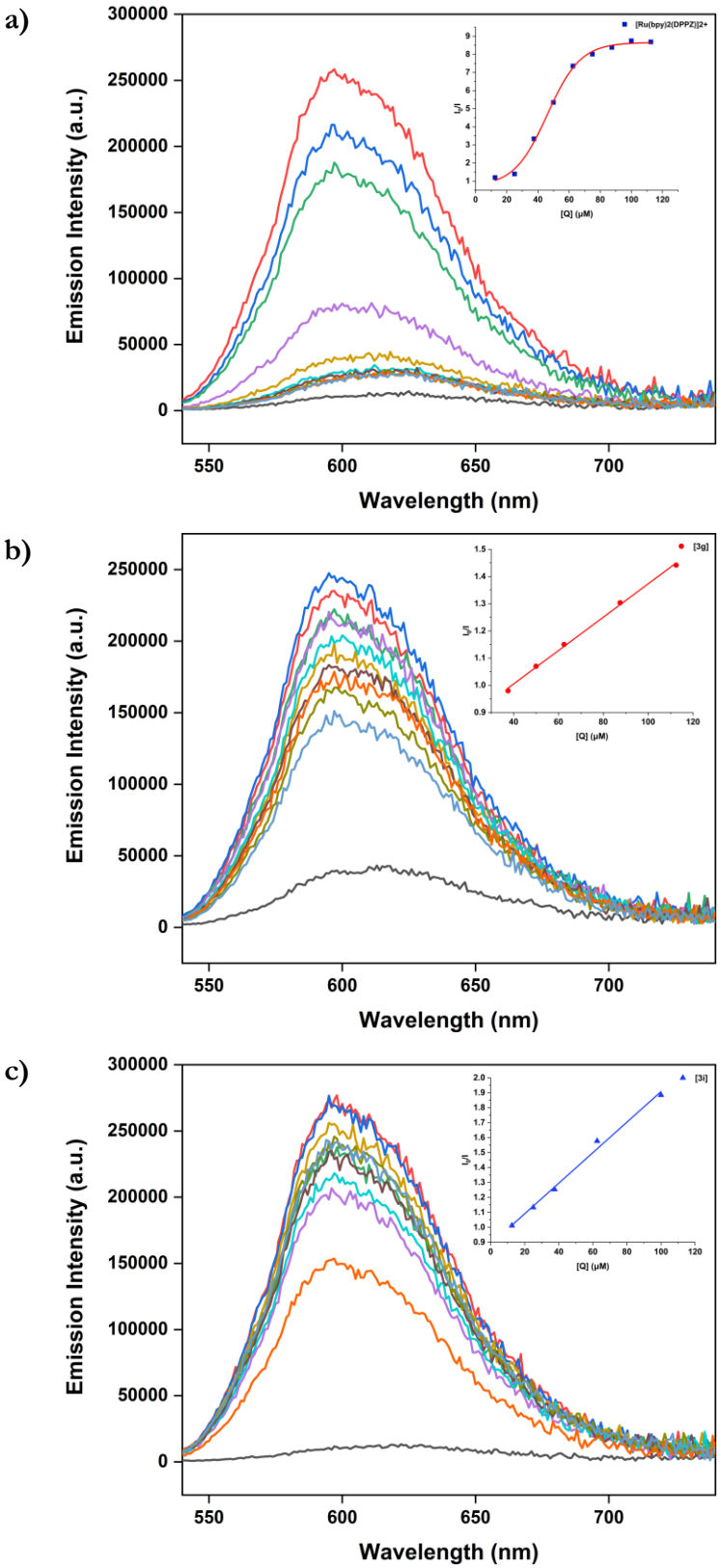

Figure 2.14. Emission spectra of CT-DNA (50 μM) and EB (5 μM) competition assay with a) $[Ru(bpy)_2(DPPZ)]^{2+}$, b) **2.17**, c) **2.19**. Inset: Stern-Volmer plots EB-CT-DNA vs. [Q] where Q = (*cis*-tach)Ru complex.

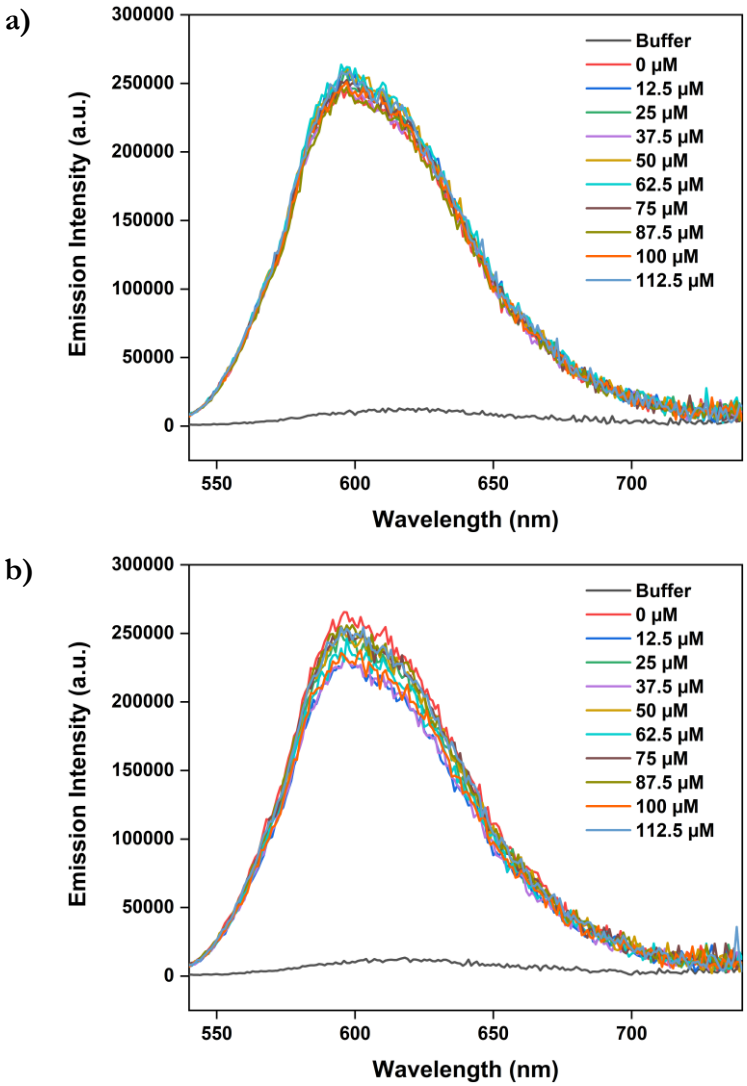

Figure 2.15. Emission spectra of CT-DNA (50 μM) and EB (5 μM) competition assay with a) **2.6**, and b) **2.10**.

Table 2.4. Binding (K_{app}) and quenching (K_{SV}) constants for the interaction of Ru complexes with CT-DNA.[a]

Complex	K_{SV} ($\times 10^3$ M^{-1})	K_{app} ($\times 10^5$ M^{-1})
2.17	6.13 ± 0.16	3.07 ± 0.07
2.18	2.31 ± 0.08	1.16 ± 0.04
2.19	10.21 ± 0.05	5.11 ± 0.25
2.6	n/a	n/a
2.10	n/a	n/a
$[Ru(bpy)_2(DPPZ)]^{2+}$	34.97 ± 0.43	17.48 ± 0.22

[a]Calculated as the average of triplicate experiments.

2.4.5 Binding to G-Quadruplex DNA

The following results were obtained with the help of Dr. Michael O'Hagan as part of a collaborative study.[85,176]

G-quadruplexes are four-stranded DNA secondary structures that form from guanine-rich sequences (Figure 2.17). They attract particular attention as an anticancer target, owing to the occurrence of quadruplex-forming motifs at chromosome telomeres and in the promoter sequences of several oncogenes, e.g., the *c-myc* gene.[177–179] These structures can adopt a variety of topologies characterised by the relative orientations (parallel/antiparallel) of the DNA strands in the folded structure.[180,181] Furthermore, the planar G-tetrads provide additional opportunities for stacking and intercalative interactions with complexes, since the dimensions are significantly larger than those of a classical Watson-Crick base pair.[182] Therefore, these DNA sequences can hypothetically be targeted with high-selectivity in order to reduce or eliminate the off-target effects resulting from indiscriminate binding to duplex DNA.[177,182]

This therapeutic hypothesis has led to many groups designing G-quadruplex binders as potential anticancer agents[183–186] and many metal complexes are known to bind G-quadruplexes effectively through covalent and non-covalent interactions.[187] For example, Liu *et al.* found that ruthenium polypyridyl complexes containing 4idip (4-indoleimidazo[4,5-f][1,10]phenanthroline) ligands were able to selectively stabilise the human telomeric G-quadruplex structure.[184,185]

As a result of the intercalating ability of **2.17-2.19** indicated by the EB assays, we investigated the ability of the complexes to stabilise G-quadruplex DNA and duplex DNA structures. The extent of stabilisation was quantified by performing a Fluorescence Resonance Energy Transfer (FRET) assay initially reported by De Cian *et al.*[188] The change in DNA melting temperature ($\Delta T_{1/2}$) induced by a Ru complex compared to that of the oligonucleotide in the absence of complex was also used as an indication of the capacity of the complex to stabilise the G-quadruplex structure. We chose to investigate three models of G-quadruplex DNA and one of duplex DNA (see Figure 2.17). The human telomeric sequence (F21T) was studied in potassium- and sodium-containing buffer owing to the known influence of the metal ion on the polymorphism of this sequence.[189,190] The G-quadruplex sequence found in the *c-myc* oncogene promoter (FmycT) was selected as a model of this anticancer target.

The results of the FRET experiments are shown in Figure 2.17 and representative DNA melt curves in Figure 2.16. Complexes **2.17** and **2.18** did not induce any appreciable stabilisation of quadruplex DNA ($\Delta T_{1/2}$ < 3 °C at 1 μM complex) but **2.19** did stabilise F21T ($\Delta T_{1/2}$ = +7.5 ± 2.3 °C) in Na^+-containing buffer. Additionally, **2.19** was selective for quadruplex DNA structures, stabilising the quadruplex sequence FmycT ($\Delta T_{1/2}$ = +6.2 ± 1.5 °C), whilst stabilisation of the duplex sequence F10T was negligible (Figure 2.17). Meanwhile, the same complex did not significantly stabilize F21T in K^+-rich buffer ($\Delta T_{1/2}$ < 3 °C), suggesting that as well as G4/duplex selectivity, the complex can also discriminate between different G-quadruplex topologies to some extent. As a control, the well-known DNA intercalator complex $[Ru(bpy)_2(DPPZ)]^{2+}$ did not significantly stabilise quadruplex DNA ($\Delta T_{1/2}$ = +1.6 ± 0.4 °C for F21T) or duplex DNA ($\Delta T_{1/2}$ = +1.2 ± 0.3 °C for F10T) as previously reported.[183]

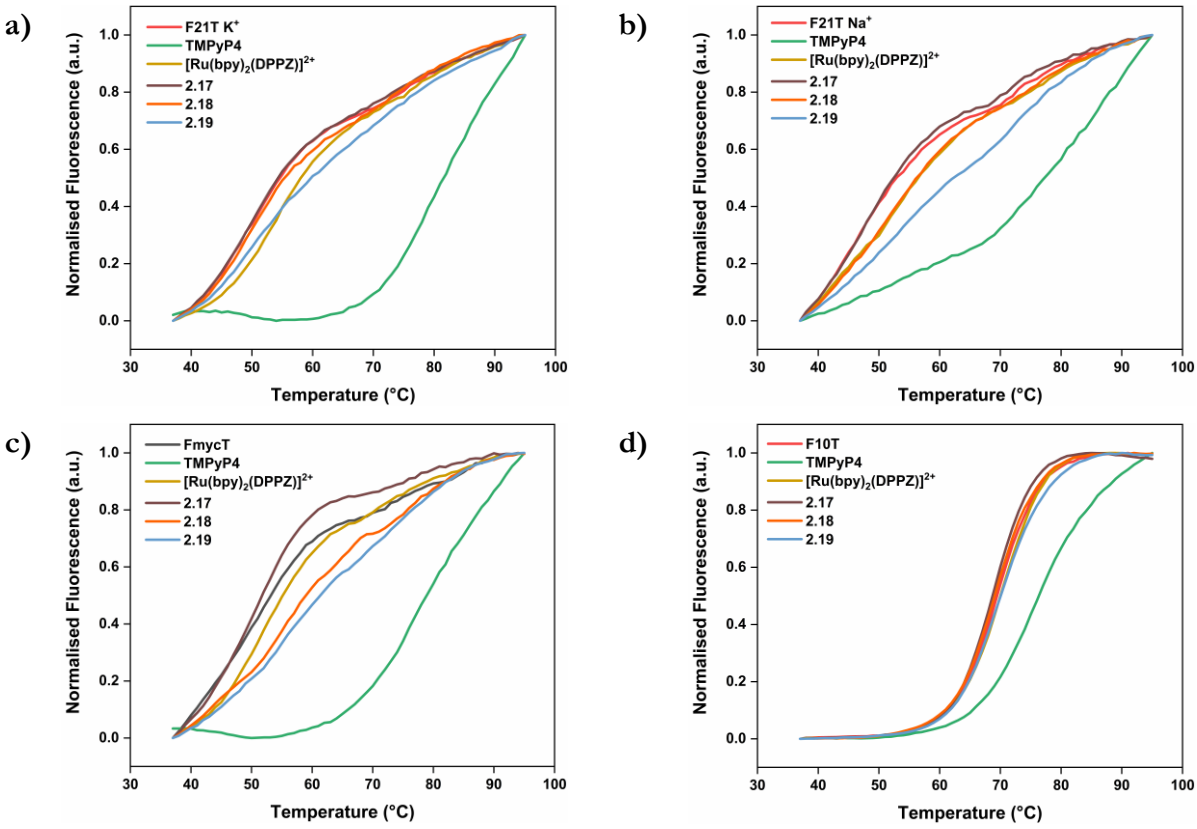

Figure 2.16. Representative thermal melting curves for **A)** F21T quadruplex (K^+ conditions); **B)** F21T quadruplex (Na^+ conditions); **C)** FmycT quadruplex (K^+ conditions); **D)** F10T duplex (K^+ conditions).

The dibenzo[f,h]quinoxaline moiety in **2.19** provides a large aromatic surface that may selectively stabilise G-quadruplex DNA through preferential association with the large G-tetrads over intercalation with Watson-Crick base pairs, akin to the 4idip examples previously reported.[184] Complex **2.19** showed stronger binding than **2.17** and **2.18** in

experiments with quadruplex DNA as well as with CT-DNA (see Table 2.4). This interesting discovery that (*cis*-tach)Ru complexes interact with quadruplex DNA warrants further study.

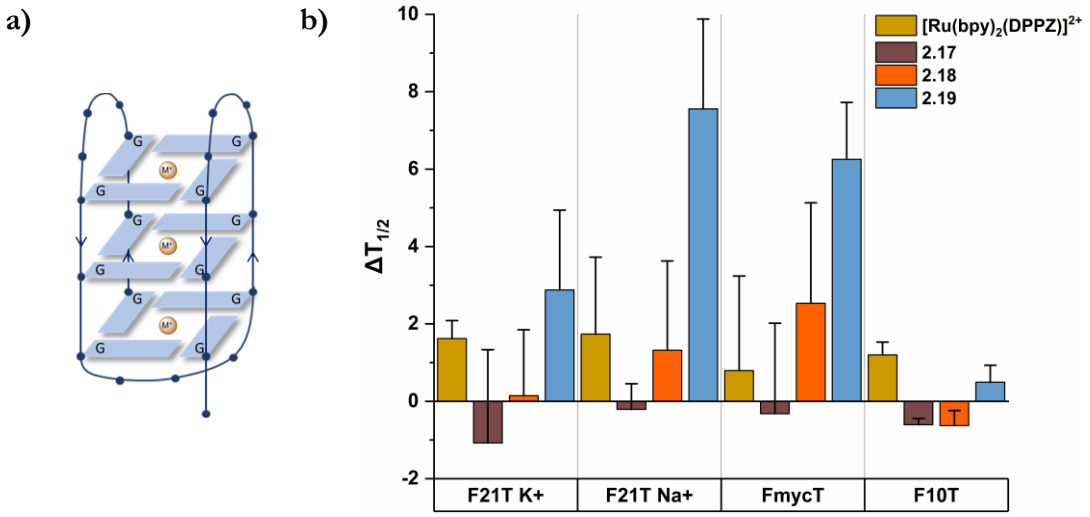

Figure 2.17. a) Schematic representation of a DNA G-quadruplex. The folding of the oligonucleotide into a four-stranded structure creates a stacked arrangement of G-tetrads, each formed by the square-planar assembly of four guanine (G) residues. The overall topology is determined by the relative orientation of the neighbouring strands (indicated by arrows) and stabilized by co-ordination to metal ions (M^+). b) Average $\Delta T_{1/2}$ for quadruplex (F21T and FmycT) and duplex (F10T) DNA after treatment with Ru complexes (1 μM). Error bars show standard deviations from four experiments.

2.5 LiveCyte Cell Imaging

The following experiments were carried out with the help of Dr. Karen Hogg and Dr. Joanne Marrison as part of a collaborative study.[85,191]

The viability of A549 cells and 293T cells was assessed using LiveCyte (Phasefocus Ltd) label-free time-lapse microscopy.[191,192] LiveCyte cell imaging does not require the cell to be labelled with antibodies or cellular dyes; the cells are unperturbed and the imaging process is not toxic to the cells; the cellular changes measured are reported with confidence to be associated with the presence of the compounds. Conventional light microscope imaging requires the cells to be labelled with a DNA binding or cytoplasmic dye and requires higher energy lasers, compared to the LiveCyte: both the labelling and the imaging light source in conventional light microscopy may be cytotoxic over prolonged time and needs to be considered when interpreting results. This technique enables quantification of the total cellular dry mass as an indicator of cell death and growth. For A549 and 293T cells, the effect of treatment with cisplatin and **2.19** is shown at 36 and 72 h time-points (Figure 2.18 and Figure 2.19).

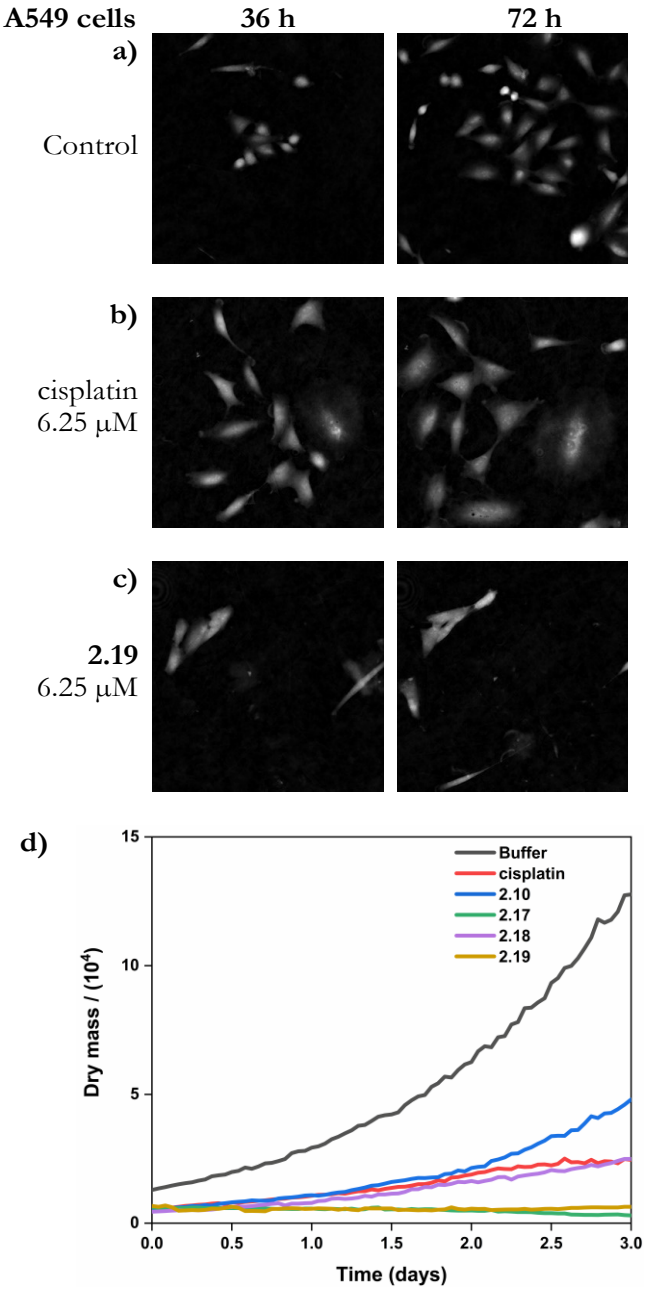

Figure 2.18. LiveCyte time-lapse images of A549 control cells (a) and after treatment with 6.25 μM cisplatin (b) and 6.25 μM **2.19** (c). (d) Dry mass plot to show growth inhibition when treated with cisplatin, **2.10**, **2.17**, **2.18**, **2.19** (all at 6.25 μM).

The MTT assay is an endpoint colorimetric readout of cell viability and does not provide any visual characteristics of the cells state. In this preliminary study, integrated image analysis software (Livecyte Cell Analysis Toolbox) was used to extract real-time changes in morphology and dry mass of each cell over time. The summed mass of the cellular components excluding water was calculated and for each treated population of cells used as a measure of the combined growth and proliferation. For A549 cells (Figure 2.18), the reduction in dry mass is greatest for **2.17** and **2.19** followed by the slightly less active derivative **2.18** (which shows comparable results to cisplatin), and **2.10** gave the smallest

decrease in dry mass of those tested. This difference in dry mass reduction between cisplatin and **2.10** is notable as the MTT assay derived IC_{50} values are within error of each other ($IC_{50} \approx 2.7$ μM).

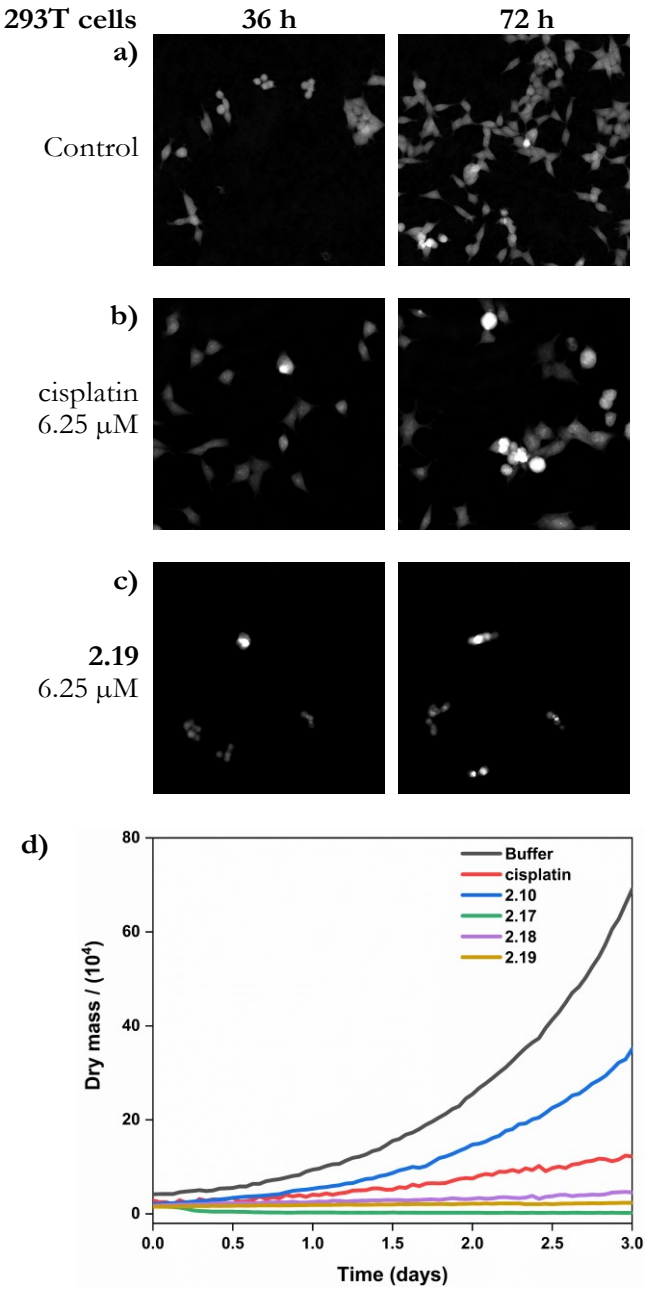

Figure 2.19. LiveCyte time-lapse images of 293T control cells (a) and after treatment with 6.25 μM cisplatin (b) and 6.25 μM **2.19** (c). (d) Dry mass plot to show growth inhibition when treated with cisplatin, **2.10**, **2.17**, **2.18**, **2.19** (all at 6.25 μM).

For 293T cells (Figure 2.19), the reduction in dry mass is even more pronounced, with **2.10** causing significantly less reduction than cisplatin. The other (*cis*-tach)Ru complexes **2.17-2.19** caused significant cell death at a concentration of 6.25 μM, evident from the cell

images and dry mass curves, and this greater activity is consistent with **2.17-2.19** exhibiting cytotoxicity by multiple mechanisms.

2.6 Conclusions

In summary, the compounds presented in this Chapter are the first reported examples of cytotoxic ruthenium(II) *cis*-tach complexes. The precursor complex [RuCl(DMSO-*S*)$_2$(*cis*-tach)]Cl (**2.1**) was obtained in high yield and is a very useful precursor for the synthesis of a range of ruthenium(II) derivatives. Complexes **2.5-2.10** and **2.17-2.19**, which contain chelating diphosphine ligands, are highly active *in vitro* against A549, A2780 and 293T cancer cell lines. In particular, complexes with flexible aliphatic backbones (**2.7** and **2.8**) or planar aromatic backbones (**2.17-2.19**) are the most cytotoxic, with activity in the A549 cell line more than twice that of cisplatin, and activity in the A2780 cell line equipotent to the clinical drug. The electron rich nature of the Ru centre afforded by the *cis*-tach ligand, coupled with favourable aquation kinetics, enables high levels of the active Ru–OH$_2$ complex in the cell nucleus.

New analogues with planar aromatic backbones have been shown to intercalate strongly with CT-DNA models, and, in the case of **2.19** also selectively stabilise G-quadruplex DNA over duplex DNA. The anti-proliferative effect has been monitored by LiveCyte, label-free, time-lapse imaging and stark differences are observed between the phenylene derivative **2.10** and the extended aromatic derivatives (**2.17** and **2.19**). Overall, these preliminary biological studies suggest that (*cis*-tach)Ru diphosphine complexes exhibit a dual-action cytotoxic effect, targeting cellular DNA by intercalation, as well as by modes of action involving covalent binding with DNA. This robust, water-soluble molecular architecture could be further developed to produce next generation ruthenium chemotherapeutic agents. Further cell studies exploiting the tunability of phosphine ligands that result in targeted metallodrugs are discussed in Chapter 3.

2.7 Future work

To further understand the interplay between covalent and intercalative binding, it would be productive to test a (*cis*-tach)Ru complex containing a chelating phosphine but lacking a chlorido ligand, e.g., [Ru(CN)(*cis*-tach)(PP)]$^+$ as this would show if a Ru–Cl bond, as well as a chelating phosphine, are essential for biological activity. The strongly bound cyano ligand would not aquate in the way the chlorido ligand does, so any activity arising from these complexes would result from non-covalent binding interactions. Further analyses

to differentiate between the activity arising from intercalative versus covalent binding could include Scatchard analysis, as a way of determining the number of binding sites occupied by these complexes with certain biomolecules.

Chapter 3. Fluorescent phosphine complex conjugates

3.1 Introduction

The ability to chemically functionalise a phosphine ligand is desirable for catalysis and medicinal applications including imaging, sensing, and therapy.[114,193,194] In this work we discuss methods to conjugate small organic fluorophores to phosphine ligands. We aim to use the metal complexes derived from these fluorescent phosphines as potential therapeutic or imaging agents. The fluorescent phosphine complex conjugates described herein will be assessed in *in vitro* studies and be compared to the (*cis*-tach)Ru complexes described in Chapter 2.

3.1.1 Methods to functionalise phosphine ligands

The strategies to chemically conjugate an organic fluorophore to a diphosphine ligand discussed in this chapter are:

- Phosphine fluorophore conjugation before metal coordination:

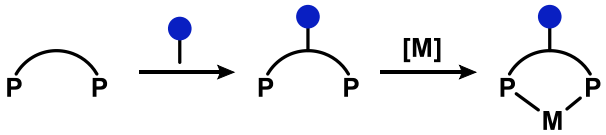

- Phosphine fluorophore conjugation after metal coordination:

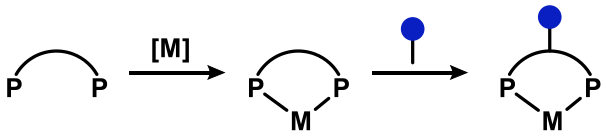

- Direct phosphine fluorophore conjugation (without a backbone tether):

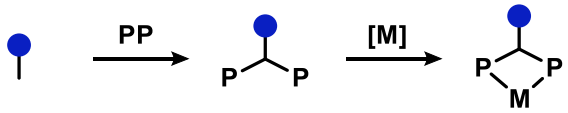

A survey of the relevant literature for these methods is presented.

3.1.1.1 Pre-coordination conjugation

Many examples of phosphine ligand conjugates have been reported (see Figure 3.1 for examples). The tethers used to incorporate an organic fluorophore include ether, ester, or amide linkages. A pyrenyl ether conjugated monophosphine (**A**) was prepared and the luminescent properties of the corresponding Ru halide complexes were reported by Wolf *et al.*[195] A mixed donor *P,S*-ligand (**B**) was reported by Mirkin *et al.*, which featured an

amide tethered pyrenyl group and the resultant Rh complexes employed as fluorescent tweezers for anion sensing.[196]

Jacquemin *et al.*[116] have synthesised ligands (**C**) by a Pd-catalysed coupling of a coumarin-containing aryl iodide with secondary aryl phosphines. The fluorescent triarylphosphine ligands (**C**) were complexed to Ru, Os and Au and the photophysical and anti-proliferative properties investigated in biological studies. Coumarin derivatives (**D**) have also been successfully conjugated to amino acid derived diphosphines reported by Smith *et al.*[197] The crystal structures of the derived MCl_2 complexes (M = Pd, Pt) showed intramolecular hydrogen bonding between the coumarin N–H and the N lone pair in the ligand backbone. To date, the luminescence properties of these complexes have not been reported.

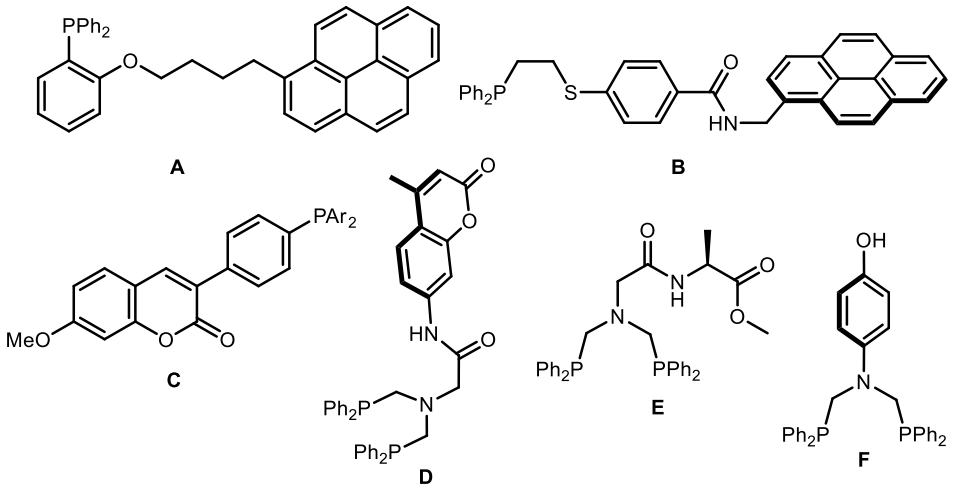

Figure 3.1. Chemical structures of previously reported phosphine ligand conjugates.

Shaw and co-workers reported ligands (**E**) derived from amide coupling between bis((diphenylphosphino)methyl)glycine and amino acid esters.[198] The Rh complexes of **E** were shown to be active in CO_2 hydrogenation which was aided by the pendent amine of the ligand facilitating an outer coordination sphere mechanism.

A versatile method of generating functionalised diphosphine conjugates such as **F** is via Ph_2PCH_2OH which Reetz[199] and Smith[197,200] have shown can be condensed with a range of primary amines containing a variety of functional groups.

3.1.1.2 Post-coordination conjugation

Conjugating phosphines after coordination is a desirable methodology as it would allow diversification from a single metal complex precursor to create a library of functional complex conjugates. Despite this advantage, post-coordination conjugation techniques have been reported less frequently in the literature than pre-coordination conjugation.

Shaw *et al.* demonstrated that HATU-mediated amide coupling of carboxylic acid functionalized diphosphines was successful on a pre-formed Rh complex (Scheme 3.1) proceeding in 42% yield.[201] In this example, a photoactive azobenzene moiety is coupled to the carboxylic acid groups of the coordinated ligands to give **G**. The light-induced *cis*/*trans* isomerization of the azobenzene motif led to structural changes in complex **G** which were studied by ^{1}H NMR spectroscopy. The Rh complex **G** was tested in CO_2 hydrogenation catalysis and results were compared for the reaction when it performed in the light and in the dark. The effect of photocontrolled azobenzene switching was not found to significantly alter the rate of CO_2 hydrogenation evidenced by the similar turn over frequencies for *cis*/*trans*-**G** (TOF = 16 ± 2 h^{-1} (*cis*-**G**) and 11 ± 2 h^{-1} (*trans*-**G**)).

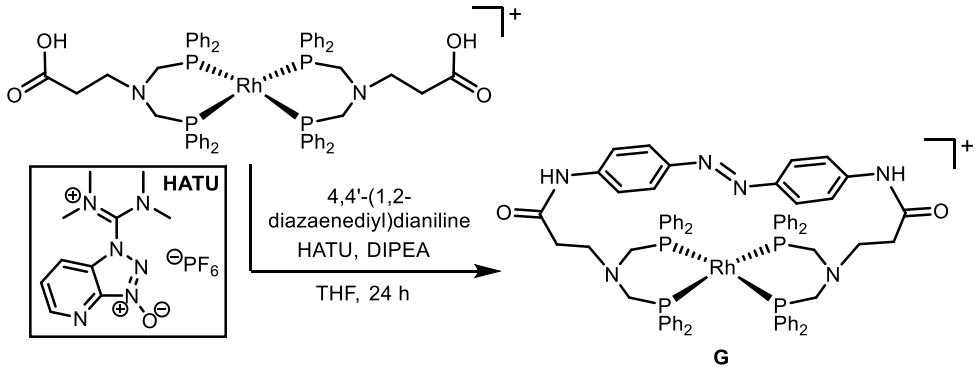

Scheme 3.1. Synthesis of a Rh diphosphine complex with diazobenzene linker, Shaw *et al.*[201]

In another example of post-coordination conjugation, Dyson *et al.* reported cytotoxic (arene)Ru (RAPTA) derivatives (**H**) with a 4-(diphenylphosphino)phenol ligand (Scheme 3.2).[171] Small drug molecules such as aspirin, ibuprofen, ethacrinic acid and indomethacin were coupled to [(η^6-*p*-cymene)Ru(PPh_2(4-C_6H_4OH)Cl_2] in a series of on-metal esterification reactions.

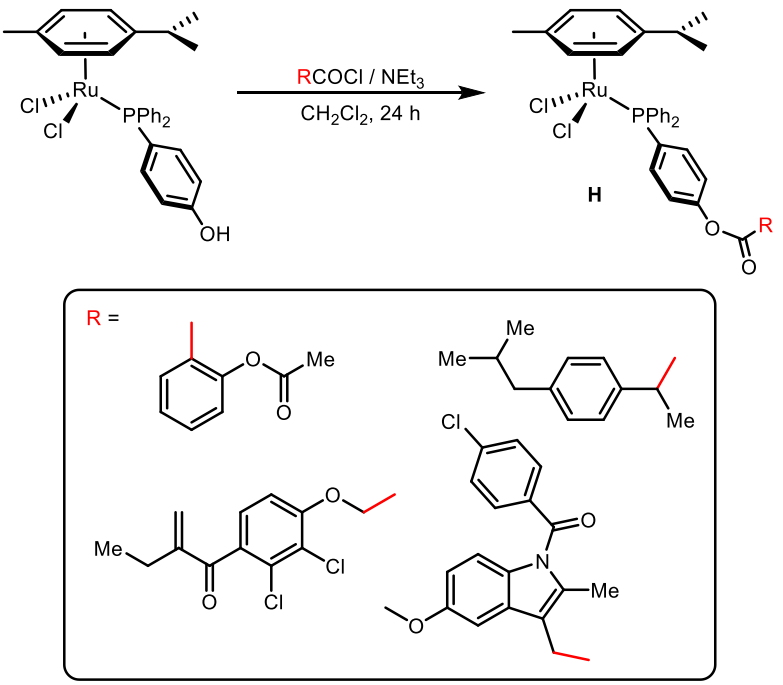

Scheme 3.2. Cytotoxic RAPTA complex conjugates (**H**), reported by Dyson *et al.*[171]

In Scheme 3.2, the acid chloride derived from each small molecule drug is formed *in situ* before reaction with [(η^6-*p*-cymene)Ru(PPh_2(4-C_6H_4OH)Cl_2] in the presence of base to give the new class of RAPTA drug conjugates. These Ru metallodrug conjugates were found to be more cytotoxic than either the Ru precursor or the small molecule drugs alone. Although the authors never observed ester cleavage of the complex conjugates, they suggest that once inside the cell, esterase enzymes could cleave this bond to separate the small drug fragment from the complex.

3.1.1.3 Direct phosphine conjugation (without a tether)

A series of diphosphine ligands derived from Mannich condensation with different amines have been reported. In these examples diphosphine conjugates (**I**) with different backbone functionalities (e.g., alkyl, alcohol, carboxylic acid) are readily formed from *in situ* generation of Ph_2PCH_2OH (from equimolar amounts of $(CH_2O)_n$ and Ph_2PH) followed by condensation with the relevant amine (Scheme 3.3).[200]

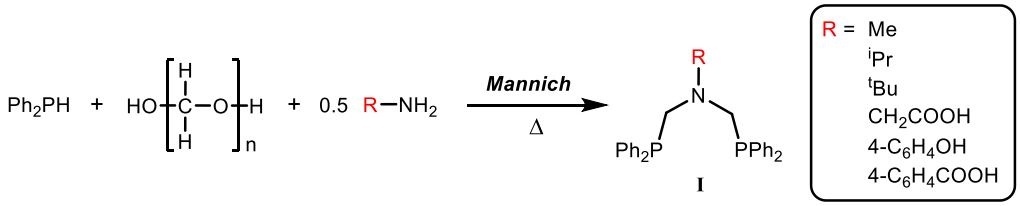

Scheme 3.3. Formation of PCNCP ligands (**I**) from condensation with functionalised amines.

Another method of directly conjugating a monophosphine with a fluorescein-type chromophore was reported by Gabbaï *et al.* (Scheme 3.4).[119] Reaction of *o*-(Ph_2P)-C_6H_4Li with 3,6-di(t-butyldimethylsiloxy)xanthone followed by work up with acetic acid give the fluorescein ligand (**J**). The photophysical and coordination properties were explored (discussed later in Section 4.1.1, Chapter 4), and **J** was found to be an efficient sensor for Au(I) and Au(III) ions in aqueous solution.

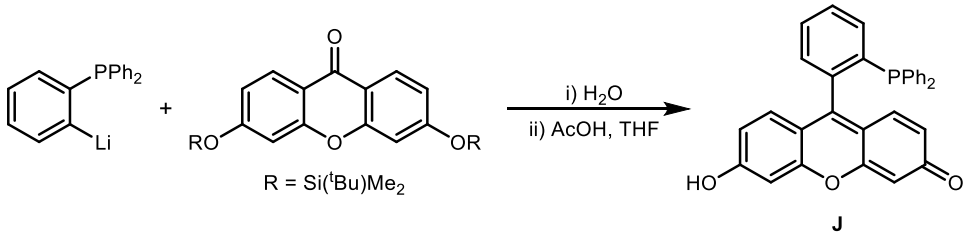

Scheme 3.4. Synthesis of *ortho*-diphenylphosphino fluorescein ligand (**J**), Gabbaï *et al.*[119]

The remainder of this chapter will focus on chemically conjugating organic fluorophores to diphosphine ligands for their application as cytotoxic (*cis*-tach)Ru complexes. This methodology is not limited to fluorophores and could be extended to the coupling of any small molecule, such as drugs, carbohydrates, or peptides.

3.1.2 Research aims

To gain an understanding of the ways to chemically conjugate phosphine ligands with small organic molecules, we aimed to carry out the following:

- Explore different coupling methods of phosphine ligands bearing a reactive functional group. By exploiting previously reported methods for Ru and Rh chemistry, we hoped that coupling could be performed both pre-metal coordination and post-metal coordination (Scheme 3.5).

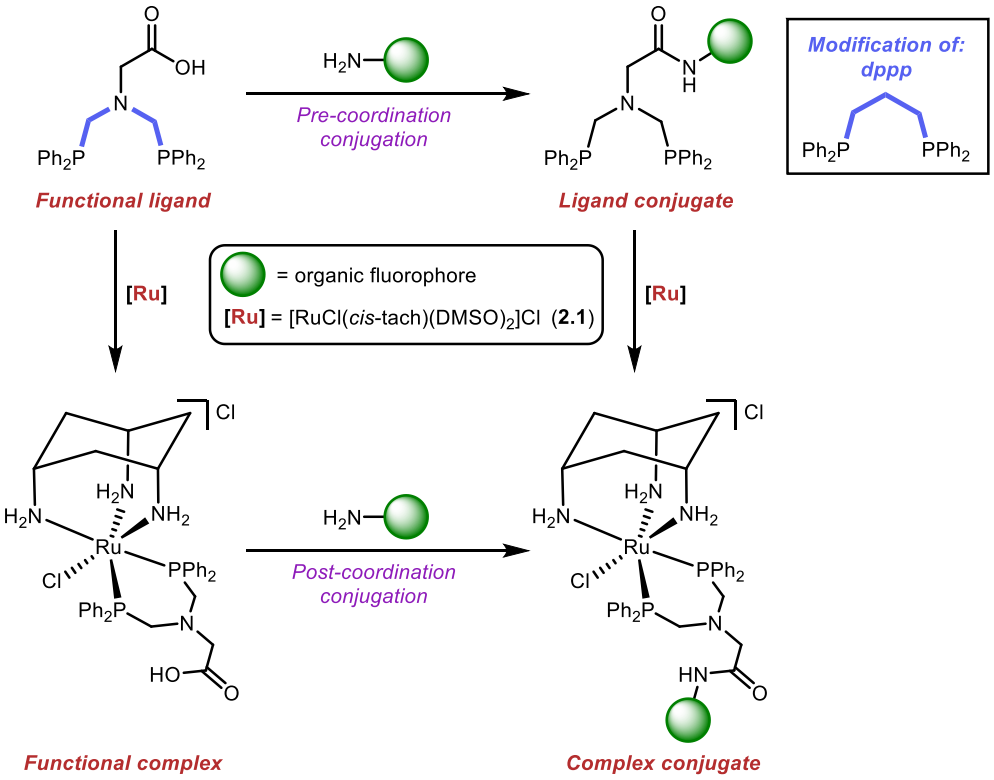

Scheme 3.5. Proposed methods for pre-coordination and post-coordination conjugation.

- Evaluate the most efficient method of synthesising fluorescent phosphine complex conjugates.
- Study the photophysical properties of (*cis*-tach)Ru phosphine complex conjugates by UV-visible and fluorescence spectroscopy.
- Assess the fluorescent (*cis*-tach)Ru complex conjugates as cytotoxic agents and gain insight into their mechanisms of action.

3.2 Synthesis of ligand conjugates

3.2.1 Pre-coordination conjugation via amide bond formation

We started with the carboxylic acid functionalised diphosphine bis((diphenylphosphino)methyl)glycine (**L3.1**). First, because of the amide coupling literature precedent on this type of ligand from Shaw *et al.*, and second, because a 3-atom backbone gave the most cytotoxic (*cis*-tach)Ru complexes (see Section 1.2.3, Chapter 2). Ligand **L3.1** was prepared by *in situ* formation of diphenylphosphinomethanol followed by condensation with glycine (Scheme 3.6).[198]

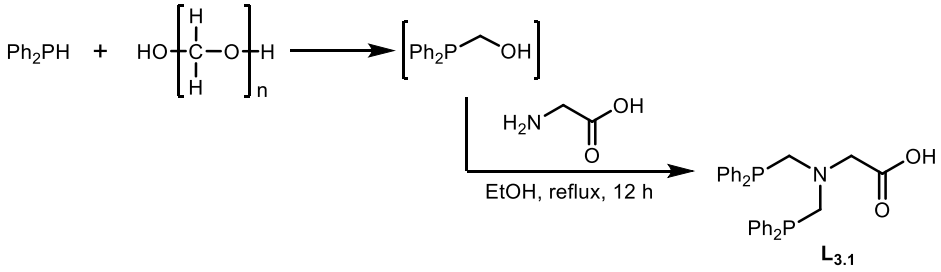

Scheme 3.6. Literature synthesis of bis((diphenylphosphino)methyl)glycine **L3.1**.[198]

Two different classes of fluorescent amines were initially selected, one a pyrene derivative, and the other a 4-methylcoumarin derivative.

First, 1-pyrenemethylamine (generated by deprotonation of the commercially available 1-pyrenemethylamine hydrochloride salt with excess triethylamine) was coupled to **L3.1** using DIPEA and HATU (Scheme 3.7). After addition of DIPEA to deprotonate the carboxylic acid the desired product **L3.2** detected, albeit as part of a mixture of products shown by the *in situ* $^{31}P\{^{1}H\}$ NMR spectrum (Figure 3.2).

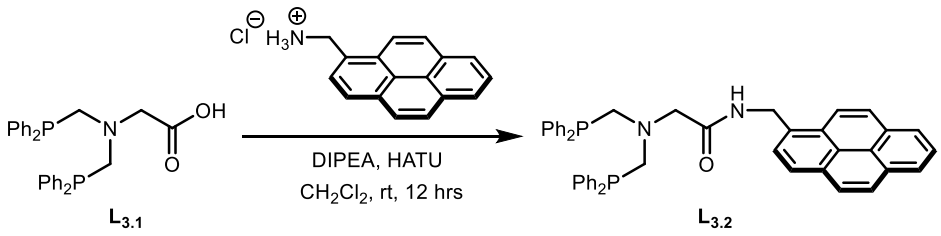

Scheme 3.7. Synthesis of **L3.2** via HATU mediated amide coupling.

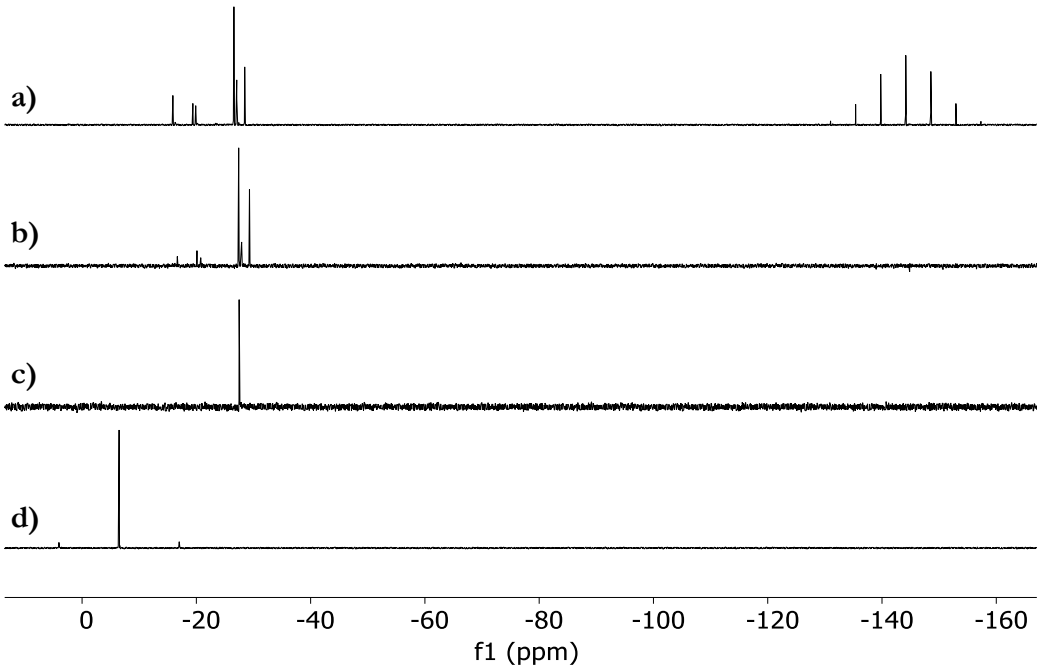

Figure 3.2. Stacked $^{31}P\{^{1}H\}$ NMR spectra for the synthesis of $\mathbf{L_{3.2}}$. a) *In situ* to show mixture of products, b) after aqueous workup, c) purified $\mathbf{L_{3.2}}$, d) Pt complex **3.2**.

The *in situ* $^{31}P\{^{1}H\}$ NMR spectrum of the mixture obtained from the reaction in Scheme 3.7 contained several singlet resonances in the region around δ_P = –27.0 ppm, typical of PCNCP ligands (see Figure 3.2).[200] There is a small difference in the ^{31}P chemical shift for the desired ligand (δ_P = –26.4 ppm) compared to the starting material $\mathbf{L_{3.1}}$ (δ_P = –27.9 ppm); however, this only becomes apparent after isolation of $\mathbf{L_{3.2}}$ from the crude reaction mixture. The hexafluorophosphate anion (present from HATU) can clearly be seen in the *in situ* $^{31}P\{^{1}H\}$ NMR (δ_P = –144.2 ppm, hept, $^{1}J_{PF}$ = 710 Hz). This byproduct was removed by aqueous work up and the pure diphosphine ligand $\mathbf{L_{3.2}}$ was obtained following column chromatography and isolated in a 15% yield. The main loss in yield was attributed to the product partially coeluting with unreacted starting material, and despite efforts, this could not be improved.

Coordination to Pt was achieved by addition of the ligand to [$PtCl_2$(cod)] in a 1:1 molar ratio (Scheme 3.8). The Pt complex **3.2** has the expected platinum satellites in the $^{31}P\{^{1}H\}$ NMR spectrum with a characteristic $^{1}J_{PPt}$ coupling constant of 3416 Hz, typical of the ligand coordinating in a *cis* fashion (Figure 3.2). The formation of complex **3.2** was confirmed by HR-ESI-MS for [**3.2**–Cl]$^{\bullet+}$ (m/z 914.1784) with the expected platinum and chlorine isotope pattern.

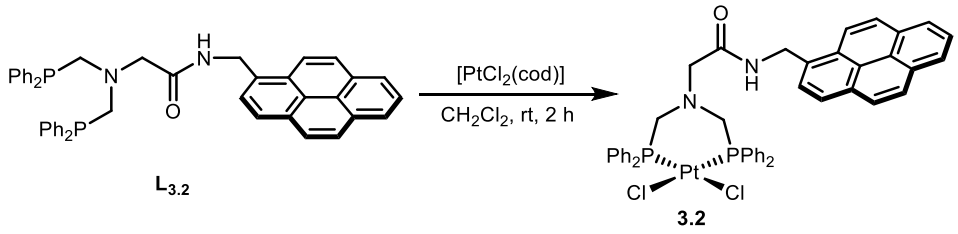

Scheme 3.8. Formation of $PtCl_2$ complex **3.2**.

The pyrene ligand conjugate $\mathbf{L_{3.2}}$ reacted with [RuCl(*cis*-tach)$(DMSO)_2$]Cl (**2.1**) in EtOH under reflux for 48 h to give complex **3.3** (Scheme 3.9). Despite the extended reaction time and elevated temperature, cleavage of the amide bond was not observed and the desired complex **3.3** was isolated in 81% yield. In the $^{31}P\{^1H\}$ NMR spectrum, the 6-membered chelate gave a singlet resonance (δ_P = 41.6 ppm), at a chemical shift similar to that of the (*cis*-tach)Ru complex of dppp (**2.7**) (δ_P = 44.0 ppm). The formation of $[\mathbf{3.3}]^{\bullet+}$ was confirmed by HR-ESI-MS (*m*/*z* 950.2465) with the expected ruthenium and chlorine isotope pattern.

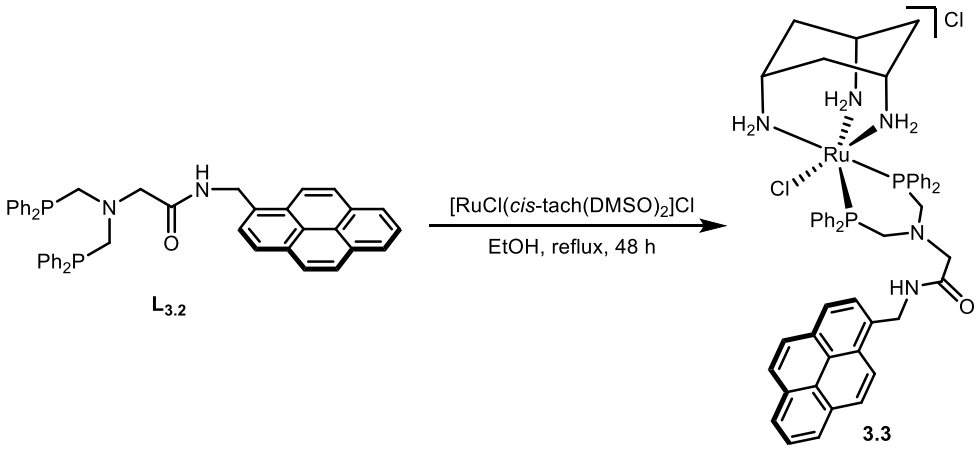

Scheme 3.9. Formation of (*cis*-tach)Ru complex **3.3**.

The amide coupling reaction was attempted with 7-amino-4-methylcoumarin[III] (Scheme 3.10) to form the same ligand reported by Smith *et al.* (compound **D** in Figure 3.1).[197] The *in situ* $^{31}P\{^1H\}$ NMR spectrum did not show a signal in the expected region. The reaction mixture contained multiple species according to the $^{31}P\{^1H\}$ NMR spectrum, with one signal tentatively assigned to the product (δ_P = –19.2 ppm); however, attempted isolation by column chromatography was not successful.

[III] Prepared from 3-aminophenol[306]

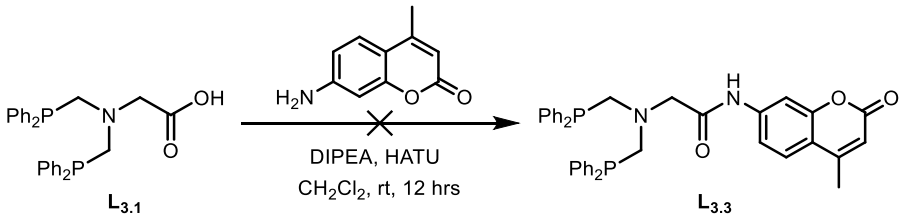

Scheme 3.10. Attempted synthesis of coumarin ligand conjugate $\mathbf{L_{3.3}}$.

We next aimed to synthesise fluorescent ligand conjugates by the direct Mannich condensation methods previously reported by Smith *et al.*[200]

3.2.2 Direct conjugation

The Mannich condensation of formaldehyde and diphenylphosphine with primary amines has previously been used as a route to new diphosphines.[197,200] In this work, ligand conjugates containing an N-bound pyrenyl or coumarin moiety were targeted. The reactions of both 1-aminopyrene and 7-amino-4-methylcoumarin with diphenylphosphinomethanol (Scheme 3.11) appeared to proceed to the monosubstituted and disubstituted phosphines as indicated by the increase in the $^{31}P\{^{1}H\}$ NMR resonance at δ_P = –27.1 ppm in both cases. Unfortunately, the reactions could not be pushed to completion (only 60% of the mixtures contained the desired diphosphine ligand according to $^{31}P\{^{1}H\}$ NMR spectroscopy) and purification of the coumarin derivative by column chromatography gave material that was only 80% pure by $^{31}P\{^{1}H\}$ NMR spectroscopy with the only inseparable impurity being the monophosphine ligand corresponding to one condensation.

The phenol substituted ligand ($\mathbf{L_{3.4}}$) was successfully prepared as previously reported, and it was suggested that the difficulty in achieving the correct stoichiometry for the preparation of $\mathbf{L_{3.5}}$ and $\mathbf{L_{3.6}}$ was due to their poor solubility in alcohol or chlorinated solvents. The formation of the coumarin derived ligand was confirmed by HR-ESI-MS (*m*/*z* 572.1921 for $[\mathbf{L_{3.5}}+H]^{\bullet+}$). For the reaction with 1-aminopyrene, after 24 h, the $^{31}P\{^{1}H\}$ NMR spectrum showed 57% of the reaction mixture was the desired product $\mathbf{L_{3.6}}$; however, the isolated material was highly insoluble and attempts to purify it further were unsuccessful.

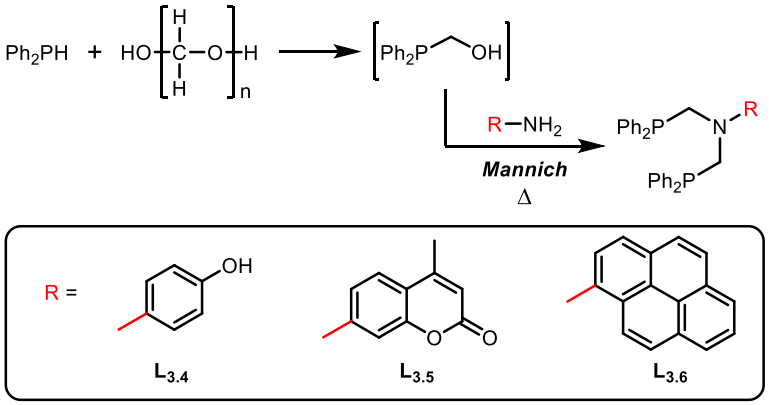

Scheme 3.11. Attempted synthesis of PCNCP ligands $\mathbf{L_{3.5}}$ and $\mathbf{L_{3.6}}$ derived from Ph_2PCH_2OH, and the synthesis of phenol conjugated ligand $\mathbf{L_{3.4}}$.

Due to the limited solubility of $\mathbf{L_{3.5}}$ and $\mathbf{L_{3.6}}$, these ligands did not react with [RuCl(*cis*-tach)$(DMSO)_2$]Cl (**2.1**) and methods to conjugate the organic fluorophore via a linker were pursued. It is noted that $\mathbf{L_{3.4}}$ bearing a 4-hydroxyphenyl group would be a useful handle for post-coordination functionalisation in a manner similar to the method reported by Dyson employing (4-hydroxyphenyl)diphenylphosphine (see Scheme 3.2).[171]

3.3 Synthesis of Ru complex conjugates

3.3.1 Post-coordination conjugation via amide bond formation

Following the successful coordination of the pyrene-conjugated diphosphine $\mathbf{L_{3.2}}$ to form Ru complex **3.3**, effort shifted to synthesise a carboxylic acid functionalised (*cis*-tach)Ru complex (to be used as a coupling precursor). Considering that a flexible, aliphatic backbone resulted in a more cytotoxic (*cis*-tach)Ru complex (see dppp and dppb complexes **2.7-2.8** in Chapter 2), bis((diphenylphosphino)methyl)glycine ($\mathbf{L_{3.1}}$) was reacted with [RuCl(*cis*-tach)$(DMSO)_2$]Cl (**2.1**), and the resulting functional complex **3.1** was isolated in 96% yield (Scheme 3.12). Pleasingly, the carboxylic acid functionality did not interfere with coordination and the ^{1}H, $^{13}C\{^{1}H\}$ and $^{31}P\{^{1}H\}$ NMR data are consistent with the structure of **3.1** shown in Scheme 3.12.

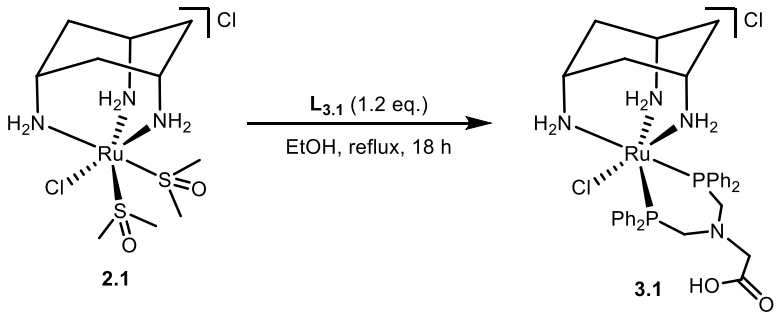

Scheme 3.12. Formation of carboxylic acid-functionalised (*cis*-tach)Ru complex **3.1**.

In the $^{31}P\{^{1}H\}$ NMR spectrum, the 6-membered chelate **3.1** gives a singlet resonance (δ_P = 40.4 ppm), in accord with the 6-membered (*cis*-tach)Ru metallacycle **2.7**. In the $^{13}C\{^{1}H\}$ NMR spectrum for **3.1**, the singlet for the carbonyl carbon (δ_C = 173.3 ppm in CD_3OD) is very slightly shielded (~0.5 ppm) compared to the free ligand $\mathbf{L_{3.1}}$ (δ_C = 173.8 ppm in CD_3OD). The HR-ESI-MS data are consistent with the expected $[\mathbf{3.1}]^{\bullet+}$ showing the expected ruthenium and chlorine isotope pattern and the IR signal (ν(CO) = 1722 cm^{-1}) (solid state) for **3.1** is typical of an alkyl carboxylic acid.

We set out to functionalise the carboxylic acid group of **3.1** with an organic fluorophore. Initial attempts, employing dicyclohexylcarbodiimide (DCC) as the amide coupling agent with either benzylamine (as a model for 1-pyrenylmethylamine) or 7-amino-4-methyl-coumarin in dichloromethane did form the expected products (detected by HR-ESI MS and IR spectroscopy). However, the isolated materials were impure by ^{1}H and $^{31}P\{^{1}H\}$ NMR spectroscopy (Scheme 3.13). By addition of 1-hydroxybenzotriazole (HOBt), which is commonly employed as an activating agent in DCC coupling reactions, analysis of the post reaction mixture revealed several resonances assigned to phosphine oxides, and thus highlighted the incompatibility of HOBt with phosphine complexes. In previous post-coordination conjugation work, Shaw *et al.* reported amide coupling chemistry between carboxylic acid functionalised Rh phosphine complexes and amines using HATU as the coupling agent.[198,201]

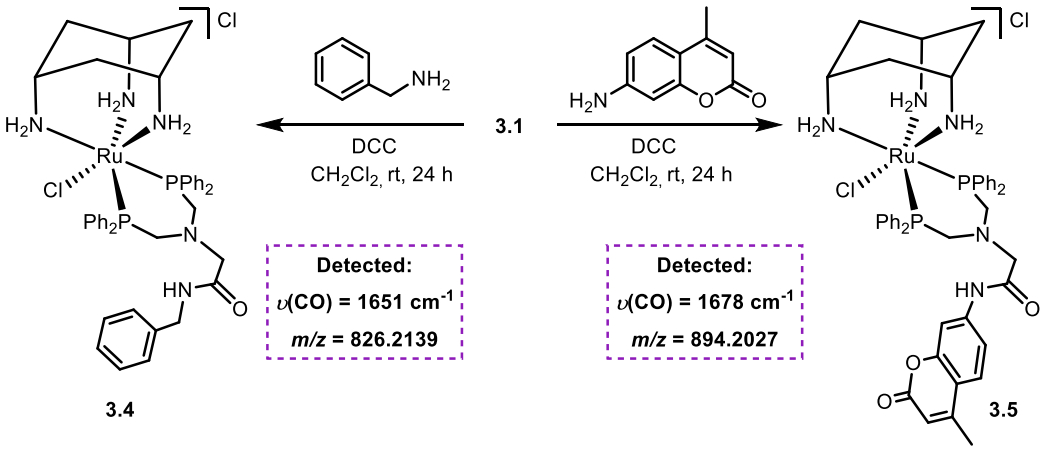

Scheme 3.13. Attempted formation of **3.4** and **3.5** via DCC promoted amide coupling.

By switching the amide coupling agent from DCC to HATU and attempting the same conditions that had worked for pre-coordination conjugation, the pyrenyl and coumarin functionalised complex conjugates were formed (as detected by HR-ESI-MS (m/z = 894.2071 for **3.5** and m/z = 950.2465 for **3.3**), however, the isolated complexes were also impure by ^{1}H NMR spectroscopy, potentially due to unwanted side products from the amide coupling agent (Scheme 3.14 and Scheme 3.15).

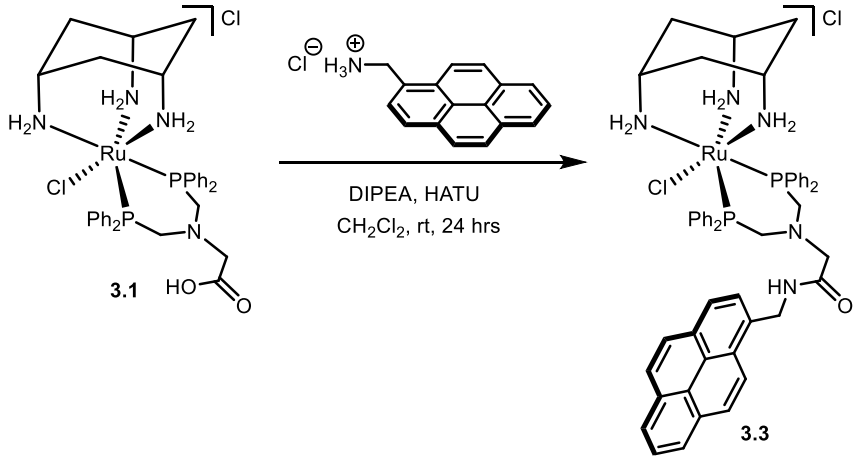

Scheme 3.14. Attempted formation of **3.3** via HATU promoted amide coupling.

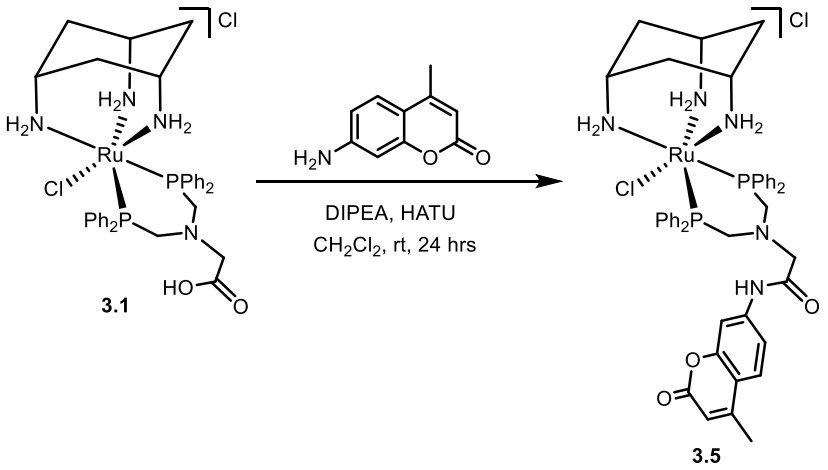

Scheme 3.15. Attempted formation of **3.5** via HATU promoted amide coupling.

As is often employed for cationic Ru complexes, purification of **3.5** by column chromatography was attempted (silica gel eluting CH_2Cl_2/MeOH 0–20%).[202,203] The unreacted 7-amino-4-methylcoumarin was easily recovered and the orange band, consisting of the Ru-containing fractions was analysed. The $^{31}P\{^1H\}$ NMR spectrum showed multiple (slightly broadened) signals in the expected region (*ca.* δ_P = 40 ppm) suggesting that there may be multiple isomers in solution, thus rendering the phosphorus nuclei inequivalent. This contrasts with the pyrene complex conjugate **3.3**, which, as expected, shows one sharp singlet in the $^{31}P\{^1H\}$ NMR spectrum (Figure 3.3).

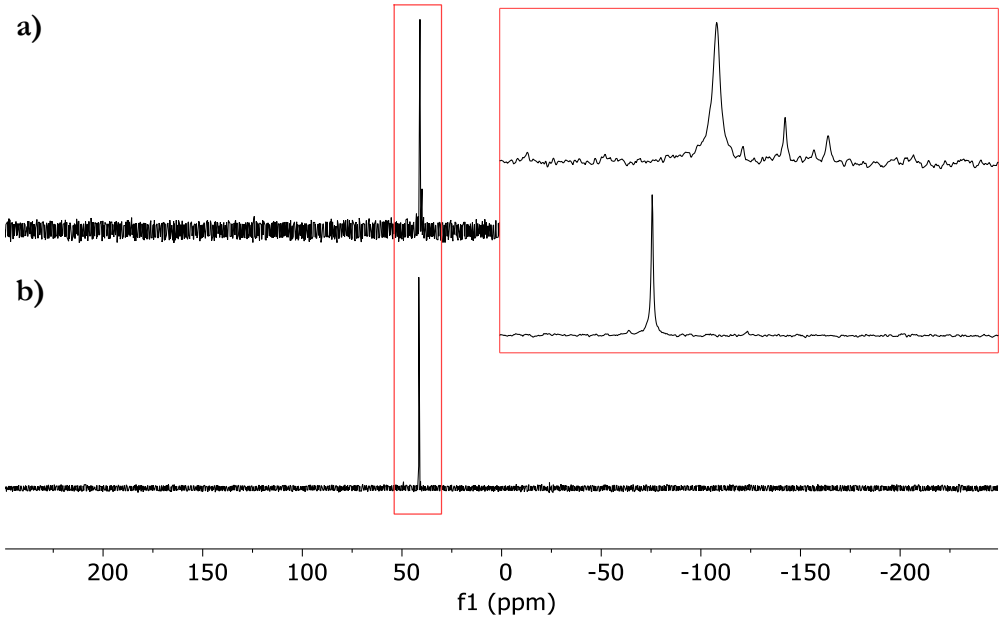

Figure 3.3. $^{31}P\{^1H\}$ NMR spectrum of coumarin complex conjugate **3.5** (a) and pyrene complex conjugate **3.3** (b). Inset: Expansion to show peak broadening for the coumarin containing complex.

We hypothesised that for **3.5**, the peak broadening in the $^{31}P\{^{1}H\}$ NMR spectrum could be due to an equilibrium between the *cis*- and *trans*-configured amide isomers. The coumarin moiety could form intramolecular hydrogen bonds with the *cis*-tach NH_2 protons, potentially stabilising the *cis*-configured isomer (shown in *cis*-**3.5**, Figure 3.4). This particular diphosphine was previously observed to form an intramolecular hydrogen bond between the coumarin N–H and the backbone nitrogen in the solid-state structure of [PdCl(CH_3)(**L**$_{3.3}$)] reported by Smith *et al.* (Figure 3.4).[197] Furthermore, Yam *et al.* have investigated the *cis*-*trans* isomerisation of Pd(II) complexes bearing acetanilide conjugated phosphine ligands.[204] The dominant *trans* isomer is observed in solution by ^{31}P NMR spectroscopy, but a shift in the equilibrium from *trans* to *cis* was induced by the addition of chloride ions, to which the amide N–Hs could form hydrogen bonds.

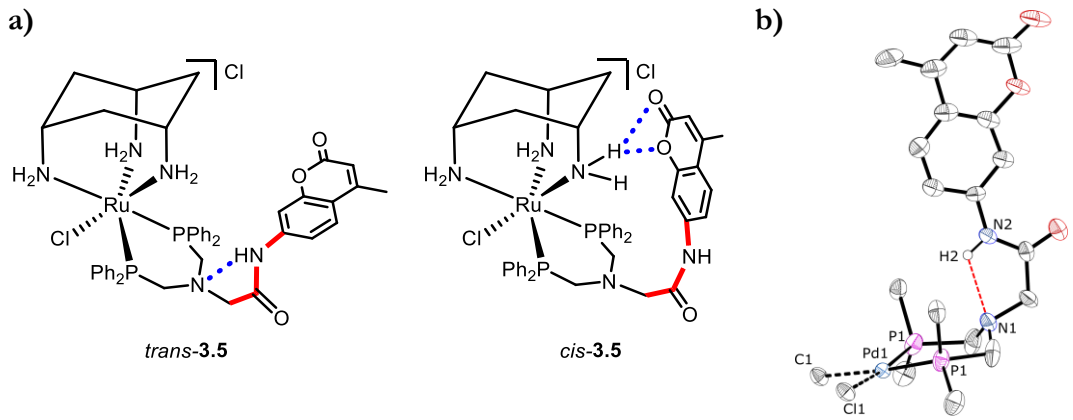

Figure 3.4. a) Possible *cis*-/*trans*- amide isomers of **3.5**. *cis*-**3.5** could form intramolecular hydrogen bonds between the coumarin oxygen and the *cis*-tach protons (highlighted in blue). b) Molecular structure of [PdCl(CH_3)(**L**$_{3.3}$)] from Smith *et al.* where PPh_2 carbons (except ipso carbons) have been omitted for clarity. Intramolecular hydrogen bond N2–H2···N1 (2.27 Å), shown in red.[197]

We aimed to understand this dynamic behaviour by VT-NMR experiments and (preliminary) DFT calculations (see below). The $^{31}P\{^{1}H\}$ NMR spectrum of **3.5** (in EtOH) was recorded at intervals from 20 °C to –80 °C (Figure 3.5). At 20 °C, two distinct broad singlets are observed (δ_P = 40.4 and 39.8 ppm) which begin to merge at –60 °C. Another set of resonances (δ_P = 36.1 and 35.5 ppm), potentially due to another amide isomer, are observed at 0 °C but merge to one signal between –50 °C and –60 °C. This is in accordance with both amide isomers existing in equilibrium at room temperature (giving rise to two sets of signals), and upon cooling, the more thermodynamically stable isomer is observed.

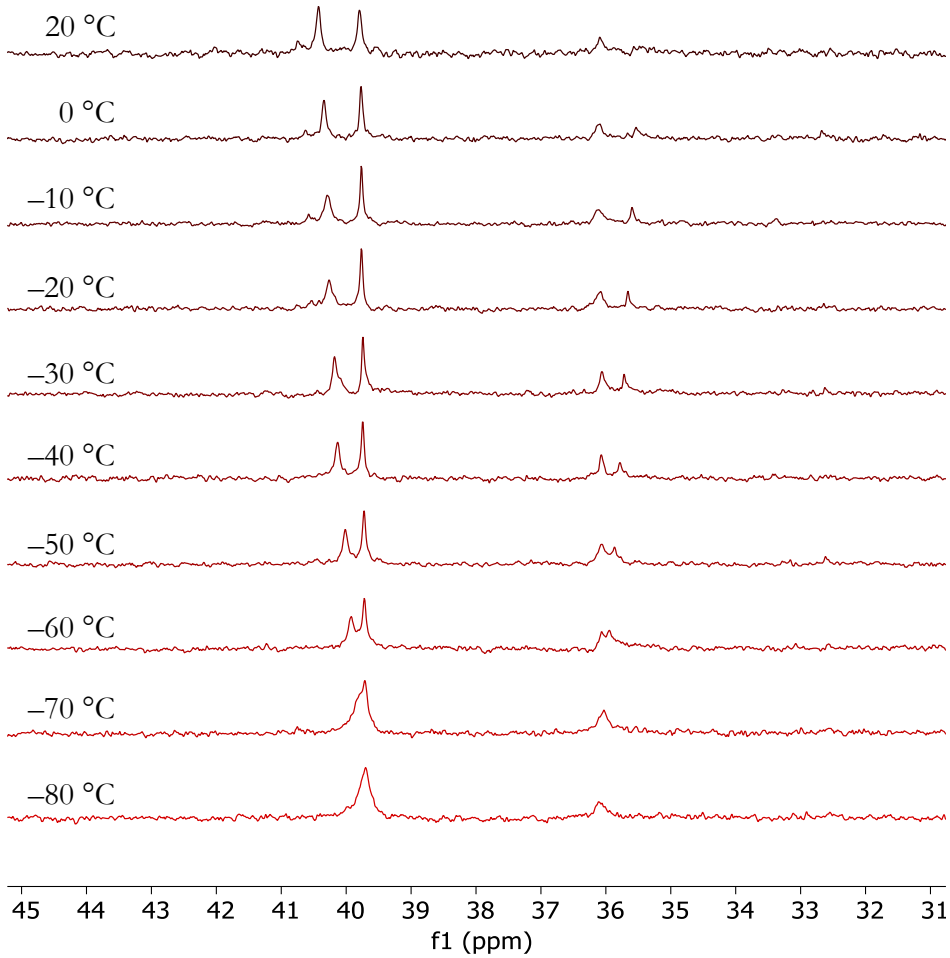

Figure 3.5. Variable temperature $^{31}P\{^{1}H\}$ NMR spectra of **3.5** in EtOH.

We also investigated the solution behaviour of **3.5** by NMR spectroscopy at elevated temperature. The $^{31}P\{^{1}H\}$ NMR spectrum of **3.5** (in EtOH) was recorded at intervals from 25 °C to 65 °C (Figure 3.6). At 25 °C, two sets of signals can be seen (one sharp set at δ_P = 36.1 and 35.8 ppm and one broad set at δ_P = 35.2 and 31.5 ppm). On heating the sample, the sharp signal at δ_P = 36.1 remains sharp and does not change chemical shift. The other signals broaden as temperature is increased and at 65 °C, the two downfield resonances have started to coalesce. From the high temperature $^{31}P\{^{1}H\}$ NMR spectra, it would appear that at least two conformations of the expected coumarin complex conjugate **3.5** exist in solution up to 65 °C.

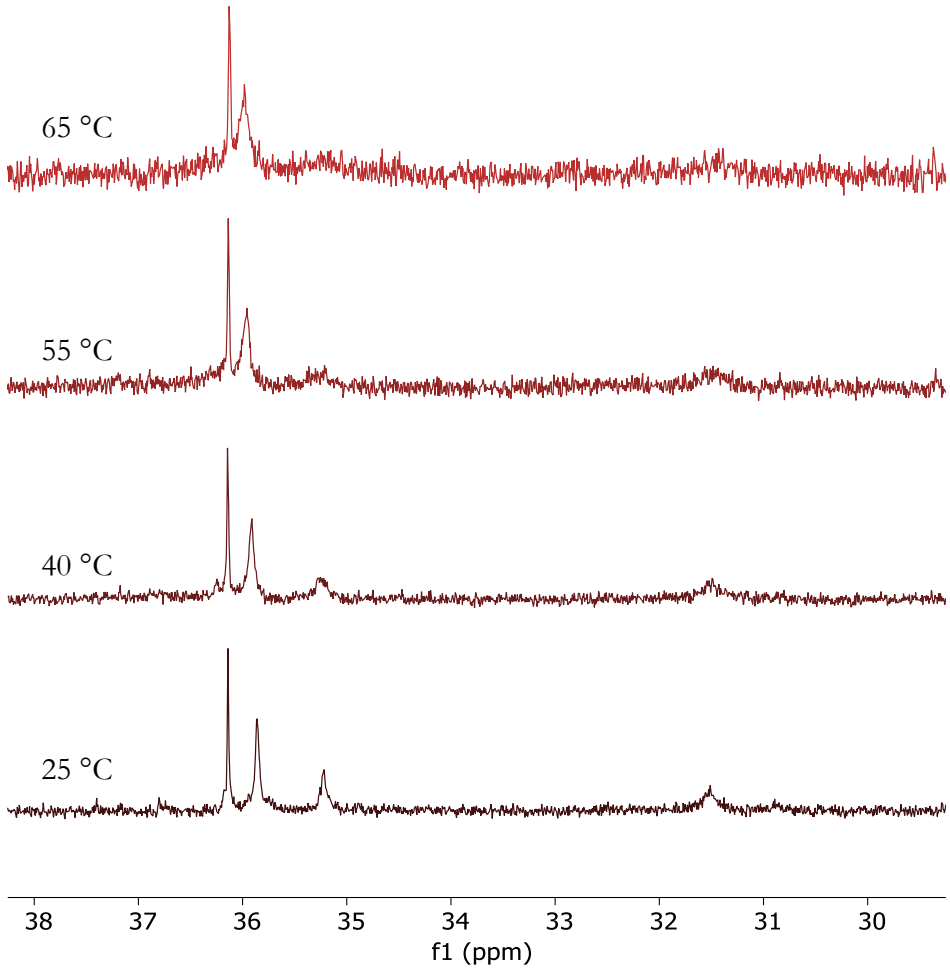

Figure 3.6. High temperature $^{31}P\{^{1}H\}$ NMR spectra of **3.5** in EtOH.

DFT was used to analyse the effect of having a tethered group capable of hydrogen bonding to *cis*-tach as in complex **3.5** (Figure 3.4) versus complexes **3.4** and **3.3** bearing benzyl and pyrenyl groups, respectively. All calculations used DFT as implemented in Schrödinger's Jaguar 8 package and the PBE0 functional. A standard 6-31G* basis set was applied on all atoms apart from Ru and Cl, where the LACV3P* basis set was used. The

calculated Gibbs free energies for the two *cis*- and *trans*-isomers of each complex are presented in Table 3.1. The difference in Gibbs energy between each conformer (ΔG / kcal mol^{-1}) indicates the slight preference for the *cis*-isomer (with both being energetically reasonable conformers at ambient temperature. In the case of the coumarin containing complex **3.5**, this energy preference is greatest with the *cis*-isomer being 5.0 kcal mol^{-1} lower in energy than the *trans*-isomer. In comparison, the *cis*-/*trans*-isomers of the benzyl and pyrenyl derivatives are closer in energy (1.8 kcal mol^{-1} and 3.0 kcal mol^{-1}, respectively) consistent with the hypothesis that the coumarin group plays a role in stabilising the *cis*-isomer by hydrogen bonding.

Table 3.1. Calculated Gibbs free energies for geometric amide isomers of **3.3-3.5**.[a]

Substituent	Complex	Total Gibbs E / a.u.[a]	ΔG / kcal mol^{-1}
pyrene	*cis*-**3.3**	-3557.126252	0.0000
	trans-**3.3**	-3557.131013	2.9876
benzyl	*cis*-**3.4**	-3174.155634	0.0000
	trans-**3.4**	-3174.158424	1.7508
coumarin	*cis*-**3.5**	-3438.639985	0.0000
	trans-**3.5**	-3438.631952	5.0408

[a]PBE0/6-31G*/LACV3P* level of theory.

The calculated amide isomer structures did not show the expected hydrogen bonding for **3.5**. Further analysis is necessary to understand the dynamic solution behaviour of phosphine ligand conjugates with the potential to form hydrogen bonds to *cis*-tach.

3.3.2 Post-coordination conjugation via ester bond formation

There are many examples of organometallic Ru-phosphine complexes that show anti-proliferative properties *in vitro* and *in vivo*.[205–209] In the widely studied RAPTA complexes, although the replacement of a 1,3,5-triaza-7-phosphaadamantane (PTA) ligand with a triarylphosphine ligand lowers the aqueous solubility of the resulting complex, the added hydrophobicity can increase cellular uptake and thus, improve cytotoxicity.[38,210] Therefore, functionalisation of a coordinated phosphine ligand may provide a potential method to chemically conjugate an organometallic complex with a small molecule to add further functionality. The work described below builds on the previously reported Ru complex bearing a (4-hydroxyphenyl)diphenylphosphine ligand (Scheme 3.16).

The [(η^6-*p*-cymene)$RuCl_2${PPh_2(4-C_6H_4OH)}] (**3.7**) was initially reported for the synthesis of metal containing dendrons (wedge shaped dendrimers).[211] It was later exploited by Dyson *et al.* for the synthesis of cytotoxic compounds; they reported the synthesis of a small library of small organic drugs that were conjugated to **3.7** by an esterification reaction (promoted by an amine base or a activating agent (1-ethyl-3-(3-dimethylaminopropyl)carbodiimide (EDCI) with DMAP)).[171] The functionalised complexes were isolated and purified by column chromatography on silica gel. This method of post-coordination conjugation obviated the need to synthesise the free, air-sensitive ligand conjugates. We viewed this methodology as a potential way to conjugate a small organic fluorophore to the Ru metallodrug. Therefore, the precursor complex **3.7** was prepared following previously reported methods[171,211] and reacted with a freshly prepared solution of 1-pyrenylcarbonyl chloride **3.6** (Scheme 3.16).

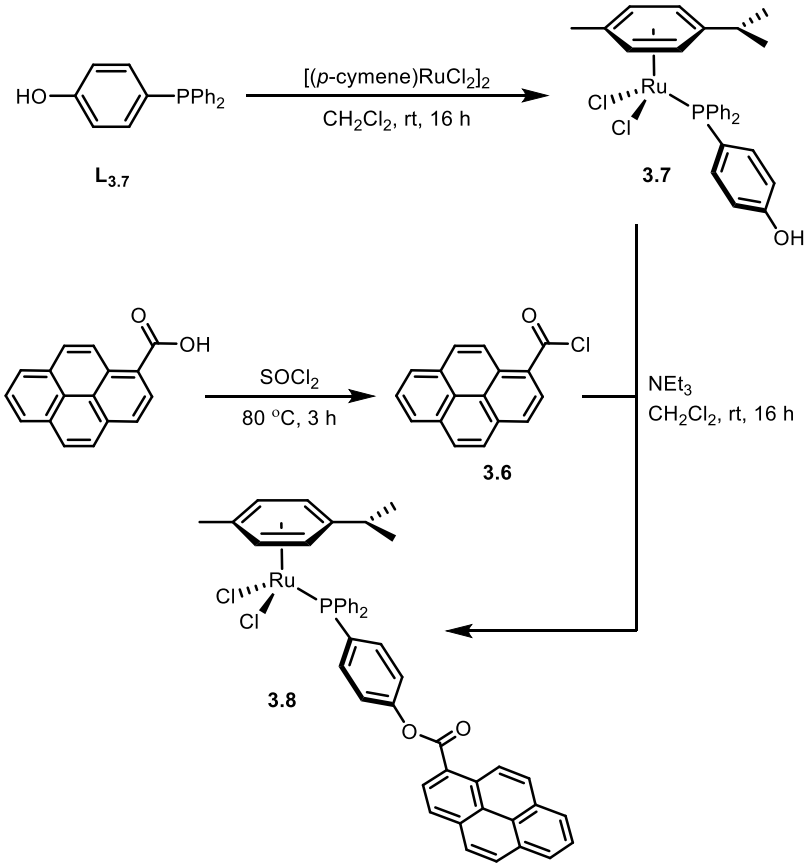

Scheme 3.16. Synthesis of **3.7** and novel fluorescent RAPTA pyrene conjugate **3.8**.[171]

The RAPTA pyrene complex conjugate **3.8** was purified by column chromatography (silica gel, eluent CH_2Cl_2/MeOH 0–10%). The disappearance of the phenolic proton of **3.7** (δ_H = 9.96 ppm) was monitored by ^{1}H NMR spectroscopy, as well as the appearance of a band in the IR spectrum (ν(C=O) = 1727 cm^{-1}) that confirmed the formation of the

ester linkage. The HR-ESI-MS also confirmed the atomic composition of **3.8** displaying the expected ruthenium and chlorine isotope pattern.

By analysing the ester carbonyl IR stretching frequency and $^{13}C\{^1H\}$ NMR signal (δ_C = 166.0 ppm for **3.8**), we observe the influence of a more electron-withdrawing pyrenyl group compared with the more electron-donating alkyl derivatives reported by Dyson *et al.* (see **H** in Scheme 3.2; δ_C = 168.9–174.8 ppm and ν(C=O) = 1746–1778 cm^{-1}).

Although RAPTA complex conjugate **3.8** was not evaluated *in vitro*, its photophysical properties due to the pyrene fluorophore could be useful for studying cellular uptake by fluorescence microscopy and comparing the activity to the wide variety of previously reported RAPTA complexes.

3.4 Fluorophore conjugation method evaluation

The coupling of organic fluorophores to diphosphine ligand $\mathbf{L_{3.1}}$ or to the functional (*cis*-tach)Ru complex **3.1** by amide bond formation are not clean reactions. In both cases of pre-coordination and post-coordination conjugation, many unwanted side-products (including phosphine oxides) are produced. The attempts at performing post-coordination conjugation with common amide coupling agents DCC and HATU gave impure material which unfortunately was not successfully purified. However, it appears the functional (*cis*-tach)Ru complex **3.1** bearing a carboxylic acid group can act as a pivotal precursor to further functionalized Ru complex conjugates. Overall, the most efficient route to the pyrene complex conjugate **3.3** is shown in Scheme 3.9 (pre-coordination conjugation), where the conjugated ligand $\mathbf{L_{3.2}}$ is isolated and then coordinated in a subsequent step to [RuCl(*cis*-tach)$(DMSO)_2$] (**2.1**).

For organometallic RAPTA complexes, post-coordination conjugation of **3.7** with 1-pyrenylcarbonyl chloride to give **3.8** followed by purification by column chromatography is a reliable route to high purity fluorescent RAPTA derivatives.

3.5 Photophysical properties of phosphine conjugates

The emission spectra for pyrene and pyrene conjugated diphosphine ligand $\mathbf{L_{3.2}}$ were recorded in CH_2Cl_2; the UV-visible absorption and emission spectra for the pyrene complex conjugate **3.3** were recorded in water and are shown in Figure 3.7. For pyrene and $\mathbf{L_{3.2}}$, the emission spectra exhibit maxima at λ_{em} = 464 nm and λ_{em} = 392 nm, respectively. The key difference is the blue-shift in the emission maximum of *ca.* 72 nm

for $\mathbf{L_{3.2}}$ compared to pyrene which is presumably due to the prevention of excimer emission from the pyrenyl moiety in the amide conjugated phosphine ligand $\mathbf{L_{3.2}}$. For the (*cis*-tach)Ru complex conjugate in aqueous solution, the characteristic absorbance bands due to pyrene are the lowest energy absorption bands (λ_{Max} = 343 nm and 327 nm) due to π–π* transitions; these assignments are in agreement with other pyrene conjugated molecules.[212,213]

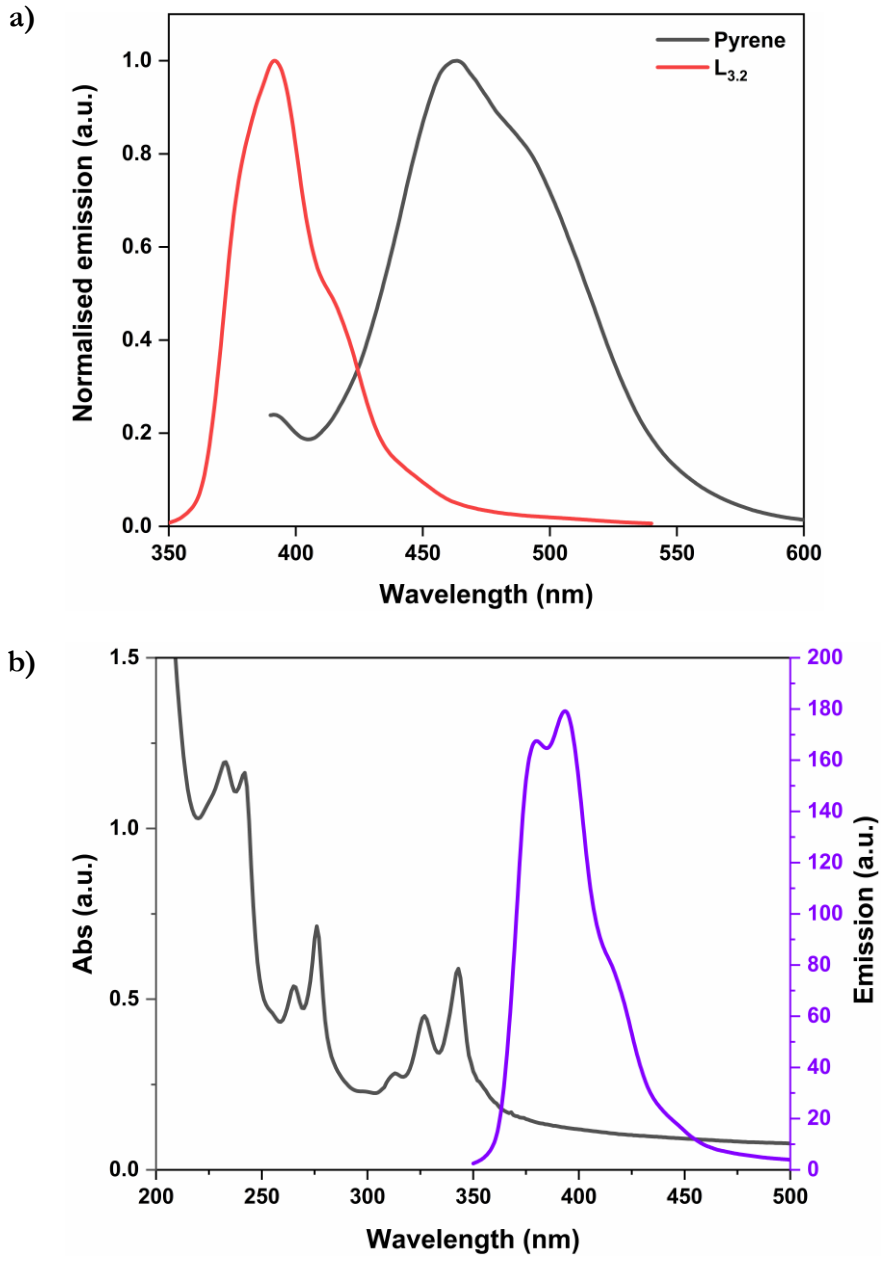

Figure 3.7. a) Emission spectra for pyrene and pyrene ligand conjugate $\mathbf{L_{3.2}}$ recorded in CH_2Cl_2. b) UV-Visible absorption and emission spectra for complex **3.3** recorded in H_2O (λ_{Ex} = 343 nm).

In aqueous solution, the emission spectrum of **3.3** is comparable to that of $\mathbf{L_{3.2}}$ with one additional shoulder peak (λ_{Em} = 375 nm), but crucially the emission intensity for **3.3** is not significantly quenched upon metal coordination or by dissolution in water. Presumably, the pyrene fluorophore is sufficiently remote from the Ru centre that any MLCT quenching is supressed. As a result of its emission properties and high aqueous solubility, we aimed to use **3.3** as a dual chemotherapeutic/imaging agent for *in vitro* studies (see Section 3.6).

The UV-visible absorption and emission spectra of 7-amino-4-methylcoumarin and the coumarin diphosphine ligand conjugate $\mathbf{L_{3.5}}$ were recorded in MeCN solution. Figure 3.8 shows the normalised spectra where interestingly the bathochromic shift for the emission maxima between the aminocoumarin and the ligand conjugate ($\Delta\lambda_{em}$ = 20 nm) is slightly greater than that for the absorbance maxima ($\Delta\lambda_{em}$ = 16 nm). The intense absorption band for 7-amino-4-methylcoumarin (λ_{abs} = 341 nm) due to a π–π^* transition is characteristic to other functionalised coumarin derivatives.[116,214]

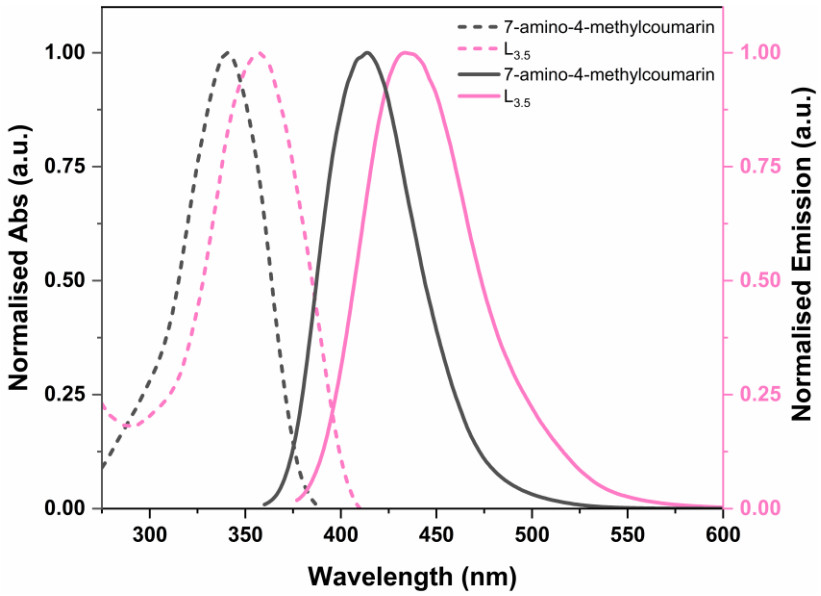

Figure 3.8. Normalised UV-visible absorption and emission spectra for 7-amino-4-methylcoumarin and the corresponding ligand conjugate $\mathbf{L_{3.5}}$ recorded in MeCN, (λ_{Ex} = 350 nm).

The bathochromic shift (red-shift) in the emission maximum could be due to an increased inductive effect from the alkyl substituents on the nitrogen as commonly seen with other, commercially available coumarin fluorophores (Figure 3.9).[215]

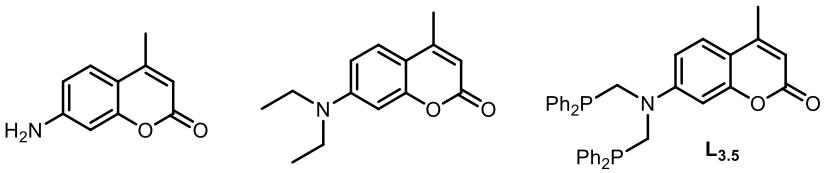

λ_{abs} = 341 nm
λ_{em} = 414 nm

λ_{abs} = 373 nm[a]
λ_{em} = 445 nm[a]

λ_{abs} = 357 nm
λ_{em} = 434 nm

Figure 3.9. Summary of the photophysical properties of $\mathbf{L_{3.5}}$ and related aminocoumarins. [a]Photophysical data taken from references 215,216.

The emission spectrum of pyrene complex conjugate **3.8** was recorded in MeCN (Figure 3.10) and displays one intense emission band (λ_{em} = 413 nm) which is red-shifted compared to the emission maximum of $\mathbf{L_{3.2}}$ (λ_{em} = 392 nm). It must be noted, however, that due to poor aqueous solubility, the emission spectrum of **3.8** has not been recorded in water. Solvatochromic effects may provide differences in the emission properties of pyrene conjugated Ru complexes, and this should be considered when designing aqueous soluble metallodrug conjugates.[217,218]

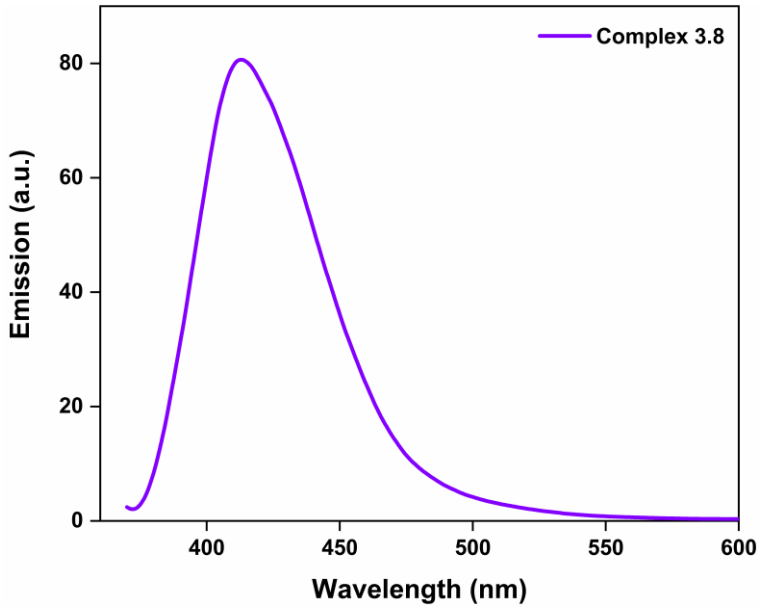

Figure 3.10. Emission spectrum of **3.8** recorded in MeCN, (λ_{Ex} = 350 nm).

3.6 Cytotoxicity

The results in this section are from preliminary cell studies carried out at the University of York and form the basis of a collaborative study. The compounds tested were prepared by the author and the cell assays and microscopy were carried out by Dr. Karen Hogg and Dr. Joanne Marrison (University of York). With the luminescent (*cis*-tach)Ru complex conjugate **3.3** in hand, the aim was to study its biological activity and compare this with the previously tested cytotoxic (*cis*-tach)Ru complexes (Chapter 2). The compounds discussed in the following studies (Figure 3.11) are (*cis*-tach)Ru complexes **2.17-2.19**, Ru pyrene complex conjugate **3.3**, and cisplatin.

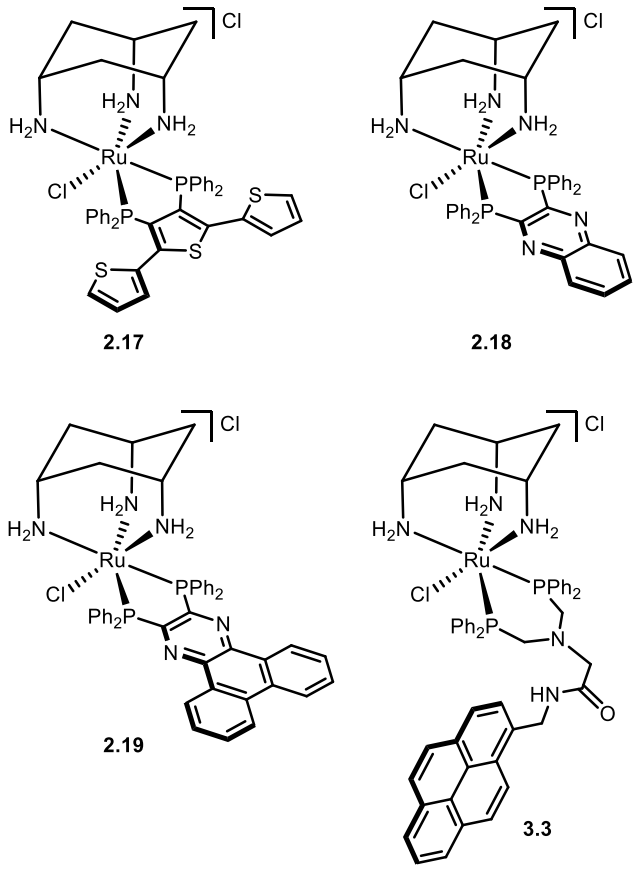

Figure 3.11. Chemical structures of the (*cis*-tach)Ru complexes assessed in the following biological studies.

3.6.1 Confocal microscopy

With pyrene and coumarin (*cis*-tach)Ru complex conjugates prepared, we tested them as dual cytotoxic/imaging agents in a series of confocal microscopy experiments. Unfortunately, despite many attempts, the nature of these organic fluorophores (excitation wavelengths below 400 nm, see Figure 3.7 and Figure 3.8) made them unsuitable for the Zeiss LSM 780 multiphoton confocal microscope. The instrument

requires a fluorophore with an excitation wavelength above 405 nm and so no confocal microscopy was possible.

3.6.2 Flow cytometry viability study

The viability of A549 and 293T cells was assessed by a DRAQ7 assay which was used to detect apoptotic or membrane-compromised cells.[191,194] DRAQ7 selectively stains damaged/dead cells and does not enter live cells; thus, by analysing the cell populations by flow cytometry, the relative uptake of the test compounds can be monitored over time. The cells were analysed after 24 h, 48 h and 7 days following treatment with the different (*cis*-tach)Ru complexes. Figure 3.12 and Figure 3.13 show representative examples of the contour plots obtained showing the live cells (bottom half of each plot) and dead cells (top left quadrant) where the analysis has been gated on single cells to avoid counting cell debris.

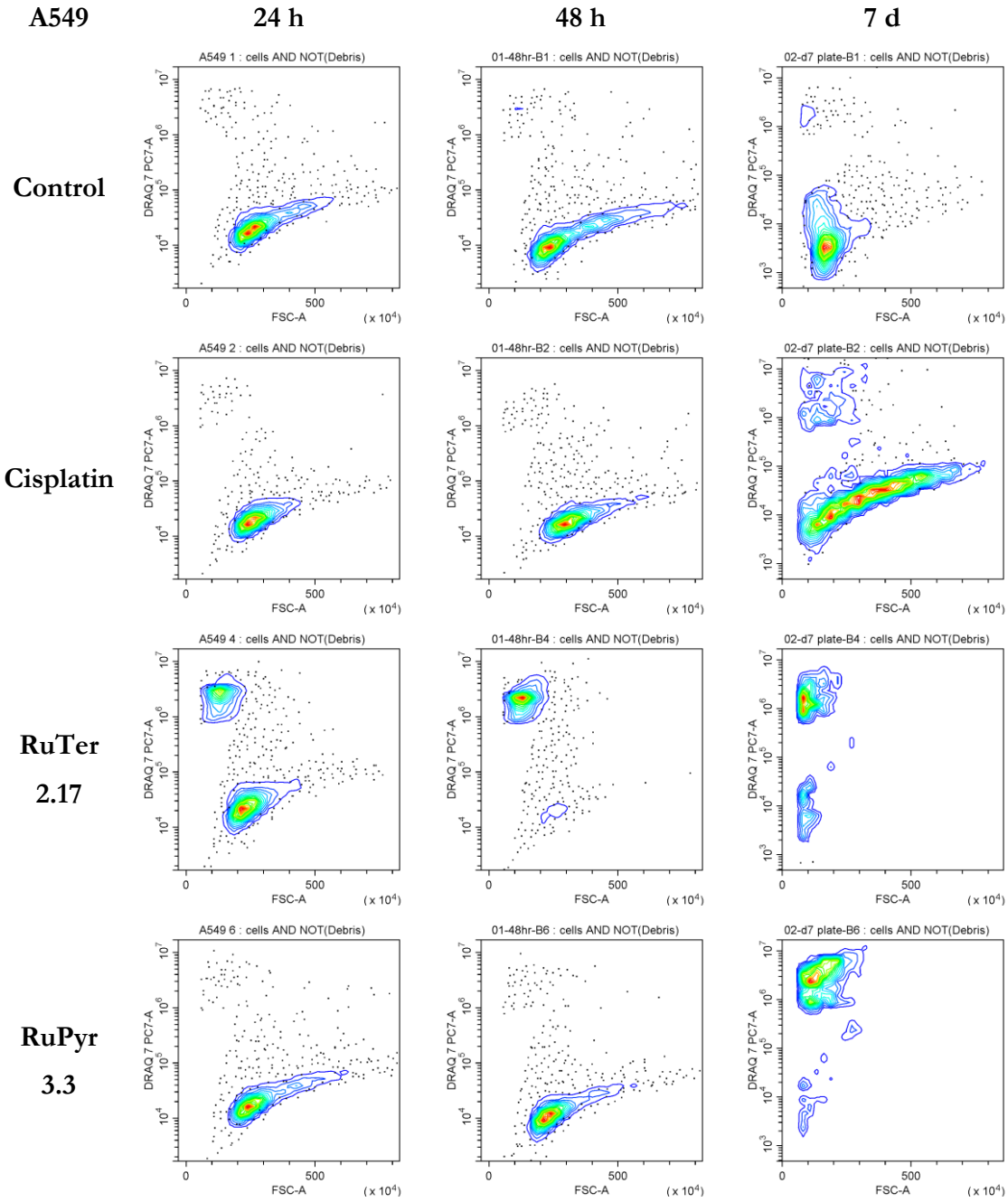

Figure 3.12. Representative contour plots generated from DRAQ7 flow cytometry assay. Plots show A549 cells treated with cisplatin and (*cis*-tach)Ru complexes (12.5 μM).

A plot summarising the 24 h and 48 h data from the DRAQ7 assay for A549 cells (Figure 3.14) shows that only compound **2.17** (Figure 3.12) had a significant cytotoxic effect after 24 h. All other compounds showed very little cytotoxicity, as determined by this assay. The data for the 7-day analysis (which based on the contour plots shows almost all the cells to be dead) has not been included in this summary plot, due to the low number of cells detected. Ideally for this type of analysis >10,000 cells would be counted and after 7 days, typically only 1,000–2,000 would be detected.

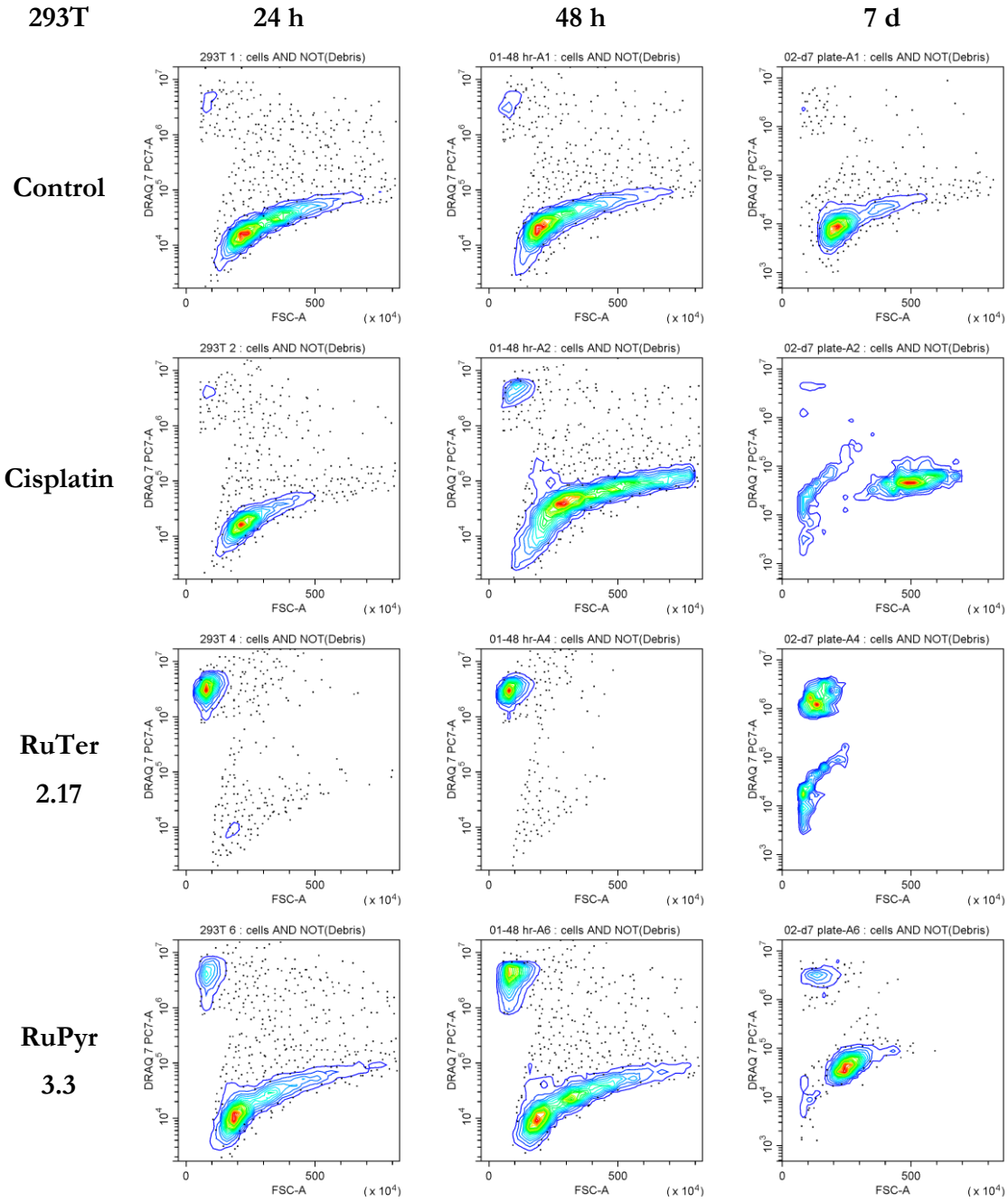

Figure 3.13. Representative contour plots generated from DRAQ7 flow cytometry assay. Plots show 293T cells treated with cisplatin and (*cis*-tach)Ru complexes (12.5 μM).

A plot summarising the 24 h and 48 h data from the DRAQ7 assay for 293T cells (Figure 3.14) shows that, although compound **2.17** was again the most cytotoxic, all the (*cis*-tach)Ru complexes had a significant cytotoxic effect after 24 h, in all cases exceeding the activity level of cisplatin.

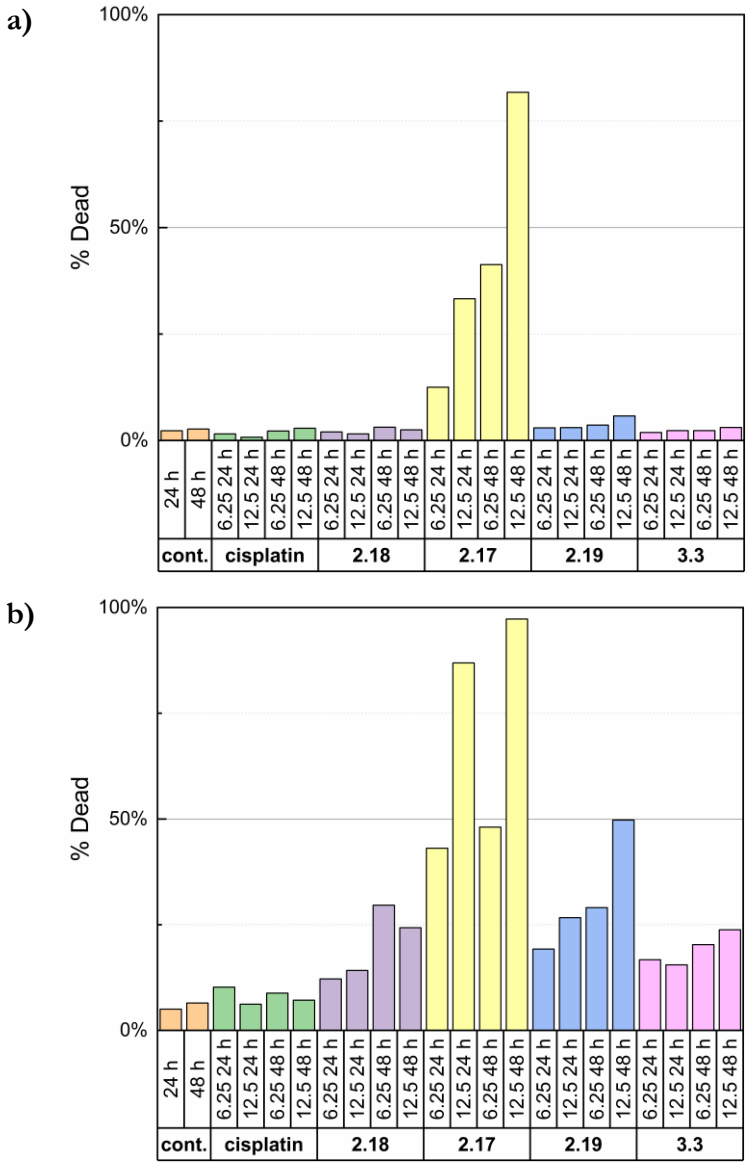

Figure 3.14. Summary plots showing data summary from DRAQ7™ assay contour plots for, a) A549 cells and b) 293T cells, treated with cisplatin, **2.17**, **2.18**, **2.19**, and **3.3** (6.25 and 12.5 μM).

Samples were taken from the 293T cells after 24 h of treatment and visualised by confocal microscopy. The different cell morphologies can be seen in the images with reference to the corresponding contour plot that shows the amount of cell death (Figure 3.15). Ruptured cell membranes (indicative of cells undergoing apoptosis) can clearly be seen in cells treated with compounds **2.17**, **2.19**, and **3.3**, in line with a high percentage of dead cells detected (25–95%). The images of the cells treated with cisplatin and **2.18** show some blebbing of the cell membrane but overall, the cells are more intact, and this correlates with a lower percentage of dead cells detected (10–15% for cisplatin and 15–25% for **2.18**).

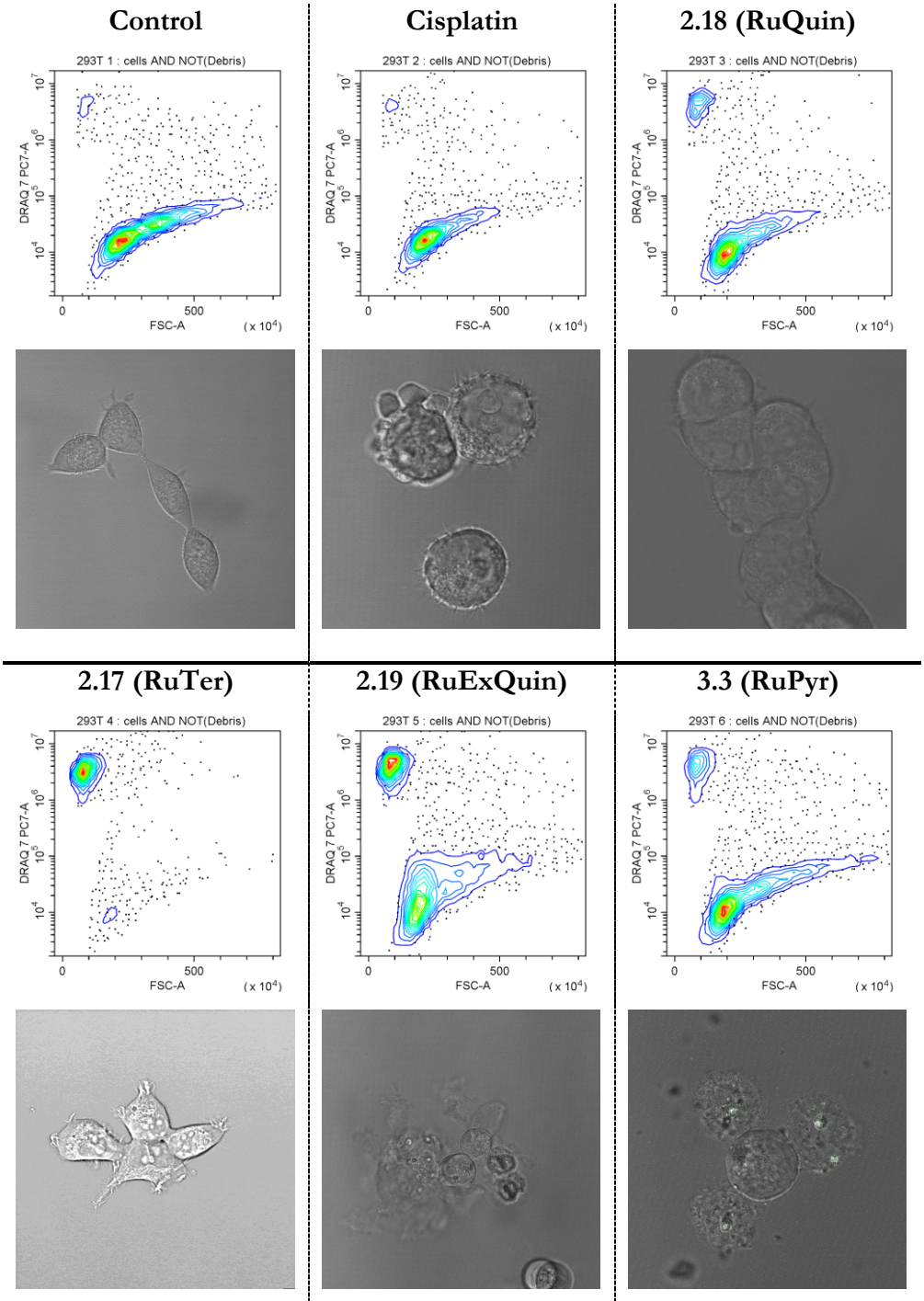

Figure 3.15. DRAQ7™ contour plots and corresponding confocal microscopy images of 293T cells after 24 h of treatment with cisplatin and (*cis*-tach)Ru complexes (12.5 μM).

3.7 Conclusions

It has been shown that using amide coupling chemistry, small organic fluorophores can be conjugated to phosphine ligands both pre- and post-metal coordination. The known diphosphine bis((diphenylphosphino)methyl)glycine **L**$_{3.1}$ is a versatile amide coupling

partner with a variety of aryl and alkyl amines. Amide coupling protocols employing HATU have successfully formed the desired ligand conjugates; however, yields are low due to side product and phosphine oxide formation, and loss of material upon purification. The useful Ru synthon **3.1** has been subjected to post-coordination conjugation conditions; however, although the complex conjugates **3.3-3.5** have been detected in the reaction mixtures, this coupling route is low-yielding and produces impure material. This leads us to conclude that, at this time, independent synthesis of fluorescent ligand conjugates (followed by coordination) is the preferred route.

We have found that phosphorus-based Mannich condensations to form ligands with organic fluorophores directly incorporated into the backbone is possible. However, due to low solubility, it is difficult to purify these materials. As high aqueous solubility has remained a priority for this project, these ligands were not investigated further.

The photophysical properties of all novel compounds have been investigated by UV-visible and fluorescence spectroscopy. In all cases, they display the expected features attributed to pyrenyl or coumarin chromophores, and the coordination of the fluorescent ligands does not quench emission intensity. However, the emission properties of both pyrene and coumarin are not suitable for confocal fluorescence microscopy in our hands, due to instrument requirements of having a minimum excitation wavelength laser of 405 nm.

The cytotoxicity of **3.3** was investigated by flow cytometry and confocal microscopy and compared to **2.17-2.19**. Changing the structure of the chelating phosphine from an all-carbon backbone to a PCNCP backbone does not have a detrimental effect on the cytotoxicity of the resulting complex. Moreover, this nitrogen atom provides a useful point of derivatization for metal diphosphine drug conjugates.

3.8 Future work

Our primary focus has been to use a (*cis*-tach)Ru complex with a suitable fluorophore for confocal fluorescence microscopy and further biological assays. Based on the examples containing fluorophores with red-shifted emission properties (see work from the Smith, Gabbaï and Higham groups), fluorescein dyes should be investigated. Many fluorescein precursors are commercially available, such as 5- or 6-aminofluorescein (Figure 3.16) and these could be applied in the Ru conjugation chemistry discussed in this Chapter.

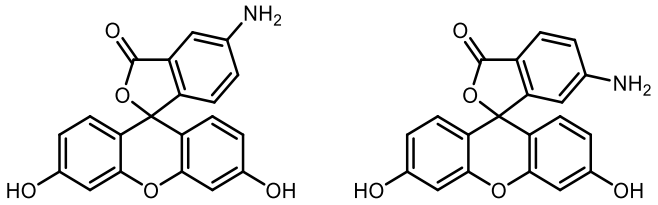

Figure 3.16. Commercially available aminofluorescein dyes. [a] Taken from reference 216.

Following productive discussions with Dr. Martin Smith (University of Loughborough), we had aimed to use some of the fluorescein and rhodamine tagged diphosphine ligands prepared in the Smith group (Figure 3.17). These preformed ligands should coordinate to [RuCl(*cis*-tach)(DMSO)$_2$]Cl in the same way as **L$_{3.2}$** and their photophysical properties are in the region of the visible spectrum that is required for microscopy and flow cytometry studies. Unfortunately, due to delays associated with COVID-19, we were not able to carry out further biological imaging studies using these ligands.

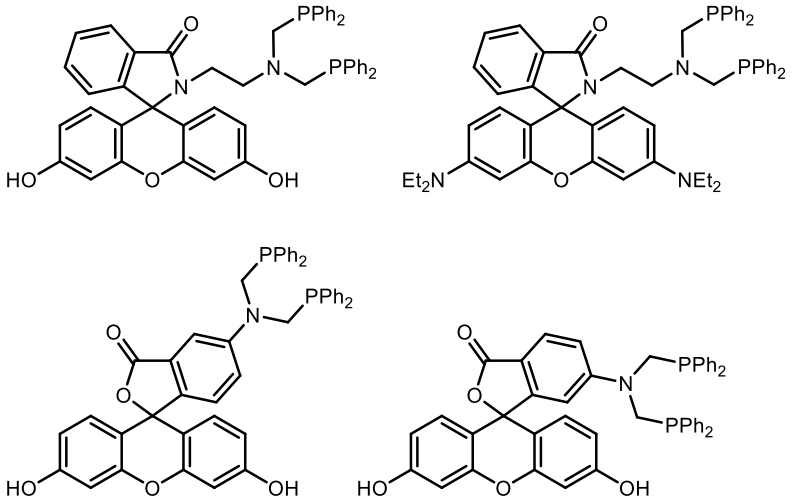

Figure 3.17. Selected fluorescein and rhodamine conjugated diphosphines, prepared by Smith and co-workers.

Chapter 4. Photophysical properties of air-stable pyrenylphosphines

4.1 Introduction

The use of organic fluorophores as a spectroscopic probe has become widespread in organic and organometallic chemistry. Organic dyes with specific luminescence properties that are amenable to microscopy are desirable for applications in imaging and catalysis.[219,220] In this chapter, the synthesis of a range of pyrene-substituted phosphine ligands and a study of their coordination and photophysical properties is reported. The highly conjugated nature of polyaromatic substituents has previously been shown to confer exceptional air-stability when compared to simple phenylphosphines.[221–223] Through a combined experimental and theoretical approach, we have systematically studied the photophysical and air stability properties of pyrenylphosphines, and their associated (arene)Ru(II) coordination chemistry.

4.1.1 Fluorescent probes

Polyaromatic hydrocarbons (PAHs) have been widely studied due to their applications as organic fluorophores, stimuli sensors, and biological imaging agents. The D_{2h} symmetric molecule, pyrene is of particular interest due to its characteristic photophysical properties, excimer formation, high quantum yield and long-lived excited states. Although pyrene has 16 π electrons and does not follow Hückel's (4n + 2) rule for aromaticity, it is planar and classified as aromatic.[224] This property makes pyrene a useful molecule to study π–π stacking interactions, intercalation chemistry, and luminescence. The chemistry of pyrene has been extensively reviewed.[196]

The luminescence properties of pyrene are concentration dependent; at low concentrations, the molecule exhibits fluorescence at 375 nm and at high concentration, an excimer state produces intense emission at 470 nm. This excimer state, combined with high fluorescence quantum yield, microenvironment sensitivity and the diverse tunability of the pyrene core, has led to it being a widely used chemical probe.

In 1987 Akasaka *et al.* reported the synthesis of diphenyl-1-pyrenylphosphine (DPPP) and its application in hydroperoxide sensing in lipids (Scheme 4.1).[225] The free phosphine is non-emissive but upon oxidation, the DPPP oxide exhibits intense blue fluorescence (λ_{Ex} = 352 nm, λ_{Em} = 380 nm).

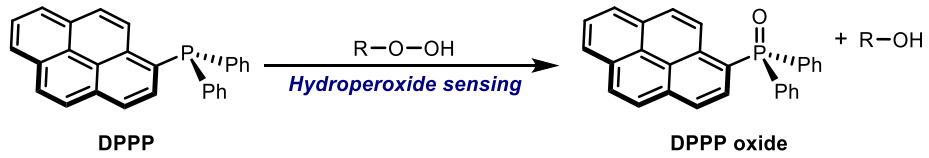

Scheme 4.1. Oxidation of DPPP by hydroperoxides, investigated by Akasaka *et al.*[225]

This difference in emission intensity of the P(III) and P(V) species has been attributed to photoelectron transfer (PeT) quenching from the phosphorus lone pair to the pyrene chromophore. As a result, DPPP was later applied to monitoring lipid peroxidation in cell membranes by Noguchi *et al.*[120] More recently, a DPPP derivative conjugated with an alkyltriphenylphosphonium iodide moiety developed by Shioji *et al.* showed that the probe selectively accumulated in the mitochondria of HepG2 cells (Scheme 4.2).[226]

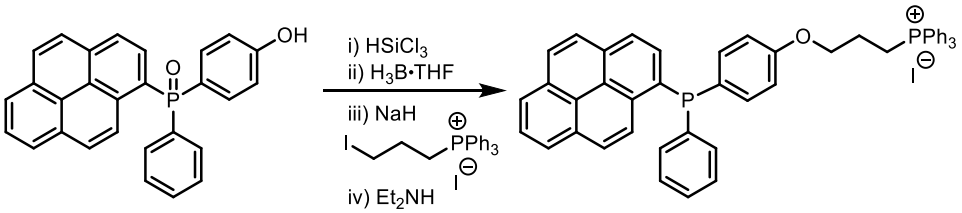

Scheme 4.2. Synthesis of a pyrene conjugated fluorescent probe designed to target the mitochondria.

The first rationally designed P(III)/P(V) molecular probes for sensing hydroperoxides via a PeT quenching mechanism were based on a substituted benzoxadiazole (Scheme 4.3a).[106] The phosphines are weakly fluorescent (Φ_F = 0.014–0.050 in MeCN) but upon oxidation with hydroperoxides, the corresponding phosphine oxides are highly emissive, as shown by significantly increased fluorescence quantum yields (Φ_F = 0.36–0.44 in MeCN). A novel phosphine, conjugated with a 7-hydroxycoumarin fluorophore also showed an immediate increase in emission intensity after treatment with H_2O_2 in aqueous conditions (Scheme 4.3b).[105]

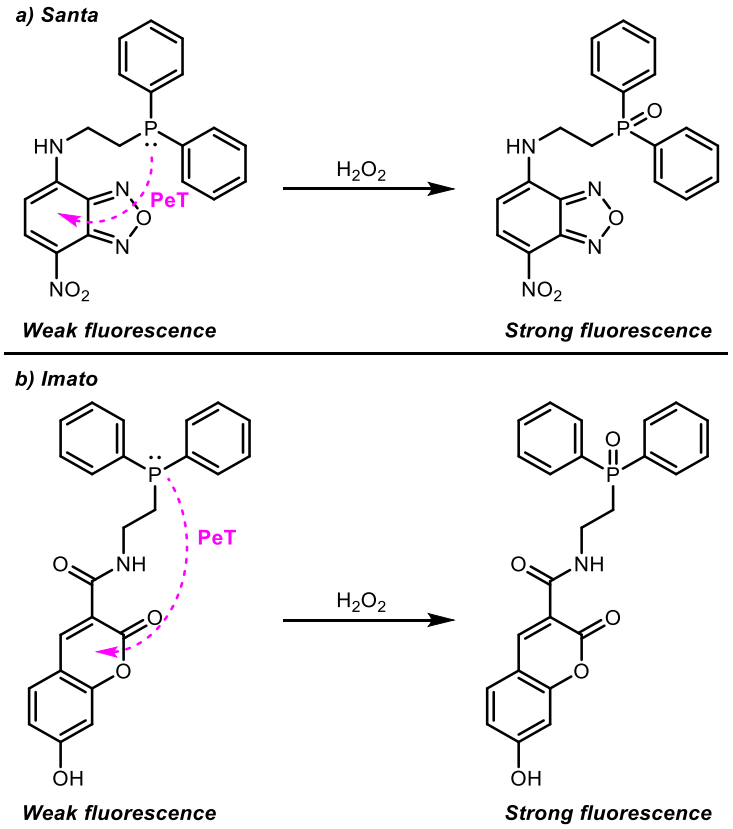

Scheme 4.3. Fluorophore conjugated phosphine PeT probes.[105,106]

The photochemistry of fluorescent phosphine conjugates was investigated by Gabbaï *et al.*[119,227] The authors exploited the phosphorus-to-fluorophore PeT quenching mechanism with a fluorescein conjugated phosphine (Scheme 4.4) by studying the emission properties of the phosphine and phosphine oxide. The emission switch-on effect was also achieved by metal coordination of the phosphine, which also prevents the PeT quenching mechanism. This concept was used to demonstrate the selective sensing of Au(III) ions in water. The quantum yields for the phosphine, phosphine oxide, and phosphine Au–Cl complex are Φ_F = 0.12, 0.54 and 0.29, respectively (Scheme 4.4).[IV]

[IV]Quantum yields relative to fluorescein in 0.1 M NaOH (Φ_F = 0.91).

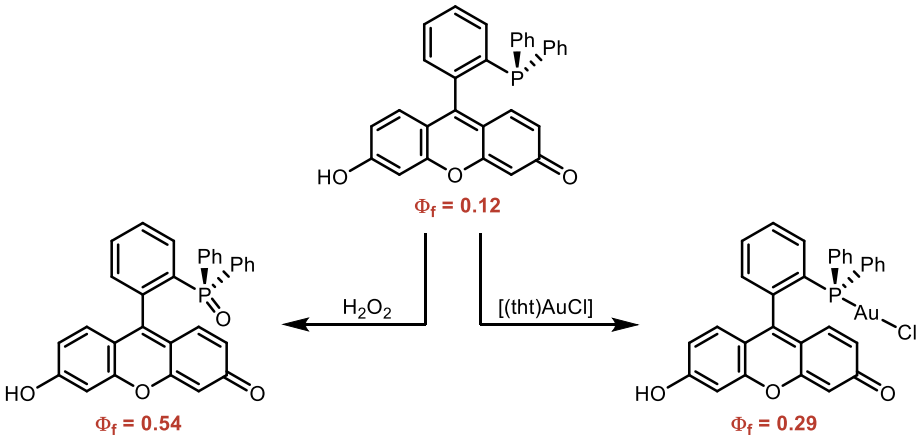

Scheme 4.4. Fluorescein conjugated phosphine and synthesis of phosphine oxide, and Au–Cl complex, Gabbaï *et al.*[119]

Unlike the examples from Gabbaï (where the fluorescein chromophore is conjugated to the phosphine by an *o*-phenylene linker), Higham *et al.* observed that there was no emission switch-on effect with BODIPY conjugated phosphines (via a *p*-phenylene linker) and no appreciable change in fluorescence quantum yield upon coordination to coinage metals (Figure 4.1).[228] This is likely due to the BODIPY chromophore being sufficiently remote from the phosphine lone pair that the PeT quenching mechanism is suppressed.

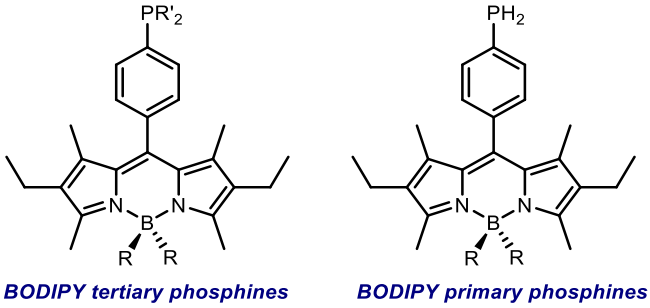

Figure 4.1. Chemical structures of BODIPY conjugated phosphines, reported by Higham *et al.*[228]

Higham developed the synthesis of BODIPY-conjugated primary phosphines (Figure 4.1). Theoretical calculations demonstrated that, by having highly conjugated groups, the HOMOs of these primary phosphines are delocalised from the phosphorus lone pairs which imparts stability to air oxidation. In addition, the primary phosphines formed the expected mono- and bis-phosphine carbonyl complexes of molybdenum and tungsten, $[M(CO)_5(H_2PR)]$ and *cis*-$[M(CO)_4(H_2PR)_2]$ (M = Mo, W). The fluorescence properties of the complexes do not show any significant reduction in the quantum yield compared to the free primary phosphine. This is presumably due the distance between the heavy metal atom and the BODIPY chromophore.[118,229]

Huang *et al.* reported a series of triaryl phosphine oxides (Pyr_xPPh_{3-x}, x = 1–3) (Figure 4.2) that exhibit temperature dependent fluorescence from –50 to 100 °C.[230] These compounds were shown to be robust over a large temperature range and could be used without deoxygenation treatment, making them suitable candidates for molecular thermometers.

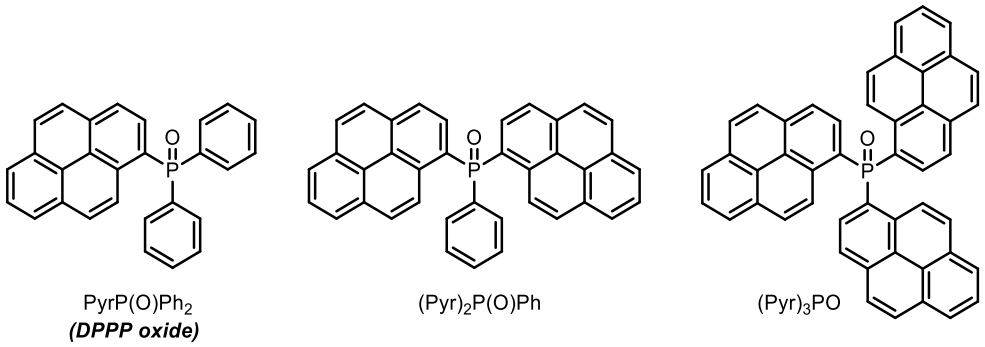

Figure 4.2. Fluorescent triarylphosphine oxides, Huang *et al.*[230]

This series of phosphine oxides led us to consider the parent primary, secondary and tertiary phosphines, which were not considered in the studies by Huang, and investigate their coordination chemistry. In 2017, during our study of pyrenylphosphines, Walensky *et al.* reported the synthesis and fluorescent properties of tris(pyrenyl)pnictogen compounds that displayed quantum yields from well below 1% to *ca.* 13% for $(Pyr)_3P$ and *ca.* 14% for the phosphine oxide $(Pyr)_3PO$ (Figure 4.3).[231] It is noted that only modest luminescent enhancement was observed for these bulky tris(pyrenyl)pnictogen compounds upon oxidation from Pn(III) to Pn(V).

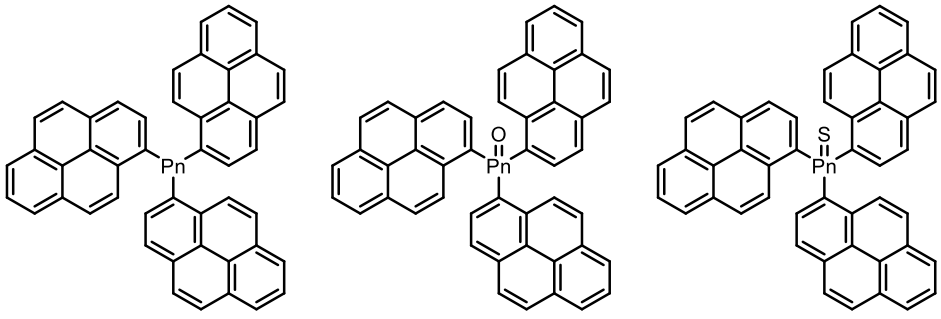

Figure 4.3. Tris(1-pyrenyl)pnictogen compounds prepared by Walensky *et al.*[231]

4.1.2 Coordination chemistry

The coordination chemistry of primary and secondary phosphines has received little attention compared to the ubiquitous use of tertiary phosphines. The resulting complexes that retain at least one reactive P–H bond are interesting for post-coordination modification. Reid *et al.* synthesised Ru halide complexes of the form *trans*-[$RuX_2(PR_3)_4$] (X = Br, Cl; PR_3 = $PhPH_2$, Ph_2PH),[232,233] and several organometallic examples including Mo(V) phosphinecarboxamide carbonyl, and (arene)Ru(II) (see below) have also been prepared.[234,235]

With the development of more air-stable primary phosphine ligands that contain ferrocenyl or mesityl substituents, the coordination chemistry of these ligands was explored.[235–237] Hey-Hawkins *et al.* extended the early studies of Reid with a series of Ru half-sandwich complexes with primary and secondary ferrocenyl phosphines of type [(*p*-cymene)$RuCl_2(PR_3)$] (PR_3 = $FcPH_2$, $FcCH_2PH_2$, $(FcCH_2)_2PH$) (Figure 4.4). The properties of the complexes were explored by NMR spectroscopy, IR spectroscopy and X-ray crystallography. [238,239] The effect of phosphine coordination on the $^1J_{PH}$ coupling constants was investigated, with the values increasing from *ca.* 200 Hz (free phosphines) to *ca.* 400 Hz in the Ru complexes. This large increase in coupling constant is thought to involve a strengthening of the P–H bond (as confirmed by an increase of ~80 cm^{-1} in the ν(P–H) IR stretching frequency). Moreover, it has been reported that metal coordination can weaken the P–H bond and lead to the formation of bridged phosphanido and phosphinidene complexes (through dehydrohalogenation), which are often insoluble, polymeric materials.[235,236]

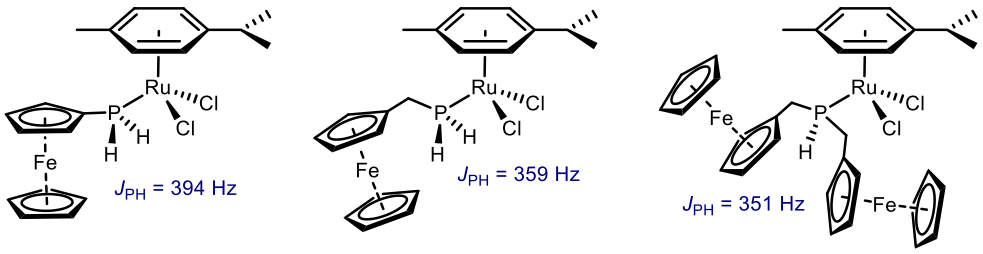

Figure 4.4. Half-sandwich (*p*-cymene)Ru complexes reported by Hey-Hawkins *et al.*[238,239]

All the ferrocenyl phosphine complexes display "three-legged piano stool" structures as expected, and the sum of the three L–M–L angles is around 250–260°, significantly lower than the idealised 270°. The Ru–P bond lengths (2.296(2)–2.312(2) Å) are shorter than typical Ru complexes of tertiary phosphines (2.34–2.37 Å) presumably due to the decrease in steric bulk at the phosphorus centre.

Interestingly, for the purpose of this work, Gamez *et al.* reported the synthesis and cytotoxicity of Ru(II) arene complexes with 1-pyrenylphosphine ligands (Scheme 4.5).[240] It was found that changing the arene capping ligand from *p*-cymene to methyl benzoate greatly increased the biological activity of the resulting complexes. In addition, the biological activity was sensitive to the phosphine substituents, with methyl groups proving more efficient than phenyl groups in most cases.[25] Despite the authors reporting many biological studies including EB-DNA displacement assays, the luminescence properties of these complexes were not evaluated.

In 2020, during our study of pyrenylphosphines, Gamez and co-workers reported the synthesis of pyrenylphosphines and phosphonites derived from (1-pyrenyl)PCl_2 and studied the cytotoxicity of the corresponding (arene)Ru(II) complexes.[241]

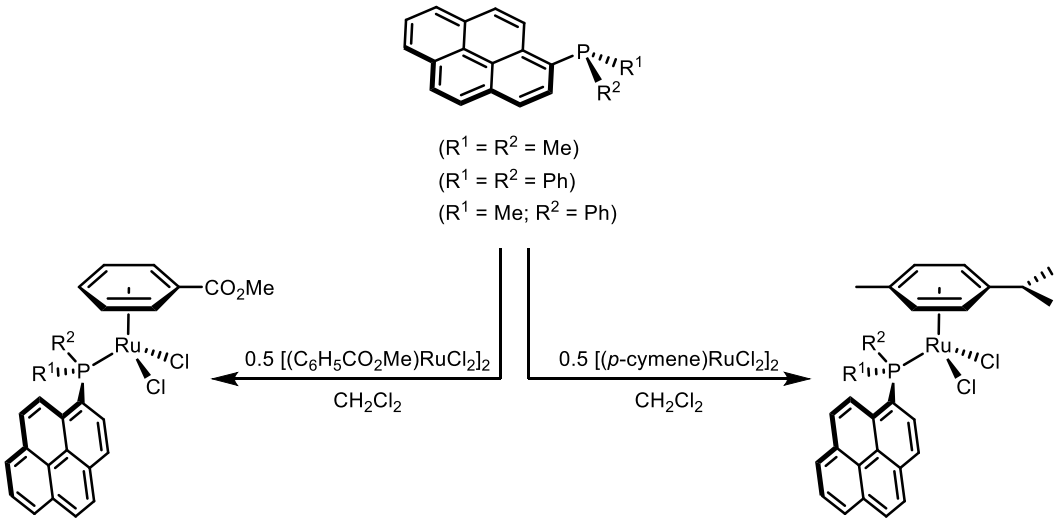

Scheme 4.5. Synthesis of pyrenylphosphine Ru complexes reported by Gamez *et al.*[240]

Diphenyl-1-pyrenylphosphine (DPPP) is prone to undergo cyclometallation, which has been shown to increase the phosphorescence efficiency for the resulting metal complexes. Yip *et al.* observed phosphorescence quantum yields of up to 1.5 $\times 10^{-2}$ (Φ_P = 1.5%) for the cyclometalated Pt complex shown in Scheme 4.6.[242]

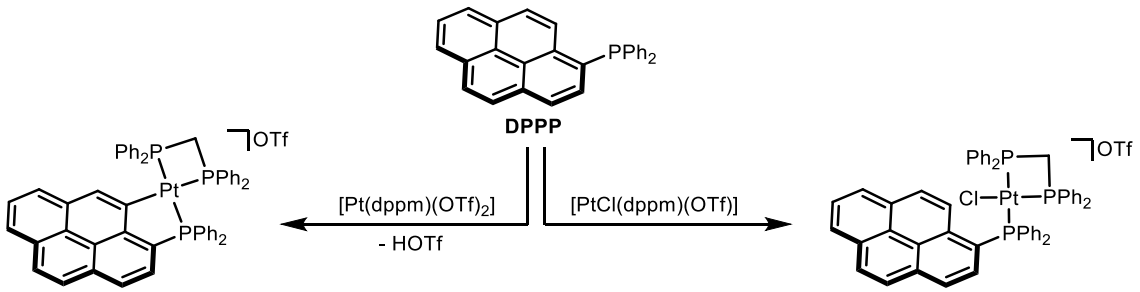

Scheme 4.6. Switching on the phosphorescence of pyrene by cycloplatination.[242]

Direct coordination of the pyrenyl ring to the Pt atom was required for increased phosphorescence, while the Pt–Cl complex showed very low emission intensity.

4.1.3 Research aims

To expand the chemistry of pyrenylphosphines, we aimed to carry out the following:

- Synthesise the set of primary, secondary, and tertiary 1-pyrenyl phosphines shown in Scheme 4.7. Apart from the previously reported $(Pyr)_3P$,[231] these phosphines and some of the required precursors would be novel.
- Expand this family of phosphines to include the 2-pyrenylphosphine regioisomers shown in Scheme 4.8 in Section 4.2.

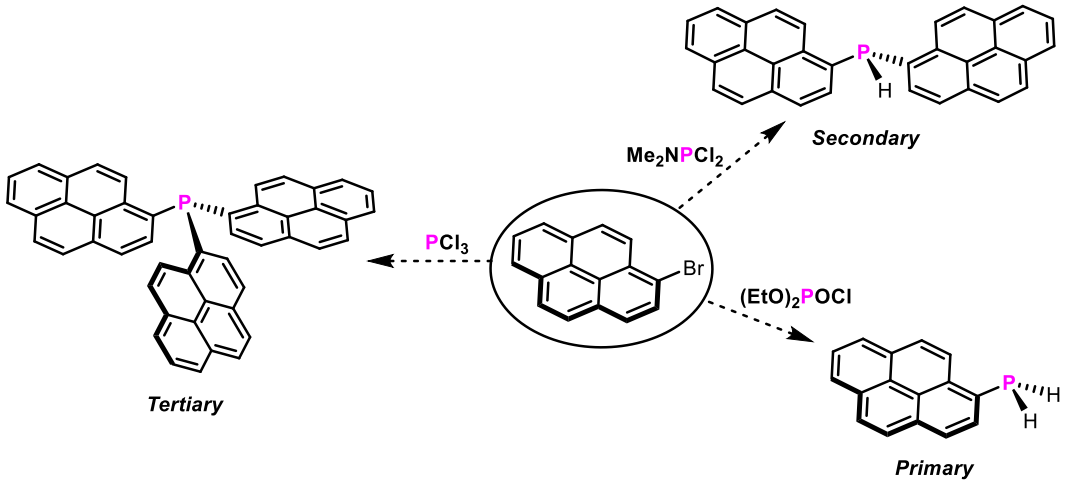

Scheme 4.7. Summary of 1-pyrenylphosphine targets for this work.

- Study the coordination behaviour of this new class of ligands, concentrating on Ru with a view to studying the resulting complexes as cytotoxic agents.
- Rationalise the photophysical properties of pyrenylphosphines using a combination of UV-visible and fluorescence spectroscopy with DFT calculations.
- Explore the air-stability of pyrenylphosphines experimentally and justify the results by calculating the SOMO energies of the phosphine radical cations.

4.2 Synthesis of pyrenylphosphines

Pyrenylphosphines are relatively bulky arylphosphines and are interesting for their luminescence properties. Walensky *et al.* reported the synthesis and fluorescence properties of tris(1-pyrenyl)pnictogen compounds including tris(1-pyrenyl)phosphine.[231] Scheme 4.8 outlines the conventional numbering for pyrene, describes the nomenclature

used in this chapter and details the synthetic procedures to access the regioisomeric 1- and 2-pyrenylphosphines.

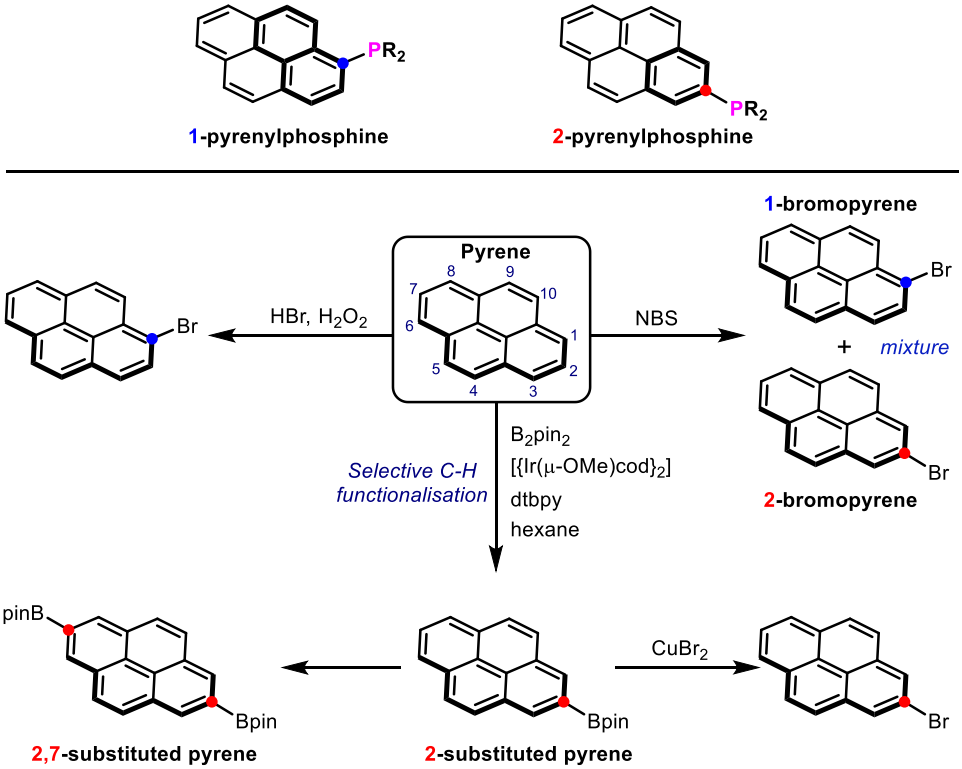

Scheme 4.8. Synthetic routes to some of the regioisomers of substituted pyrenes.

The steric profile of 1-pyrenylphosphines is analogous to 1-naphthylphosphines, whereas 2-pyrenylphosphines have a similar steric profile to analogous phenylphosphines. Herein, we report the synthesis of primary and secondary phosphines derived from 1-bromopyrene. An Ir-catalysed C–H functionalisation reaction, initially reported by Marder *et al.* selectively activates the C–H bonds at the 2- and 7-positions of pyrene.[243] These useful aryl boronic esters can be converted to 2-bromopyrene by reaction with $CuBr_2$ (Scheme 4.8). Following this transformation, 2-bromopyrene could be used as a precursor to phosphines in an analogous way to 1-bromopyrene to give novel pyrene conjugated ligands with different steric properties.

In 2018, Mathey *et al.* reported a simple method for the preparation of 2- or 2,7-functionalised pyrenes via a 1,2-phosphinyl migration from the corresponding 1- or 1,6-substituted derivatives (Scheme 4.9).[244] The reaction employed a $AlCl_3$/NaCl melt and proved an effective way to generate 2-pyrenyl compounds with various phosphine, phosphine oxide and phosphonium substituents. The newly formed 2-functionalised

pyrenes could be used as building blocks for 2-pyrenyl substituted aryl or alkenyl compounds via Pd-catalysed C–P bond cleavage.

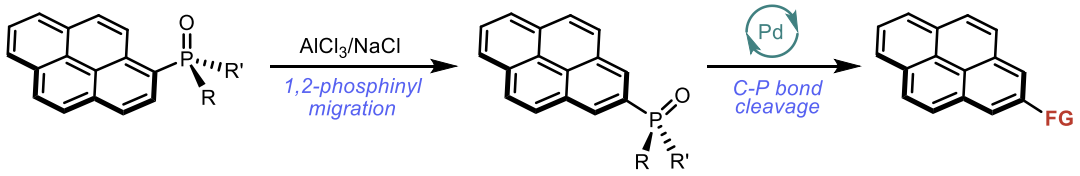

Scheme 4.9. Regioselective synthesis of 2- or 2,7-functionalised pyrenes via phosphinyl migration (FG = functional group; alkenyl ($CHCHCO_2C(CH_3)_3$) or aryl ($4\text{-}MeOC_6H_4$)), reported by Mathey *et al.*[244]

To begin our study, 1-bromopyrene **4.2** was prepared from pyrene by oxidative bromination conditions employing HBr and H_2O_2 following the reported procedure (Scheme 4.10).[245]

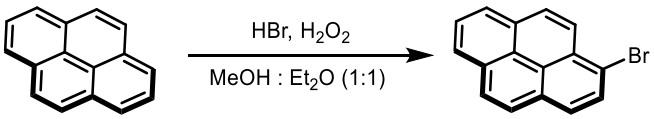

4.1 **4.2**

Scheme 4.10. Literature method for the synthesis of **4.2**.[245]

The following section describes the syntheses and characterisation of phosphines derived from 1-bromopyrene **4.2**. To date, attempts to prepare phosphines from 2-bromopyrene have been unsuccessful (see Section 4.2.5).

4.2.1 Synthesis of 1-pyrenylphosphine

Yip *et al.* reported the synthesis of diethyl(1-pyrenyl)phosphonate (**4.3**) by lithium-halogen exchange of **4.2** using ^{t}BuLi, followed by reaction with diethyl chlorophosphate.[246] In this work, reduction of the phosphonate **4.3** with lithium aluminium hydride resulted in the novel 1-pyrenylphosphine $\mathbf{L_{4.1}}$ (Scheme 4.11).

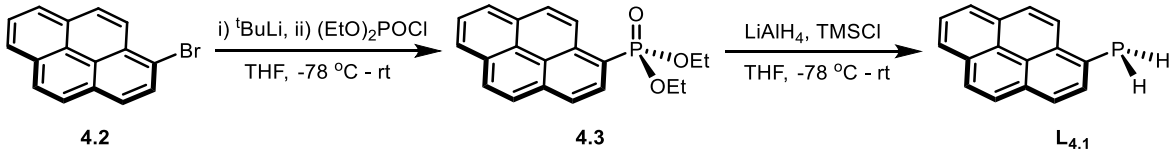

4.2 **4.3** $\mathbf{L_{4.1}}$

Scheme 4.11. Synthesis of diethyl 1-pyrenylphosphonate **4.3** and the synthesis of 1-pyrenylphosphine $\mathbf{L_{4.1}}$.

In the $^{31}P\{^{1}H\}$ NMR spectrum of $\mathbf{L_{4.1}}$, a sharp singlet resonance (δ_P = –132.2 ppm) is observed, characteristic of an aryl primary phosphine (cf. $PhPH_2$, δ_P = –131 ppm). In the ^{31}P NMR spectrum, a triplet of doublets is seen with a characteristically large one bond P–H coupling ($^{1}J_{PH}$ = 203 Hz, Figure 4.5). The triplet is further split by a second coupling presumably due to the proton at the 2 position of pyrene ($^{3}J_{PH}$ = 7 Hz). In the ^{1}H NMR spectrum (Figure 4.5) the $–PH_2$ protons appear as a doublet (δ_H = 4.45 ppm, $^{1}J_{HP}$ = 204 Hz) which integrates for 2H. The product was isolated as a pale-yellow solid which is resistant to air oxidation in an uncapped $CDCl_3$ solution for over 24 h (see Section 4.5).

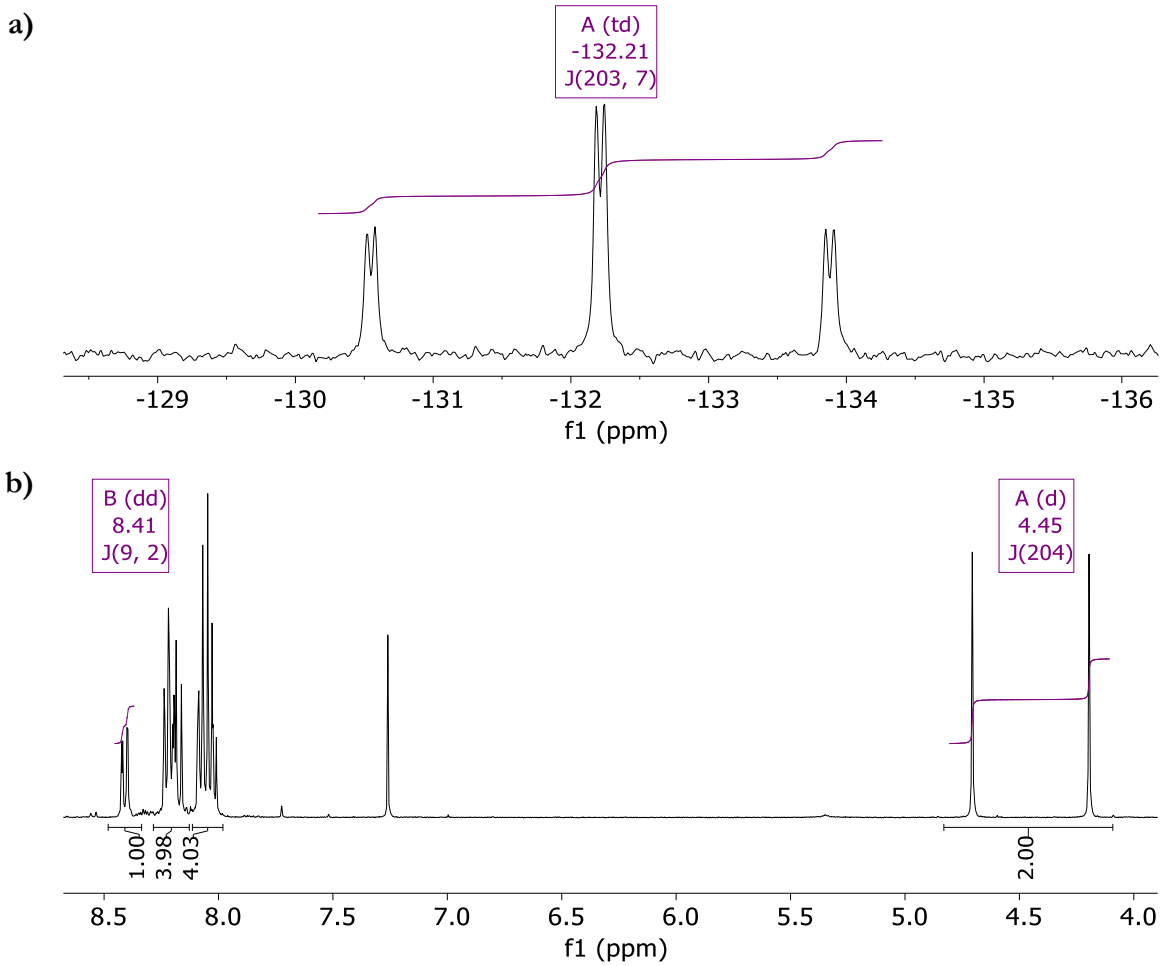

Figure 4.5. a) ^{31}P NMR spectrum of **L**$_{4.1}$. b) ^{1}H NMR spectrum of **L**$_{4.1}$, recorded in $CDCl_3$.

4.2.2 Synthesis of bis(1-pyrenyl)phosphine

The bis(1-pyrenyl)phosphine **L**$_{4.2}$ was synthesised by two independent routes. First, as with the synthesis of many secondary phosphine oxides (SPOs), reaction of 1-pyrenylmagnesium bromide **4.4** with diethylphosphite gave secondary phosphine oxide **4.5**. An *in situ* ^{31}P{^{1}H} NMR resonance at δ_P = 20.3 ppm with a $^{1}J_{PH}$ of 482 Hz was assigned to **4.5**. However, analysis of the isolated material indicated that a major component was unreacted 1-bromopyrene, indicating that Grignard conditions would need to be improved. Reduction of the crude **4.5** was achieved with DIBAL-H to give the desired **L**$_{4.2}$ although in a modest yield of 20% following isolation by filtration through silica (Scheme 4.12).

By modifying this route with the addition of NaH to deprotonate the diethylphosphite prior to addition of a solution of **4.4**, the yield of **4.5** was improved to 50%. The SPO **4.5** was purified by trituration with a methyl tert-butyl ether (MTBE)/hexane mixture to remove unreacted diethylphosphite. The ^{31}P NMR spectrum of **4.5** clearly shows a characteristically large one bond P–H coupling ($^{1}J_{PH}$ = 482 Hz) and the resonance is

further split into a doublet of triplets with a ($^3J_{PH}$ = 16 Hz, Figure 4.6) due to the two pyrenyl 2-H protons. In the ^{1}H NMR spectrum the P–H resonance is at δ_H = 9.39 ppm ($^1J_{HP}$ = 482 Hz, see Figure 4.6).

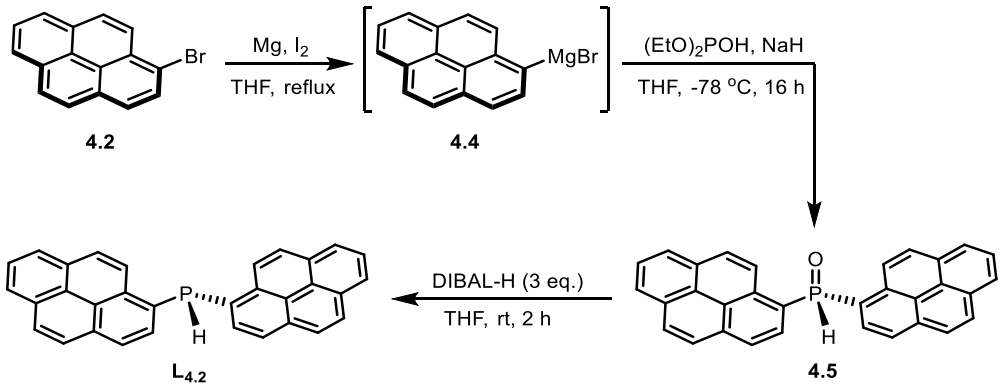

Scheme 4.12. Synthesis of bis(1-pyrenyl)phosphine **L**$_{4.2}$ via the SPO **4.5**.

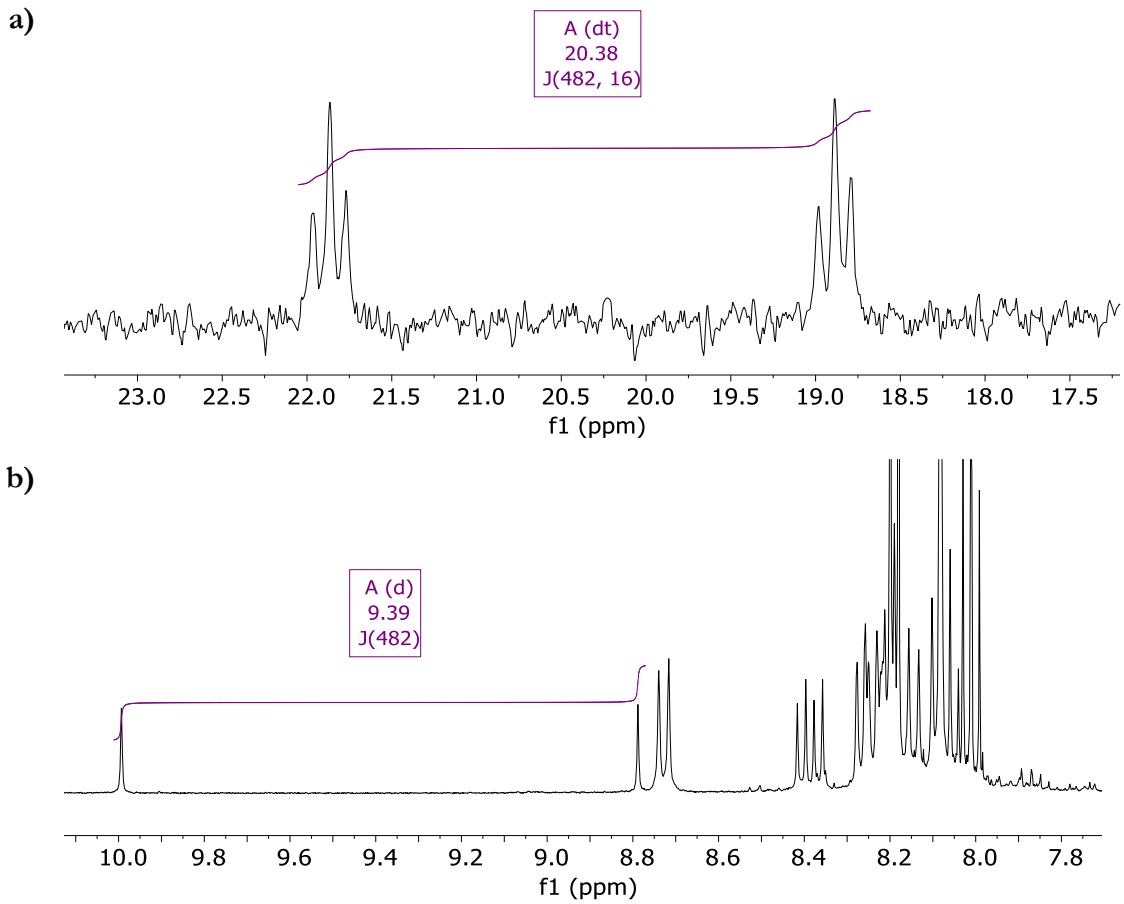

Figure 4.6. a) ^{31}P NMR spectrum of **4.5**. b) ^{1}H NMR spectrum of **4.5** with the P–H resonance highlighted to show the large coupling constant ($^1J_{HP}$ = 482 Hz).

Reduction of **4.5** with DIBAL-H to give bis(1-pyrenyl)phosphine **L**$_{4.2}$ appeared to be quantitative by ^{31}P{^{1}H} NMR spectroscopy but isolated yields of the desired phosphine

were always low (~25%), probably due to losses during the removal of the aluminium salts by filtration.

Thus, an alternative route, avoiding generation of the SPO, which could also be carried out as a one-pot procedure was developed which gave the secondary phosphine $\mathbf{L}_{4.2}$ in a 76% yield (Scheme 4.13). Lithiation of 1-bromopyrene, followed by reaction with Me_2NPCl_2, gave the amino phosphine **4.6.** This could be isolated or immediately converted to the chlorophosphine by treatment with an excess of HCl (2 M in Et_2O). The chlorophosphine **4.7** was reduced with $LiAlH_4$ to give $\mathbf{L}_{4.2}$.

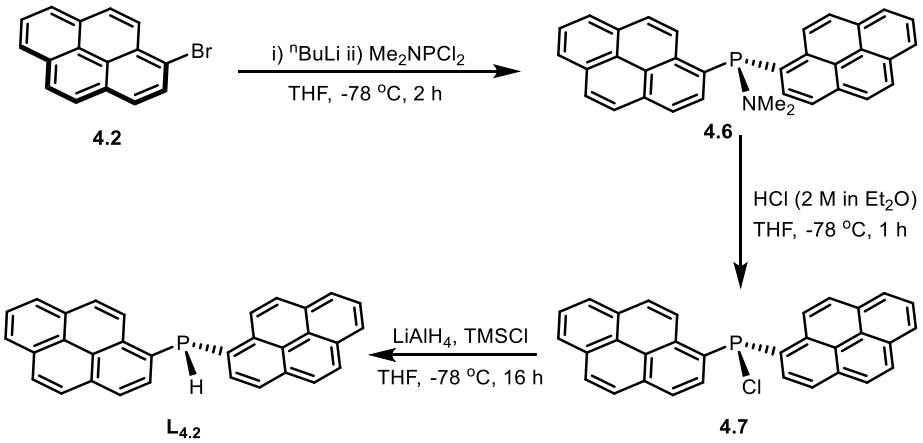

Scheme 4.13. Synthesis of bis(1-pyrenyl)phosphine $\mathbf{L}_{4.2}$ via chlorophosphine **4.7**.

The ^{31}P NMR resonance for $\mathbf{L}_{4.2}$ at δ_P = –59.5 ppm ($^1J_{PH}$ = 223 Hz) is upfield of diphenylphosphine (*cf.* δ_P = –40.0 ppm). Each step of the reaction depicted in Scheme 4.13 was followed by *in situ* $^{31}P\{^1H\}$ NMR spectroscopy (Figure 4.7).

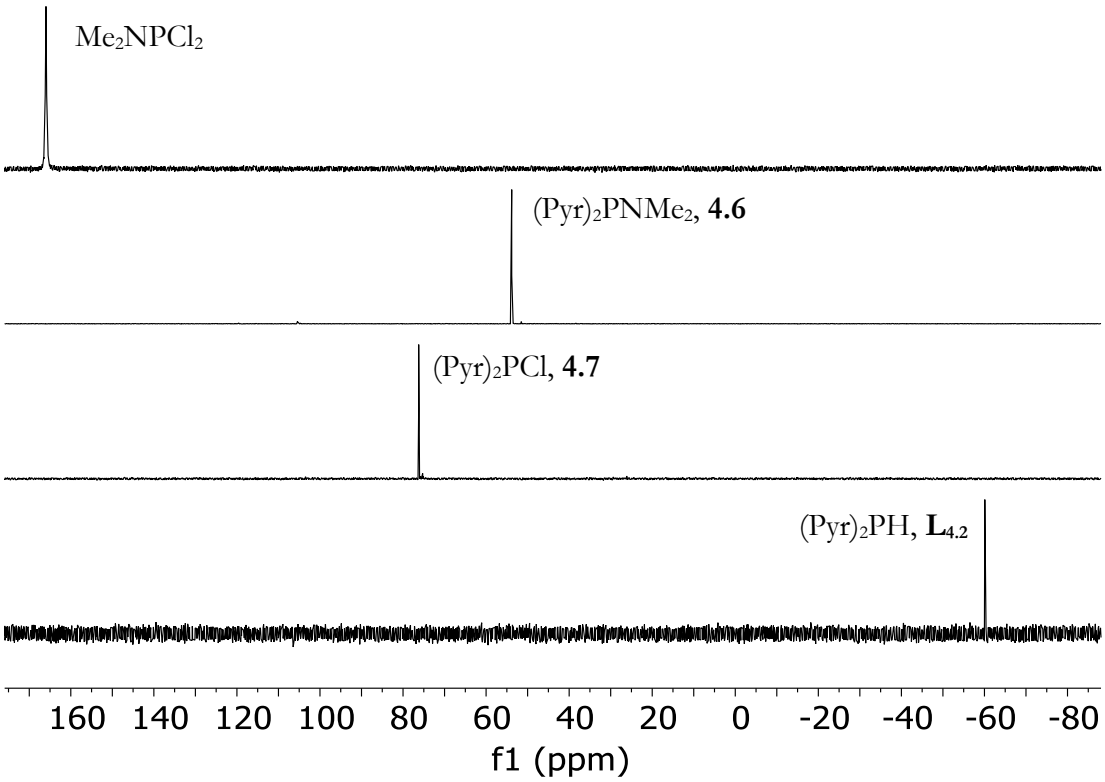

Figure 4.7. *In situ* $^{31}P\{^{1}H\}$ NMR reaction monitoring for the synthesis of $\mathbf{L_{4.2}}$.

4.2.3 Synthesis of tris(1-pyrenyl)phosphine

To access tris(1-pyrenyl)phosphine, reaction of **4.2** with PCl_3 or $P(OEt)_3$ was attempted (Scheme 4.14). The route employing $P(OEt)_3$ was reported by Huang *et al.* however, the authors never isolated the tertiary phosphine, en route to the phosphine oxide. In addition, the authors did not report any $^{31}P\{^{1}H\}$ NMR data, characterising the products only by ^{1}H, ^{13}C and MALDI mass spectrometry.

The tris(1-pyrenyl)phosphine $\mathbf{L_{4.3}}$ was prepared following the procedure recently reported by Walensky *et al.* After full consumption of PCl_3 (as determined by *in situ* $^{31}P\{^{1}H\}$ NMR spectroscopy) a new species at δ_P = –30.6 ppm was observed which corresponded to the desired compound, in agreement with the literature value (Scheme 4.14).[231]

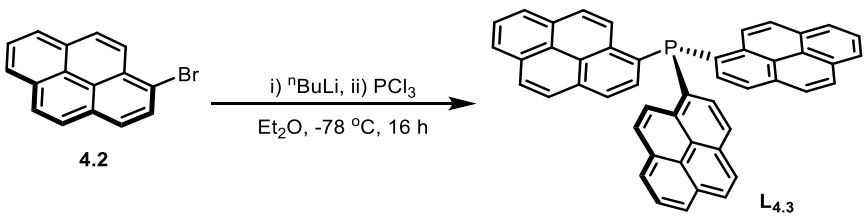

Scheme 4.14. Synthesis of tris(1-pyrenyl)phosphine $\mathbf{L_{4.3}}$.[231]

With pure samples of the primary, secondary, and tertiary pyrenyl phosphines **L4.1**-**L4.3** in hand, their coordination behaviour was investigated.

4.2.4 Synthesis and Ru coordination of bidentate pyrenylphosphine ligands

This section details synthetic attempts to make diphosphine ligands bearing pyrenyl (Pyr) substituents. We predicted that the luminescence properties of these diphosphines could be exploited as biological imaging agents when used in combination with (*cis*-tach)Ru complexes. The unsymmetrical diphosphine precursor $Ph_2PCH_2CH_2PCl_2$ was prepared and was reacted with the Grignard reagent of 1-bromopyrene (Scheme 4.15). The *in situ* $^{31}P\{^1H\}$ NMR spectrum showed full consumption of the $–PCl_2$ resonance of the starting material with δ_P = 196.4 ppm (d, $^3J_{PP}$ = 30 Hz) and after 1 h, the $^{31}P\{^1H\}$ NMR spectrum showed the expected signals for **L4.4** with a new doublet resonance corresponding to $–P(Pyr)_2$ (δ_P = –35.2 ppm, $^3J_{PP}$ = 38 Hz).

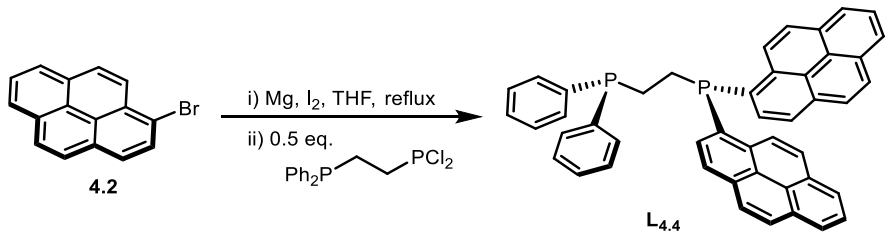

Scheme 4.15. Synthesis of unsymmetrical diphosphine ligand **L4.4**.

The unsymmetrical ligand **L4.4** was reacted with [RuCl(*cis*-tach)$(DMSO)_2$]Cl (**2.1**) in a mixture of THF (to dissolve the ligand) and MeOH (to dissolve the Ru precursor) (Scheme 4.16). Although **L4.4** was only partially soluble, analysis of the solid obtained displayed two new resonances in the $^{31}P\{^1H\}$ NMR spectrum (Figure 4.8) consistent with formation of the desired chelate complex [RuCl(**L4.4**)(*cis*-tach)]Cl **4.8** (δ_P = 72.0 ppm (d, $^3J_{PP}$ = 23 Hz), 69.7 ppm (d, $^3J_{PP}$ = 23 Hz)).

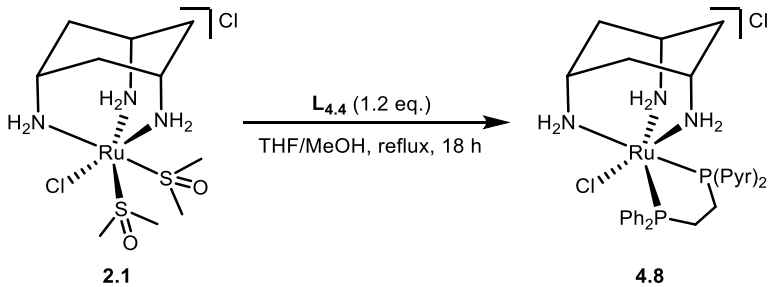

Scheme 4.16. Formation of (*cis*-tach)Ru complex **4.8**.

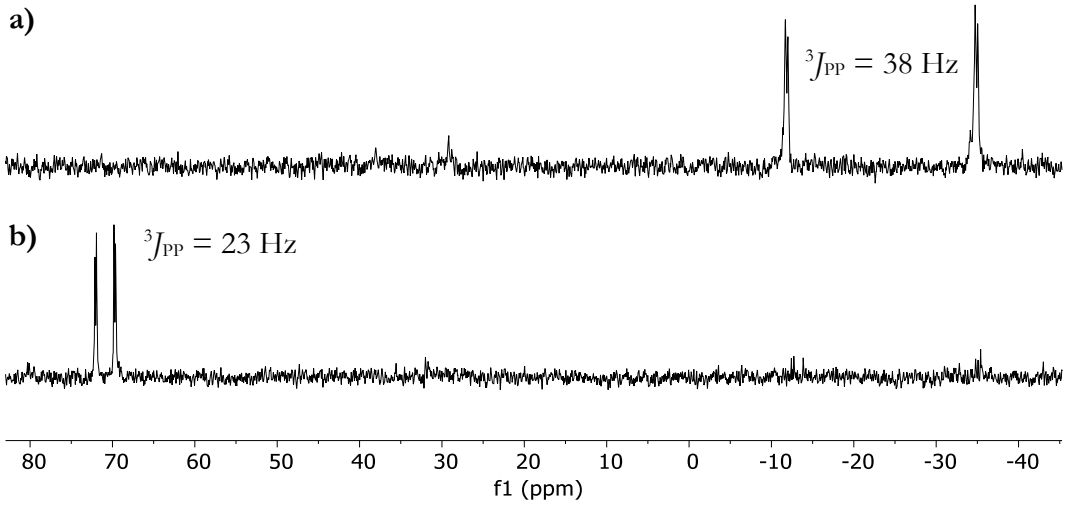

Figure 4.8. $^{31}P\{^1H\}$ NMR spectra for a) diphosphine $\mathbf{L_{4.4}}$, and b) [RuCl($\mathbf{L_{4.4}}$)(*cis*-tach)]Cl **4.8**.

The steric bulk and limited solubility of ligands bearing two pyrenyl substituents makes them challenging to work with. To mitigate this, we aimed to incorporate a spacer/linker between the phosphorus and pyrenyl moieties. As seen before, complexes with a pyrene group tethered from the metal centre, can exhibit interesting luminescence properties due to the pyrene excimer state.[107] We aimed to install an alkyl tethered pyrenyl group to unsymmetrical diphosphine ligand precursors with ethylene and phenylene backbones. Using purely alkyl tethers to attach a pyrenyl fluorophore was paused at this stage and instead we turned our attention to the use of solubilising groups, such as esters or amides. The methods to functionalise diphosphine ligands with organic fluorophores using these linkers are presented in Chapter 3.

4.2.5 Synthesis of 2-pyrenylphosphines

Marder *et al.* reported the selective functionalisation of the C–H bonds in the 2-position of pyrene.[243] The reaction of pyrene with bis(pinacolato)diboron (B_2pin_2) catalysed by [$Ir_2(\mu\text{-OMe})_2(cod)_2$]/dtbpy forms the desired monosubstituted product **4.11** (Scheme 4.17). Unfortunately, competing disubstitution to form the 2,7-bis(boryl)pyrene **4.12** cannot be fully suppressed and necessitates the use of column chromatography, which leads to a modest yield of **4.11**.

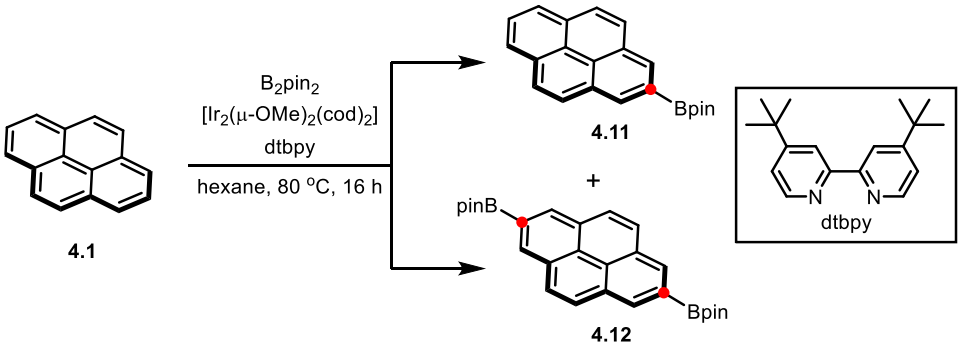

Scheme 4.17. Synthesis of **4.11** and **4.12**, reported by Marder *et al.*[243]

In the recent report, Bonifazi *et al.* described the use of **4.11** as a precursor to *O*-annulated medium-ring polycyclic aromatic hydrocarbons.[247] In a private communication with Dr. Davide Bonifazi (Cardiff University), we learned that they also observed disubstitution giving significant quantities of **4.12**. Acting on their advice of keeping the reaction temperature <80 °C to disfavour the second borylation, and always using fresh, dry SiO_2 for column chromatography, we were able to improve the isolated yields of **4.11** from ~10% to ~50% (comparable to Bonifazi *et al.*).

The monosubstituted pyrenyl boronic ester **4.11** can be converted to 2-bromopyrene **4.13** by reaction with 3 equiv. of $CuBr_2$ (Scheme 4.18). On isolation of **4.13**, the white solid rapidly darkened on exposure to ambient light.

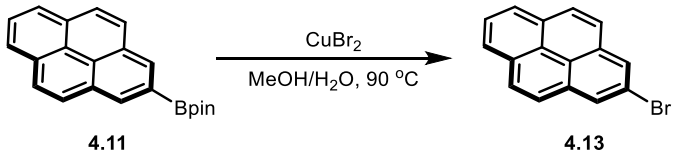

Scheme 4.18. Synthesis of **4.13**, reported by Marder *et al.*[243]

Despite the sensitivity of **4.13**, the synthesis of primary and tertiary 2-pyrenylphosphines was attempted by the methods (i-iv) shown in Scheme 4.19. Unfortunately, none of the proposed methods given in Scheme 4.19 gave the desired products, as briefly detailed below.

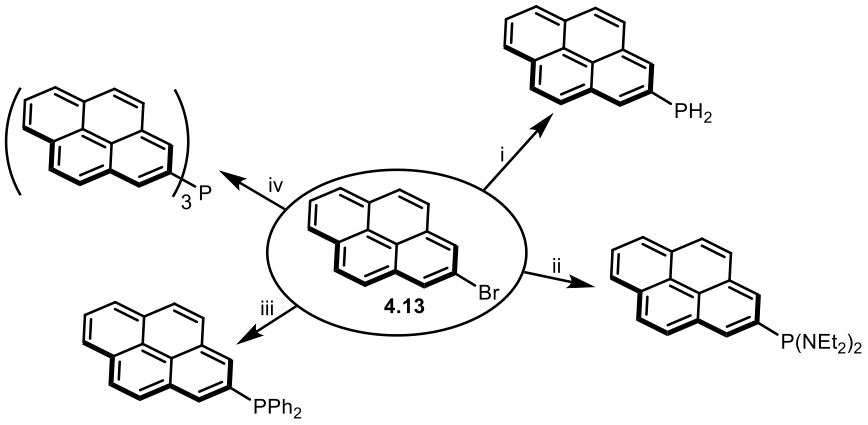

Scheme 4.19. Conditions for the attempted syntheses of 2-pyrenylphosphines. i) ^{n}BuLi, –78 °C, THF, $(EtO)_2P(O)Cl$, $LiAlH_4$, TMSCl. ii) ^{n}BuLi, –78 °C, THF, $(Et_2N)_2PCl$. iii) Ph_2PH, $Pd(OAc)_2$ (5 mol%), DMF, 130 °C. iv) ^{n}BuLi, –78 °C, THF, PCl_3.

Attempted method i: The addition of $(EtO)_2P(O)Cl$ to 2-lithiopyrene produced a purple solution which gave approx. 8 broad resonances in the region δ_P = +30 to –15 ppm in the *in situ* $^{31}P\{^1H\}$ NMR spectrum.

Attempted method ii: The addition of $(Et_2N)_2PCl$ to 2-lithiopyrene produced a bright green solution which gave a broad resonance at δ_P = 83 ppm ($\omega_{½}$ ~ 120 Hz) in the *in situ* $^{31}P\{^1H\}$ NMR spectrum. Interestingly, addition of two equivalents of HCl (in Et_2O solution) caused the solution to rapidly darken and did provide another broad resonance in the expected $–PCl_2$ region δ_P = 132 ppm ($\omega_{½}$ ~ 140 Hz), along with another unidentified broad resonance at δ_P = 127 ppm ($\omega_{½}$ ~ 130 Hz). After addition of $LiAlH_4$ to this mixture, the *in situ* $^{31}P\{^1H\}$ NMR spectrum revealed two broad resonances, one of which at δ_P = –139 ppm ($\omega_{½}$ ~ 85 Hz) was tentatively assigned to the primary 2-pyrenylphosphine. The second signal at δ_P = 33 ppm ($\omega_{½}$ ~ 85 Hz) is in the expected region for the primary phosphine oxide. Attempted isolation of this material by filtration of the THF solution through a small silica plug returned a sticky black solid which contained no observable ^{31}P NMR resonances.

Attempted method iii: The attempted cross-coupling of 2-bromopyrene with Ph_2PH catalysed by $Pd(OAc)_2$ in DMF gave a dark brown solution. After 30 h at 130 °C, the only $^{31}P\{^1H\}$ NMR resonance observed was due to Ph_2PH, albeit significantly broadened, at δ_P = –39 ppm ($\omega_{½}$ ~ 90 Hz).

Attempted method iv: The attempted synthesis of tris(2-pyrenyl)phosphine by addition of 2-lithiopyrene to PCl_3 produced a green solution immediately which gave approx. 12 species in the *in situ* $^{31}P\{^1H\}$ NMR spectrum in the region δ_P = +65 to –10 ppm.

Summary of attempted syntheses i-iv: In each of the syntheses described above, the reaction mixtures were intensely coloured (purple, green, brown, or black) and contained multiple species, in contrast to the relatively clean analogous reactions of 1-lithiopyrene. It is suggested that radicals may be formed that give rise to the deeply coloured mixtures, and that paramagnetic species are producing the peak broadening in the ^{31}P NMR spectra. It is known that 2-pyrenyl radicals are formed from boron or nitrogen substituted pyrene cores, such as 2,7-bis($BMes_2$)pyrene.[248,249] As a result of the failure of each of these routes, the proposed investigation of the luminescence properties and coordination chemistry of 2-pyrenylphosphines could not be completed. Further studies into the nature of these materials, their photophysical properties, and possible radical reactivity is warranted.

4.3 Coordination chemistry

4.3.1 Ruthenium coordination chemistry

The primary, secondary, and tertiary pyrenylphosphines (**L4.1**-**L4.3**) were reacted in a 2:1 molar ratio with [(*p*-cymene)$RuCl_2$]$_2$ to give mononuclear complexes of the form [(*p*-cymene)Ru(PR_3)Cl_2]. The primary phosphine **L4.1** was reacted with [(*p*-cymene)$RuCl_2$]$_2$ in CH_2Cl_2 at room temperature (Scheme 4.20), and within 1 h full conversion to the expected complex was observed by a downfield shift in the $^{31}P\{^1H\}$ NMR resonance from –132.2 ppm to –26.9 ppm ($\Delta\delta_P$ = 105.3 ppm).

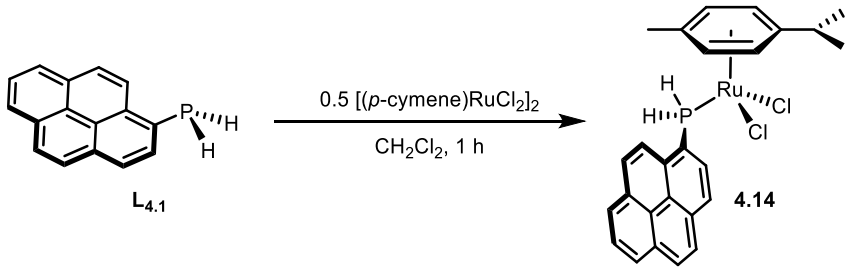

Scheme 4.20. Formation of Ru complex **4.14**.

Single crystals suitable for X-ray diffraction were grown by slow evaporation of a concentrated CH_2Cl_2 solution of **4.14** at room temperature (Figure 4.9). The Ru–P bond length of 2.298(2) Å is within the range for previously reported primary phosphine complexes of Ru (2.296(2)–2.312(2) Å). The sum of the L–M–L angles, Σ_{L-M-L} (which

should be 270° for a symmetric octahedral complex where the arene occupies one face) is significantly smaller for **4.14** (Σ_{L-M-L} = 254.5°), in good agreement with previously reported Ru ferrocenylphosphine derivatives (Σ_{L-M-L} = 250.6° to 254.4°).[238,250] The bulky pyrene moiety is oriented away from the cymene iso-propyl group and the C(11)–P(1)–Ru(1) bond angle is 120.2(2)°.

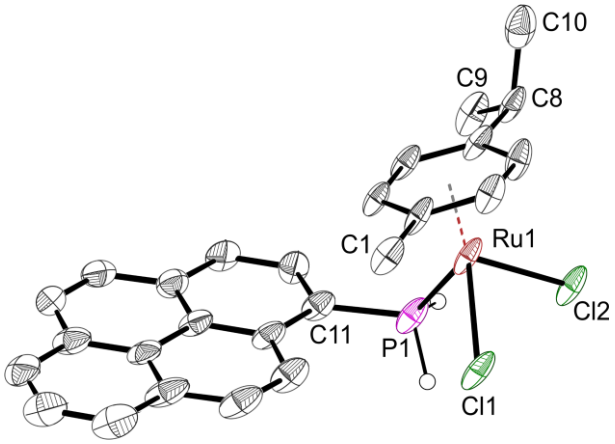

Figure 4.9. Single crystal X-ray crystallography structure of **4.14**. Hydrogen atoms (except for the –PH_2 group) have been omitted for clarity. Thermal ellipsoids at 50% probability level. Selected bond lengths (Å) and angles (°): Ru1–Cl1 2.4093(17), Ru1–Cl2 2.4082(15), Ru1–P1 2.298(2), P1–C11 1.808(7); Cl2–Ru1–Cl1 87.14(6), P1–Ru1–Cl1 84.86(7), P1–Ru1–Cl2 82.54(7), C11–P1–Ru1 120.2(2).

A diagram showing the crystal packing for **4.14** is shown in Figure 4.10. The pyrene groups are stacking with a slipped parallel arrangement commonly observed with other pyrene-containing molecules. For example, short pyrenyl-pyrenyl distances are present in the diruthenium complexes reported by Therrien *et al.* (3.49 Å)[251] and 1-pyrenyl-carbothioamides and carboxamides (3.32–3.36 Å).[252] In the later examples pyrene stacking in the solid state increased the fluorescence quantum yield of these compounds.

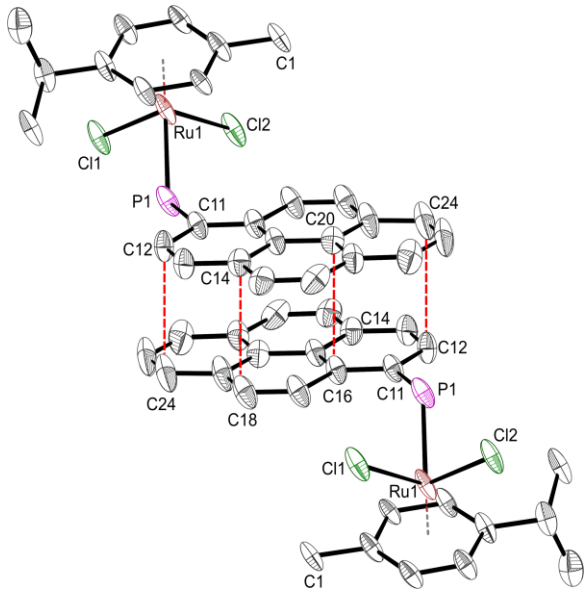

Figure 4.10. Crystal packing diagram of **4.14** to show intermolecular pyrenyl-pyrenyl interactions with the centroid-centroid distances marked in red.

Closer analysis of the crystal structure of **4.14** shows the slipped parallel stacking of the pyrenyl groups (Figure 4.11). The pyrenyl carbon atoms with the shortest distances: C12–C24 (3.484 Å), C14–C18 (3.533 Å) and C16–C20 (3.526 Å) are highlighted in Figure 4.10 and are within the normal range of pyrene stacked compounds. The average of these inter-atomic distances (3.51 Å) is around 0.1 Å longer than the sum of the van der Waals' radii for carbon (3.40 Å). As a result, this interaction could arise from weak van der Waals' forces or merely be a crystal packing effect.

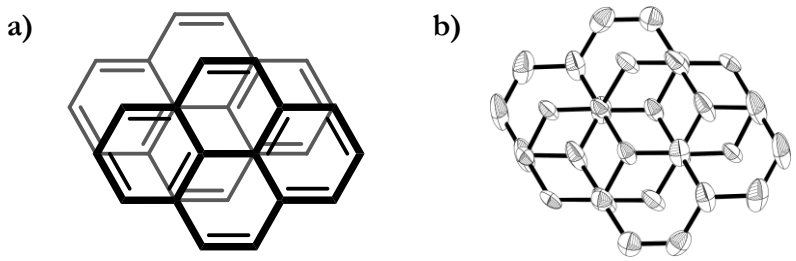

Figure 4.11. a) Schematic to show the slipped parallel stacking arrangement of pyrene. b) The crystal structure of **4.14** to show packing arrangement. (All atoms except pyrene omitted for clarity).

We considered whether cyclometallation of the primary phosphine Ru complex **4.14** would change the photophysical properties, in a manner similar to cycloplatinated pyrene complexes previously reported (see Scheme 4.6). It was hoped that the pyrenyl substituent would undergo a cyclometallation reaction to give a 5-membered metallacycle while leaving the P–H bonds intact. However, $\mathbf{L}_{4.1}$ did not cyclometallate under the conditions employed to give **4.15** (Scheme 4.21) and the yellow precipitate that was obtained

produced 7 singlets in the $^{31}P\{^{1}H\}$ NMR spectrum. Complete consumption of the starting material **L4.1** was observed and the main resonance at δ_P = –58 ppm coupled with a broad ^{1}H NMR spectrum may indicate a phosphide-bridged species (see Scheme 4.21) resulting from deprotonation of the primary phosphine by NaOAc, or decomposition of the Ru complex.

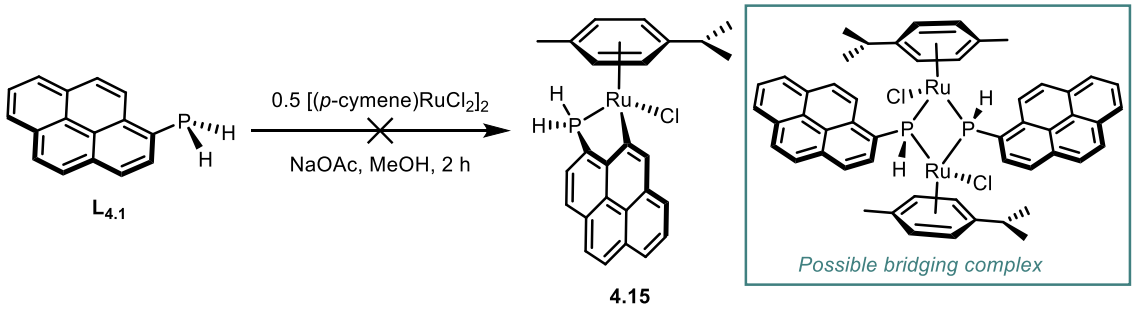

Scheme 4.21. Attempted cyclometallation of **L4.1** to give Ru complex **4.15** and suggested structure of bridged species.

In contrast to the chemistry displayed by **L4.1**, the DPPP ligand is readily cyclometalated in the presence of NaOAc to give Ru complex **4.16** (Scheme 4.22). Clean formation of the expected 5-membered metallacycle is evidenced by the characteristic $^{31}P\{^{1}H\}$ NMR resonance (δ_P = 67.1 ppm; *cf.* δ_P = 66.0 ppm for the analogous naphthyldiphenylphosphine derivative).[253]

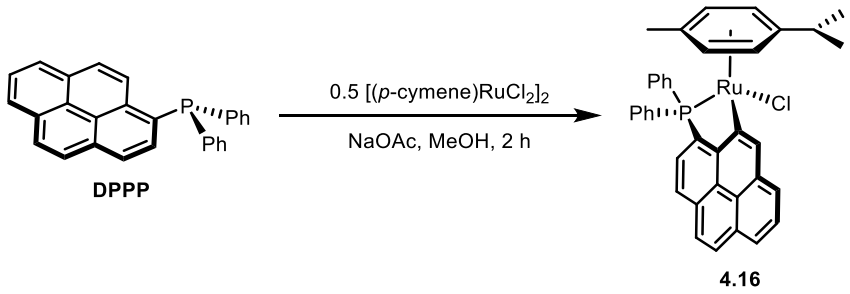

Scheme 4.22. Formation of **4.16** by cyclometallation of DPPP with NaOAc.

The secondary pyrenylphosphine **L4.2** was reacted with [(*p*-cymene)$RuCl_2]_2$ in CH_2Cl_2 at room temperature and within 2 h, full conversion to the expected complex was observed by a downfield shift in the $^{31}P\{^{1}H\}$ NMR resonance from δ_P = –58.0 ppm to δ_P = +5.2 ppm ($\Delta\delta_P$ = 63.2 ppm).

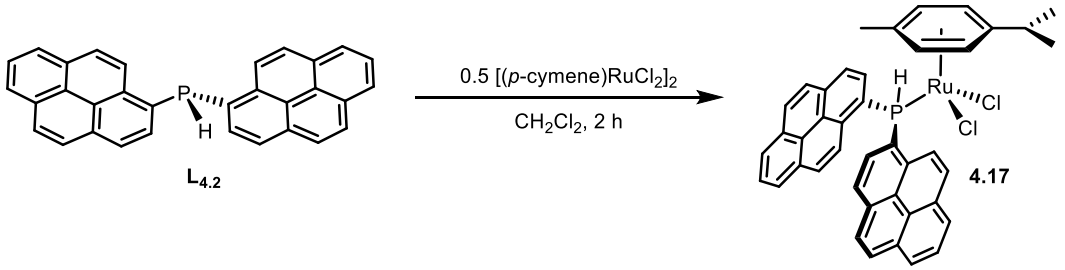

Scheme 4.23. Formation of Ru complex **4.17**.

The coordination chemical shifts for the Ru(II) complexes of $\mathbf{L_{4.1}}$ ($\Delta\delta_P$ = +105.3 ppm) and $\mathbf{L_{4.2}}$ ($\Delta\delta_P$ = +63.2 ppm) are in agreement with known Ru complexes of primary and secondary phosphines.[238] As expected, from the data for other primary phosphine metal complexes, the $^1J_{PH}$ coupling constants significantly increased by *ca.* 200 Hz, in accordance with donation of the phosphine lone pair into the Ru 4d t_{2g} orbitals, similar to primary phosphine complexes previously reported.[254,255] This phenomenon is rationalised by Bent's rules where, upon coordination, the P–H bond(s) have more s-orbital character consistent with a rehybridization towards sp^2, resulting in a large increase in the coupling constant.[256,257]

On coordination of **L**$_{4.1}$ to Ru, the $^{3}J_{PH}$ coupling constant also increases from 7 Hz to 13 Hz. To understand the origin of this additional coupling a $^{1}H–^{31}P\{^{1}H\}$ HMBC correlation spectrum of [(*p*-cym)RuCl$_2$(**L**$_{4.1}$)] (**4.14**) was obtained (Figure 4.12). This showed the intense correlation peak corresponding to the large P–H coupling and an additional correlation peak to one of the pyrenyl protons (δ_H = 8.37 ppm, d, $^{3}J_{PH}$ = 13 Hz).

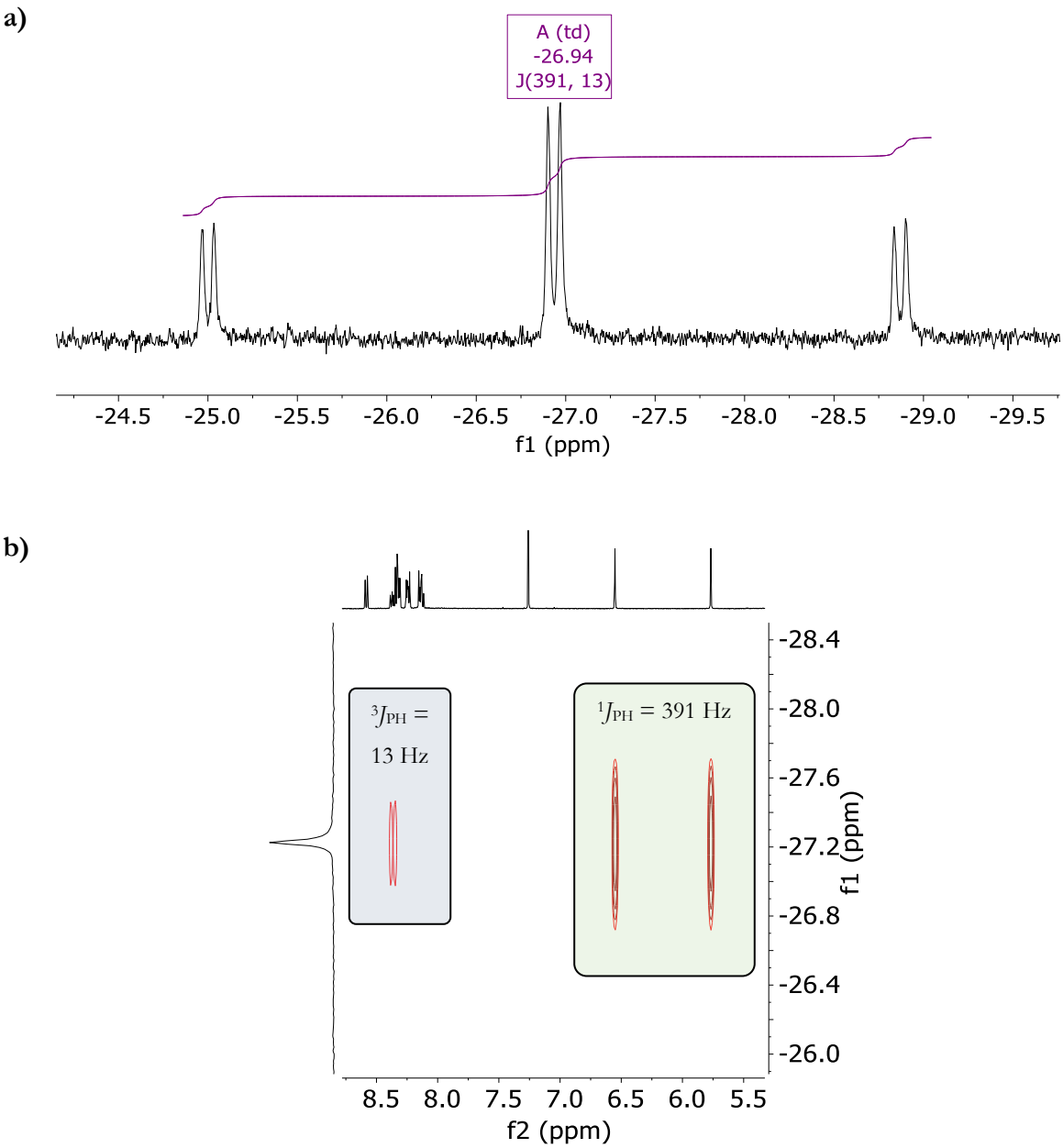

Figure 4.12. a) The ^{31}P NMR spectrum of **4.14**. b) Selected region of the $^{1}H–^{31}P\{^{1}H\}$ HMBC NMR spectrum of **4.14** showing the most intense $^{1}H–^{31}P$ correlations.

The observed FTIR data for the ν(P–H) stretching mode(s) also indicate a strengthening of the P–H bond because the stretching frequencies increase by *ca.* 70–90 cm^{-1} (see Table 4.1) which is consistent with the behaviour of phenylphosphines,[232] mesitylphosphines, and ferrocenylphosphines.[239] A summary of the NMR and FTIR data for

pyrenylphosphines **L4.1-L4.3** and the corresponding (*p*-cymene)Ru complexes is given in Table 4.1.

Table 4.1. Selected FTIR and NMR data of pyrenylphosphines (**L4.1-L4.3**) and (*p*-cymene)Ru complexes.

Compound	ν(P–H) (cm^{-1})[a]	δ(^{31}P, ppm)[b]	$^{1}J_{PH}$ (Hz)	$^{3}J_{PH}$ (Hz)	δ(^{1}H, ppm)[b]
$PyrPH_2$, **L4.1**	2274, 2298	–132.2	203	7	4.5
Pyr_2PH, **L4.2**	2294	–58.0[d]	223	–[c]	6.2[d]
Pyr_2POH, **4.5**	2296	20.4	482	–[c]	9.4
Pyr_3P, **L4.3**	–	–30.4	–	–	–
$RuPyrPH_2$, **4.14**	2352, 2386	–26.9	391	13	6.2
$RuPyr_2PH$, **4.17**	2369	5.2	405	–[c]	8.0

[a]FTIR obtained neat. [b]NMR spectrum obtained in $CDCl_3$. [c]Signal too broad to resolve coupling. [d]NMR spectrum obtained in C_6D_6.

The tertiary phosphine **L4.3** was reacted with $[(p\text{-cymene})RuCl_2]_2$ in CH_2Cl_2 at room temperature (Scheme 4.24). As previously observed with tris(1-naphthyl)phosphine, no coordination was detected, even after extended reaction time, presumably due to the bulk of this tertiary phosphine. Over the course of 3 h, a yellow solid precipitated, analysis of which showed it to be the free ligand. Since, over time, **L4.3** also precipitates out of a chloroform solution, it was proposed that the tertiary phosphine forms a poorly soluble solvate with chlorinated solvents.

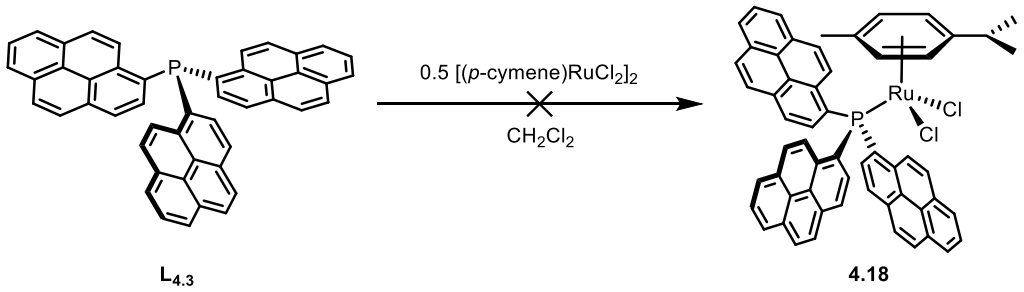

L4.3 **4.18**

Scheme 4.24. Attempted formation of Ru complex **4.18**.

4.3.2 Platinum coordination chemistry

To form their $PtCl_2$ complexes, both **L4.3** and tris(1-naphthyl)phosphine (PNp_3) were reacted in a 1:1 molar ratio with $[PtCl_2(cod)]$ (Scheme 4.25 and Scheme 4.26). No coordination was observed in either reaction with only free ligand present in solution which, after 3 h, began to precipitate.

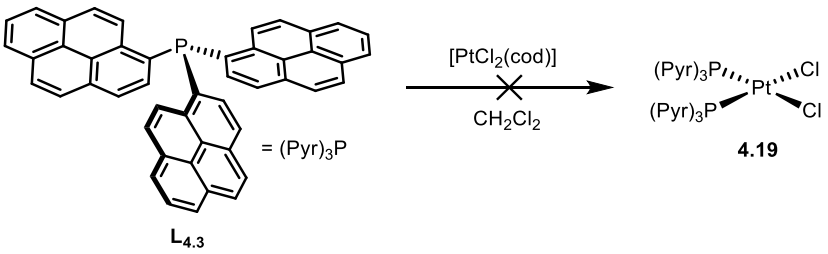

Scheme 4.25. Attempted formation of Pt complex $[PtCl_2(\mathbf{L_{4.3}})_2]$ (**4.19**).

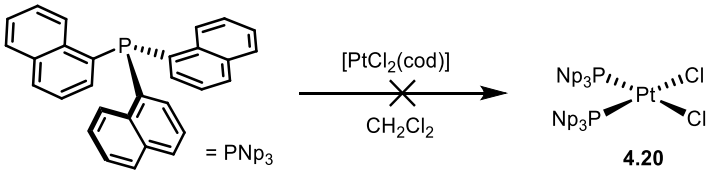

Scheme 4.26. Attempted formation of Pt complex $[PtCl_2(PNp_3)_2]$ (**4.20**).

Mingos *et al.* reported that by employing the more reactive Pt precursor $[Pt(NCMe)_4](BF_4)_2$, all complexes derived from bulky arylphosphines were formed as the *trans* isomer, *trans*-$[Pt(NCMe)_2(PR_3)_2](BF_4)_2$. When the reaction was attempted with the PNp_3 ligand (Scheme 4.27), a mixture of partially soluble products including one tentatively assigned to *trans*-$[Pt(NCMe)_2(PNp_3)_2](BF_4)_2$ based on the $^1J_{PPt}$ coupling constant was obtained.[258]

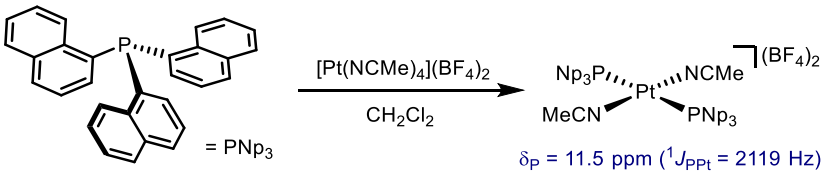

Scheme 4.27. Reported formation of *trans*-$[Pt(NCMe)_2(PNp_3)_2](BF_4)_2$, Mingos *et al.*[258]

4.3.3 Gold coordination chemistry

The tertiary phosphine $\mathbf{L_{4.3}}$ was reacted in a 1:1 molar ratio with [(tht)AuCl] in CH_2Cl_2 at room temperature and monitored by *in situ* $^{31}P\{^1H\}$ NMR spectroscopy (Scheme 4.28). After 7 h, a white precipitate had formed and the $^{31}P\{^1H\}$ NMR spectrum of the solution contained several broad signals (δ_P = 8.1, 17.0, 20.0 ppm). In the report from Mingos *et al.*,[258] the reaction between tris(1-naphthyl)phosphine and [(tht)AuCl] gave a $^{31}P\{^1H\}$ NMR resonance at δ_P = 7.0 ppm but the isolation of the desired $[(Np_3P)AuCl]$ was unsuccessful.

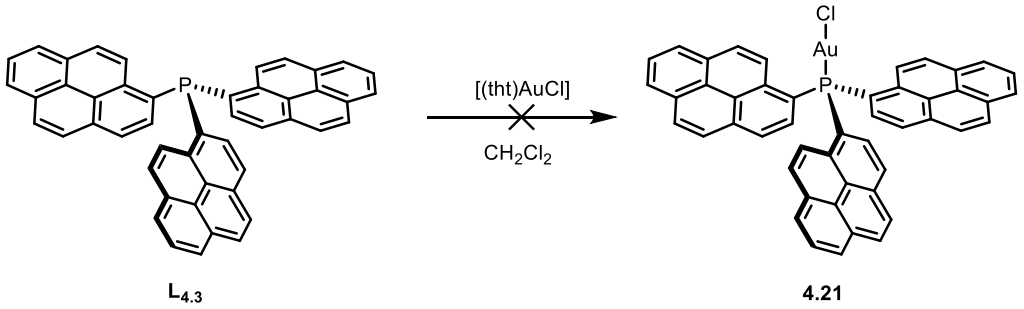

Scheme 4.28. Attempted formation of Au complex [(**L**$_{4.3}$)AuCl] (**4.21**).

As a comparison, the previously prepared diphenyl(1-pyrenyl)phosphine (DPPP) ligand was reacted in a 1:1 molar ratio with [(tht)AuCl] in CH_2Cl_2 at room temperature (Scheme 4.29). Quantitative conversion to complex **4.22** occurred over 7 h and it was characterised by a singlet resonance in the $^{31}P\{^1H\}$ NMR spectrum at δ_P = 27.5 ppm, (*cf.* δ_P = 33.2 ppm for [(Ph_3P)AuCl]).[259]

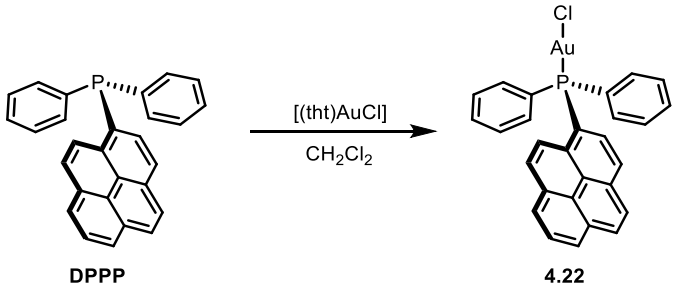

Scheme 4.29. Formation of [(DPPP)AuCl] (**4.22**).

These results are in agreement with the study of Mingos *et al.* on the Au coordination chemistry of naphthyl and anthracenyl phosphines.[258] Reduction in the steric bulk by replacing two pyrenyl groups with two phenyl groups, appears to have enabled formation of the Au complex **4.22**. As the linear Au–Cl complex [(**L**$_{4.3}$)AuCl] would not form, it appears that the bulk of the three 1-pyrenyl substituents of **L**$_{4.3}$ inhibits metal coordination.

It would be worthwhile to study the non-coordinating properties of **L**$_{4.3}$ further, for example in combination with bulky boranes for use in Frustrated Lewis Pair (FLP) chemistry. The inherent luminescent behaviour could be a useful spectroscopic reporter for the reactions of **L**$_{4.3}$ derived FLPs with small molecules.

4.4 Photophysical properties of pyrenylphosphines and Ru complexes

The UV-visible absorption spectra in CH_2Cl_2 were recorded for **$L_{4.1}$**, **$L_{4.2}$**, **4.5** and the corresponding (*p*-cymene)Ru complexes **4.14** and **4.17** (Table 4.2). The spectra all display vibronically structured absorption features attributed to $\pi\rightarrow\pi^*$ transitions within the pyrene moiety (Figure 4.13 and Figure 4.14). In addition to these transitions, a lower energy absorption is observed at *ca.* 354 nm for **$L_{4.2}$** and **4.5** (ε = 25,600 and 19,000 M^{-1} cm^{-1} respectively). The calculated electronic transitions are indicated by the black bars overlaid on the UV-visible absorption spectra (for details, see 4.4.1).

Table 4.2. Absorption and emission data for **$L_{4.1}$**, **$L_{4.2}$**, **4.5** and (*p*-cymene)Ru complexes **4.14** and **4.17**.

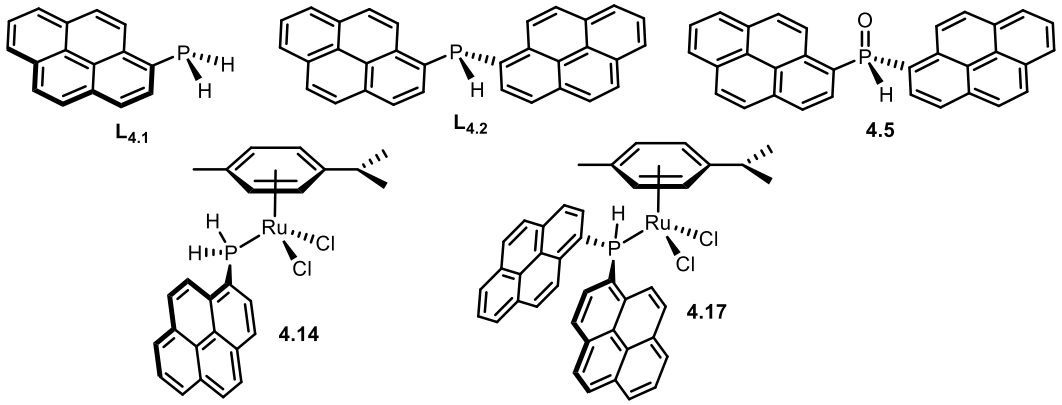

Compound	λ_{abs} [nm] (ε [10^3 M^{-1} cm^{-1}])[a]	λ_{em} [nm]	Φ_f[b]
$PyrPH_2$, **$L_{4.1}$**	337 (12), 322 (7), 274 (13), 242 (25)	384	0.09
Pyr_2PH, **$L_{4.2}$**	337 (31), 322 (18), 274 (35), 242 (63)	383	0.14
Pyr_2POH, **4.5**	337 (53), 321 (33), 274 (61), 242 (110)	386	0.18
Ru $PyrPH_2$, **4.14**	337 (16), 322 (9), 274 (20), 242 (41)	387	0.04
Ru Pyr_2PH, **4.17**	337 (16), 322 (12), 273 (22), 241 (37)	388	0.03

[a]Measured in deaerated CH_2Cl_2. [b]Φ_f = fluorescence quantum yield, reference: Quinine sulfate (Φ_f = 0.58, λ_{ex} = 350 nm, in 0.1 M H_2SO_4).

The UV-visible absorption spectra for the (*p*-cymene)Ru complexes are dominated by the same ligand centred $\pi\rightarrow\pi^*$ transitions as the free ligands albeit with a slight loss of fine vibronic structure. No additional lower energy absorption bands were observed for the Ru complexes **4.14** and **4.17** (Figure 4.13 and Figure 4.14).

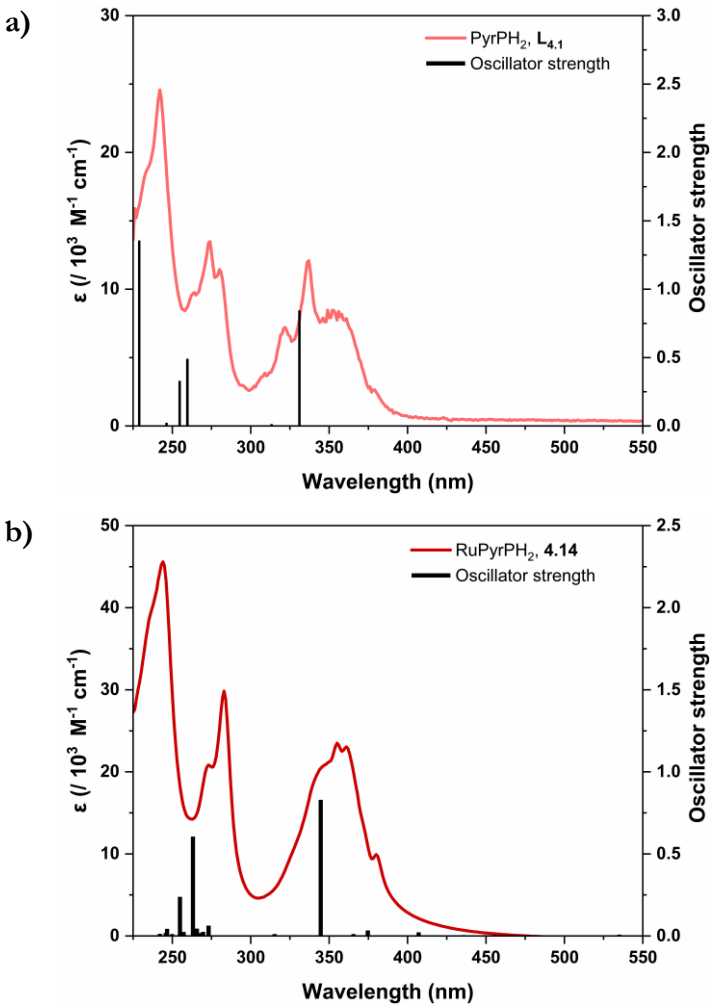

Figure 4.13. Experimental solution state (CH_2Cl_2) UV-visible absorption spectra for a) $\mathbf{L}_{4.1}$, and b) [(*p*-cym)$RuCl_2$($\mathbf{L}_{4.1}$)] (**4.14**). The oscillator strength axes correspond to the calculated electronic transitions (black bars) at the CAM-B3LYP/6-31G(d)/LANL2DZ level of theory.

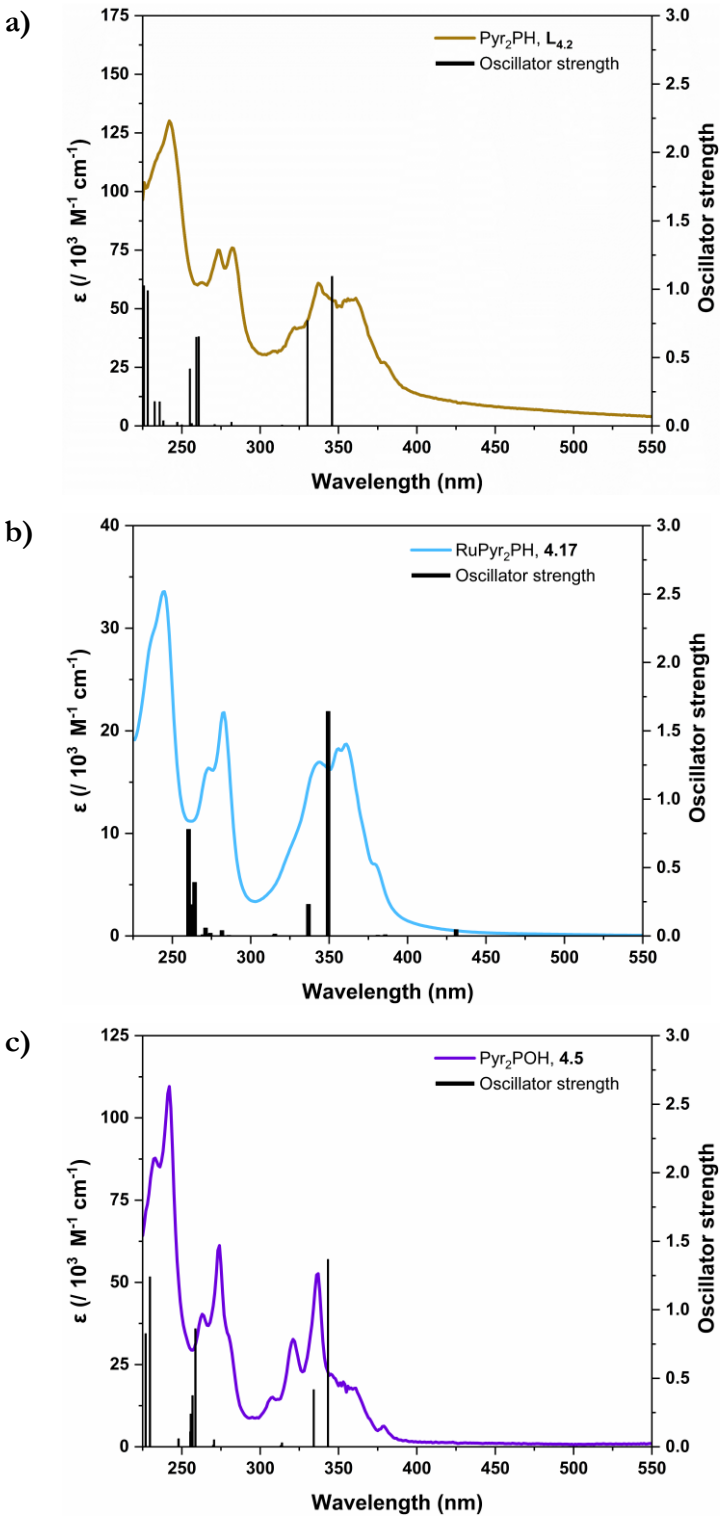

Figure 4.14. Experimental solution state (CH_2Cl_2) UV-visible absorption spectra for a) **L**$_{4.2}$, b) [(*p*-cym)RuCl$_2$(**L**$_{4.2}$)] (**4.17**), and c) Pyr$_2$POH **4.5**. The oscillator strength axes correspond to the calculated electronic transitions (black bars) at the CAM-B3LYP/6-31G(d)/LANL2DZ level of theory.

The emission spectra were recorded for all compounds in deaerated CH_2Cl_2 solution (1.2×10^{-5} M) and in each case an emission profile consistent with pyrene monomer emission is observed (λ_{em} = 383–388 nm). The emission spectra are broad and unstructured in

contrast to some other pyrenylphosphines reported.[195,260] Analysis of the emissive properties of **L**$_{4.2}$, **4.5** and [(*p*-cym)RuCl$_2$(**L**$_{4.2}$)] (**4.17**) reveal that oxidation of the phosphine increases the measured emission intensity, whereas phosphine coordination to Ru dramatically decreases emission intensity (Figure 4.15). The emission 'switch-on' effect by oxidation has been previously studied and is attributed to the preclusion of P lone pair-to-fluorophore PeT quenching. It was hypothesised that coordination to Ru could also induce emission switch-on; however, quenching mechanisms due to the presence of a heavy Ru atom are known.[261,262]

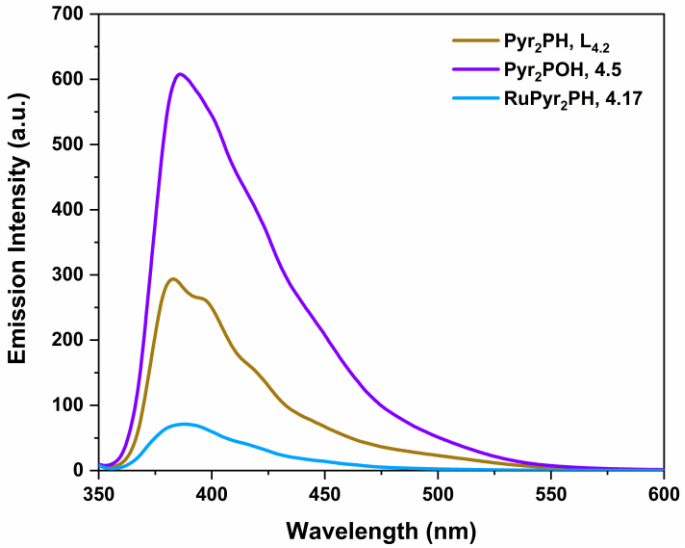

Figure 4.15. Experimental solution state (CH_2Cl_2) emission spectra of **L**$_{4.2}$, **4.5** and [(*p*-cym)RuCl$_2$(**L**$_{4.2}$)] (**4.17**) all exhibit λ_{max} at ca. 385 nm. The quantum yields for the free phosphine, phosphine oxide and Ru complex are Φ_f = 14%, 18% and 3%, respectively.

Fluorescence quantum yields (Φ_f) were measured in deaerated CH_2Cl_2 using quinine sulfate (0.1 M in H_2SO_4) as standard (see Experimental for details). As expected, the fluorescence quantum yield for **L**$_{4.1}$ and **L**$_{4.2}$ is significantly reduced compared to pyrene (Φ_f = 0.58, λ_{ex} = 333 nm, in cyclohexane), presumably due to PeT quenching from the phosphine lone pair.[263] An approximately 2-fold increase in quantum yield was observed going from **L**$_{4.1}$ to **L**$_{4.2}$, as expected due to two pyrenyl substituents per molecule in the latter case. In CH_2Cl_2, there is an increase in emission intensity upon oxidation of **L**$_{4.2}$ to **4.5** (Φ_f = 14% and 18% respectively). Although this effect may not be considered a dramatic fluorescence switch-on, it is in accord with the modest luminescence enhancements reported by Walensky for (Pyr)$_3$P (Φ_f = 13%) going to phosphine oxide (Pyr)$_3$PO (Φ_f = 14%).[231]

We have observed significant fluorescence quenching of the pyrene chromophore in [(*p*-cym)$RuCl_2$(**L**$_{4.1}$)] (**4.14**) and [(*p*-cym)$RuCl_2$(**L**$_{4.2}$)] (**4.17**) with Φ_f = 4% and 3% respectively, possibly due to non-radiative decay processes associated with the heavy-atom effect (Ru).

The electronic basis of the observed absorption and fluorescence properties for **L**$_{4.1}$-**L**$_{4.2}$, **4.5**, **4.14**, and **4.17** have been investigated by DFT calculations.

4.4.1 TD-DFT calculations

Time-dependent density functional theory (TD-DFT) calculations were performed in Gaussian 09 (D.01).[264] Initial geometry optimizations were performed on all ligands and complexes using the B3LYP functional,[265–268] Pople basis set 6-31G(d) on all atoms, apart from Ru, where an additional LANL2DZ basis set and effective core potential was used.[269] A converged ground state was found for each molecule and a frequency calculation returned no imaginary frequencies indicating the structure to be a minimum on the potential energy surface. Where a crystal structure was available as for [(*p*-cym)$RuCl_2$(**L**$_{4.1}$)] (**4.14**), the computed geometry agreed with the structure determined by X-ray crystallography.

TD-DFT was used to calculate the UV-visible absorption properties using the CAM-B3LYP functional and the previously mentioned basis set.[270] Solvation corrections were included using the polarisable continuum model with CH_2Cl_2 (ε = 9.1) as solvent.[271] The LANL2DZ basis set has been used before to accurately model the excited states of Fe and Ru complexes, and in our studies, it produced reasonable agreement with experiment.[218,272] We calculated the first 20 vertical singlet excited states for each ligand **L**$_{4.1}$, **L**$_{4.2}$, **4.5** and Ru complex and the excited state of interest (selected by the presence of a high oscillator strength (f), which is a measure of the probability of that excitation to occur) was investigated. In all cases, the lowest energy electronic transitions involved HOMO→LUMO transitions centred around 345 nm (3.6 eV, f = 0.828 for **4.14**). The TD-DFT derived vertical singlet excitations agree quite well with the recorded UV-visible absorption spectra with the most significant excitations corresponding to $S_0 \rightarrow S_1$ and $S_0 \rightarrow S_2$ transitions within the pyrene substituents.

To understand the absence of any low energy absorption bands with MLCT character, we analysed the frontier molecular orbitals involved. For [(*p*-cym)$RuCl_2$(**L**$_{4.1}$)] (**4.14**), the TD-DFT derived contour surface diagrams of the HOMO-1 to LUMO+1 are shown in Figure 4.16.

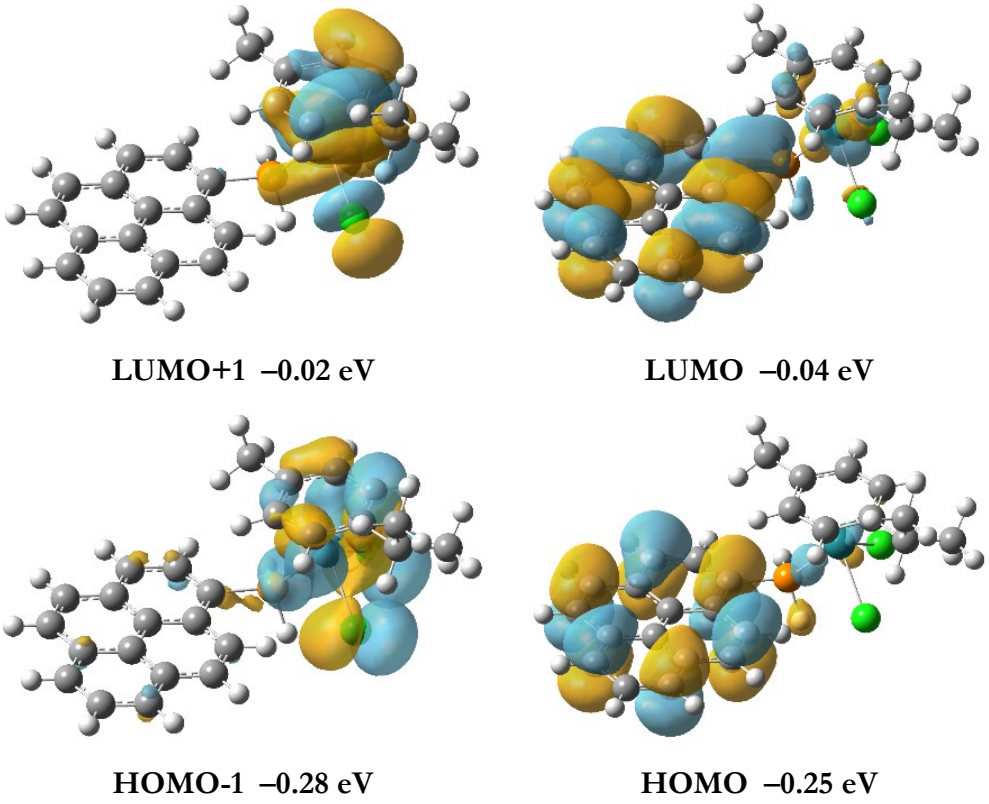

Figure 4.16. CAM-B3LYP/6-31G(d)/LANL2DZ-derived surface diagrams of the MOs of [(*p*-cym)$RuCl_2$(**L**$_{4.1}$)] (**4.14**), (isovalue = 0.02). The dominant transition is a HOMO→LUMO transition centred on pyrene.

From our calculations, for **4.14**, the lowest energy transition that contains contributions from a MLCT band (HOMO-1→LUMO) is predicted to be at 449 nm (2.76 eV) and has a very low oscillator strength (f = 0.003) and therefore has a very low probability of occurring.

4.5 Air stability of pyrenylphosphines

Significant progress towards predicting the air-stability of primary phosphines has been made by Higham and co-workers.[221,223,273,274] Their work, summarised in the following section, provides a qualitative trend between phosphine orbital distribution and experimentally assessed air-stability. A combined experimental and theoretical analysis of ~30 phosphines has allowed for the design and prediction of new air-stable derivatives.[115,229]

First, the authors established that the calculated HOMO orbital energies increased with increasing conjugation (e.g., HOMO E, phenylphosphine = –6.87 eV; 1-naphthylphosphine = –5.80 eV). Moreover, for phosphines containing substituents with

more extended π-systems, the HOMO comprised no significant phosphorus character, which indicated enhanced stability to air oxidation.

Second, when the phosphine radical cations were modelled, in each case, the singly occupied molecular orbital (SOMO) was found to incorporate the phosphorus atom. The use of sterically bulky, heteroatom-containing, or highly conjugated substituents can raise the computed SOMO energy of the phosphine radical cation. In 2011, Higham *et al.* reported that if the computed SOMO energy is higher than –10 eV then, for the set of phosphines analysed, they were generally resistant to air-oxidation. Phosphines with a SOMO energy below –10 eV were found to be air-sensitive and experimental oxidation monitoring by ^{31}P NMR spectroscopy of the neat samples as well as in solution confirmed these findings for a relatively small selection of 7 phosphines.[274] It is noted that the calculated "threshold" energy of –10 eV is significant, but would need to be expanded to a much larger set of phosphine structures to test the model and further understand the mechanism of phosphine oxidation by O_2.

4.5.1 Radical cation SOMO calculations

The radical cation SOMO energies may be used as a predictor of air-stability for a variety of phosphine ligands. The SOMO energies for the phenylphosphines follow the trend: $PhPH_2$ < Ph_2PH < Ph_3P which explains the experimental observation that the primary phosphine oxidises rapidly in air, the tertiary phosphine is air-stable, and the secondary phosphine displays moderate air-sensitivity. Building on the results of Higham *et al.*, by comparison, the 1-pyrenylphosphines have much higher SOMO energies, rendering even the primary phosphine $\mathbf{L}_{4.1}$ air-stable (see Figure 4.17). For completeness, the SOMO energies for primary, secondary, and tertiary 1-naphthylphosphines have been calculated, and unsurprisingly, these display intermediate behaviour compared to the phenyl and 1-pyrenyl derivatives. It is noted that the radical cation SOMO energies correlate with the degree of conjugation of the aryl phosphine substituent: pyrenyl > naphthyl > phenyl, and this can be used as a useful design principle for air-stable phosphines.

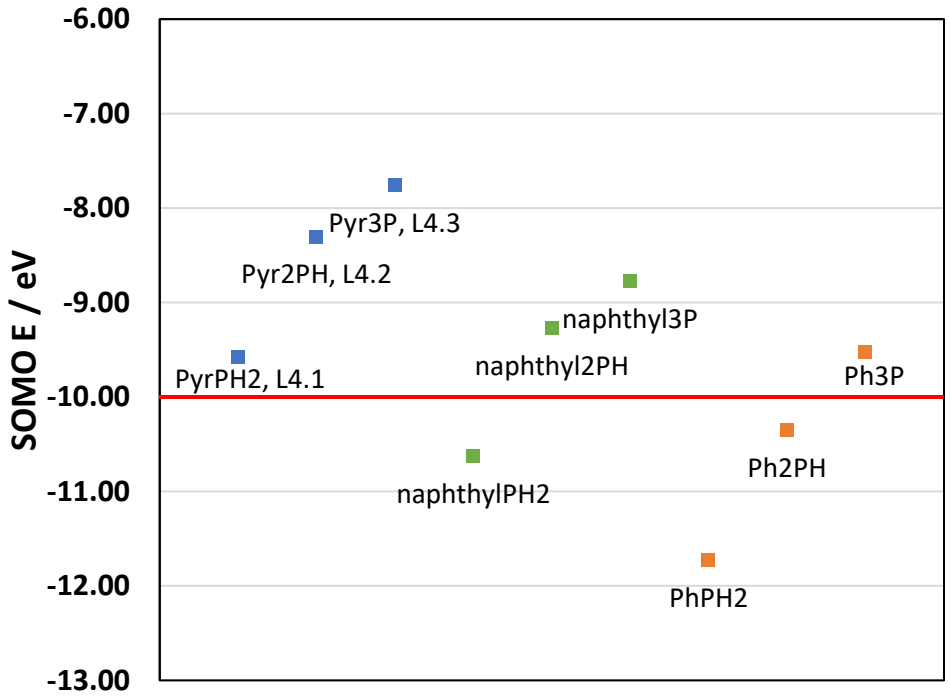

Figure 4.17. Plot of the radical cation SOMO energies of 1-pyrenylphosphines **L**$_{4.1}$-**L**$_{4.3}$ (■), 1-naphthylphosphines (■), and phenylphosphines (■). Red line indicates –10 eV stability threshold.

We sought to understand the inherent air-stability of **L**$_{4.1}$-**L**$_{4.2}$ through analysis of the frontier molecular orbitals. As previously seen with phosphines containing conjugated substituents, if the HOMO is delocalised from the phosphorus lone pair, enhanced air-stability may be observed.[223,275] For the primary pyrenylphosphine **L**$_{4.1}$, the HOMO is delocalised away from the phosphorus atom over the π-system of the pyrene substituent (Figure 4.18). For the secondary phosphine **L**$_{4.2}$, the HOMO is partially located at the phosphorus lone pair but also highly delocalised over the pyrene substituents and thus, the SOMO energies for these two compounds are particularly high (–9.58 eV for **L**$_{4.1}$ and –8.30 eV for **L**$_{4.2}$). This indicates that they should display enhanced air-stability (*cf.* SOMO energy for Ph_3P = –9.51 eV).

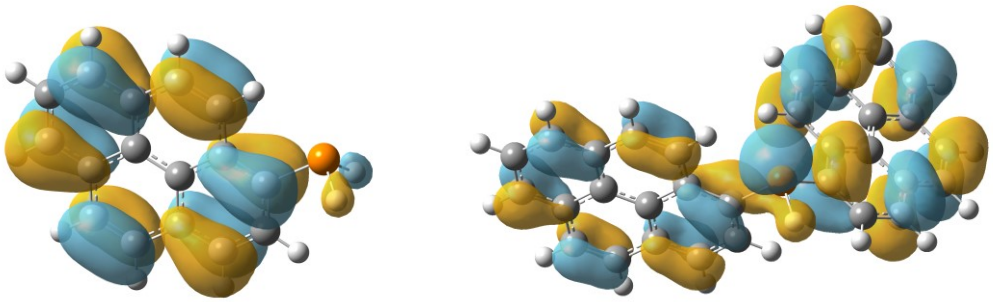

$L_{4.1}$ **$L_{4.2}$**

Figure 4.18. B3LYP/6-31G(d)-derived surface diagrams of the HOMOs of **$L_{4.1}$-$L_{4.2}$**, (isovalue = 0.02).

By comparing the calculated SOMO energies of **$L_{4.1}$-$L_{4.3}$** with air-stable phosphines known in the literature, we expect 1-pyrenylphosphines to display significant resistance to air oxidation.[115,221]

4.5.2 Experimental air stability

The relative air-stability of pyrenylphosphines were assessed by ^{31}P NMR spectroscopy and compared to other phosphines. Experiments were carried out by dissolving 20 mg of each compound in aerated $CDCl_3$ in a vial open to air. The solutions were kept uncapped and static, and a proton-coupled ^{31}P NMR spectrum was obtained (3 s relaxation delay, NOE effects removed) immediately to record any initial oxidation, and then at intervals over 120 h. The sample solutions were stored in uncapped NMR tubes for the duration of the experiment. The following points summarise the key findings:

- The primary pyrenylphosphine **$L_{4.1}$** (SOMO energy = –9.58 eV) oxidised around 20% over the duration of the experiment, and the secondary and tertiary pyrenylphosphines **$L_{4.2}$-$L_{4.3}$** showed no sign of oxidation.

- The following phosphines were found to be persistent (i.e., showed <1% oxidation) in solution after 120 h, (SOMO energies given in brackets): $P(C_6F_5)_3$ (–10.50 eV), P(*o*-tolyl)$_3$ (–9.52 eV), $PhPMe_2$ (–10.42 eV), 2-dicyclohexylphosphino-2',4',6'-tri-isopropylbiphenyl (XPhos) (–9.21 eV), and (2,4,6-tri-tert-butylphenyl)phosphine (Mes*PH_2) (–10.28 eV).

- It is surprising that $P(C_6F_5)_3$ and $PhPMe_2$ were not oxidised during the experiment as their SOMO energies are below the –10 eV threshold while, as expected, P(*o*-tolyl)$_3$ was stable to air oxidation.

In addition to $\mathbf{L_{4.1}}$ and $\mathbf{L_{4.2}}$ showing minimal air-oxidation in solution over 120 h, the primary and secondary pyrenylphosphine complexes **4.14** and **4.17** are completely stable in solution over a period >3 months as determined by no change in their $^{31}P\{^{1}H\}$ and ^{1}H NMR spectra. With a greater understanding of the luminescence and stability properties of pyrenylphosphines $\mathbf{L_{4.1}}$-$\mathbf{L_{4.3}}$, further investigation into what makes a phosphine ligand stable is warranted.

4.6 Conclusions

It has been shown that 1-bromopyrene is a suitable precursor for the synthesis of primary, secondary, and tertiary 1-pyrenylphosphines $\mathbf{L_{4.1}}$-$\mathbf{L_{4.3}}$. The secondary phosphine $\mathbf{L_{4.2}}$ can either be synthesised in a three-step (one-pot) procedure via aminophosphine **4.6** and chlorophosphine **4.7**, or by formation of the pyrenyl Grignard reagent **4.4** and reaction with diethylphosphite to give the SPO **4.5** followed by reduction. As the number of pyrenyl substituents on the phosphine increases, the solubility in common organic solvents decreases. As a result, this renders the synthesis of bidentate pyrenylphosphines difficult, with only $\mathbf{L_{4.4}}$ being reported and shown to coordinate to Ru(II). As previously observed with tris(1-naphthyl)phosphine, the solution phase chemistry of $\mathbf{L_{4.3}}$ is limited as it forms a highly insoluble solvate with chlorinated solvents, and we struggled to study its chemistry further in non-chlorinated solvents, such as hexane, benzene, and DMSO.

The primary and secondary pyrenyl phosphines $\mathbf{L_{4.1}}$-$\mathbf{L_{4.2}}$ cleanly form mononuclear Ru complexes when reacted with $[(p\text{-cymene})RuCl_2]_2$. The coordination behaviour has been explored spectroscopically and for **4.14** by single crystal X-ray diffraction. Intermolecular π–π interactions are observed in the solid state, and the structural parameters agree with similar interactions observed in other pyrene-containing molecules. These complexes are ideal candidates for further P–H bond modification, and reactions to the corresponding phosphinidine complexes could shed more light on the ligand coordination properties.

The photophysical properties of pyrenylphosphines and their Ru complexes have been explored spectroscopically and by supporting TD-DFT calculations. In CH_2Cl_2, there is a modest increase in emission intensity upon oxidation of $\mathbf{L_{4.2}}$ to **4.5** (Φ_f = 14% and 18% respectively). However, an intense fluorescence quenching effect is observed when coordinating $\mathbf{L_{4.1}}$-$\mathbf{L_{4.2}}$ to Ru, which is attributed to non-radiative decay processes of the excited state due to the proximity of the metal centre to the pyrene chromophore.

Due to the extended π-systems of the pyrenylphosphines they display superior air-stability compared to phenylphosphines. This has been investigated by experimental and theoretical studies which show the SOMO energies of pyrenylphosphine radical cations to be high in energy in line with other air-stable primary and secondary phosphines.

4.7 Future work

The synthesis of a bidentate pyrenylphosphine ligand with –PPh(Pyr) substituents could afford the desired photophysical properties without the solubility and coordination difficulties associated with –P(Pyr)$_2$ groups. The synthesis was attempted from PhClPCH$_2$CH$_2$PClPh and several resonances were observed in the *in situ* $^{31}P\{^1H\}$ NMR spectrum, of which about 55% of the mixture was two singlet resonances (δ_P = –24.3 and –24.5 ppm) which were tentatively assigned to the *rac*- and *meso*- forms of the ligand. Recrystallisation of the crude material did not improve the purity. Further development of methods to synthesise bidentate pyrenylphosphines with alkyl or solubilising linkers would be worthwhile.

An exploration of the photophysical properties of these ligands and complexes by using higher level DFT calculations to optimise the excited state geometries may lead to a better understanding of the significant metal coordination quenching effect which could direct ligand design to phosphines with fluorescence sensing applications, for example as a sensitive method for catalyst detection.

In an ongoing collaboration with Dr. Natalie Fey (University of Bristol) and Dr. Lee Higham (Newcastle University), the aim is to explore air-stability descriptors for a large set of phosphines from the Ligand Knowledge Base (LKB). The hope is that this would lead to reliable predictions of ligand air-stability based on calculations.

Chapter 5. Non-symmetric PCP metallacycles for alkylation catalysis

5.1 Introduction

There have been numerous reports describing pincer complexes as versatile catalysts for many types of organic transformations such as transfer hydrogenation, Heck and Suzuki–Miyaura cross-coupling, hydroamination, allylic alkylation, and many more.[124] Since the pioneering work on cyclometalated phosphine pincer complexes by Shaw *et al.* and amine pincer complexes by van Koten *et al.* in the 1970s, chemists have exploited the tunability of pincer complexes to develop many thousands of variants.[276,277] This is due to the many points of derivatisation available, such as the donor atoms and substituents, backbone structure, metal centre, and ancillary ligands. The area of transition metal pincer complexes has been extensively reviewed.[124,145,278] A Web of Science search for "pincer complex" (articles and reviews, conducted February 2021) shows the rapid increase in reports that started in the late 1990s (Figure 5.1). In contrast, a Web of Science search for "non-symmetric pincer" returns only 22 reports, and this field has not experienced anything like the exponential growth over the last two decades. Of the 5,000+ reports on pincer complexes, fewer than five (~0.1% of the total) concern phosphine complexes with non-symmetric metallacycles. Considering the few early reports on non-symmetric pincer complexes show promising results for highly active catalysts, this underexplored area of organometallic chemistry has considerable scope for development. In this chapter, a series of symmetric and non-symmetric *PCP*-pincer complexes and an evaluation of their activity in catalytic allylic alkylation is reported.

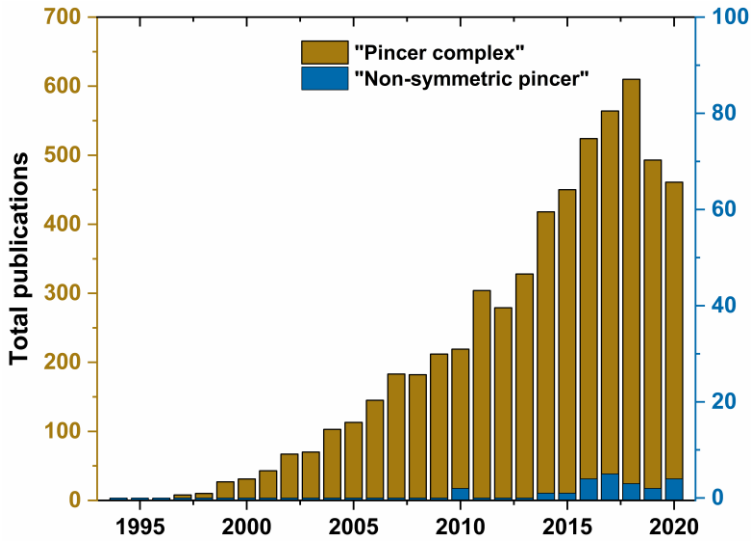

Figure 5.1. Web of Science, total publications by year for "pincer complex" and "non-symmetric pincer" (articles and reviews), search conducted February 2021.

Most pincer complexes are derived from C_{2v} symmetric ligands which give rise to complexes with two fused 5-membered metallacycles (i.e., 5,5-metallacycles). Very few examples with non-symmetric metallacycles are known due to lengthy ligand syntheses. Although several non-symmetric examples containing two different donor atoms are known, the least developed class of pincer complexes are those that contain two metallacycles of different size (see 5,6-metallacycles, Figure 5.2). The inclusion of non-symmetric metallacycles allows modulation of the ligand bite angle and more flexible derivatives have been shown to have superior catalytic properties compared to more rigid 5,5-metallacyclic systems.[144]

5.1.1 Non-symmetric pincer ligands

Figure 5.2 shows the different sized *PCP*-pincer complexes with examples of symmetric (5,5-, 6,6- and 7,7-metallacyclic) and non-symmetric (4,5-, and 5,6-metallacyclic) systems. For additional examples, including larger metallacycles, see the recent reviews of Morales-Morales *et al.*[126,127] It is worth noting that the only known examples of 5,6-metallacycles are either bis-phosphite or mixed phosphine-phosphite Pd complexes, reported by Eberhard *et al.*[144,279] There are no literature examples of 4,5- or 4,6-metallacyclic *PCP*-pincer complexes or all-carbon based 5,6-metallacycles as depicted in Figure 5.2.

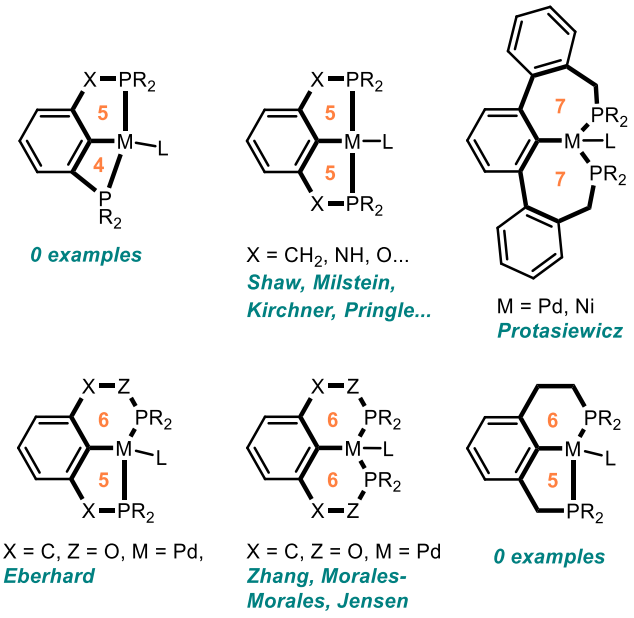

Figure 5.2. The different sized metallacycles discussed in this Chapter. L = ancillary ligand.

In the 2018 review from Crabtree *et al.*,[124] the authors noted that there were very few examples of pincer ligands with non-symmetric metallacycles, only highlighting the 5,6-Pd(II) bis-phosphite complex studied by Eberhard and co-workers 15 years previously.[144]

5.1.2 Applications of pincer complexes in medicine and catalysis

Due to the enhanced thermal stability that pincer complexes display compared to many other organometallic complexes, they have been widely used in biological and catalytic contexts. The following examples demonstrate the enhanced reactivity that may be gained when using larger, non-symmetric metallacycles.

Zhang *et al.* reported P-chiral ligands that would result in the formation of 6,6-metallacycles. The ligands were applied in Pd-catalysed asymmetric allylic alkylation of 1,3-diphenyl-2-propenyl acetate with dimethyl malonate (Scheme 5.1).[280] Under the conditions used, high yields (90–99%) and moderate enantioselectivities (50–75% ee) were achieved. The authors reported the observation of a singlet resonance in the ^{31}P NMR spectrum (δ_P = 18.7 ppm) of the reaction mixture for the reaction between $[(\eta^3\text{-}C_3H_5)PdCl_2]_2$ and the *PNP*-pincer ligand, implying two chemically equivalent phosphine environments. No further coordination chemistry of these ligands has been reported. The ligands were also applied in Ru-catalysed asymmetric hydrosilylation which resulted in high yields (85–98%) and modest enantioselectivities (47–66%). The authors did not report any coordination studies on the Ru pincer complexes.[281]

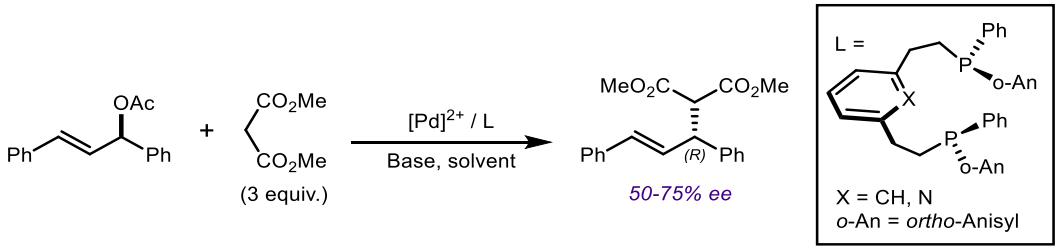

Scheme 5.1. P-chiral ligands reported by Zhang *et al.* for asymmetric allylic alkylation catalysis.[280]

Both symmetric and non-symmetric metallacycles have been used as cytotoxic agents against many cancer cell lines. Novel, bimetallic Au(III) 5,5-metallacycles that contain a Pd(II) diphosphine moiety have been investigated for activity against some cisplatin-resistant human cancer cell lines.[282] The high activity of the complexes was attributed to the inhibition of thioredoxin reductase and glutathione reductase, which in turn caused cell death by apoptosis. In addition, a series of Pd(II) pincer complexes based on amino acid functionalised picolinylamide ligands has been reported to be highly cytotoxic to several human cancer cell lines.[283] Of these palladacycles that contain *NNN*- and *NNS*-donors, some of the most active variants are 5,6-metallacycles (Figure 5.3).

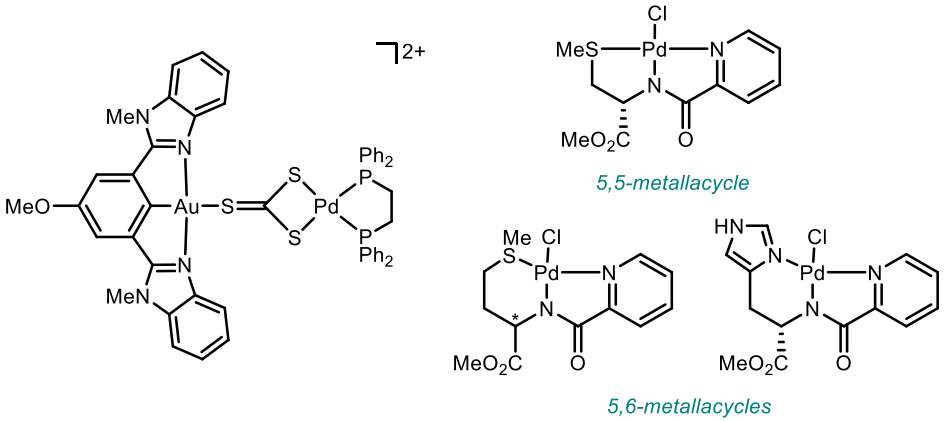

Figure 5.3. Representative examples of cytotoxic Au and Pd pincer complexes.[282,283]

Milstein *et al.* studied the difference in reactivity between a 'normal' 5,5-metallacyclic Pt(II) complex and the 'long-arm' variant (5,6-metallacyclic Pt(II) complex, Scheme 5.2).[284,285] The hemilability of the 6-membered amine chelate was implicated in the quantitative formation of a trimeric Pt cluster when the *PCN*-Pt(II) pincer complex was reduced with H_2 (5 atm.) at 65 °C, (Scheme 5.2). Under the same conditions, the 'normal' 5,5-metallacycle was found to be completely inert, demonstrating the influence of the amine arm length on hemilability.

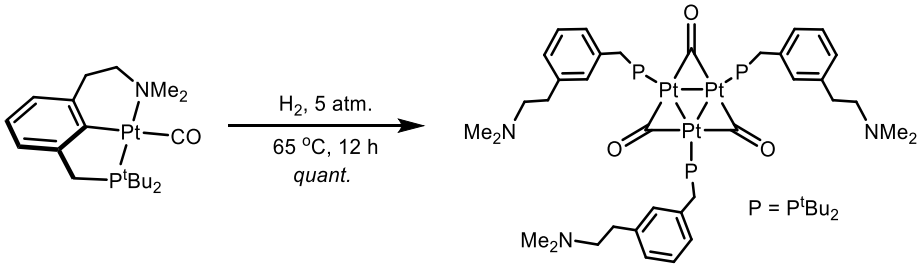

Scheme 5.2. Example of studies investigating metallacycle ring size of *PCN*-Pt(II) complexes reported by Milstein *et al.*[285]

The groups of van Leeuwen and Kamer published a series of studies detailing the effect of diphosphine bite angle in Pd-catalysed allylic alkylation.[286–290] For the alkylation of 2-hexenylacetate with sodium diethyl(methyl)malonate, the authors employed catalysts derived from $[Pd(DBA)_2]$ and diphosphine. As the ligand bite angle increased, a slight decrease in catalytic activity was observed, coupled with a stronger preference for the linear alkylation product 2-(2-hexen-1-yl)-2-methylmalonate (Scheme 5.3).[286] For the largest bite angle Pd diphosphine complex employing Xantphos (bite angle = 110°), exclusive formation of the linear product was observed, which was attributed to a steric effect of the diphosphine embracing the allyl fragment, thus inhibiting formation of the branched regioisomer. Despite the increased selectivity towards the linear products with

catalysts derived from the widest bite angle ligands Xantphos (110°) and Sixantphos (106.5°), the reaction rate for these catalysts was diminished. The best linear selectivity while maintaining high catalyst activity was achieved with the moderately wide bite angle ligand DPEPhos (102.7°).

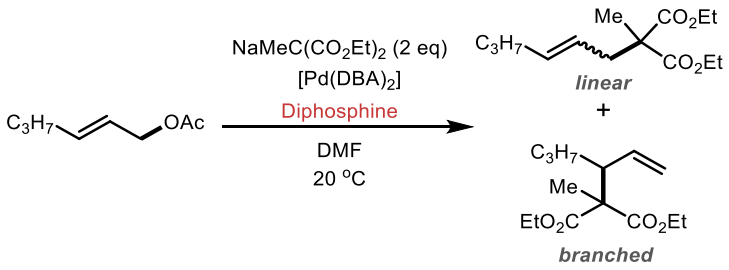

Diphosphine	Bite angle (°)	Linear (%)
dppe	78.1	96.2
dppp	86.2	96.6
dppb	98.6	97.7
dppf	99.1	99.0
DPEPhos	102.7	99.7
Sixantphos	106.5	99.6
Xantphos	110.0	100.0

Scheme 5.3. Allylic alkylation of 2-hexenylacetate with sodium diethyl methylmalonate catalysed by Pd(II) pincer complexes, reported by van Leeuwen *et al.*[286]

In a later study, Kamer *et al.* reported a series of DPEPhos ligands modified with chiral carboxylic acid or ether auxiliaries.[291] The asymmetric induction of these new ligands was assessed in Pd-catalysed asymmetric allylic alkylation, where moderate enantioselectivities (up to 70% ee) were achieved when using cyclohexyl-2-enyl acetate as the substrate with dimethyl malonate as the nucleophile.

A structure-activity relationship for symmetric 5,5- and non-symmetric 5,6-metallacyclic Pd(II) pincer complexes was reported by Eberhard *et al.* (Scheme 5.4).[144,279] This was the first report of a Pd(II) pincer complex being used as a catalyst for this alkylation reaction. The pincer complexes were applied as catalysts for the alkylation of cinnamyl acetate with sodium dimethyl malonate and the regioselectivity was found to be sensitive to the ligand structure. The more flexible 5,6-metallacycles were found to be far more active catalysts than the 5,5-metallacycles while maintaining high linear to branched product ratios (up to 95 : 5 linear selectivity). The authors reported that the synthesis of the analogous Pd(II) complexes with two 6-membered metallacycles was not successful. It was predicted that 6,6-metallacycles would show even higher catalytic activity in allylic alkylation.

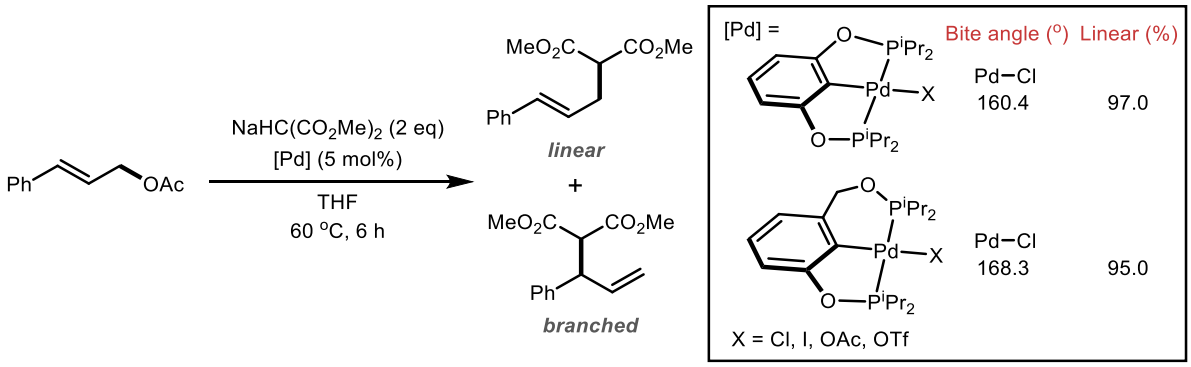

Scheme 5.4. Allylic alkylation of cinnamyl acetate with sodium dimethyl malonate catalysed by Pd(II) pincer complexes, reported by Eberhard *et al.*[144,280]

5.1.3 Research aims

In order to investigate the effect of metallacycle ring size on the Pd coordination chemistry and catalytic activity of organometallic pincer complexes, we aimed to:

- Synthesise pincer complexes with both symmetric and non-symmetric metallacycles (Figure 5.4).

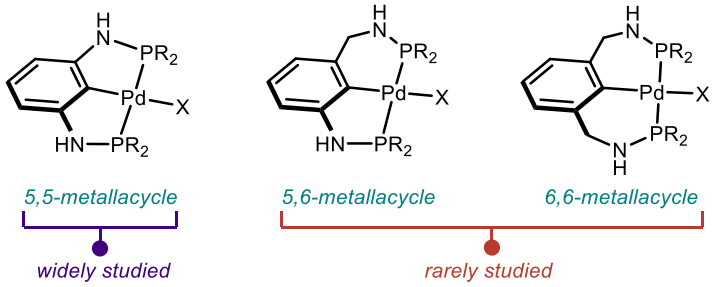

Figure 5.4. Chemical structures of the aminophosphine 5,5-, 5,6-, and 6,6-metallacycles discussed in this chapter.

- Analyse the structural features of the more rarely studied derivatives and compare these to known 5,5-metallacycles.
- Target an all-carbon backbone pincer ligand that would result in 5,6-metallacycles.
- Develop structure-activity relationships for aminophosphine organopalladium pincer complexes as catalysts in the allylation of dimethylmalonate, and to compare our novel derivatives to the current state-of-the-art catalysts.

5.2 Synthesis of ligands and precursors

5.2.1 Aminophosphine ligands

5.2.1.1 From 1,3-diaminobenzene

The symmetric aminophosphine ligand **L5.1**, previously prepared by Liu and co-workers for use in Ir-catalysed transfer hydrogenation, was prepared from deprotonation of 1,3-diaminobenzene with ^{n}BuLi followed by reaction with $^{t}Bu_2PCl$ at elevated temperature (Scheme 5.5).[131] After the reported reaction time of 16 h, the *in situ* $^{31}P\{^{1}H\}$ NMR spectrum showed that only 63% of the mixture corresponded to the desired product. Full consumption of the starting material to give **L5.1** was achieved after 48 h under reflux. After precipitation of the LiCl with pentane, **L5.1** was isolated in 78% yield with the $^{31}P\{^{1}H\}$ NMR chemical shift matching the literature value (δ_P = 58.2 ppm).

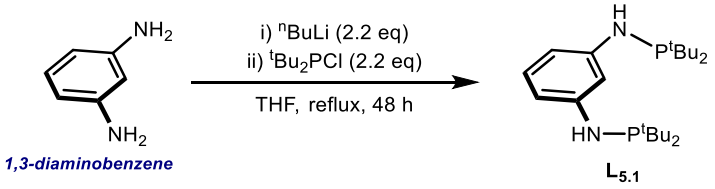

Scheme 5.5. Synthesis of symmetric aminophosphine ligand **L5.1**.[131]

5.2.1.2 From 3-aminobenzylamine

The analogous reaction was performed with 3-aminobenzylamine (Scheme 5.6). After full consumption of $^{t}Bu_2PCl$, the *in situ* $^{31}P\{^{1}H\}$ NMR spectrum showed the clean formation of the new ligand **L5.2** in 72% yield, comparable to the symmetric variant **L5.1**.

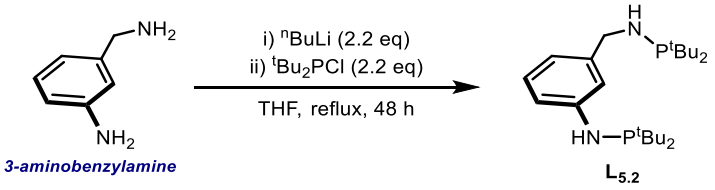

Scheme 5.6. Synthesis of non-symmetric aminophosphine ligand **L5.2**.

The ligand was characterised by two singlet resonances for **L5.2** (δ_P = 81.6 and 59.3 ppm). The resonance for the C_6H_4–NH–P$^{t}Bu_2$ phosphine agrees with **L5.1**, and the resonance for the CH_2–NH–P$^{t}Bu_2$ phosphine is ~21 ppm further downfield. As expected, the two phosphorus nuclei do not observably couple to each other as they are seven bonds apart.

In the ^{1}H NMR spectrum, two overlapping doublets corresponding to the two sets of P^{t}Bu$_2$ protons are seen (δ_H = 1.13 and 1.10 ppm). In addition, each of the four aryl-C–H protons, as well as the benzylic hydrogens can be distinguished.

In the ^{13}C{^{1}H} NMR spectrum for **L$_{5.2}$**, the magnitudes of the J_{CP} coupling constants are of note. There are two doublet resonances corresponding to the two sets of -C(CH_3)$_3$ substituents (δ_C = 28.2 ppm (d, $^{2}J_{CP}$ = 15 Hz)) and δ_C = 28.5 ppm (d, $^{2}J_{CP}$ = 15 Hz)). Next, the -PC(CH$_3$)$_3$ carbons give two doublet resonances (δ_C = 34.3 ppm (d, $^{1}J_{CP}$ = 19 Hz)) and δ_C = 34.4 ppm (d, $^{1}J_{CP}$ = 19 Hz)) with only slightly larger coupling than the $^{2}J_{CP}$ coupling constants. The -CH$_2$ carbon gives a doublet resonance (δ_C = 55.2 ppm (d, $^{2}J_{CP}$ = 30 Hz)) with a larger coupling constant than the other $^{2}J_{CP}$ and $^{1}J_{CP}$ couplings.

5.2.1.3 From *m*-xylylenediamine

The ligand precursor to 6,6-metallacyclic complexes was prepared from the reaction with *m*-xylylenediamine (Scheme 5.7). Deprotonation of both amine groups with ^{n}BuLi gave a purple suspension. After full consumption of ^{t}Bu$_2$PCl, the *in situ* ^{31}P{^{1}H} NMR spectrum showed the clean formation **L$_{5.3}$** containing one singlet resonance (δ_P = 81.6 ppm), almost identical to the resonance for the CH$_2$–NH–P^{t}Bu$_2$ phosphine of **L$_{5.2}$**. In the ^{1}H NMR spectrum, the symmetry of the molecule results in just three aryl-C–H signals and one benzylic hydrogens environment.

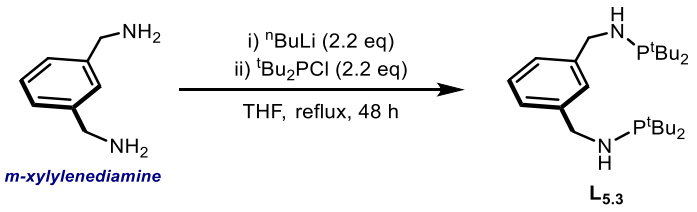

Scheme 5.7. Synthesis of symmetric aminophosphine ligand **L$_{5.3}$**.

5.2.1.4 Less bulky phosphine substituents

The reactions highlighted above can be extended to other chlorophosphines, with ^{i}Pr$_2$PCl and Ph$_2$PCl also forming the desired aminophosphine pincer ligands following deprotonation with either ^{n}BuLi or 4-dimethylaminopyridine (DMAP) (Scheme 5.8). With this series of nine 5,5-, 5,6-, and 6,6-ligands **L$_{5.1}$-L$_{5.9}$** in hand, we could investigate the influence of metallacycle size and phosphorus substituent on the coordination behaviour and catalytic activity.

For the synthesis of all-carbon backbone pincer ligands that would result in 5,6- and 6,6-metallacycles (compounds **5.4**-**5.7** and **L$_{5.10}$**) see Section 5.6.2.

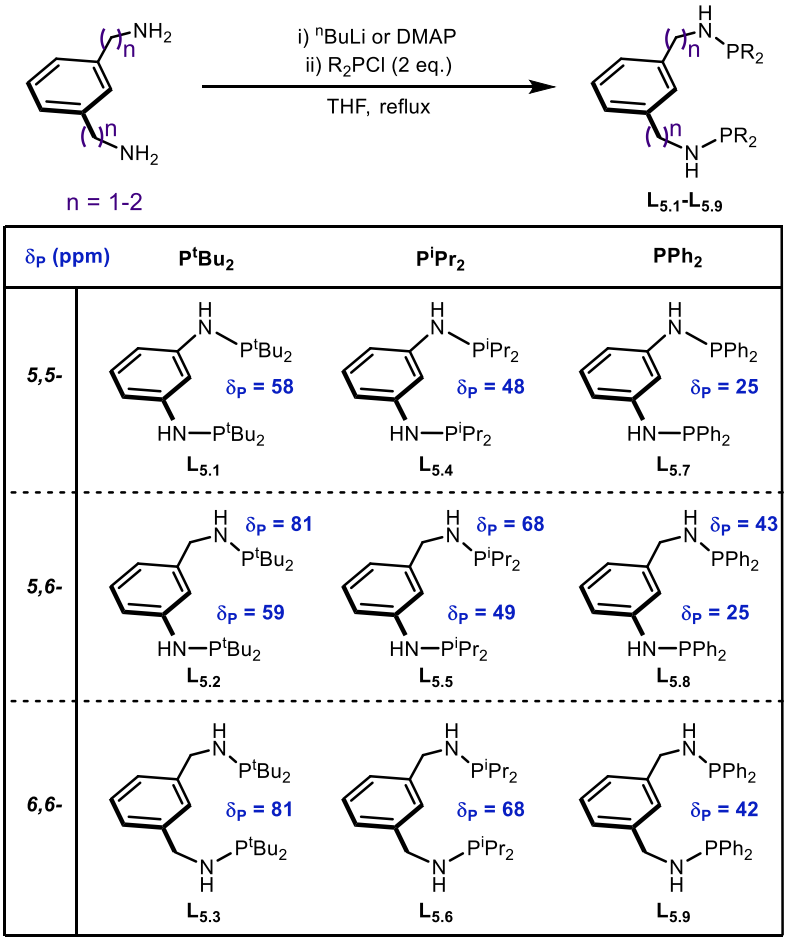

Scheme 5.8. Synthesis of aminophosphine ligands **$L_{5.1}$-$L_{5.9}$**, shown with $^{31}P\{^{1}H\}$ NMR chemical shifts.

5.3 Pd coordination chemistry

We started our study with the Pd coordination of the P^{t}Bu$_2$ substituted aminophosphine ligands **$L_{5.1}$-$L_{5.3}$**. The symmetrical pincer **$L_{5.1}$** was reacted in a 1:1 molar ratio with [$PdCl_2$(cod)] in toluene under reflux for 18 h (Scheme 5.9). Analysis of the *in situ* $^{31}P\{^{1}H\}$ NMR spectrum showed a singlet resonance (δ_P = 119.5 ppm) assigned to the pincer complex **5.8**. The formation of the 5,5-metallacycle is associated with a large coordination chemical shift ($\Delta\delta_P$ = 61.3 ppm). As with the free ligands, the symmetry of the molecule means there are only two aryl-C–H resonances in the ^{1}H NMR spectrum. Formation of the desired Pd–Cl complex was confirmed by comparison to the previously reported NMR and HR-MS data.

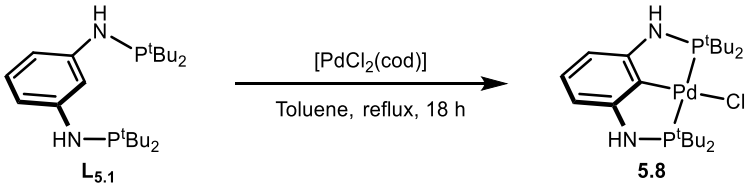

Scheme 5.9. Formation of 5,5-Pd–Cl complex **5.8**.

The coordination of the 5,6-P^{t}Bu$_2$ ligand $\mathbf{L_{5.2}}$ is surprisingly facile compared to $\mathbf{L_{5.1}}$. Immediately upon addition of a dichloromethane solution of $\mathbf{L_{5.2}}$ to [PdCl$_2$(NCPh)$_2$], the *in situ* ^{31}P{^{1}H} NMR spectrum showed the expected AB pattern consisting of two doublet resonances with large coupling constants ($^2J_{PP}$ = 406 Hz) assigned to **5.9** (Scheme 5.10). The coordination of the inequivalent phosphorus nuclei (which do not show coupling to each other in the free ligand) now give a large coupling constant, characteristic of the phosphines arranged in a *trans* geometry. The $^2J_{PP}$ coupling constant falls within the normal range for related Pd complexes.[144,279] The different chelate ring sizes have a significant influence on the coordination chemical shift which, for the 6-membered metallacycle is small ($\Delta\delta_P$ = 8.2 ppm), and for the 5-membered metallacycle is large ($\Delta\delta_P$ = 63.0 ppm), in agreement with the $\Delta\delta_P$ for complex **5.8**.

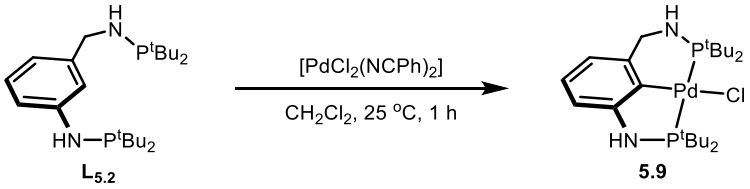

Scheme 5.10. Formation of 5,6-Pd–Cl complex **5.9**.

Crystals of **5.9** suitable for X-ray diffraction were grown by evaporation of a concentrated solution of **5.9** in dichloromethane at room temperature (Figure 5.5). The molecular structure showed bond lengths that fall within the typical range for similar complexes, with Pd1–P2 (in the 6-membered ring) slightly longer than Pd1–P1 (2.3436(4) vs. 2.3096(4) Å). The complex adopts a distorted square planar geometry with the 6-membered metallacycle in a boat conformation and the 5-membered metallacycle in an envelope conformation. From the front-on view of the structure, a significant deviation from planarity can be seen from the P1–Pd1–P2 bond angle (161.693(14)°) which holds the P^{t}Bu$_2$ groups significantly above and below the aryl-Pd–Cl plane.

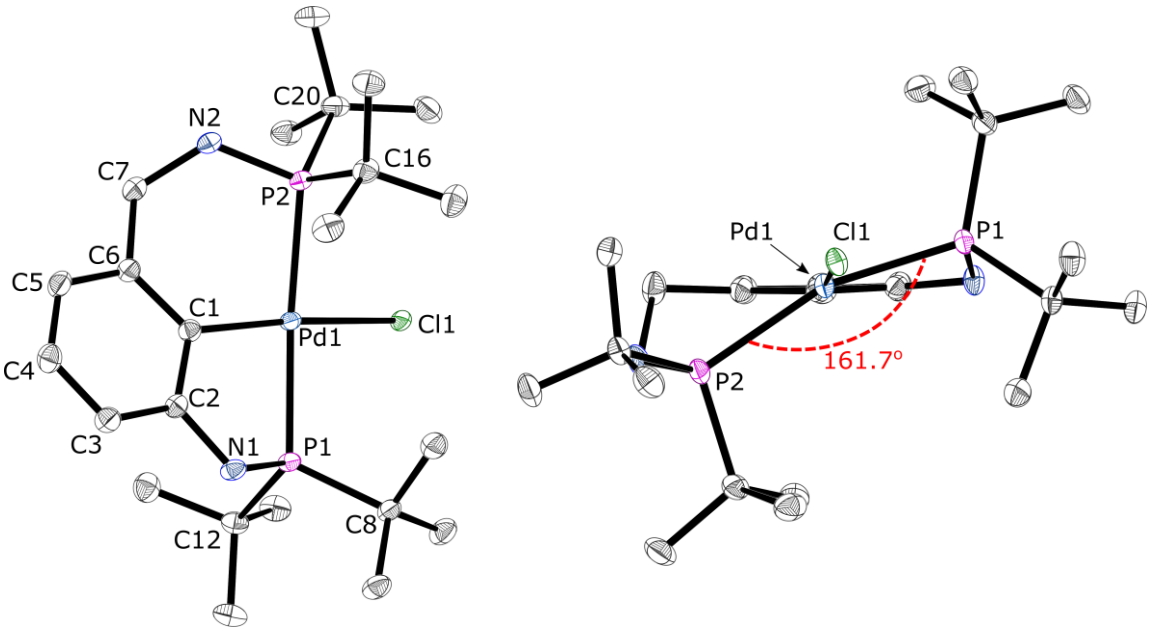

Figure 5.5. Single crystal X-ray crystallography structure of **5.9** (side view and front-on view). Hydrogen atoms have been omitted for clarity. Thermal ellipsoids at 50% probability level. Selected bond lengths (Å) and angles (°): Pd1–Cl1 2.4171(3), Pd1–P1 2.3096(4), Pd1–P2 2.3436(4), Pd1–C1 2.0392(14); Cl1–Pd1–P1 94.460(12), Cl1–Pd1–P2 94.674(12), P1–Pd1–P2 161.693(14), C1–Pd1–Cl1 172.96(4), C1–Pd1–P1 81.70(4), C1–Pd1–P2 90.67(4).

Clearly, there is a difference in kinetics of the C–H bond activation of $\mathbf{L}_{5.1}$ and $\mathbf{L}_{5.2}$ by Pd with 5,5-metallacycle formation requiring elevated temperature and extended reaction time while the 5,6-metallacycle formation occurs rapidly at room temperature. Therefore, we anticipated the formation of a symmetric 6,6-metallacycle to be rapid. We began by taking a solution of $\mathbf{L}_{5.3}$ and [$PdCl_2$(cod)] in toluene and heating (Scheme 5.11), at which point a yellow solution with some insoluble material was observed.

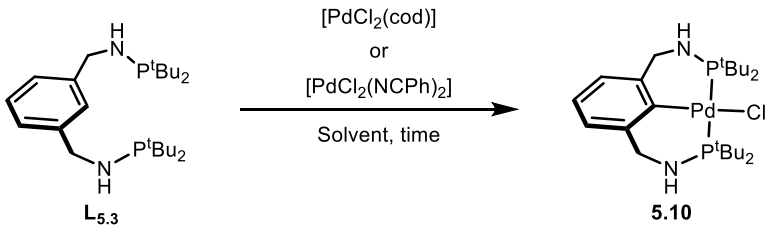

Scheme 5.11. Reactions for the attempted formation of 6,6-Pd–Cl complex **5.10**.

The *in situ* $^{31}P\{^1H\}$ NMR spectrum of the toluene solution showed a singlet resonance in the expected region (δ_P = 88 ppm), as well as an additional resonance attributed to the unreacted ligand. However, ESI-MS did not detect the desired complex in the mixture. Next, we tried to synthesise **5.10** by reaction of $\mathbf{L}_{5.3}$ with [$PdCl_2$(NCPh)$_2$] as the Pd

precursor. When either dichloromethane or toluene were used, the same two broad signals (δ_P = 78 and 79 ppm) were observed in the *in situ* $^{31}P\{^1H\}$ NMR spectra. Analysis of the reaction mixture from **L5.3** and $[PdCl_2(NCPh)_2]$ in dichloromethane by HR-ESI-MS, the molecular ion corresponding to $[M–H]^{\bullet+}$ for the 6,6-metallacycle (**5.10**) (m/z 563.1713) with the expected palladium and chlorine isotope pattern was detected. However, the $^{31}P\{^1H\}$ NMR spectrum of the isolated complex (following precipitation from hexane) showed a sharp singlet resonance (δ_P = 79.6 ppm) which when compared to the ligand gives an upfield coordination chemical shift of ~2 ppm and was tentatively assigned to the expected complex.

This unexpected coordination chemical shift and limited solubility of the isolated complex led us to assign the product to a diphos-bridged polymeric material. When repeating the reaction between **L5.3** and $[PdCl_2(cod)]$ in toluene under reflux (Scheme 5.11), after 4 h, the *in situ* $^{31}P\{^1H\}$ NMR spectrum showed a singlet resonance in the expected region (δ_P = 89 ppm). This time, after removal of the volatiles, extraction of the resulting solid into hexane provided the expected complex **5.10** with a characteristic downfield coordination chemical shift, consistent with forming a 6-membered metallacycle ($\Delta\delta_P$ = 8.3 ppm). HR-ESI-MS also confirmed formation of the desired complex with the molecular ion corresponding to $[M–H]^{\bullet+}$ for **5.10** observed (m/z 563.1713) with the expected palladium and chlorine isotope pattern. In conclusion, due to the formation of a coordination polymer, the symmetric 6,6-Pd–Cl complex was more difficult to synthesise than the non-symmetric 5,6-Pd–Cl complex, contrary to our predictions.

Analysis of the ^1H NMR spectra was also indicative of the formation of the desired pincer complexes (Figure 5.6). In each case, formation of the pincer complex caused a downfield shift of the $P(C(CH_3)_3)_2$ resonances of ~0.5 ppm accompanied by a change in the splitting. In the case of the free ligands, the signals are doublets due to coupling to one ^{31}P nucleus. Upon coordination, the $P(C(CH_3)_3)_2$ resonances are apparent triplets for **5.8** and **5.10**, as the protons are split by two P nuclei, and are overlapping doublets in the case of **5.9**. The aromatic region of the ^1H NMR spectra are also informative, with the spectra for the 5,5-metallacycle showing three aryl C–H resonances for the free ligand **L5.1** and two for the complex **5.8**. For the non-symmetric 5,6-metallacycle, the free ligand **L5.2** clearly has four distinct aryl C–H resonances and the complex **5.9** has three. For the symmetric 6,6-metallacycle, the free ligand **L5.3** contains three aryl C–H resonances and only two for the complex **5.10** (Figure 5.6). In the ^1H NMR spectrum for **5.10** there are two resonances for the $P(C(CH_3)_3)_2$ each of which integrates for 18H (δ_H = 0.98 ppm (t, $^3J_{HP}$ = 7 Hz) and

1.60 ppm (t, $^{3}J_{HP}$ = 7 Hz)), indicating their chemical inequivalence, despite the complex being symmetric.

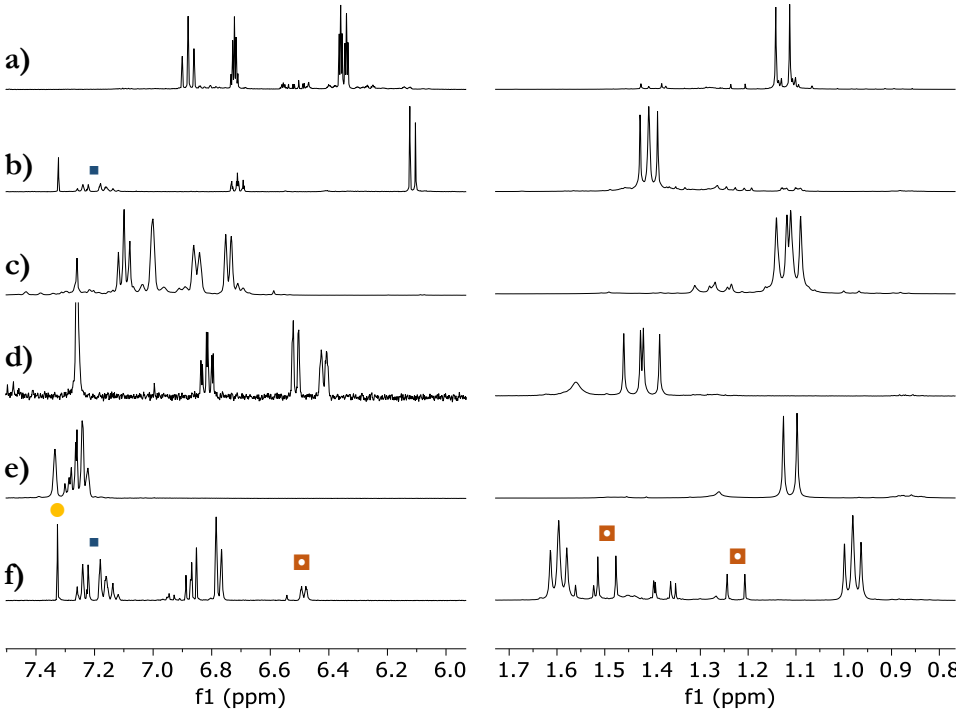

Figure 5.6. Selected regions of the ^{1}H NMR spectra for a) **L**$_{5.1}$, b) **5.8**, c) **L**$_{5.2}$, d) **5.9**, e) **L**$_{5.3}$, f) **5.10**. ▪ = $[PdCl_2(NCPh)_2]$, ● = $CDCl_3$, ◘ = unknown impurity.

Colourless crystals of **5.10** suitable for X-ray diffraction were grown by slow evaporation of its concentrated hexane solution at room temperature (Figure 5.7).

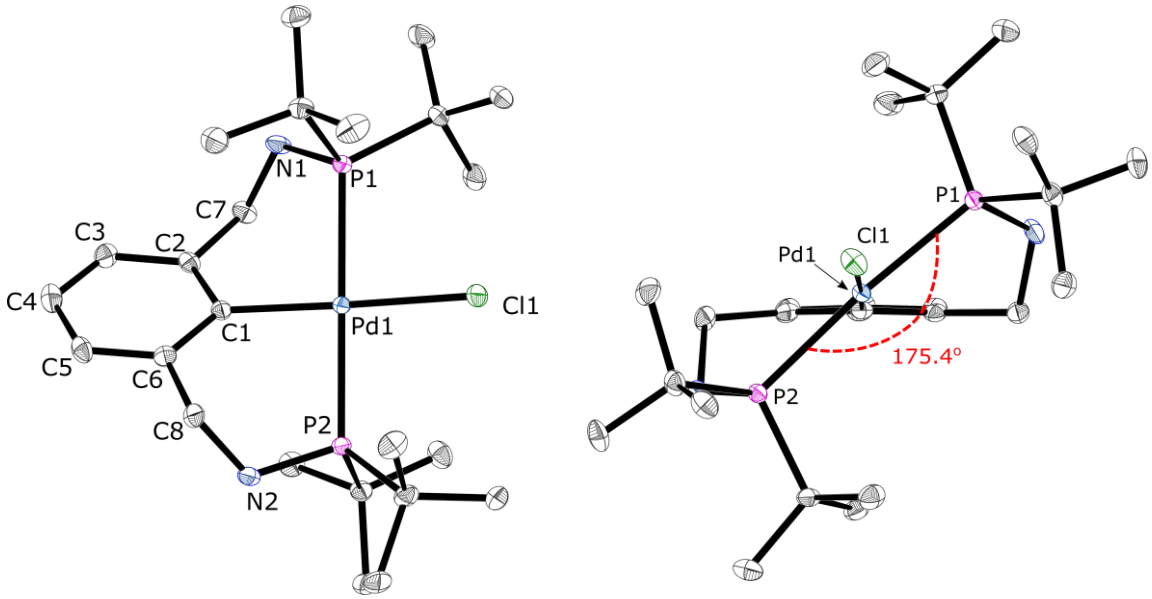

Figure 5.7. Single crystal X-ray crystallography structure of **5.10** (side view and front-on view). Hydrogen atoms have been omitted for clarity. Thermal ellipsoids at 50% probability level. Selected bond lengths (Å) and angles (°): Pd1–Cl1 2.3812(5), Pd1–P1 2.3631(5), Pd1–P2 2.3382(5), Pd1–C1 2.0580(18); P1–Pd1–Cl1 89.437(17), P2–Pd1–Cl1 92.083(18), P2–Pd1–P1 175.400(18), C1–Pd1–Cl1 174.86(5), C1–Pd1–P1 89.96(5), C1–Pd1–P2 88.91(5).

Due to the two methylene groups in the ligand backbone, the P^{t}Bu$_2$ substituents are held high above and below the aryl-Pd–Cl plane. The crystal structure of **5.10** (Figure 5.7) shows the conformation of the ring is half chair with pseudo axial and equatorial ^{t}Bu groups and the NMR inequivalence implies that conformational fluxionality is slow on the NMR timescale. This could be the reason for inequivalent P(C(CH_3)$_3$)$_2$ protons in the solution ^{1}H NMR spectrum. Due to the additional methylene unit in the ligand backbone, the bite angle (P1–Pd1–P2) for **5.10** is relaxed to 175.4° which is ~14° larger than for the non-symmetric 5,6-metallacycle **5.9**. This bite angle is greater than the one reported for 5,6-P^{i}Pr$_2$ Pd–Cl complex reported by Eberhard (P–Pd–P = 168.3°), which, in turn, is ~8° larger than the analogous 5,5-P^{i}Pr$_2$ Pd–Cl complex (P–Pd–P = 160.4°, see Scheme 5.4).[144]

The Pd–P bond lengths in **5.10** (2.3631(5) and 2.3382(5) Å) are comparable to the Pd1–P2 bond length for the 6-membered metallacycle of complex **5.9** (2.3436(4) Å, see Table 5.1). In **5.9**, the Pd–P bond length of the 5- membered metallacycle is significantly shorter (2.3096(4) Å), presumably to accommodate the extra ring strain.

Table 5.1. Selected bond lengths (Å) and bond angles (°) in 5,6-metallacycle (**5.9**) and 6,6-metallacycle (**5.10**).

Bond	5,6-Pd–Cl (**5.9**) (Å)	6,6-Pd–Cl (**5.10**) (Å)
Pd1–Cl1	2.4171(3)	2.3812(5)
Pd1–P1	2.3096(4)	2.3631(5)
Pd1–P2	2.3436(4)	2.3382(5)
Pd1–C1	2.0392(14)	2.0580(18)
Angle	5,6-Pd–Cl (**5.9**) (°)	6,6-Pd–Cl (**5.10**) (°)
P1–Pd1–Cl1	94.460(12)	89.437(17)
P2–Pd1–Cl1	94.674(12)	92.083(18)
P1–Pd1–P2	161.693(14)	175.400(18)
C1–Pd1–Cl1	172.96(4)	174.86(5)

We encountered difficulties when attempting to form non-symmetric 5,6- and symmetric 6,6-Pd–Cl metallacycles using ligands with less bulky phosphorus substituents than P^{t}Bu$_2$ (e.g., P^{i}Pr$_2$ and PPh$_2$). In the attempted synthesis of complexes derived from P^{i}Pr$_2$ ligands **L$_{5.5}$-L$_{5.6}$** and PPh$_2$ ligands **L$_{5.8}$-L$_{5.9}$**, mixtures containing very insoluble precipitates were obtained (Scheme 5.12).[292]

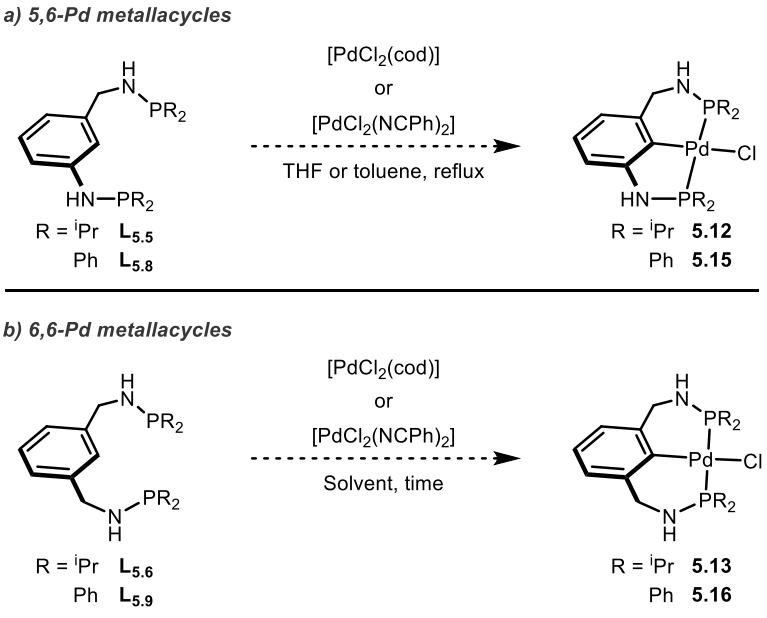

Scheme 5.12. a) Reactions for the attempted formation of 5,6-Pd–Cl complexes **5.12** and **5.15**. b) Reactions for the attempted formation of 6,6-Pd–Cl complexes **5.13** and **5.16**.

The *in situ* $^{31}P\{^1H\}$ NMR spectra of the mixtures from the attempted synthesis of **5.12** and **5.15** did display the expected AB pattern along with unknown impurities. In both

cases, the isolated material was highly insoluble. Analysis by HR-ESI-MS confirmed the formation of non-symmetric 5,6-metallacycles (m/z = 459.1321 for P^iPr_2 (**5.12**) and m/z = 595.0683 for PPh_2 (**5.15**)). The difficulties associated with the formation of monomeric Pd–Cl complexes has been documented in the literature.[144,293] For a related 5,5-bis(phosphite) *PCP*-pincer ligand, Pringle *et al.* reported that coordination to $[PdCl_2(NCPh)_2]$ was very slow under thermal conditions. Over the course of 6 days under reflux in 1,2-dichloroethane, the observed polymeric material very slowly dissolved to form the desired complex in 77% yield (Scheme 5.13). The slow reaction rate was enhanced by performing the reaction under microwave conditions at 150 °C in 1,2-dichloroethane (92% yield after 1 h).

In another example, Eberhard *et al.* noted that when attempting to form the 6,6-Pd bis(phosphite) *PCP*-pincer complex with P^iPr_2 substituents, only polymeric species were recovered, and a successful synthesis was not reported (Scheme 5.13).[144]

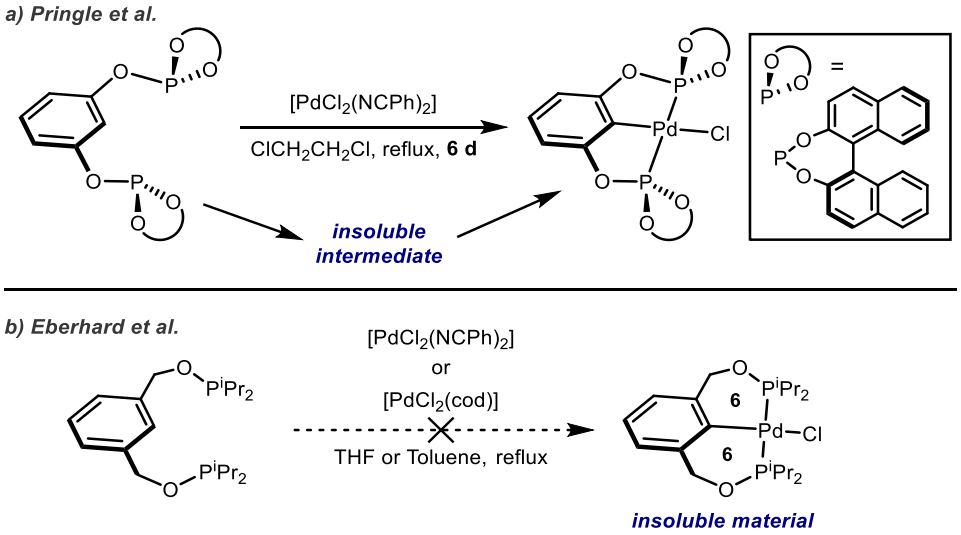

Scheme 5.13. a) Pringle *et al.* previously reported the synthesis of a 5,5-Pd bis(phosphite) *PCP*-pincer complex via insoluble polymeric species.[293] b) Eberhard *et al.* attempted synthesis of 6,6-Pd bis(phosphite) *PCP*-pincer complex where only polymeric species were recovered.[144]

To investigate this interesting behaviour further, Pd(II) trifluoroacetate, $[Pd(TFA)_2]$ was used and found to be a suitable precursor to soluble, monomeric Pd–TFA complexes with any metallacycle size, and phosphine substituent. Moreover, these complexes form rapidly under mild conditions (25 °C, 20 min), rather than the harsh conditions required to form some Pd–Cl complexes (110 °C, 6 h) (Scheme 5.14).

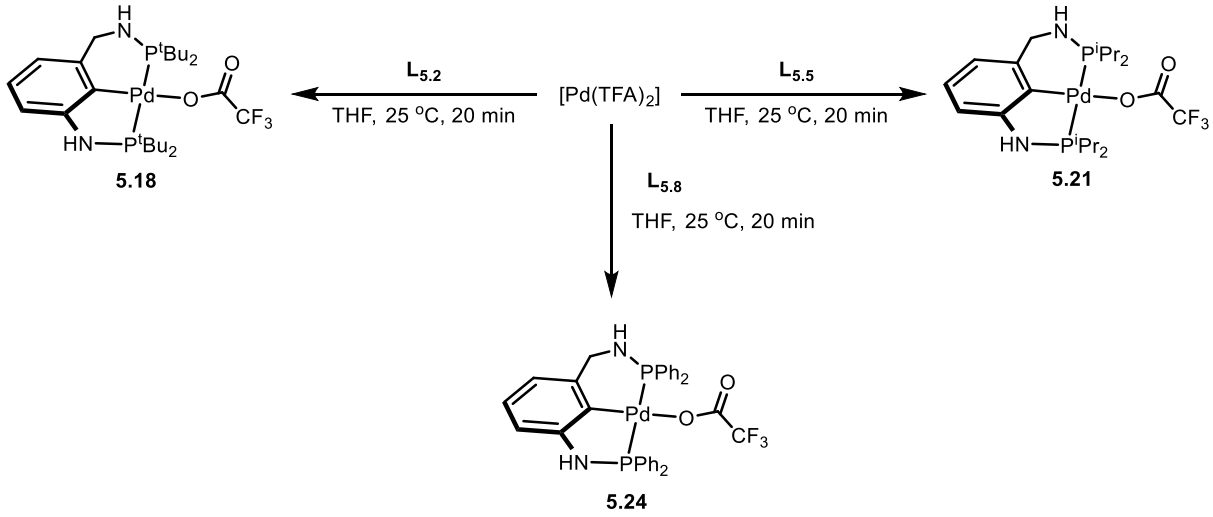

Scheme 5.14. Formation of 5,6-Pd–TFA complexes **5.18**, **5.21**, and **5.24**.

For the 5,6-metallacycles, the $^{31}P\{^1H\}$ NMR spectra exhibit the expected AB patterns (Figure 5.8). For the non-symmetric P^{i}Pr$_2$ complex **5.21**, $^2J_{PP}$ = 388 Hz, for the non-symmetric PPh$_2$ complex **5.24**, $^2J_{PP}$ = 447 Hz and for the non-symmetric P^{t}Bu$_2$ complex **5.18**, ($^2J_{PP}$ = 367 Hz). For **5.18**, the $^2J_{PP}$ is considerably smaller than in the analogous Pd–Cl complex **5.10** ($^2J_{PP}$ = 406 Hz). This trend in coupling constants for 5,6-Pd–TFA complexes ($^2J_{PP}$: P^{t}Bu$_2$ < P^{i}Pr$_2$ < PPh$_2$) reflects the *trans* influence of the phosphine donor substituents (i.e., two good σ-donating P ligands will mutually weaken their bonds to the metal leading to a smaller $^2J_{PP}$ coupling).

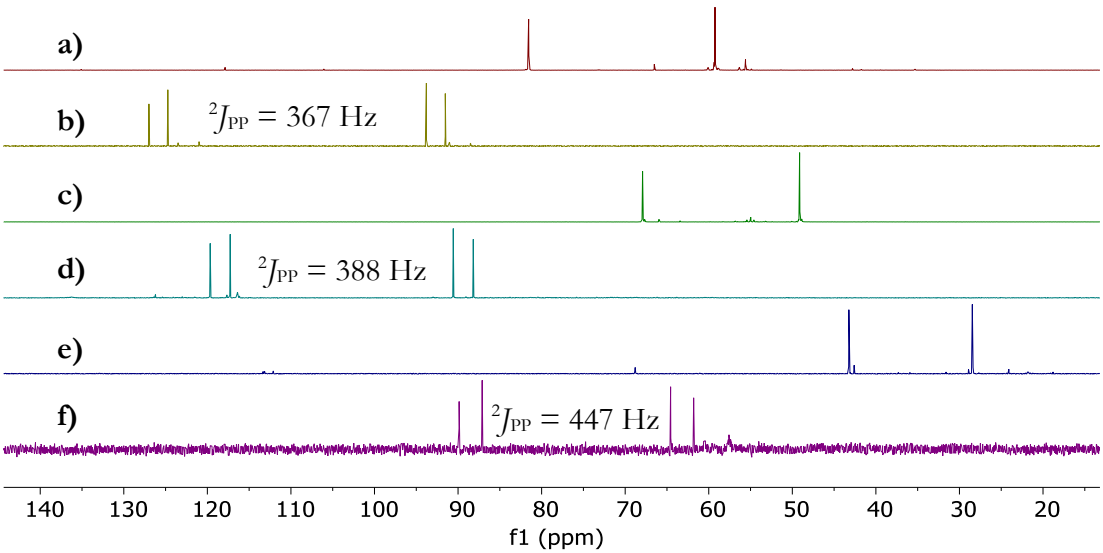

Figure 5.8. $^{31}P\{^1H\}$ NMR spectra for a) 5,6-P^{t}Bu$_2$ (**L**$_{5.2}$), b) **5.18**, c) 5,6-P^{i}Pr$_2$ (**L**$_{5.5}$), d) **5.21**, e) 5,6-PPh$_2$ (**L**$_{5.8}$), f) **5.24**.

The numbering schemes for Pd aminophosphine complexes with chloride or trifluoroacetate ligands are summarised in Figure 5.9. These complexes are stable to air,

moisture, and elevated temperatures (up to 100 °C), making them suitable catalysts for reactions that employ forcing conditions. We did not observe hydrolysis of the P–N bonds for any of these complexes by $^{31}P\{^{1}H\}$ NMR spectroscopy, even in solvents that were not rigorously dried.

	P^tBu_2		P^iPr_2		PPh_2	
	$L_{5.1}$		$L_{5.4}$		$L_{5.7}$	
5,5-	[($L_{5.1}$)PdCl]	**5.8**	[($L_{5.4}$)PdCl]	**5.11**	[($L_{5.7}$)PdCl]	**5.14**
	[($L_{5.1}$)Pd(TFA)]	**5.17**	[($L_{5.4}$)Pd(TFA)]	**5.20**	[($L_{5.7}$)Pd(TFA)]	**5.23**
	$L_{5.2}$		$L_{5.5}$		$L_{5.8}$	
5,6-	[($L_{5.2}$)PdCl]	**5.9**	[($L_{5.5}$)PdCl]	**5.12**	[($L_{5.8}$)PdCl]	**5.15**
	[($L_{5.2}$)Pd(TFA)]	**5.18**	[($L_{5.5}$)Pd(TFA)]	**5.21**	[($L_{5.8}$)Pd(TFA)]	**5.24**
	$L_{5.3}$		$L_{5.6}$		$L_{5.9}$	
6,6-	[($L_{5.3}$)PdCl]	**5.10**	[($L_{5.6}$)PdCl]	**5.13**	[($L_{5.9}$)PdCl]	**5.16**
	[($L_{5.3}$)Pd(TFA)]	**5.19**	[($L_{5.6}$)Pd(TFA)]	**5.22**	[($L_{5.9}$)Pd(TFA)]	**5.25**

Figure 5.9. Summary of Pd aminophosphine complexes.

For the formation of the 5,6-P^tBu_2 complex, as well as the main set of resonances assigned to the Pd–TFA complex **5.18** ($^2J_{PP}$ = 367 Hz), a second pair of doublets corresponding to the Pd–Cl complex **5.9** (~2% of the mixture by $^{31}P\{^{1}H\}$ NMR spectroscopy) was observed ($^2J_{PP}$ = 406 Hz, Figure 5.10). We assumed that this chloride impurity could come from the palladium(II) trifluoroacetate (97%) commercial starting material as the reagent is prepared by reaction of $PdCl_2$ with aqueous hydrochloric acid, then sodium hydroxide solution, followed by treatment with excess trifluoroacetic acid. For the case of the P^iPr_2 and PPh_2 complexes, although the same batch of [Pd(TFA)$_2$] was used, the Pd–Cl impurity was not detected.

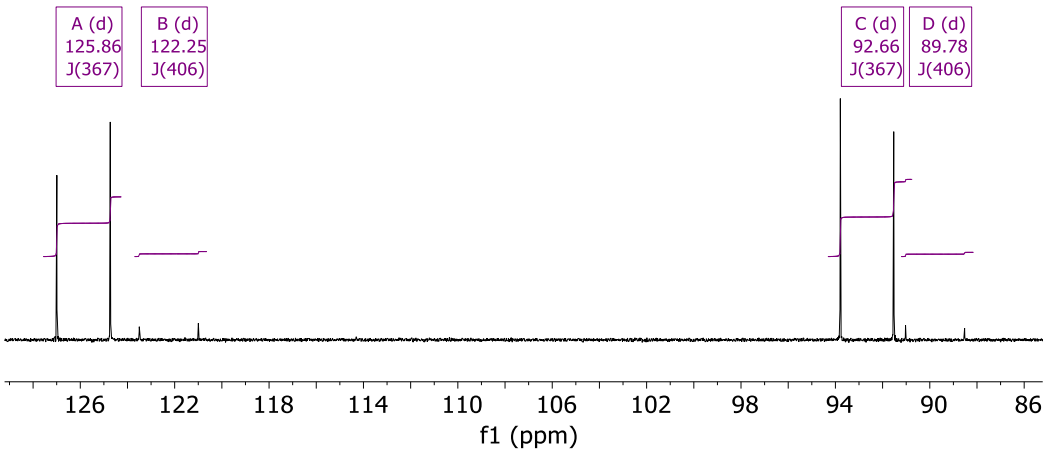

Figure 5.10. $^{31}P\{^{1}H\}$ NMR spectrum for the isolated material 5,6-P^{t}Bu$_2$ Pd–TFA complex **5.18**, with Pd–Cl **5.9** impurity.

The formation of soluble 6,6-metallacyclic Pd–TFA complexes was also possible using the corresponding 6,6-ligand $\mathbf{L_{5.3}}$ and [Pd(TFA)$_2$] at room temperature (Scheme 5.15). For the P^{t}Bu$_2$ substituted ligand this corresponded to a small downfield coordination chemical shift ($\Delta\delta_P$ = 11 ppm), thus clarifying the previously ambiguous result of the formation of Pd–Cl complex **5.10** (see Scheme 5.11). Initially a $\Delta\delta_P$ of ~2 ppm upfield was observed, but after extraction of **5.10** into hexane, we found a more expected coordination shift ($\Delta\delta_P$ = 8 ppm).

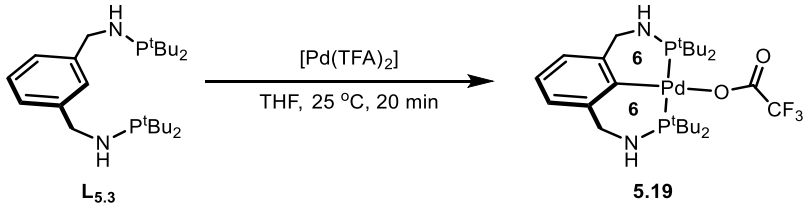

Scheme 5.15. Formation of 6,6-Pd–TFA complex **5.19**.

The weakly bound nature of the trifluoroacetate ligand was evident in the ESI-MS experiments. For the non-symmetric 5,6-P^{t}Bu$_2$ Pd–TFA complex **5.18**, a minor peak corresponding to the $[M–H]^{\bullet+}$ ion was present (m/z = 627.1703), but the most abundant ion detected was due to loss of trifluoroacetate, $[M–TFA]^{\bullet+}$ (m/z = 515.1991) upon ionisation. It is proposed that a weakly bound ligand in this position could lead to a more active catalyst, where an incoming substrate may bind to the Pd centre following ligand dissociation in this position.

A summary of the NMR spectroscopy data for $\mathbf{L_{5.1}}$-$\mathbf{L_{5.9}}$ and associated Pd complexes is given in Table 5.2.

Table 5.2. Selected $^{31}P\{^{1}H\}$ NMR spectroscopy data for **$L_{5.1}$-$L_{5.9}$** and associated Pd aminophosphine complexes.

Compound number	Ligand/Complex	δ_P / ppm[a]	$\Delta\delta_P$[b]	$^2J_{PP}$ / Hz
$L_{5.1}$	5,5-P^{t}Bu$_2$	58.2[c]	–	–
5.8	[(**$L_{5.1}$**)PdCl]	119.5[c]	61.3	–
5.17	[(**$L_{5.1}$**)Pd(TFA)]	119.9[c]	61.7	–
$L_{5.2}$	5,6-P^{t}Bu$_2$	81.6, 59.3	–	–
5.9	[(**$L_{5.2}$**)PdCl]	122.2, 89.7	62.9, 8.1	406
5.18	[(**$L_{5.2}$**)Pd(TFA)]	125.9, 92.7[c]	66.6, 11.1	367
$L_{5.3}$	6,6-P^{t}Bu$_2$	81.6	–	–
5.10	[(**$L_{5.3}$**)PdCl]	89.9[c]	8.3	–
5.19	[(**$L_{5.3}$**)Pd(TFA)]	92.7[c]	11.1	–
$L_{5.4}$	5,5-P^{i}Pr$_2$	46.0[c]	–	–
5.11	[(**$L_{5.4}$**)PdCl]	114.3[c,e]	68.3	–
$L_{5.5}$	5,6-P^{i}Pr$_2$	67.9, 49.1[c]	–	–
5.21	[(**$L_{5.5}$**)Pd(TFA)]	118.5, 89.4	69.4, 21.5	388
$L_{5.6}$	6,6-P^{i}Pr$_2$	68.0[c]	–	–
5.22	[(**$L_{5.6}$**)Pd(TFA)]	84.9	16.9	–
$L_{5.7}$	5,5-PPh$_2$	24.8[c]	–	–
5.14	[(**$L_{5.7}$**)PdCl]	76.9[d,e]	52.1	–
$L_{5.8}$	5,6-PPh$_2$	41.7, 25.0	–	–
5.24	[(**$L_{5.8}$**)Pd(TFA)]	88.5, 63.2	63.5, 21.5	447
$L_{5.9}$	6,6-PPh$_2$	42.7[c]	–	–
5.25	[(**$L_{5.9}$**)Pd(TFA)]	59.7	17.0	–

[a]Chemical shifts recorded in $CDCl_3$ and given in ppm. [b]Coordination chemical shifts ($\Delta\delta_P$) are relative to the free ligands ($\Delta\delta_P = \delta_P$(complex) – δ_P(ligand)). [c]NMR spectrum recorded in CD_2Cl_2. [d]NMR spectrum recorded in DMSO-d_6. [e]From reference 133.

5.4 Catalytic allylation of dimethylmalonate

5.4.1 Catalysis under standard conditions

With the set of symmetric and non-symmetric aminophosphine pincer ligands **$L_{5.1}$-$L_{5.9}$** in hand, we investigated their performance as ligands for catalysts for the allylation of dimethylmalonate. Using the conditions reported by Eberhard,[144] we employed two equivalents of sodium dimethylmalonate with respect to the limiting substrate cinnamyl acetate to push the reaction to high conversion (Scheme 5.16 and Table 5.3).

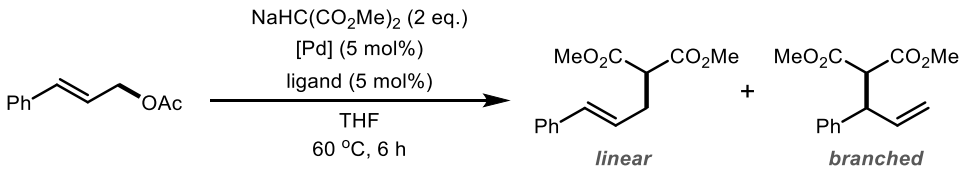

Scheme 5.16. Regioselectivity in the allylation of sodium dimethylmalonate.

Table 5.3. Catalytic allylation of dimethylmalonate under standard conditions.[a]

Entry	Ligand	% Conversion[b] with $[PdCl_2(NCPh)_2]$	% Linear selectivity	% Conversion[b] with $[Pd(TFA)_2]$	% Linear selectivity
1	5,5-^{t}Bu$_2$ **$L_{5.1}$**	17	>99	11	>99
2	5,5-^{i}Pr$_2$ **$L_{5.4}$**	>99	67	10	78
3	5,5-Ph$_2$ **$L_{5.7}$**	>99	94	>99	92
4	5,6-^{t}Bu$_2$ **$L_{5.2}$**	24	>99	48	91
5	5,6-^{i}Pr$_2$ **$L_{5.5}$**	>99	67	>99	69
6	5,6-Ph$_2$ **$L_{5.8}$**	>99	90	>99	91
7	6,6-^{t}Bu$_2$ **$L_{5.3}$**	>99	80	>99	80
8	6,6-^{i}Pr$_2$ **$L_{5.6}$**	>99	94	>99	66
9	6,6-Ph$_2$ **$L_{5.9}$**	>99	87	>99	89

[a]Reaction conditions: 0.5 mmol of cinnamyl acetate, 1.0 mmol of sodium dimethylmalonate, 2.5×10^{-2} mmol of [Pd], 2.5×10^{-2} mmol of ligand, in THF (total volume = 10 mL), 60 °C, 6 h. [b]Conversion and selectivity determined by GC-MS using dodecane as internal standard.

It should be noted that for the low conversion runs (<20%), the observed linear selectivity is very high (>99%). When the reaction was run without ligand, using either [Pd(TFA)$_2$], [PdCl$_2$(cod)], or [PdCl$_2$(NCPh)$_2$], the conversions were: <1%, 12%, and <1% respectively, indicating both a strong reliance on the pincer ligand for catalytic activity, as well as a modest amount of background activity for [PdCl$_2$(cod)]. Some trends can be discerned from the data presented in Table 5.3:

- The catalysts derived from 5,5- and 5,6-P^{t}Bu$_2$ substituted aminophosphine ligands (**L$_{5.1}$-L$_{5.2}$**) (Table 5.3, Entries 1 and 4) showed significantly lower activity (11–48% conversion) after 6 h than the ligands with smaller P^{i}Pr$_2$ and PPh$_2$ substituents.
- The 6,6-metallacyclic catalysts showed superior activity to the other metallacycle sizes, with all derivatives giving >99% conversion (Table 5.3, Entries 7-9).
- In general, PPh$_2$ substituents show the highest linear selectivity (87–94%), followed by P^{t}Bu$_2$ substituents (80–91%), followed by P^{i}Pr$_2$ substituents (66–69%). However, the 6,6-P^{i}Pr$_2$ (**L$_{5.6}$**) derived Pd–Cl catalyst afforded >99% conversion and 94% linear selectivity (Table 5.3, Entry 8), far higher than the average of the other P^{i}Pr$_2$ derivatives.

This intriguing result with **L$_{5.6}$** led us to investigate this highly active and selective catalyst further. We studied the catalytic activity of **L$_{5.6}$** with [Pd(TFA)$_2$] and [PdCl$_2$(NCPh)$_2$] monitoring the reaction after 2 h and varying the catalyst loading from 1.25–5 mol% and temperatures from 25–60 °C (Table 5.4). These results demonstrated the enhanced activity gained from using [Pd(TFA)$_2$] as Pd source, where at 60 °C, full conversion was achieved at 1.25 mol% whilst retaining good linear selectivity, compared with only 48% conversion when using the [PdCl$_2$(NCPh)$_2$] precursor (Table 5.4, Entry 3). Using [Pd(TFA)$_2$] and reducing the temperature to 40 °C did not decrease the conversion (>99% conversion over 2 h). Surprisingly, a slight reduction in linear selectivity (60%) was observed at the lower temperature (Table 5.4, Entries 4-6). Excellent linear selectivity (>99%) was restored by reducing the reaction temperature to 25 °C where, after 2 h, the reaction conversion was <10%. By extending the reaction time to 20 h, the 5 and 2.5 mol% runs had gone to ~50% conversion (Table 5.4, Entries 7-8).

Table 5.4. Catalytic allylation of dimethylmalonate using 6,6-P^{i}Pr$_2$ ligand **L$_{5.6}$** at various temperatures and catalyst loading.[a]

Entry	[Pd]/L mol%	T/ °C	% Conversion[b] with $[PdCl_2(NCPh)_2]$	% Linear selectivity	% Conversion[b] with $[Pd(TFA)_2]$	% Linear selectivity
1	5	60	>99	78	>99	67
2	2.5	60	95	87	>99	63
3	1.25	60	48	92	>99	78
4	5	40	–	–	>99	60
5	2.5	40	–	–	>99	60
6	1.25	40	–	–	>99	61
7	5	25	–	–	49[c]	>99
8	2.5	25	–	–	48[c]	96
9	1.25	25	–	–	12[c]	>99

[a]Reaction conditions: 0.5 mmol of cinnamyl acetate, 1.0 mmol of sodium dimethylmalonate, 2.5×10^{-2} – 6.25×10^{-3} mmol of [Pd], 2.5×10^{-2} – 6.25×10^{-3} mmol of **L$_{5.6}$**, in THF (total volume = 10 mL), 2 h. [b]Conversion and selectivity determined by GC-MS using dodecane as internal standard. [c]Reaction time 20 h.

5.4.2 Structure-activity relationships

The strong influence of metallacycle size and phosphine substituent on the linear selectivity of the alkylation product is not straightforward. Overall, some interesting trends were observed: (i) for the P^{t}Bu$_2$ and PPh$_2$ substituted ligands, the linear selectivity decreased as the metallacycle size is increased (5,5- > 5,6- > 6,6-); (ii) for P^{i}Pr$_2$ substituted ligands, the linear selectivity was low with linear-to-branched ratio of 2:1 for 5,5- and 5,6-metallacycles; the linear-to-branched ratio was dramatically greater at 15:1 for the 6,6-metallacycle; (iii) as the ligand bite angle increases (162° for 5,6-metallacycle **5.9** to 175° for 6,6-metallacycle **5.10**), we observe an increase in catalytic activity.

Through a short optimisation of temperature and catalyst loading, as well as variation of the Pd–X ancillary ligand from chloride to trifluoroacetate, we achieved significantly increased catalytic activity with good conversion and excellent linear selectivity (linear-to-branched ratio of >20:1) at ambient temperature.

5.4.3 Identifying unexpected alkylation product

The GC chromatogram (Figure 5.11) shows the outcome of the reaction (full consumption of cinnamyl acetate) run using the catalyst derived from [Pd(TFA)$_2$] and 6,6-P^{i}Pr$_2$ ligand **L$_{5.6}$** (Table 5.4, Entry 3). When the reaction proceeds to high conversion, another product (t = 11.3 min) is produced in significant quantities.

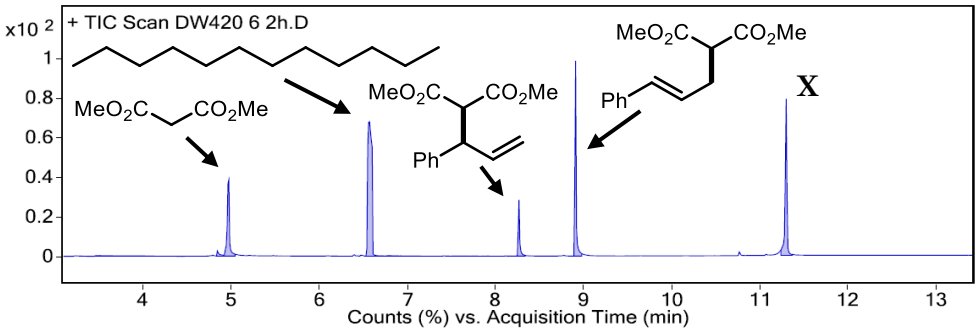

Figure 5.11. Representative GC chromatogram for the allylation of dimethylmalonate.

This unknown compound (**X**) was isolated from the post-reaction mixture by column chromatography and analysed by ^{1}H and ^{13}C NMR spectroscopy, HR-EI-MS and IR spectroscopy. The accurate mass for **X** (m/z = 304.1456) was found to be an exact match for $C_{21}H_{20}O_2$, seemingly a dimerisation product of cinnamyl acetate.

The Pd-catalysed dimerisation of cinnamyl acetate was reported by Garg *et al.* as a useful procedure for the synthesis of the fluorescent probe molecule, diphenylhexatriene (Scheme 5.17).[294] The reaction conditions they used gave the *Z*-triene in quantitative yield. Furthermore, these conditions were suitable to convert the branched isomer of cinnamyl acetate, as well as cinnamyl pivalate and cinnamyl chloride to diphenylhexatriene in high yield (70-95%). Cinnamyl carbonate was the only substrate tested which gave a low yield of diphenylhexatriene (27%).

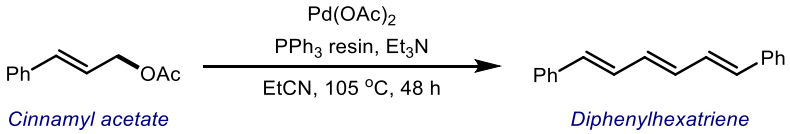

Scheme 5.17. Pd catalysed synthesis of diphenylhexatriene, Garg *et al.*[294]

Under our catalytic conditions, it is surprising that a cinnamyl acetate dimerisation product would form in a significant quantity since two equivalents of sodium dimethylmalonate were used. Moreover, the additions of the two substrates to the catalyst were carried out in quick succession before heating the reaction mixture to temperature.

The IR spectra (carbonyl region) for cinnamyl acetate, dimethyl malonate, the linear/branched allylation product, and **X** are shown in Figure 5.12. It is not conclusive that the unknown product **X** (ν(C=O) = 1731 and 1747 cm^{-1}) contains an acetate or malonate group, as the stretching frequency is comparable to both cinnamyl acetate (ν(C=O) = 1734 cm^{-1}) and dimethyl malonate (ν(C=O) = 1736 and 1754 cm^{-1}) carbonyl stretching frequencies.

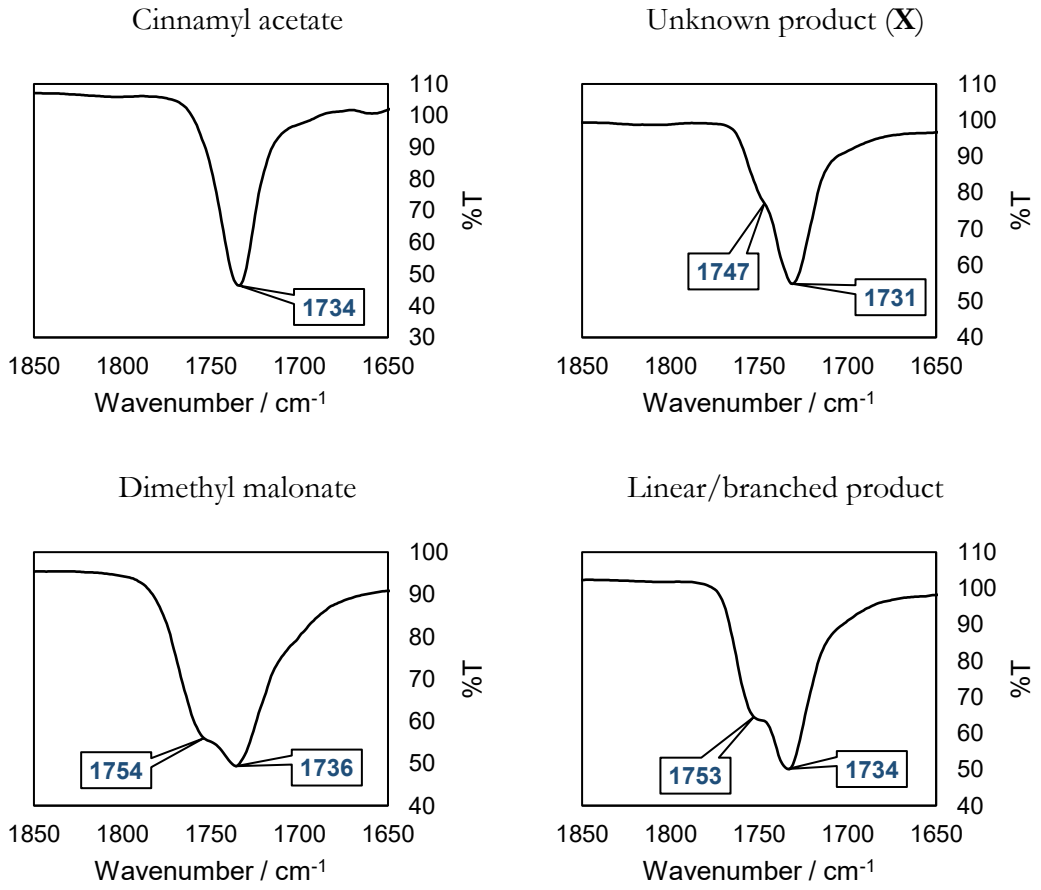

Figure 5.12. IR spectra (carbonyl region) of cinnamyl acetate, unknown product (**X**), dimethyl malonate, and the linear/branched allylation product.

The ^{1}H NMR spectra for cinnamyl acetate, the unknown **X**, and an analytical sample of methyl (*E*)-4-phenylbut-3-enoate are shown in Figure 5.13. It is apparent that **X** does not contain an acetate group, due to the lack of signals for the methyl protons at δ_H = 2.10 ppm and the methylene protons at δ_H = 4.73 ppm. The ^{1}H NMR spectrum of purified **X** appears to correspond to a symmetrical compound with 24 protons, which could be formed from di-allylation of dimethylmalonate. The signal for the methylene protons at δ_H = 2.85 ppm is further upfield than the methylene protons for (*E*)-4-phenylbut-3-enoate (δ_H = 3.26 ppm), consistent with being alpha to a quaternary carbon, rather than alpha to a carbonyl.

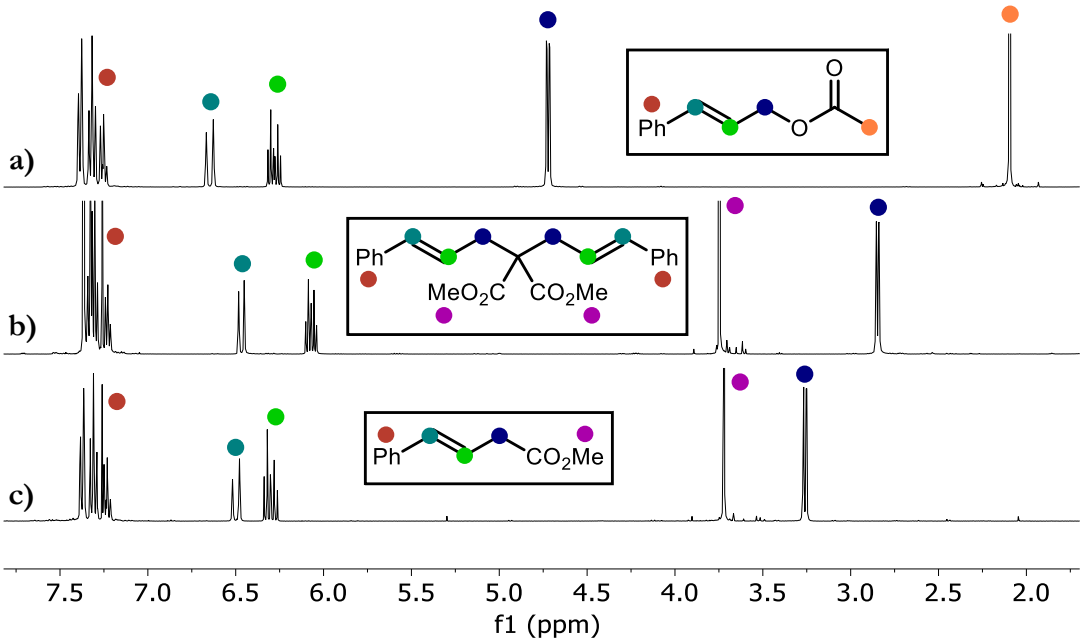

Figure 5.13. ^{1}H NMR spectra in $CDCl_3$ for a) cinnamyl acetate, and b) purified product **X**, and c) methyl (*E*)-4-phenylbut-3-enoate.

Initially, we were confused that the NMR spectroscopy and mass spectrometry data were not consistent for the proposed structure of this product. The observed accurate mass is consistent with loss of one CO_2Me group to give the $[M–CO_2Me]^{\bullet+}$ ion (m/z = 304.1456). All NMR spectroscopy data are in accord with the di-allylation product shown in Figure 5.13. It is still surprising that di-allylation occurs when the molar ratio of sodium dimethylmalonate to cinnamyl acetate is 2:1.

5.5 Conclusions

We have shown that aminophosphine ligands form palladacycles with 5,5-, 5,6-, or 6,6-membered rings (Figure 5.14), whose chemistry is sensitive to the phosphine substituents and whether the fourth ligand is Cl or CF_3CO_2 (TFA). The bulky P^tBu_2 ligands form very stable, soluble, monomeric Pd–Cl complexes in any of the three metallacycle sizes. When smaller P^iPr_2 of PPh_2 substituents are present, insoluble Pd-coordination polymers are produced. On switching the anionic ligand from chloride to trifluoroacetate, not only are the desired monomeric pincer complexes formed, but the C–H activation reaction is much more rapid and occurs under mild conditions. This provides access to highly active Pd(II) catalysts with a weakly bound TFA ligand and these have been applied in the catalytic allylation of dimethylmalonate.

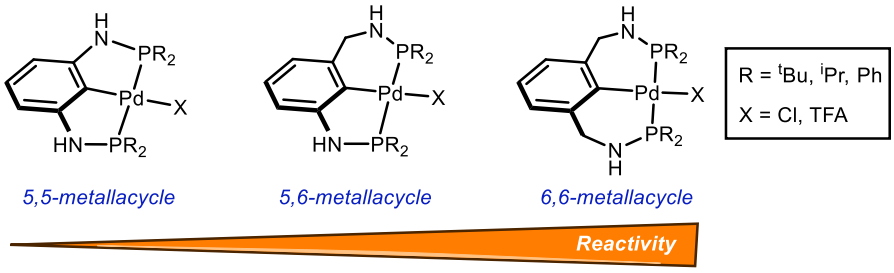

Figure 5.14. Aminophosphine Pd(II) pincer complexes discussed in this work.

Promising preliminary results indicate that the activity of these catalysts generally increases with increasing metallacycle size: 5,5- < 5,6- < 6,6-, which mirrors earlier studies of Eberhard *et al.* using pincer complexes derived from phosphinite donors. In addition, the linear selectivity for the allylation product is highest for PPh_2 substituted complexes; the most highly active and selective pincer catalyst discovered was with **L**$_{5.6}$ containing P^iPr_2 donors. Overall, we have discovered readily synthesised aminophosphine organopalladium pincer complexes that catalyse the allylation of dimethylmalonate with high activity and excellent linear selectivity under mild conditions.

5.6 Future work

There are three main strands that we propose should be pursued in future work building on the Pd-pincer complexes described above.

5.6.1 High-throughput screening

First, a high-throughput screening approach using the Chemspeed parallel synthesis platform should be applied to obtain a clearer picture of the factors that influence catalyst activity and selectivity. The parameters that would be varied would be the phosphine ligand structure (**L**$_{5.1}$-**L**$_{5.9}$), Pd source, catalyst loading, temperature, and solvent. This study may lead to a deeper understanding of the catalysis and then to logical developments for improving the design of new catalysts for the allylation reaction and indeed to other catalytic processes.

5.6.2 Attempted preparation of all-carbon-backbone pincer ligands

Secondly, all carbon-backbone non-symmetric pincer ligands could also be targeted that would compliment the range of aminophosphine and phosphite pincer ligands that have proved fruitful ligand classes for catalysis. This will require more work to develop phosphine syntheses from the non-symmetric ligand precursors that are required. To date, although many examples of all-carbon-backbone ligands that form symmetric

metallacycles exist, there are no reports of phosphine pincer complexes with non-symmetric metallacycles. This is most likely due to the high number of steps required to synthesise these ligands (see examples from Milstein[285] incorporating both NMe_2 and P^tBu_2 donor groups (Scheme 5.2) and examples from Eberhard[279] incorporating mixed phosphine-phosphinite donors (Scheme 5.4)).

Jensen *et al.* have shown that a 6,6-metallacyclic Pd–Cl complex with a bis(phosphinite) ligand is an effective catalyst for the Heck reaction (see Figure 5.2).[137] We were interested in phosphines that would give symmetric 6,6-metallacycles; therefore, the symmetric diol **5.5** was prepared by $LiAlH_4$ reduction of 1,3-$C_6H_4(CH_2CO_2H)_2$ **5.4**.[295] Next, tosylation using conditions reported by Sigman *et al.* with TsCl, NEt_3, and DMAP gave the novel bis-tosylate **5.6** (Scheme 5.18). Analogous chemistry could be carried out with the non-symmetric diol (see Scheme 5.18) reported by Mann *et al.*,[296] which is prepared in four steps from commercially available *m*-toluoyl chloride.

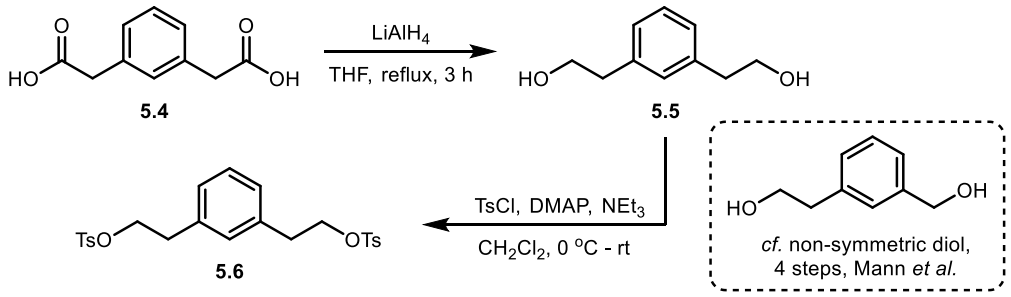

Scheme 5.18. Preparation of novel bis-tosylate ligand precursor **5.6**.

The OTs groups of **5.6** were displaced with two equivalents of $^tBu_2PLi(BH_3)$ to give the novel borane protected ligand **5.7** (Scheme 5.19). Removal of the borane groups required forcing conditions (DABCO, 10 equiv.), as simply stirring with the weaker base diethylamine was ineffective. The mechanism of phosphine borane deprotection has been studied by Lloyd-Jones and co-workers and they report that similarly harsh conditions are necessary to remove the borane groups from trialkyl phosphines.[297] Monitoring the deprotection by *in situ* $^{31}P\{^1H\}$ NMR spectroscopy over 18 h showed the disappearance of the broad signal at δ_P = 44.5 ppm (corresponding to phosphine-borane **5.7**) and a new sharp singlet at δ_P = 29.5 ppm (corresponding to the free phosphine $\mathbf{L_{5.10}}$).

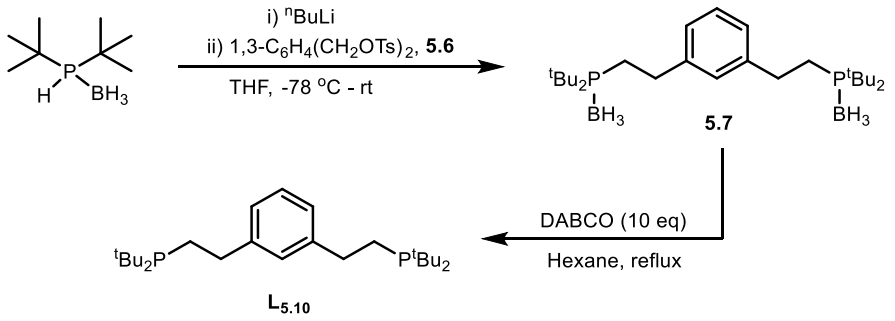

Scheme 5.19. Synthesis of 6,6-P^{t}Bu$_2$ ligand $\mathbf{L_{5.10}}$.

Due to the difficulties with phosphine-borane deprotection, only a small-scale preparation of $\mathbf{L_{5.10}}$ has been possible. The presence of excess DABCO prohibited successful Pd coordination of $\mathbf{L_{5.10}}$. When a solution of $\mathbf{L_{5.10}}$ was added to [PdCl$_2$(NCPh)$_2$], the solution instantly deposited a black precipitate, possibly due to DABCO reducing the Pd(II) to Pd(0). Due to the difficulties in forming non-symmetric all-carbon-backbone ligands from phosphine-borane precursors, these have not been tested in catalysis alongside aminophosphine ligands $\mathbf{L_{5.1}}$-$\mathbf{L_{5.9}}$.

5.6.3 Mechanism of allylic alkylation

Finally, the mechanism of allylic alkylation catalysed by Pd(II)-pincer complexes is not yet understood. This section is a discussion of the mechanism for allylic alkylation catalysed by *PCP*-Pd(II) pincer complexes and provides a commentary on related literature examples where Pd(0)/Pd(II) and Pd(II)/Pd(IV) redox cycles are proposed. In the study performed by Eberhard *et al.* utilising bis(phosphite)-Pd(II) pincer complexes, the alkylation of deuterated allylic acetate substrate resulted in products with a 1:1 ratio of C(sp^3)-deuteration and C(sp^2)-deuteration, implying the reaction proceeds through a symmetrical (η^3-allyl)Pd intermediate (Scheme 5.20).[144] In their study, it was not determined whether the X$^-$ ligand (chloride, acetate, or triflate) remained bound to Pd during the catalytic cycle, and neither a Pd(0)/Pd(II) nor a Pd(II)/Pd(IV) cycle was proposed.

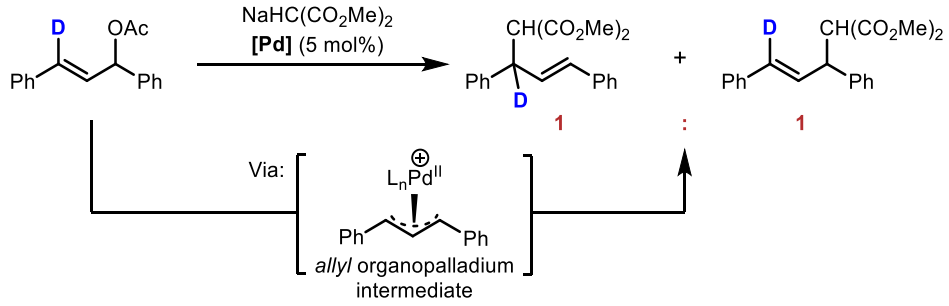

Scheme 5.20. Alkylation of deuterated allylic acetate, Eberhard *et al.*[144]

In 2004, Szabó and co-workers provided evidence for bis(phosphite)-Pd(II) pincer complex catalysed allylation of aldehydes and imines via (η^1-allyl)Pd intermediates.[298] In 2009, the Szabó group reported that Pd(II) pincer complexes could catalyse the coupling of alkenes with diaryliodonium salts via proposed aryl-Pd(IV) intermediates.[146] In the same year they reported allylic C–H acetoxylation via proposed (η^3-allyl)Pd(IV) intermediates.[147] On the basis of the observations from Szabó and from Eberhard, we propose that aminophosphine Pd(II) pincer complexes could catalyse allylic alkylation via (η^1-allyl)Pd(II) intermediates or via (η^3-allyl)Pd(IV) intermediates.

For the latter case, the properties of the *PCP*-pincer ligands (tridentate, rigid, monoanionic chelating ligand), may allow stabilisation of Pd(IV) intermediates. This led us to propose the following mechanism for allylic alkylation (Scheme 5.21): (i) oxidative addition of cinnamyl acetate to give an (η^1-allyl)Pd(IV) intermediate; (ii) η^3-allyl formation by deprotonation (loss of AcOH) to give a cationic (η^3-allyl)Pd(IV) intermediate; (iii) nucleophilic attack on the η^3-allyl predominantly at the less hindered terminus; (iv) product dissociation to complete the catalytic cycle.

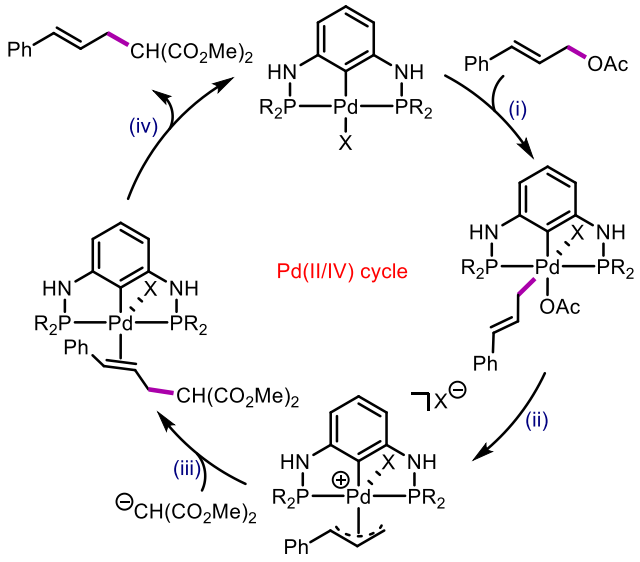

Scheme 5.21. Proposed catalytic cycle for allylic alkylation via (η^3-allyl)Pd(IV) intermediate.

Although the oxidative addition of cinnamyl acetate has not been observed with Pd(II) complexes, the formation of a Pd(IV) complex following oxidative addition with an allyl bromide was reported by Malinakova *et al.* (Scheme 5.22).[299] This work demonstrates that Pd(IV) oxidative addition complexes can be accessed without the use of strongly oxidising iodine(III) reagents.

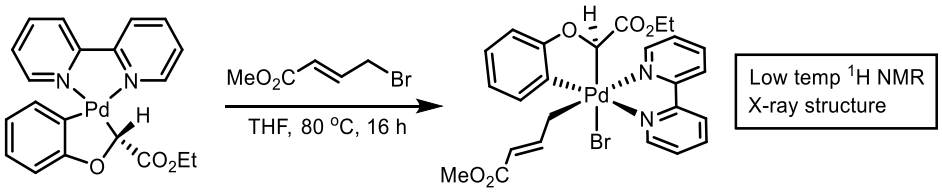

Scheme 5.22. Formation of (η^1-allyl)Pd(IV) complex via oxidative addition of Pd(II) complex with allyl bromide, Malinakova *et al.*[299]

Through further studies, it may be possible to observe whether Pd(IV) aminophosphine pincer complexes are viable intermediates under the catalytic conditions. This could then be extended to other allyl electrophiles and strongly oxidising iodonium salts to see if similar results to those of Szabó *et al.* are obtained.[146,147] Experimental mechanistic studies should be supported by a computational study of the mechanism, in particular the oxidative addition step to see if (η^1-allyl)Pd(II) or (η^3-allyl)Pd(IV) intermediates are realistic.

By carrying out the project extensions outlined above, it is hoped that a deeper understanding of the enhanced catalytic activity of larger palladacycles will be obtained.

Chapter 6. Experimental

6.1 General

Unless otherwise stated, all manipulations were carried out under an inert atmosphere (N_2) using standard Schlenk line techniques or in a glovebox (Ar). All glassware was oven-dried (200 °C) and cooled under vacuum prior to use. Unless otherwise stated, chemicals and reagents were purchased from commercial suppliers and used without further purification. Anhydrous solvents (Et_2O, THF, MeCN, hexane, toluene, CH_2Cl_2) were used unless otherwise stated. These were obtained from an Anhydrous Engineering alumina column drying system based on the Grubbs design and deoxygenated prior to use by successive freeze-pump-thaw cycles or by sparging with nitrogen and stored over 4 Å molecular sieves. $CDCl_3$, CD_2Cl_2, THF-d_8, and C_6D_6 were distilled from CaH_2 and stored over 4 Å molecular sieves. Anhydrous pentane and EtOH were purchased from Sigma, stored over 4 Å molecular sieves and deoxygenated by sparging with nitrogen. Anhydrous MeOH and CD_3OD were purchased, stored over 3 Å molecular sieves and deoxygenated by sparging with nitrogen. DMSO-d_6 was purchased from Sigma and used without further purification.

All NMR spectra were acquired at ambient temperature on Jeol ECS300, Jeol ECS400, Varian 400, Varian VNMRS 500, Bruker 400 or Bruker Avance III HD CryoCarbon 500 MHz spectrometer equipped with a ^{13}C-observe (DCH) cryogenic probe. Chemical shifts (δ) are quoted in parts per million (ppm) and ^{1}H and ^{13}C{^{1}H} NMR spectra are referenced relative to the deuterated solvent. ^{31}P{^{1}H} NMR spectra are referenced relative to 85% H_3PO_4 as an external standard. Mass spectrometry was carried out by the Mass Spectrometry Service, University of Bristol on either a VG Analytical Autospec (EI) or VG Analytical Quattro (ESI) spectrometer. UV-vis studies were performed on an Agilent Cary 300 spectrophotometer. Photophysical data were obtained on a Perkin Elmer LS-45 fluorescence spectrometer. X-ray crystallography was performed by the University of Bristol Crystallography Service using a Bruker AXS Microstar or a Bruker Kappa Apex II diffractometer. Elemental analyses were performed by the University of York Microanalytical service.

The following starting materials and reagents were purchased from commercial suppliers and purified prior to use. Amines (NEt_3, EtN^iPr_2, NBu_3, pyridine) and $ClSiMe_3$ were each distilled from CaH_2 under vacuum and stored over activated 4 Å molecular sieves. Chlorophosphines (Ph_2PCl, $^tBu_2PCl$, $^iPr_2PCl$, $PhPCl_2$, PCl_3) and phosphines (Ph_2PH, $^tBu_2PH$) were distilled under vacuum.

The following compounds were prepared from literature procedures and spectroscopic data agreed with that reported:

cis-[$RuCl_2$(DMSO-*S*)$_3$(DMSO-*O*)],[300] *cis,cis*-1,3,5-triaminocyclohexane (*cis*-tach),[67] *cis*-[$PtCl_2(NH_3)_2$],[301] [$PtMe_2$(cod)],[302] [$PtCl_2$(cod)],[303] 3',4'-dibromo-2,2':5',2''-terthiophene,[167] 2,3-bis(diphenylphosphino)quinoxaline $\mathbf{L_{2.12}}$,[304] **2.14**,[169] $(Ph_2P)_2NH$,[305] **2.5-2.9**,[82] 7-amino-4-methylcoumarin,[306] 1-bromopyrene (**4.2**),[307] diethyl 1-pyrenylphosphonate (**4.3**),[246] diphenyl(1-pyrenyl)phosphine (DPPP),[240] Mes*PH_2,[308] **4.11-4.13**,[243] [(tht)AuCl],[259] 2-(3-(hydroxymethyl)phenyl)ethanol (**5.1**),[296] [$PdCl_2$(cod)],[309] and [$PdCl_2(NCPh)_2$].[310]

All other commercial reagents were used without further purification.

6.2 Experimental procedures and characterising data for Chapter 2 – Ru metallodrugs with DNA intercalating diphosphine ligands

6.2.1 NMR Assignments for Ru complexes

For Ru complexes **2.10** and **2.17-2.19**, the following NMR assignment labels are used:

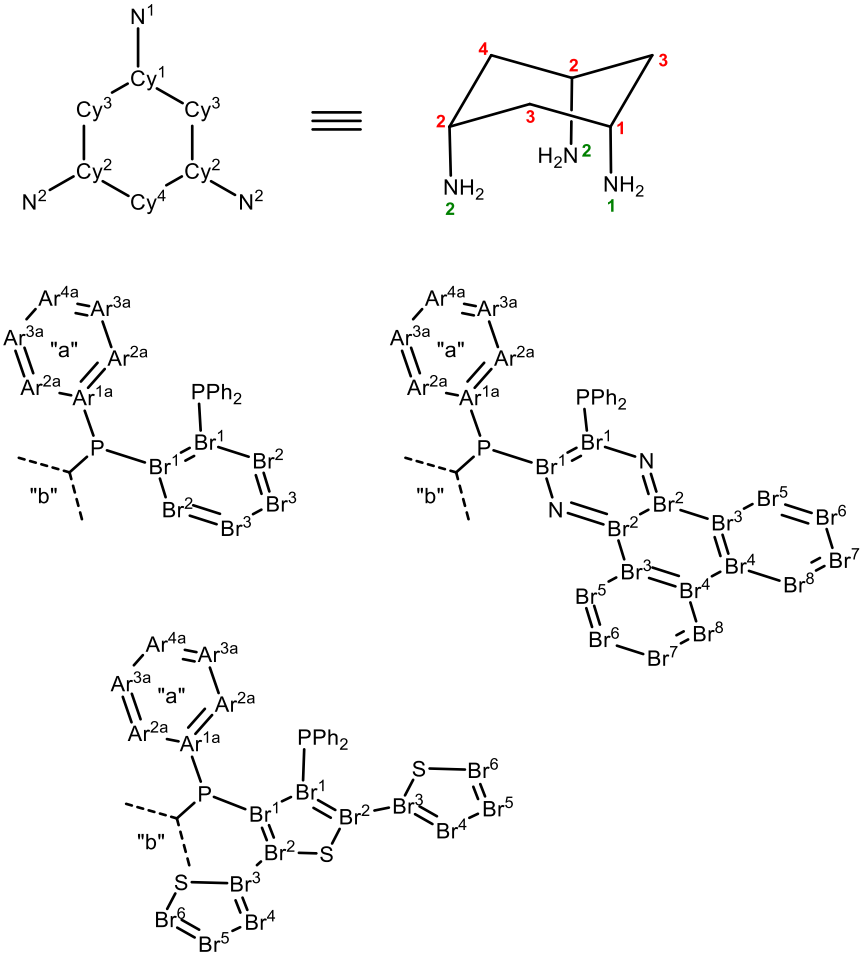

6.2.2 Synthesis of ligands and complexes

6.2.2.1 Synthesis of [RuCl(DMSO-*S*)$_2$(*cis*-tach)]Cl, 2.1

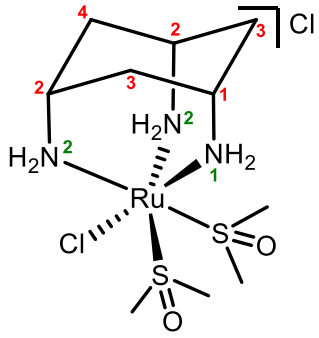

Following the reported procedure,[82] *cis,cis*-1,3,5-triaminocyclohexane (330 mg, 2.55 mmol) was added to a solution of *cis*-[RuCl$_2$(DMSO)$_4$] (1.24 g, 2.55 mmol) in DMSO (100 mL). The mixture was heated to 130 °C for 1 h yielding a yellow solution before being cooled and the complex precipitated by addition of EtOAc (1000 mL). The mixture was then cooled to –20 °C for 18 h to form more precipitate. The precipitate was filtered off, washed with EtOAc (200 mL) and dried *in vacuo* to give **2.1** as a pale yellow solid. Yield: 795 mg (74%). **^{1}H NMR** (400 MHz, D_2O) (δ, ppm): 4.50 (d, $^2J_{HH}$ = 12.2 Hz, 2H, N*H*$_2$, N^2), 4.21 (d, $^2J_{HH}$ = 12.2 Hz, 2H, N*H*$_2$, N^2), 3.86 (s, 2H, N*H*$_2$, N^1), 3.50 (s, 2H, C*H*, Cy^2), 3.33 (s, 12H, (C*H*$_3$)SO), 3.23 (s, 1H, C*H*, Cy^1), 2.19–1.94 (m, 4H, C*H*$_2$, Cy^3 + Cy^4), 1.81 (d, $^2J_{HH}$ = 15.2 Hz, 2H, C*H*$_2$, Cy^3). **^{13}C{^{1}H} NMR** (101 MHz, D_2O) (δ, ppm): 44.5 (s, (*C*H$_3$)$_2$SO), 43.9 (s, *C*H, Cy^1), 42.8 (s, *C*H, Cy^2), 33.0 (s, *C*H$_2$, Cy^4), 32.1 (s, *C*H$_2$, Cy^3). **HRMS (ESI)**: *m*/*z* calculated for $C_{10}H_{27}ClN_3O_2RuS_2$ $[M]^{\bullet+}$ = 422.0269, found = 422.0263.

6.2.2.2 Synthesis of 3',4'-bis(diphenylphosphino)-2,2':5',2''-terthiophene, L$_{2.11}$

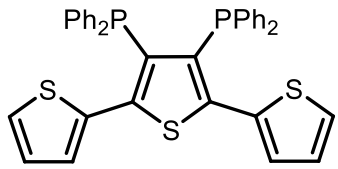

A solution of 3',4'-dibromo-2,2':5',2''-terthiophene **2.11** (914 mg, 2.25 mmol) in Et_2O (30 mL) was cooled to –78 °C and a solution of ^{n}BuLi (1.6 M in hexane) (1.55 mL, 2.48 mmol) was added dropwise. A yellow precipitate was observed, and the solution was stirred at –78 °C for 2 h before Ph_2PCl (0.41 mL, 2.25 mmol) was added dropwise over 10 min. The mixture was then slowly warmed to room temperature and stirred for 18 h. The resulting mixture was filtered to remove the LiCl precipitate and then the solvent removed *in vacuo* to give the monophosphine intermediate as a yellow powder. The procedure was repeated to give the diphosphine. The residue was purified by a short (2 × 1 cm) silica column (50% Et_2O/CH_2Cl_2) to obtain the product as a yellow solid. Yield: 0.275 g (20%). Crystals suitable for X-ray diffraction were grown by slow evaporation of a saturated CH_2Cl_2 solution of the product at room temperature. **^{1}H NMR** (400 MHz, $CDCl_3$) (δ, ppm): 7.25 – 7.19 (m, 8H, P*Ph*$_2$), 7.12 – 7.09 (m, 12H, P*Ph*$_2$), 7.07 (dd, $^3J_{HH}$ = 5.1 Hz, $^4J_{HH}$ = 1.3 Hz, 2H, C*H*), 6.63 (dd, $^3J_{HH}$ = 5.1 Hz, $^4J_{HH}$ = 3.6 Hz, 2H, C*H*), 6.60 (dd, $^3J_{HH}$ = 3.6, $^4J_{HH}$ = 1.2 Hz, 2H, C*H*). **^{13}C{^{1}H} NMR** (101 MHz, $CDCl_3$) (δ,

ppm): 144.0, 139.3, 135.5, 134.1, 132.5, 129.4, 127.9, 127.7, 127.2, 126.9. **^{31}P{^{1}H} NMR** (162 MHz, $CDCl_3$) (δ, ppm): –17.3 (s, 2P). **HRMS (MALDI):** *m/z* calculated for $C_{36}H_{26}P_2S_3$ $[M+H]^{\bullet+}$ = 617.0745, found = 617.0752.

6.2.2.3 Synthesis of 2,3-dichlorodibenzo[f,h]quinoxaline, 2.16

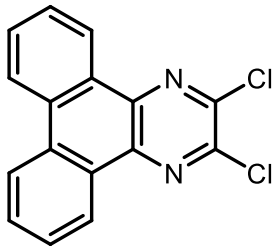

1,4-dihydrodibenzo[f,h]quinoxaline-2,3-dione **2.14** (600 mg, 2.30 mmol), PCl_3 (4.0 mL, 46.0 mmol) and DMF (9 mL) were heated to 100 °C for 16 h. The dark red solution was cooled to room temperature and the product precipitated by the addition of degassed water. The yellow solid was then filtered off, washed with EtOH, and dried *in vacuo*. Yield: 0.75 g (84%). **^{1}H NMR** (400 MHz, $CDCl_3$) (*δ*, ppm): 9.07 (d, $^{3}J_{HH}$ = 7.5 Hz, 2H, C*H*), 8.63 (d, $^{3}J_{HH}$ = 8.2 Hz, 2H, C*H*), 7.83 (t, $^{3}J_{HH}$ = 7.2 Hz, 2H, C*H*), 7.75 (t, $^{3}J_{HH}$ = 7.5 Hz, 2H, C*H*). **^{13}C{^{1}H} NMR** (100 MHz, $CDCl_3$) (*δ*, ppm): 139.6, 137.3, 131.9, 130.4, 128.2, 126.0, 126.0, 123.0. **HRMS (APCI):** *m/z* calculated for $C_{16}H_8N_2Cl_2$ $[M]^{\bullet+}$ = 299.0137, found = 299.0130. *APCI mass spectrum exhibited the expected chlorine isotope pattern.*

6.2.2.4 Synthesis of 2,3-bis(diphenylphosphino)dibenzo[f,h]quinoxaline, $L_{2.13}$

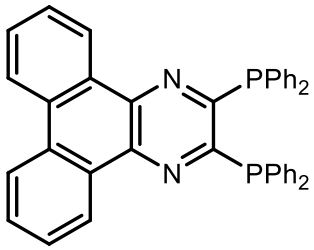

A solution of Ph_2PH (0.35 mL, 2.0 mmol) in THF (10 mL) was cooled to –78 °C and a solution of ^{n}BuLi (1.6 M in hexane, 1.38 mL, 2.20 mmol) was added dropwise. The orange solution was stirred at this temperature for 2 h before a solution of 2,3-dichlorodibenzo[f,h]quinoxaline **2.16** (270 mg, 0.90 mmol) in THF (5 mL) was added dropwise and stirred for a further 12 h with warming to room temperature. The solution was then quenched at –78 °C by the addition of sat. aq. NH_4Cl (5 mL) and warmed to room temperature. The aqueous layer was extracted with THF (3 × 10 mL) and filtered through silica. The volatiles were removed *in vacuo*, the residue dissolved in EtOAc and filtered off to remove soluble impurities. The remaining solid was recrystallised from EtOAc to give a yellow solid. Yield: 0.12 g (22%). **^{1}H NMR** (400 MHz, $CDCl_3$) (δ, ppm): 8.67 (dd, $^3J_{HH}$ = 8.0 Hz, $^4J_{HH}$ = 1.4 Hz, 2H, C*H*), 8.57 – 8.53 (m, 2H, C*H*), 7.72 (ddd, $^3J_{HH}$ = 8.4 Hz, $^3J_{HH}$ = 7.0 Hz, $^4J_{HH}$ = 1.5 Hz, 2H, C*H*), 7.56 (ddd, $^3J_{HH}$ = 8.1 Hz, $^3J_{HH}$ = 7.0 Hz, $^4J_{HH}$ = 1.2 Hz, 2H, C*H*), 7.44 – 7.36 (m, 8H, P*Ph*$_2$), 7.34 – 7.25 (m, 12H, P*Ph*$_2$). **^{13}C{^{1}H} NMR** (100 MHz, $CDCl_3$) (δ, ppm): 162.3 – 162.0 (m), 140.2, 136.1, 134.8, 131.7, 130.1, 129.7, 128.9, 128.3, 127.8, 125.8, 122.7. **^{31}P{^{1}H} NMR** (162 MHz, $CDCl_3$) (δ, ppm): –10.24 (s, 2P). **HRMS (ESI):** *m*/*z* calculated for $C_{40}H_{29}N_2P_2$ $[M+H]^{\bullet+}$ = 599.1800, found = 599.1809.

6.2.2.5 Synthesis of [RuCl(dppbz)(*cis*-tach)]Cl complex, 2.10

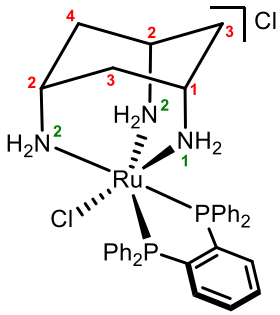

A solution of **2.1** (50 mg, 0.11 mmol) and 1,2-bis(diphenylphosphine)benzene (80 mg, 0.18 mmol, 1.8 eq) in MeOH (15 mL) was heated under reflux for 48 h. The solution was cooled, unreacted phosphine was removed by filtration and the solution was concentrated (approx. 5 mL). Et_2O (90 mL) was added to precipitate the product which was filtered off and dried to give a pale yellow solid. Yield: 62 mg (77%). **^{1}H NMR** (500 MHz, CD_3OD) (δ, ppm): 8.07 (ddd, $^3J_{HP}$ = 9.8 Hz, $^3J_{HH}$ = 5.4 Hz, $^4J_{HH}$ = 1.9 Hz, 4H, P*Ph*$_2$, Ar^{2a}), 7.55 – 7.49 (m, 6H; 2H, P*Ph*$_2$, Ar^{4a}, 4H, PC$_6$*H*$_4$P, Br^2 + Br^3), 7.45 (t, $^3J_{HH}$ = 7.7 Hz, 4H, P*Ph*$_2$, Ar^{3a}), 7.41 – 7.37 (m, 4H, P*Ph*$_2$, Ar^{3b}), 7.37 – 7.32 (m, 2H, P*Ph*$_2$, Ar^{4b}), 7.15 (ddd, $^3J_{HP}$ = 9.5 Hz, $^3J_{HH}$ = 5.9 Hz, $^4J_{HH}$ = 1.6 Hz, 4H, P*Ph*$_2$, Ar^{2b}), 4.92 (d, $^2J_{HH}$ = 12.1 Hz, 2H, N*H*$_2$, N^2), 3.86 (d, $^2J_{HH}$ = 12.0 Hz, 2H, N*H*$_2$, N^2), 3.56 (s, 2H, C*H*, Cy^2), 2.72 (s, 1H, C*H*, Cy^1), 2.29 (d, $^2J_{HH}$ = 15.1 Hz, 1H, C*H*$_2$, Cy^4), 2.14 (d, $^2J_{HH}$ = 15.3 Hz, 1H, C*H*$_2$, Cy^4), 1.86 (d, $^2J_{HH}$ = 15.0 Hz, 2H, C*H*$_2$, Cy^3), 1.74 (d, $^2J_{HH}$ = 15.9 Hz, 2H, C*H*$_2$, Cy^3), 1.39 (s, 2H, N*H*$_2$, N^1). **^{13}C{^{1}H} NMR**

(126 MHz, CD_3OD) (δ, ppm): 145.6 (vt, $|^1J_{PC} + {}^2J_{P'C}|$ = 82 Hz, PC_6H_4P, Br^1), 136.8 (t, $|^2J_{PC} + {}^4J_{P'C}|$ = 10 Hz, PPh_2, Ar^{2a}), 133.6 (m PPh_2, Ar^{1a} + Ar^{1b}), 133.5 (t, $|^2J_{PC} + {}^3J_{P'C}|$ = 16 Hz, PC_6H_4P, Br^2), 133.0 (t, $|^3J_{PC} + {}^4J_{P'C}|$ = 9 Hz, PPh_2, Ar^{2b}), 131.8 (s, PC_6H_4P, Br^3), 131.7 (s, PPh_2, Ar^{4a}), 131.1 (s, PPh_2, Ar^{4b}), 130.5 (t, $|^3J_{PC} + {}^5J_{P'C}|$ = 9 Hz, PPh_2, Ar^{3b}), 129.5 (t, $|^3J_{PC} + {}^5J_{P'C}|$ = 9 Hz, PPh_2, Ar^{3a}), 44.8 (s, *C*H, Cy^2), 44.4 (s, *C*H, Cy^1), 35.6 (s, *C*H_2, Cy^4), 34.3 (s, *C*H_2, Cy^3). **$^{31}P\{^1H\}$ NMR** (162 MHz, CD_3OD) (δ, ppm): 73.0 (s, 2P). **Elemental analysis** for [RuCl(dppbz)(*cis*-tach)]Cl.CH_2Cl_2 ($C_{37}H_{41}Cl_4N_3P_2Ru$): calcd. C, 53.38; H, 4.96; N, 5.05%. Found: C, 53.61; H, 4.84; N, 5.14%. **HRMS (ESI):** *m/z* calculated for $C_{36}H_{39}ClN_3P_2RuS_3$ $[M]^{\bullet+}$ = 712.1352, found = 712.1357. *ESI mass spectrum exhibited the expected ruthenium/chlorine isotope pattern for* ***2.10****.*

6.2.2.6 Synthesis of [RuCl($L_{2.11}$)(*cis*-tach)]Cl complex, 2.17

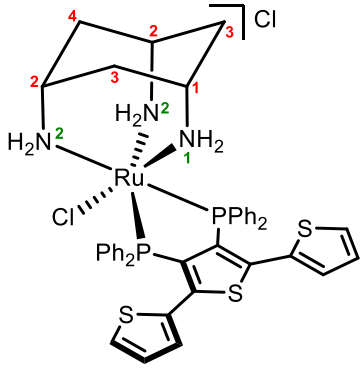

A solution of **2.1** (27 mg, 0.060 mmol) and $\mathbf{L_{2.11}}$ (67 mg, 0.11 mmol, 1.8 eq) in MeOH (15 mL) was heated under reflux for 18 h. The solution was cooled, unreacted phosphine was removed by filtration and the solvent was removed *in vacuo*. The residue was dissolved in CH_2Cl_2 (1 mL), and Et_2O (15 mL) was added to precipitate the product which was filtered off and dried to give a pale yellow solid. Yield: 36 mg (65%). **^{1}H NMR** (500 MHz, CD_2Cl_2) (*δ*, ppm): 7.81 – 7.76 (m, 4H, PPh_2, Ar^{2a}), 7.67 – 7.59 (m, 4H, PPh_2, Ar^{2b}), 7.54 (t, $^3J_{HH}$ = 7.7 Hz, 4H, PPh_2, Ar^{3a}), 7.42 (t, $^3J_{HH}$ = 7.4 Hz, 4H, PPh_2, Ar^{4a}), 7.18 (t, $^3J_{HH}$ = 7.4 Hz, 2H, PPh_2, Ar^{4b}), 7.08 (dd, $^3J_{HP}$ = 15.5 Hz, $^3J_{HH}$ = 6.9 Hz, 4H, PPh_2, Ar^{3b}), 7.04 (dd, $^3J_{HH}$ = 5.1 Hz, $^4J_{HH}$ = 1.2 Hz, 2H, C*H*, Br^6), 6.51 (dd, $^3J_{HH}$ = 5.1 Hz, $^4J_{HH}$ = 3.6 Hz, 2H, C*H*, Br^5), 6.39 (dd, $^3J_{HH}$ = 3.6 Hz, $^4J_{HH}$ = 1.2 Hz, 2H, C*H*, Br^4), 4.21 (d, $^2J_{HH}$ = 12.0 Hz, 2H, N*H*$_2$, N^2), 3.58 (s, 2H, C*H*, Cy^2), 3.21 (d, $^2J_{HH}$ = 12.0 Hz, 2H, N*H*$_2$, N^2), 2.80 (s, 1H, C*H*, Cy^1), 2.07 – 1.89 (m, 4H; 2H, C*H*$_2$, Cy^3, 2H, C*H*$_2$, Cy^4), 1.81 (d, $^2J_{HH}$ = 15.8 Hz, 2H, C*H*$_2$, Cy^3), 1.46 (s, 2H, N*H*$_2$, N^1). **$^{13}C\{^1H\}$ NMR** (126 MHz, CD_2Cl_2) (δ, ppm): 143.9 (vt, $|^1J_{PC} + {}^2J_{P'C}|$ = 84 Hz, P$C_{12}S_3$P, Br^1), 134.7 (t, $|^2J_{PC} + {}^4J_{P'C}|$ = 10 Hz, PPh_2, Ar^{2a}), 132.5 (t, $|^2J_{PC} + {}^4J_{P'C}|$ = 10 Hz, PPh_2, Ar^{2b}), 132.3 (s, P$C_{12}S_3$P, Br^2), 130.7 (s, PPh_2, Ar^{4a} + Ar^{4b}), 130.3 (s, PPh_2, Ar^{3a}), 130.2 – 130.0 (m, P$C_{12}S_3$P, Br^4 + Br^3, Ar^{1a} + Ar^{1b}), 128.3 (s, P$C_{12}S_3$P, Br^6), 128.1 (t, $|^3J_{PC} + {}^5J_{P'C}|$ = 10 Hz, PPh_2, Ar^{3b}), 127.7 (s, P$C_{12}S_3$P, Br^5), 43.7 (s, *C*H, Cy^1), 43.6 (s, *C*H, Cy^2), 35.4 (s, *C*H_2, Cy^4), 34.2 (s, *C*H_2, Cy^3). **$^{31}P\{^1H\}$ NMR** (162 MHz, CD_2Cl_2) (δ, ppm): 56.2 (s, 2P). **Elemental analysis** for [RuCl($\mathbf{L_{2.11}}$)(*cis*-tach)]Cl.CH_2Cl_2 ($C_{43}H_{43}Cl_4N_3P_2RuS_3$): calcd. C, 51.50; H, 4.32; N, 4.19%. Found: C, 51.52; H, 4.40; N, 4.20%. **HRMS (ESI):** *m/z* calculated for $C_{42}H_{41}ClN_3P_2RuS_3$

$[M]^{\bullet+}$ = 882.0671, found = 882.0685. *ESI mass spectrum exhibited the expected ruthenium/chlorine isotope pattern for* ***2.17****.*

6.2.2.7 Synthesis of [RuCl($L_{2.12}$)(*cis*-tach)]Cl complex, 2.18

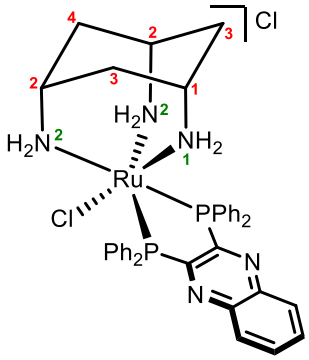

A solution of **1** (27 mg, 0.060 mmol) and **L2** (54 mg, 0.11 mmol, 1.8 eq) in MeOH (15 mL) was heated under reflux for 48 h. The solution was cooled, unreacted phosphine was removed by filtration and the solvent was removed *in vacuo*. The residue was dissolved in CH_2Cl_2 (1 mL), and Et_2O (15 mL) was added to precipitate the product which was filtered off and dried to give a red solid. Yield: 21 mg (44%). Crystals suitable for X-ray diffraction were grown by slow evaporation of a saturated MeOH solution of [**2.18**]PF_6 at room temperature. **^{1}H NMR** (500 MHz, CD_3OD) (δ, ppm): 8.19 (ddd, $^3J_{HP}$ = 7.9 Hz, $^3J_{HH}$ = 7.1 Hz, $^4J_{HH}$ = 3.3 Hz, 4H, P*Ph*$_2$, Ar^{2a}), 8.08 (dd, $^3J_{HH}$ = 6.5 Hz, $^4J_{HH}$ = 3.5 Hz, 2H, C*H*, Br^3), 7.93 (dd, $^3J_{HH}$ = 6.5 Hz, $^4J_{HH}$ = 3.5 Hz, 2H, C*H*, Br^4), 7.52 (t, $^3J_{HH}$ = 7.2 Hz, 4H, P*Ph*$_2$, Ar^{4a}), 7.45 (t, $^3J_{HH}$ = 7.0 Hz, 4H, P*Ph*$_2$, Ar^{3a}), 7.38 – 7.34 (m, 6H, P*Ph*$_2$, Ar^{3b} + Ar^{4b}), 7.14 (ddd, $^3J_{HP}$ = 7.9 Hz, $^3J_{HH}$ = 7.2 Hz, $^4J_{HH}$ = 3.3 Hz, 4H, P*Ph*$_2$, Ar^{2b}), 5.10 (d, $^2J_{HH}$ = 12.0 Hz, 2H, N*H*$_2$, N^2), 4.15 (d, $^2J_{HH}$ = 11.9 Hz, 2H, N*H*$_2$, N^2), 3.62 (s, 2H, C*H*, Cy^2), 2.78 (s, 1H, C*H*, Cy^1), 2.40 (d, $^2J_{HH}$ = 15.0 Hz, 1H, C*H*$_2$, Cy^4), 2.18 (d, $^2J_{HH}$ = 15.0 Hz, 1H, C*H*$_2$, Cy^4), 1.90 (d, $^2J_{HH}$ = 15.6 Hz, 2H, C*H*$_2$, Cy^3), 1.76 (d, $^2J_{HH}$ = 15.3 Hz, 2H, C*H*$_2$, Cy^3), 1.58 (s, 2H, N*H*$_2$, N^1). **^{13}C{^{1}H} NMR** (126 MHz, CD_3OD) (δ, ppm): 159.9 (vt, $|^1J_{PC} + {}^2J_{P'C}|$ = 111 Hz, PC_8N_2P, Br^1), 138.1 (t, $|^2J_{PC} + {}^4J_{P'C}|$ = 10 Hz, P*Ph*$_2$, Ar^{2a}), 133.7 (s, PC_8N_2P, Br^4), 132.9 (t, $|^2J_{PC} + {}^4J_{P'C}|$ = 10 Hz, P*Ph*$_2$, Ar^{2b}), 131.9 (s, P*Ph*$_2$, Ar^{4a} + Ar^{4b}), 131.2 (s, PC_8N_2P, Br^2), 131.1 (s, PC_8N_2P, Br^3), 130.6 (t, $|^3J_{PC} + {}^5J_{P'C}|$ = 9 Hz, P*Ph*$_2$, Ar^{3a}), 128.9 (t, $|^3J_{PC} + {}^5J_{P'C}|$ = 9 Hz, P*Ph*$_2$, Ar^{3b}), 44.8 (s, *C*H, Cy^2), 44.4 (s, *C*H, Cy^1), 35.5 (s, *C*H$_2$, Cy^4), 34.3 (s, *C*H$_2$, Cy^3). **^{31}P{^{1}H} NMR** (162 MHz, CD_3OD) (δ, ppm): 63.9 (s, 2P). **Elemental analysis** for [RuCl(**L**$_{2.12}$)(*cis*-tach)]Cl.CH_2Cl_2 ($C_{39}H_{41}Cl_4N_3P_2Ru$): calcd. C, 52.95; H, 4.67; N, 7.92%. Found: C, 52.69; H, 4.69; N, 7.71%. **HRMS (ESI):** *m*/*z* calculated for $C_{38}H_{39}ClN_5P_2Ru$ $[M]^{\bullet+}$ = 764.1414, found = 764.1411. *ESI mass spectrum exhibited the expected ruthenium/chlorine isotope pattern for* ***2.18****.*

6.2.2.8 Synthesis of [RuCl($L_{2.13}$)(*cis*-tach)]Cl complex, 2.19

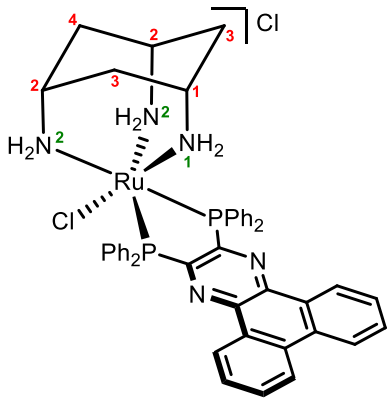

A solution of **2.1** (32 mg, 0.070 mmol) and **L2.13** (54 mg, 0.091 mmol, 1.3 eq) in EtOH (20 mL) was heated under reflux for 48 h. The solution was cooled, unreacted phosphine was removed by filtration and the solvent was removed *in vacuo*. The residue was dissolved in CH_2Cl_2 (1 mL), and Et_2O (15 mL) was added to precipitate the product which was filtered off and dried to give a red solid. Yield: 25 mg (40%). **^{1}H NMR** (500 MHz, CD_3OD) (δ, ppm): 8.49 – 8.42 (m, 6H; 4H, P*Ph*$_2$, Ar^{2a}, 2H, C*H*, Br^6), 7.78 (d, $^3J_{HH}$ = 7.8 Hz, 2H, C*H*, Br^5), 7.68 (t, $^3J_{HH}$ = 7.1 Hz, 2H, P*Ph*$_2$, Ar^{3b}), 7.63 (t, $^3J_{HH}$ = 7.4 Hz, 4H, P*Ph*$_2$, Ar^{4a} + Ar^{4b}), 7.34 – 7.26 (m, 6H; 4H, P*Ph*$_2$, Ar^{3a}, 2H, P*Ph*$_2$, Ar^{3b}), 7.21 – 7.12 (m, 8H; 4H, P*Ph*$_2$, Ar^{2b}, 2H, C*H*, Br^7, 2H, C*H*, Br^8), 5.33 (d, $^2J_{HH}$ = 11.8 Hz, 2H, N*H*$_2$, N^2), 4.27 (d, $^2J_{HH}$ = 11.8 Hz, 2H, N*H*$_2$, N^2), 3.69 (s, 2H, C*H*, Cy^2), 2.72 (s, 1H, C*H*, Cy^1), 2.48 (d, $^2J_{HH}$ = 15.0 Hz, 1H, C*H*$_2$, Cy^4), 2.24 (d, $^2J_{HH}$ = 15.0 Hz, 1H, C*H*$_2$, Cy^4), 1.91 (d, $^2J_{HH}$ = 15.5 Hz, 2H, C*H*$_2$, Cy^3), 1.74 (d, $^2J_{HH}$ = 15.4 Hz, 2H, C*H*$_2$, Cy^3), 1.45 (s, 2H, N*H*$_2$, N^1). **^{13}C{^{1}H} NMR** (126 MHz, CD_3OD) (δ, ppm): 158.8 (vt, $|^1J_{PC} + {}^2J_{P'C}|$ = 112 Hz, P*C*$_4$N$_2$P, Br^1), 141.3 (s, P*C*$_{16}$N$_2$P, Br^3), 138.7 ($|^2J_{PC} + {}^4J_{P'C}|$ = 10 Hz, P*Ph*$_2$, Ar^{2a}), 133.1 (m P*Ph*$_2$, Ar^{1a} + Ar^{1b}), 132.9 (t, $|^2J_{PC} + {}^4J_{P'C}|$ = 10 Hz, P*Ph*$_2$, Ar^{2b}), 132.1 (s, P*C*$_{16}$N$_2$P, Br^8), 132.0 (s, P*Ph*$_2$, Ar^{4a} + Ar^{4b}), 131.1 (s, P*C*$_{16}$N$_2$P, Br^2), 130.5 (t, $|^3J_{PC} + {}^5J_{P'C}|$ = 9 Hz, P*Ph*$_2$, Ar^{3a}), 129.6 (s, P*C*$_{16}$N$_2$P, Br^4), 128.9 (t, $|^3J_{PC} + {}^5J_{P'C}|$ = 9 Hz, P*Ph*$_2$, Ar^{3b}), 128.5 (s, P*C*$_{16}$N$_2$P, Br^7), 126.5 (s, P*C*$_{16}$N$_2$P, Br^6), 123.4 (s, P*C*$_{16}$N$_2$P, Br^5), 44.8 (s, *C*H, Cy^2), 44.4 (s, *C*H, Cy^1), 35.7 (s, *C*H$_2$, Cy^4), 34.3 (s, *C*H$_2$, Cy^3). **^{31}P{^{1}H} NMR** (162 MHz, CD_3OD) (δ, ppm): 63.3 (s, 2P). **Elemental analysis** for [RuCl(**L$_{2.13}$**)(*cis*-tach)]Cl.1.5CH_2Cl_2 ($C_{47.5}H_{46}Cl_5N_5P_2Ru$): calcd. C, 55.54; H, 4.51; N, 6.82%. Found: C, 55.54; H, 4.78; N, 7.17%. **HRMS (ESI):** *m*/*z* calculated for $C_{46}H_{43}ClN_5P_2Ru$ $[M]^{\bullet+}$ = 864.1726, found = 864.1710. *ESI mass spectrum exhibited the expected ruthenium/chlorine isotope pattern for* ***2.19***.

6.2.2.9 Synthesis of [RuCl(dppa)(*cis*-tach)]Cl complex, 2.20

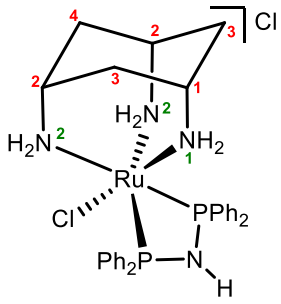

A solution of **2.1** (27 mg, 0.060 mmol) and $(Ph_2P)_2NH$ (42 mg, 0.11 mmol, 1.8 eq) in MeOH (15 mL) was heated under reflux for 18 h. The solution was cooled, unreacted phosphine was removed by filtration and the solvent was removed *in vacuo*. The residue was dissolved in CH_2Cl_2 (1 mL), and Et_2O (15 mL) was added to precipitate the product which was filtered off and dried to give a yellow solid. Yield: 31 mg (76%). Crystals suitable for X-ray diffraction were grown by slow evaporation of a saturated MeOH solution of the product at room temperature. **^{1}H NMR** (500 MHz, CD_3OD) (δ, ppm): 7.85 – 7.73 (m, 4H, P*Ph*$_2$,), 7.71 – 7.63 (m, 4H, P*Ph*$_2$,), 7.58 – 7.43 (m, 6H, P*Ph*$_2$,), 7.39 – 7.31 (m, 6H, P*Ph*$_2$,), 5.06 (d, $^2J_{HH}$ = 12.0 Hz, 2H, N*H*$_2$, N^2), 3.59 (s, 2H, C*H*, Cy^2), 3.54 (d, $^2J_{HH}$ = 12.0 Hz, 2H, N*H*$_2$, N^2), 2.85 (s, 1H, C*H*, Cy^1), 2.24 (d, $^2J_{HH}$ = 15.0 Hz, 1H, C*H*$_2$, Cy^4), 2.16 (s, 1H, C*H*$_2$, Cy^4), 1.96 – 1.87 (m, 2H, C*H*$_2$, Cy^3), 1.56 (d, $^2J_{HH}$ = 15.1 Hz, 2H, C*H*$_2$, Cy^3), 1.30 (s, 2H, N*H*$_2$, N^1). **^{31}P{^{1}H} NMR** (162 MHz, CD_3OD) (δ, ppm): 64.3 (s, 2P). **^{13}C{^{1}H} NMR** (126 MHz, CD_3OD) (δ, ppm): 137.9 – 137.5 (m, P*Ph*$_2$,), 137.6 – 137.1 (m, P*Ph*$_2$,), 132.7 (t, J = 6.0 Hz, P*Ph*$_2$,), 131.3 (s, P*Ph*$_2$,), 131.1 (t, J = 6.0 Hz, P*Ph*$_2$,), 131.0 (s, P*Ph*$_2$,), 130.5 (t, $|^3J_{PC} + {}^5J_{P'C}|$ = 5 Hz, P*Ph*$_2$), 128.9 (t, J = 5.3 Hz, P*Ph*$_2$,), 44.7 (s, *C*H, Cy^2), 44.5 (s, *C*H, Cy^1), 35.8 (s, *C*H$_2$, Cy^4), 34.7 (s, *C*H$_2$, Cy^3). **HRMS (ESI):** *m*/*z* calculated for $C_{30}H_{36}ClN_4P_2Ru$ $[M]^{\bullet+}$ = 651.1147, found 651.1144. *ESI mass spectrum exhibited the expected ruthenium/chlorine isotope pattern for* ***2.20***.

6.2.2.10 Synthesis of *cis*-[PtCl$_2$(L$_{2.12}$)] complex, 2.21

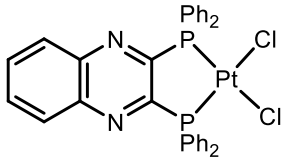

A solution of **L$_{2.12}$** (59 mg, 0.11 mmol) in CH_2Cl_2 (1.5 mL) was added to a solution of [$PtCl_2$(cod)] (38 mg, 0.10 mmol) in CH_2Cl_2 (1.5 mL) and stirred at room temperature for 2 h. The solution was concentrated to 1 mL, and Et_2O (15 mL) was added to precipitate the product which was filtered off and dried to give a yellow solid. Yield: 48 mg (63%). Crystals suitable for X-ray diffraction were grown by slow evaporation of a CH_2Cl_2 solution of the product. **^{1}H NMR** (400 MHz, $CDCl_3$) (δ, ppm): 8.20 (dd, $^3J_{HH}$ = 6.5 Hz, $^4J_{HH}$ = 3.5 Hz 2H), 7.96 (m, 10H), 7.51 (m, 4H), 7.44 (m, 8H). **^{31}P{^{1}H} NMR** (162 MHz, $CDCl_3$) (δ, ppm): 21.0 (s, $^1J_{PPt}$ = 3449 Hz). **^{13}C{^{1}H} NMR** (100 MHz, $CDCl_3$) (δ, ppm): 162.0 – 161.1 (m), 136.2, 130.4, 129.8, 127.0, 124.8, 122.3. **HRMS (ESI):** *m*/*z* calculated for $C_{32}H_{24}ClN_2P_2Pt$ [M–Cl]$^{\bullet+}$ = 728.0751, found 728.0742.

6.2.2.11 Synthesis of *cis*-[$PtCl_2(L_{2.13})$] complex, 2.22

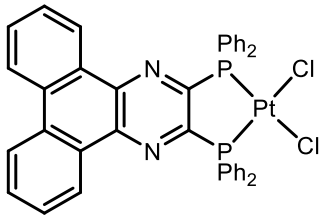

A solution of $\mathbf{L_{2.13}}$ (30 mg, 0.050 mmol) in CH_2Cl_2 (1.5 mL) was added to a solution of [$PtCl_2$(cod)] (19 mg, 0.050 mmol) in CH_2Cl_2 (1.5 mL) and stirred at room temperature for 2 h. The solution was concentrated to 1 mL, and Et_2O (15 mL) was added to precipitate the product which was filtered off and dried to give a yellow solid. Yield: 22 mg (50%). Crystals suitable for X-ray diffraction were grown by diffusion of Et_2O into a CH_2Cl_2 solution of the product. **^{1}H NMR** (400 MHz, $CDCl_3$) (δ, ppm): 9.04 (dd, $^3J_{HH}$ = 8.1, $^4J_{HH}$ = 1.4 Hz, 2H), 8.59 (d, $^3J_{HH}$ = 8.2 Hz, 2H), 8.10 – 7.99 (m, 8H), 7.87 (m, 2H), 7.73 (m, 2H), 7.56 – 7.41 (m, 12H). **^{31}P{^{1}H} NMR** (162 MHz, $CDCl_3$) (δ, ppm): 21.6 (s, $^1J_{PPt}$ = 3500 Hz). **^{13}C{^{1}H} NMR** (100 MHz, $CDCl_3$) (δ, ppm): 161.3 – 161.0 (m), 139.2, 136.8, 135.0, 131.4, 130.3, 129.3, 128.9, 127.9, 127.8, 125.1, 122.9. **HRMS (ESI):** m/z calculated for $C_{40}H_{28}ClN_2P_2Pt$ $[M–Cl]^{\bullet+}$ = 828.1064, found 828.1083.

6.2.2.12 Synthesis of *cis*-[$PtCl_2(L_{2.11})$] complex, 2.23

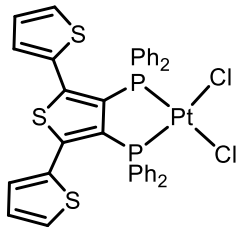

A solution of $\mathbf{L_{2.11}}$ (16 mg, 0.030 mmol) in CH_2Cl_2 (1.0 mL) was added to a solution of [$PtCl_2$(cod)] (10 mg, 0.030 mmol) in CH_2Cl_2 (1.0 mL) and stirred at room temperature for 2 h. The solution was concentrated to 0.5 mL, and Et_2O (10 mL) was added to precipitate the product which was filtered off and dried to give a yellow solid. Yield: 18 mg (82%). Spectroscopic data matched that previously reported.[311] **^{1}H NMR** (400 MHz, $CDCl_3$) (δ, ppm): 7.80 – 7.68 (m, 9H), 7.53 – 7.48 (m, 2H), 7.47 – 7.40 (m, 5H), 7.40 – 7.32 (m, 10H). **^{31}P{^{1}H} NMR** (162 MHz, $CDCl_3$) (δ, ppm): 11.8 (s, $^1J_{PPt}$ = 3580 Hz).

6.3 Experimental procedures and characterising data for Chapter 3 – Fluorescent phosphine complex conjugates

6.3.1 Synthesis of $(Ph_2PCH_2)_2NCH_2COOH$, $L_{3.1}$

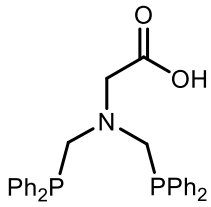

Following an adapted literature procedure.[198] A solution of Ph_2PH (4.18 mL, 24.0 mmol) and paraformaldehyde (0.83 g, 27.6 mmol) in degassed EtOH (100 mL) was heated under reflux until the reaction mixture became a homogeneous solution (approx. 1 h). Glycine (0.90 g, 11.9 mmol) was added, and the mixture heated under reflux for 18 h. The solvent was removed *in vacuo* to give the product as a white solid. Yield: 4.97 g (88%). Spectroscopic data matched that previously reported. **^{1}H NMR** (400 MHz, $CDCl_3$) (δ, ppm): 7.40 – 7.28 (m, 20H, P*Ph*$_2$), 3.68 (d, $^2J_{HP}$ = 4.0 Hz, 4H, PCH_2), 3.65 (s, 2H, COCH_2). **^{31}P{^{1}H} NMR** (162 MHz, $CDCl_3$) (δ, ppm): –26.6 (s, 2P).

6.3.2 Synthesis of $(Ph_2PCH_2)_2NCH_2$-1-Pyr, $L_{3.2}$

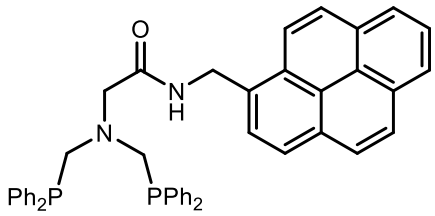

NEt_3 (1.20 mL, 8.50 mmol) was added to a solution of 1-pyrenylmethylamine hydrochloride (220 mg, 0.83 mmol) in CH_2Cl_2 (5 mL). After stirring the mixture for 30 min to ensure complete deprotonation, this solution was added to a suspension of **$L_{3.1}$** (350 mg, 0.75 mmol) and HATU (314 mg, 0.83 mmol) in CH_2Cl_2 (20 mL). The flask was shielded from the light and stirred for 16 h before water (10 mL) was added. The aqueous layer was extracted with CH_2Cl_2 (3 × 20 mL), dried ($MgSO_4$) and concentrated *in vacuo*. The compound was purified by silica column chromatography (30% EtOAc/hexane) to give a yellow solid. Yield: 75 mg (15%). **^{1}H NMR** (400 MHz, $CDCl_3$) (δ, ppm): 8.20 (dd, $^3J_{HH}$ = 7.6 Hz, $^4J_{HH}$ = 1.8 Hz, 2H, CH_{Pyr}), 8.11 – 7.98 (m, 5H, CH_{Pyr}), 7.53 (d, $^3J_{HH}$ = 7.8 Hz, 1H, CH_{Pyr}), 7.19 (td, $^3J_{HH}$ = 7.1 Hz, $^4J_{HH}$ = 1.5 Hz, 8H, P*Ph*$_2$), 7.13 (d, $^3J_{HH}$ = 6.5 Hz, 4H, P*Ph*$_2$), 7.06 (td, $^3J_{HH}$ = 7.1 Hz, $^4J_{HH}$ = 1.4 Hz, 8H, P*Ph*$_2$), 6.71 (t, $^3J_{HH}$ = 6.0 Hz, 1H, CH_{Pyr}), 4.71 (d, $^3J_{HH}$ = 6.0 Hz, 2H, NHCH_2), 3.67 (s, 2H, COCH_2), 3.52 (d, $^2J_{HP}$ = 4.4 Hz, 4H, PCH_2). **^{31}P{^{1}H} NMR** (162 MHz, $CDCl_3$) (δ, ppm): –26.8 (s, 2P). **^{13}C{^{1}H} NMR** (100 MHz, $CDCl_3$) (δ, ppm): 170.1 (s, *C*O), 136.7, 136.6, 133.2, 133.0, 131.4, 131.1, 131.0, 128.9, 128.6, 128.5, 128.1, 127.5, 127.0, 126.1, 125.4, 125.3, 124.6, 123.2, 61.3 – 60.9 (m, CO*C*H_2), 60.2 – 59.8 (m, P*C*H_2), 40.9 (s, NH*C*H_2). **HRMS (ESI):** *m*/*z* calculated for $C_{45}H_{39}N_2OP_2$ $[M+H]^{\bullet+}$ = 685.2538, found = 685.2534.

6.3.3 Synthesis of [RuCl($L_{3.1}$)(*cis*-tach)]Cl complex, 3.1

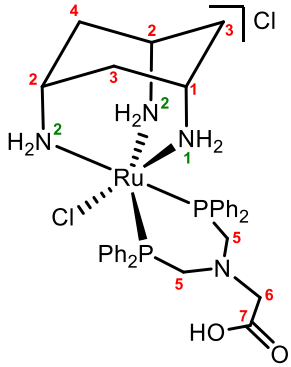

A solution of [RuCl(DMSO-*S*)$_2$(*cis*-tach)]Cl **2.1** (160 mg, 0.35 mmol) and $\mathbf{L_{3.1}}$ (198 mg, 0.42 mmol) was heated under reflux in EtOH (50 mL) for 18 h. The solvent was removed, CH_2Cl_2 (1 mL) was added and the complex was precipitated from Et_2O (10 mL). The solid was then filtered off, washed with Et_2O and dried *in vacuo* to give the product as a pale-yellow solid. Yield: 260 mg (96%). **^{1}H NMR** (400 MHz, CD_3OD) (δ, ppm): 7.96 (m, 4H, P*Ph*$_2$), 7.82 (m, 4H, P*Ph*$_2$), 7.46 (m, 12H, P*Ph*$_2$), 4.26 (d, $^2J_{HH}$ = 12.2 Hz, 2H, N*H*$_2$, N^2), 4.04 (d, $^2J_{HH}$ = 12.2 Hz, 2H, N*H*$_2$, N^2), 3.70 – 3.62 (m, 2H, C*H*$_2$, C5), 3.60 (s, 2H, C*H*$_2$, C6), 3.55 – 3.44 (m, 4H; 2H, C*H*, Cy^2, 2H, C*H*$_2$, C5), 2.65 (s, 1H, C*H*, Cy^1), 2.27 (d, $^2J_{HH}$ = 15.6 Hz, 2H, C*H*$_2$, Cy^4), 2.05 (d, $^2J_{HH}$ = 15.6 Hz, 2H, C*H*$_2$, Cy^4), 1.78 (d, $^2J_{HH}$ = 15.2 Hz, 2H, C*H*$_2$, Cy^3), 1.65 (d, $^2J_{HH}$ = 15.3 Hz, 2H, C*H*$_2$, Cy^3), 1.46 (s, 2H, N*H*$_2$, N^1). **^{31}P{^{1}H} NMR** (162 MHz, CD_3OD) (δ, ppm): 40.4 (s, 2P). **^{13}C{^{1}H} NMR** (101 MHz, CD_3OD) (δ, ppm): 173.3 (s, *C*O, C7), 135.9 (P*Ph*$_2$), 133.6 (P*Ph*$_2$), 131.5 (P*Ph*$_2$), 130.9 (P*Ph*$_2$), 130.2 (P*Ph*$_2$), 129.7 (P*Ph*$_2$), 63.8 (vt, $^3J_{CP}$ = 9 Hz, *C*H$_2$, C6), 57.6 (vt, $^1J_{CP}$ = 20 Hz, *C*H$_2$, C5), 44.6 (s, *C*H, Cy^2), 44.2 (s, *C*H, Cy^1), 35.4 (s, *C*H$_2$, Cy^4), 34.2 (s, *C*H$_2$, Cy^3). **HRMS (ESI):** *m*/*z* calculated for $C_{34}H_{42}ClN_4O_2P_2Ru$ $[M]^{\bullet+}$ = 737.1516, found = 737.1523.

6.3.4 Synthesis of [$PtCl_2$($L_{3.2}$)] complex, 3.2

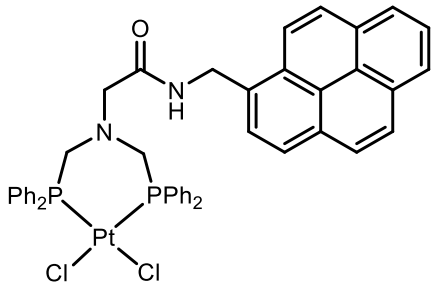

A solution of $\mathbf{L_{3.2}}$ (21 mg, 0.050 mmol) in CH_2Cl_2 (1.5 mL) was added dropwise to a solution of [$PtCl_2$(cod)] (11 mg, 0.050 mmol) in CH_2Cl_2 (1.5 mL). After 1 h the volume was reduced to 1 mL and Et_2O was added to precipitate the product which was filtered off and dried *in vacuo*. Yield: 10 mg (35%). **^{1}H NMR** (400 MHz, $CDCl_3$) (δ, ppm): 8.25 (d, $^3J_{HH}$ = 7.6 Hz, 1H), 8.20 (d, $^3J_{HH}$ = 7.5 Hz, 1H), 8.16 – 8.00 (m, 4H), 7.95 (d, $^3J_{HH}$ = 9.2 Hz, 1H), 7.85 (d, $^3J_{HH}$ = 9.3 Hz, 1H), 7.79 – 7.66 (m, 8H), 7.55 (d, $^3J_{HH}$ = 7.8 Hz, 1H), 7.25 – 7.16 (m, 14H), 6.06 (t, $^3J_{HH}$ = 5.9 Hz, 1H), 4.70 (d, $^3J_{HH}$ = 5.9 Hz, 2H), 3.62 (m, 4H), 3.26 (s, 2H). **^{31}P{^{1}H} NMR** (162 MHz, $CDCl_3$) (δ, ppm): –6.5 (s, $^1J_{PPt}$ = 3416 Hz, 2P). **^{13}C{^{1}H} NMR** (100 MHz, $CDCl_3$) (δ, ppm): 170.2 (s, *C*O), 134.0, 131.7, 128.7, 128.6, 128.0. 127.7, 127.3, 126.5, 125.9, 125.6, 124.8, 122.6, 66.1, 56.7, 41.0. **HRMS (ESI):** *m*/*z* calculated for $C_{45}H_{38}N_2OP_2Pt$ $[M–Cl]^{\bullet+}$ = 914.1796, found = 914.1784.

6.3.5 Synthesis of [RuCl($L_{3.2}$)(*cis*-tach)]Cl complex, 3.3

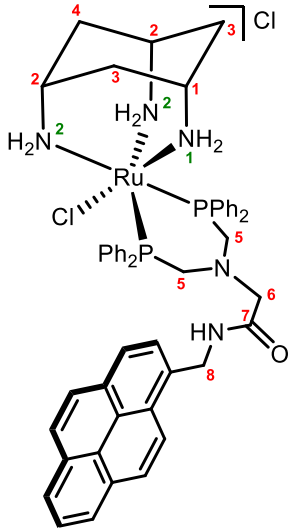

A solution of [RuCl(DMSO-*S*)$_2$(*cis*-tach)]Cl **2.1** (28 mg, 0.050 mmol) and $\mathbf{L_{3.2}}$ (62 mg, 0.090 mmol) was heated under reflux in EtOH (20 mL) for 48 h. The solvent was removed, CH_2Cl_2 (1 mL) was added and the product was precipitated from Et_2O (10 mL). Yield: 48 mg (81%). **^{1}H NMR** (500 MHz, CD_3OD) (δ, ppm): 8.29 (d, $^3J_{HH}$ = 9.3 Hz, 1H, C*H*$_{Pyr}$), 8.25 (d, $^3J_{HH}$ = 7.6 Hz, 1H, C*H*$_{Pyr}$), 8.12 (d, $^3J_{HH}$ = 9.0 Hz, 1H, C*H*$_{Pyr}$), 8.08 – 8.04 (m, 3H, C*H*$_{Pyr}$), 8.02 (t, $^3J_{HH}$ = 7.5 Hz, 1H, C*H*$_{Pyr}$), 7.96 (d, $^3J_{HH}$ = 7.8 Hz, 1H, C*H*$_{Pyr}$), 7.84 (m, 4H, P*Ph*$_2$), 7.73 – 7.63 (m, 4H, P*Ph*$_2$), 7.53 (d, $^3J_{HH}$ = 9.2 Hz, 1H, C*H*$_{Pyr}$), 7.49 (t, $^3J_{HH}$ = 7.6 Hz, 4H, P*Ph*$_2$), 7.42 (t, $^3J_{HH}$ = 7.5 Hz, 2H, P*Ph*$_2$), 7.18 (t, $^3J_{HH}$ = 7.5 Hz, 2H, P*Ph*$_2$), 6.91 (t, $^3J_{HH}$ = 7.6 Hz, 3H, P*Ph*$_2$), 5.10 (s, 2H, C*H*$_2$, C8), 4.15 (d, $^2J_{HH}$ = 11.9 Hz, 2H, N*H*$_2$, N^2), 3.96 (d, $^2J_{HH}$ = 12.4 Hz, 2H, N*H*$_2$, N^2), 3.54 – 3.46 (m, 2H, C*H*$_2$, C5), 3.40 (s, 2H, C*H*, Cy^2), 3.32 (s, 2H, C*H*$_2$, C6), 3.05 (dt, $^2J_{HH}$ = 13.4 Hz, $^4J_{HH}$ = 2.9 Hz, 2H, C*H*$_2$, C5), 2.57 (s, 1H, C*H*, Cy^1), 2.19 (d, $^2J_{HH}$ = 15.1 Hz, 1H, C*H*$_2$, Cy^4), 1.97 (d, $^2J_{HH}$ = 15.0 Hz, 1H, C*H*$_2$, Cy^4), 1.70 (d, $^2J_{HH}$ = 15.3 Hz, 2H, C*H*$_2$, Cy^3), 1.56 (d, $^2J_{HH}$ = 15.3 Hz, 2H, C*H*$_2$, Cy^3), 1.32 (s, 2H, N*H*$_2$, N^1). **^{31}P{^{1}H} NMR** (162 MHz, CD_3OD) (δ, ppm): 41.6 (s, 2P). **^{13}C{^{1}H} NMR** (126 MHz, CD_3OD) (δ, ppm): 169.9 (s, *C*O, C7), 135.8 (P*Ph*$_2$), 133.7 (P*Ph*$_2$), 132.9, 132.7, 132.6, 132.1, 131.2, 131.0, 130.3 (P*Ph*$_2$), 130.1, 129.5 – 129.3 (P*Ph*$_2$), 129.1, 128.5, 127.2, 126.5, 126.4, 125.8, 124.4, 67.4 (t, $^3J_{CP}$ = 11.5 Hz, *C*H$_2$, C6), 58.1 (vt, $|^1J_{PC} + {}^3J_{PC'}|$ = 85 Hz, *C*H$_2$, C5), 44.6 (s, *C*H, Cy^2), 44.1 (s, *C*H, Cy^1), 42.3 (s, *C*H, C8), 35.3 (s, *C*H$_2$, Cy^4), 34.2 (s, *C*H$_2$, Cy^3). **HRMS (ESI):** *m*/*z* calculated for $C_{51}H_{53}ClN_5O_2P_2Ru$ $[M]^{\bullet+}$ = 950.2457, found = 950.2465.

6.3.6 Attempted synthesis of [RuCl($L_{3.2}$)(*cis*-tach)]Cl complex, 3.3

NEt_3 (0.30 mL, 2.0 mmol) was added to a solution of 1-pyrenylmethylamine hydrochloride (16 mg, 0.064 mmol) in CH_2Cl_2 (2 mL). After stirring the mixture for 30 min to ensure complete deprotonation, this solution was added to a solution of **3.1** (31 mg, 0.040 mmol), HATU (17 mg, 0.045 mmol), and DIPEA (10 µL, 0.060 mmol) in CH_2Cl_2 (20 mL). The flask was shielded from the light and stirred for 16 h before water (1 mL) was added. The aqueous layer was extracted with CH_2Cl_2 and Et_2O was added. The precipitate contained trace amounts of **3.3** but was highly impure by ^{1}H NMR spectroscopy.

6.3.7 Attempted synthesis of complex, 3.4

A solution of **3.1** (19 mg, 0.030 mmol) and DCC (6 mg, 0.031 mmol) in CH_2Cl_2 (5 mL) was stirred at room temperature for 10 min. After observation of a white precipitate, benzylamine (3.5 μL, 0.030 mmol) was added and the mixture stirred at room temperature for 18 h. The suspension was filtered, solvent concentrated *in vacuo* and Et_2O (10 mL) was added. The precipitate contained trace amounts of **3.4** but was highly impure by ^{1}H NMR spectroscopy.

6.3.8 Attempted synthesis of complex, 3.5

A solution of **3.1** (39 mg, 0.050 mmol) and DCC (12 mg, 0.062 mmol) in CH_2Cl_2 (10 mL) was stirred at room temperature for 10 min. After observation of a white precipitate, 7-amino-4-methylcoumarin (11 mg, 0.060 mmol) was added and the mixture stirred at room temperature for 18 h. The suspension was filtered, solvent concentrated *in vacuo* and Et_2O (10 mL) was added. The precipitate contained trace amounts of **3.5** but was highly impure by ^{1}H NMR spectroscopy.

6.3.9 Synthesis of [(η^6-*p*-cym)$RuCl_2(PPh_2(4\text{-}C_6H_4OH))$] complex, 3.7

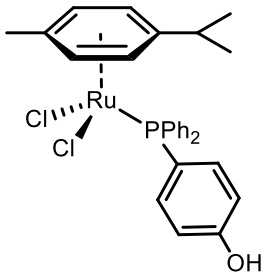

Following an adapted literature procedure.[171] A solution of [(η^6-*p*-cymene)$RuCl_2$]$_2$ (250 mg, 0.42 mmol) and $PPh_2(4\text{-}C_6H_4OH)$ (250 mg, 0.90 mmol) in CH_2Cl_2 (10 mL) was stirred at room temperature for 18 h. The suspension was filtered, and the orange solid was washed with Et_2O and dried *in vacuo* at 45 °C. Yield: 410 mg (78%). **^{1}H NMR** (400 MHz, $(CD_3)_2SO$) (δ, ppm): 9.96 (s, 1H), 7.77 – 7.66 (m, 4H), 7.62 – 7.52 (m, 2H), 7.46 – 7.32 (m, 6H), 6.78 (d, $^3J_{HH}$ = 6.9 Hz, 1H), 5.30 (d, $^3J_{HH}$ = 6.2 Hz, 2H), 5.20 (d, $^3J_{HH}$ = 5.4 Hz, 2H), 2.55 (hept, $^3J_{HH}$ = 6.9 Hz, 1H), 1.76 (s, 3H), 0.96 (d, $^3J_{HH}$ = 6.9 Hz, 6H). **^{31}P{^{1}H} NMR** (162 MHz, $(CD_3)_2SO$) (δ, ppm): 23.5 (2, 1P).

6.3.10 Synthesis of [(η^6-*p*-cym)RuCl$_2$(PPh$_2$(4-C$_6$H$_4$OCO-Pyr))] complex, 3.8

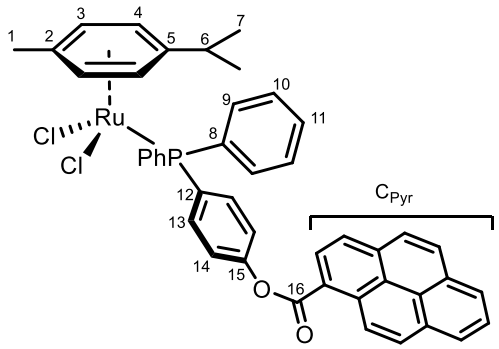

Following an adapted literature procedure.[171] Pyrene-1-carboxylic acid (100 mg, 0.42 mmol) and $SOCl_2$ (2.0 mL, 17.0 mmol) were heated at 80 °C for 4 h. Conversion to the acid chloride was monitored by IR spectroscopy before the volatiles were removed *in vacuo* and the yellow residue dissolved in CH_2Cl_2 (10 mL). This freshly prepared solution of pyrene-1-carbonyl chloride **3.6** was added to a solution of **3.7** (140 mg, 0.25 mmol) in CH_2Cl_2 followed by NEt_3 (0.04 mL, 0.3 mmol). The red solution was stirred at room temperature for 16 h and the volatiles were removed *in vacuo*. The residue was purified by silica column chromatography (0–10% MeOH/CH_2Cl_2). The red band was collected, concentrated *in vacuo* and the product precipitated from addition of Et_2O. Yield: 50 mg (25%). **^{1}H NMR** (500 MHz, $CDCl_3$) (δ, ppm): 9.35 (d, $^2J_{HH}$ = 9.5 Hz, 1H), 8.85 (d, $^2J_{HH}$ = 8.1 Hz, 1H), 8.33 – 8.20 (m, 4H), 8.16 – 8.06 (m, 2H), 8.05 – 7.95 (m, 2H), 7.94 – 7.86 (m, 3H), 7.47 – 7.32 (m, 10H), 5.24 (d, $^3J_{HH}$ = 6.0 Hz, 2H, C4-H), 5.05 (d, $^3J_{HH}$ = 4.9 Hz, 2H, C3-H), 2.88 (hept, $^3J_{HH}$ = 6.8 Hz, 1H, C6-H), 1.91 (s, 3H, C1-H), 1.14 (d, $^3J_{HH}$ = 7.0 Hz, 6H, C7-H). **^{31}P{^{1}H} NMR** (162 MHz, $CDCl_3$) (*δ*, ppm): 23.7 (s, 1P). **^{13}C{^{1}H} NMR** (126 MHz, $CDCl_3$) (*δ*, ppm): 166.0 (C16), 152.8 (d, $^4J_{CP}$ = 2.7 Hz, C15), 136.2 (d, $^2J_{CP}$ = 10.4 Hz, C13), 135.3 (C_{Pyr}), 134.4 (d, $^2J_{CP}$ = 9.5 Hz, C9), 134.1 (d, $^1J_{CP}$ = 45.2 Hz, C12), 132.2 (C_{Pyr}), 131.1 (C_{Pyr}), 131.1 (d, $^1J_{CP}$ = 47.0 Hz, C8), 130.5 (d, $^4J_{CP}$ = 2.6 Hz, C11), 130.4 (C_{Pyr}), 130.2 (C_{Pyr}), 129.2 (C_{Pyr}), 128.2 (d, $^3J_{CP}$ = 9.9 Hz, C10), 127.3 (C_{Pyr}), 126.9 (C_{Pyr}), 126.7 (C_{Pyr}), 126.7 (C_{Pyr}), 125.1 (C_{Pyr}), 124.8 (C_{Pyr}), 124.4 (C_{Pyr}), 124.2 (C_{Pyr}), 121.8 (C_{Pyr}), 121.7 (d, $^3J_{CP}$ = 10.6 Hz, C14), 111.4 (d, $^2J_{CP}$ = 3.1 Hz, C5), 96.2 (C2), 89.3 (d, $^2J_{CP}$ = 3.1 Hz, C3), 87.3 (d, $^2J_{CP}$ = 5.5 Hz, C4), 30.4 (C6), 22.0 (C7), 17.9 (C1). **HRMS (ESI):** *m*/*z* calculated for $C_{45}H_{37}O_2PClRu$ $[M–Cl]^{\bullet+}$ = 777.1263, found = 777.1279.

6.4 Experimental procedures and characterising data for Chapter 4 – Photophysical properties of air-stable pyrenylphosphines

6.4.1 Synthesis of diethyl 1-pyrenylphosphonate, 4.3

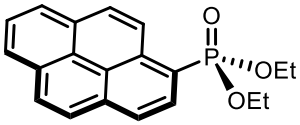

The compound was prepared according to a literature procedure and spectroscopic data matched that reported.[246] **^{1}H NMR** (400 MHz, $CDCl_3$) (δ, ppm): 8.86 (d, $^3J_{HH}$ = 9.3 Hz, 1H, C*H*), 8.67 (dd, $^3J_{HH}$ = 14.3 Hz, $^4J_{HH}$ = 7.9 Hz, 1H, C*H*), 8.33 – 8.16 (m, 5H, C*H*), 8.14 – 8.02 (m, 2H, C*H*), 4.36 – 4.20 (m, 2H, CH_2), 4.18 – 4.05 (m, 2H, CH_2), 1.33 (t, $^3J_{HH}$ = 7.1 Hz, 6H, CH_3). **^{31}P{^{1}H} NMR** (162 MHz, $CDCl_3$) (δ, ppm): 20.5 (s, 1P).

6.4.2 Synthesis of 1-pyrenylphosphine, $L_{4.1}$

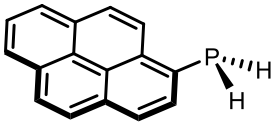

A solution of TMSCl (0.51 mL, 4.05 mmol) in THF (10 mL) was cooled to –35 °C before $LiAlH_4$ (0.175 g, 4.35 mmol) was added. The grey suspension was warmed to room temperature and stirred for 1.5 h. The suspension was cooled to –78 °C and a solution of **4.3** (0.51 g, 1.50 mmol) in THF (5 mL) was added. The mixture was warmed to room temperature and stirred for 18 h. The reaction was quenched with H_2O (0.5 mL), NaOH (15% w/w, 0.5 mL) and H_2O (0.5 mL). The precipitate was removed by filtration and the solvent removed *in vacuo* to give **$L_{4.1}$** as a white solid. Yield: 65 mg (19%). **^{1}H NMR** (400 MHz, $CDCl_3$) (δ, ppm): 8.41 (dd, $^3J_{HH}$ = 9.1 Hz, $^4J_{HH}$ = 1.9 Hz, 1H, C*H*), 8.25 – 8.15 (m, 4H, C*H*), 8.10 – 8.00 (m, 4H, C*H*), 4.45 (d, $^1J_{HP}$ = 204.1 Hz, 2H, PH_2). **^{13}C{^{1}H} NMR** (101 MHz, $CDCl_3$) (δ, ppm): 133.9 (d, J_{CP} = 11.4 Hz), 128.0, 128.0, 127.6, 126.3, 126.0, 125.8, 125.7, 125.6, 124.5. **^{31}P{^{1}H} NMR** (162 MHz, $CDCl_3$) (δ, ppm) –132.2 (s, 1P). **^{31}P NMR** (162 MHz, $CDCl_3$) (δ, ppm) –132.2 (td, $^1J_{PH}$ = 203 Hz, $^4J_{PH}$ = 7 Hz). **HRMS (MALDI):** m/z calculated for $C_{16}H_{11}P$ $[M]^{\bullet+}$ = 234.0593, found = 234.0599.

6.4.3 Synthesis of di(1-pyrenyl)phosphine oxide, 4.5

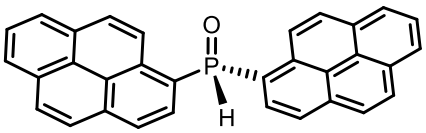

Mg turnings (480 mg, 20.0 mmol) and one crystal of I_2 were covered with THF. A solution of 1-bromopyrene **4.2** (5.12 g, 18.2 mmol) in THF (50 mL) was added with heating to gentle reflux. In a second flask, NaH (185 mg, 7.7 mmol) in THF (20 mL) was cooled to 0 °C and $(EtO)_2POH$ (0.90 mL, 7.0 mmol) was added dropwise. This solution was cooled to –78 °C and the freshly prepared 1-pyrenylmagnesium bromide was added dropwise *via* cannula. The solution was warmed to room temperature and stirred for 18 h. The reaction was quenched at 0 °C with sat. aq.

NH_4Cl and concentrated *in vacuo*. The crude product was extracted with CH_2Cl_2, washed with brine, dried ($MgSO_4$) and concentrated *in vacuo*. The mixture was triturated (MTBE/hexane, 3:1, 10 mL) to remove excess $(EtO)_2POH$ and the precipitate filtered off and dried to give **4.5** as a yellow solid. Yield: 490 mg (15%). **^{1}H NMR** (400 MHz, $CDCl_3$) (δ, ppm): 9.39 (d, $^1J_{HP}$ = 481.6 Hz, 1H, P*H*), 8.74 (d, $^3J_{HH}$ = 9.2 Hz, 2H, C*H*), 8.48 – 8.33 (m, 2H, C*H*), 8.31 – 8.13 (m, 7H, C*H*), 8.12 – 7.97 (m, 7H, C*H*). **^{31}P{^{1}H} NMR** (162 MHz, $CDCl_3$) (δ, ppm): 20.4 (s, 1P). **^{31}P NMR** (162 MHz, $CDCl_3$) (δ, ppm): 20.36 (dt, $^1J_{PH}$ = 482 Hz, $^4J_{PH}$ = 16 Hz). **HRMS (ESI):** *m*/*z* calculated for $C_{32}H_{19}OP$ $[M]^{\bullet+}$ = 451.1251, found = 451.1242.

6.4.4 Synthesis of (1-Pyr)$_2$PNMe$_2$, 4.6

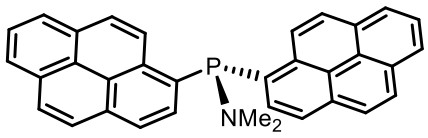

A solution of 1-bromopyrene **4.2** (1.13 g, 4.00 mmol) in Et_2O (40 mL) was cooled to –78 °C and a solution of ^{n}BuLi (1.6 M in hexane) (2.75 mL, 4.40 mmol) was added dropwise. After 1 h stirring at 0 °C, $(Me_2N)PCl_2$ (0.23 mL, 2.0 mmol) was added dropwise and the mixture warmed to room temperature. After 2 h the solvent was removed *in vacuo* and LiCl was extracted into MeOH (30 mL). The remaining yellow solid was dried *in vacuo*. Yield: 650 mg (68%). **^{1}H NMR** (400 MHz, $CDCl_3$) (δ, ppm): 8.62 (dd, $^3J_{HH}$ = 9.2 Hz, $^4J_{HH}$ = 3.9 Hz, 2H, C*H*), 8.20 (t, $^3J_{HH}$ = 7.6 Hz, 4H, C*H*), 8.13 – 7.98 (m, 9H, C*H*), 7.87 (dd, $^3J_{HH}$ = 7.9 Hz, $^4J_{HH}$ = 4.1 Hz, 2H, C*H*), 2.90 (d, $^3J_{HP}$ = 8.8 Hz, 6H, CH_3). **^{31}P{^{1}H} NMR** (162 MHz, $CDCl_3$) (δ, ppm): 53.8 (s, 1P). **HRMS (ESI):** *m*/*z* calculated for $C_{32}H_{19}OP$ $[M]^{\bullet+}$ = 477.1646, found $[M+CH_3]^{\bullet+}$= 492.1881.

6.4.5 Synthesis of di(1-pyrenyl)phosphine, L$_{4.2}$

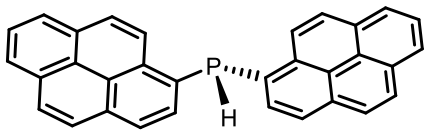

A solution of 1-bromopyrene **4.2** (1.20 g, 5.00 mmol) in THF (40 mL) was cooled to –78 °C and a solution of ^{n}BuLi (1.6 M in hexane) (3.44 mL, 5.50 mmol) was added dropwise. After 1 h $(Me_2N)PCl_2$ (0.29 mL, 2.5 mmol) was added and the solution warmed to room temperature for 2 h. The solution was cooled to –78 °C and a solution of HCl (2 M in Et_2O) (2.50 mL, 5.00 mmol) was added dropwise. After 1 h, $LiAlH_4$ (142 mg, 3.8 mmol) and TMSCl (0.50 mL, 3.8 mmol) were added at –78 °C and the mixture was warmed to room temperature and stirred for 16 h. The solution was quenched with degassed water (1 mL) and filtered through silica. The solvent was removed *in vacuo* to give the product as a yellow solid. Yield: 820 mg (76% from **4.2**). **^{1}H NMR** (400 MHz, C_6D_6) (δ, ppm): 8.81 (s, 1H), 8.10 – 7.51 (m, 10H, C*H*), 7.28 – 6.87 (m, 7H, C*H*), 6.20 (d,

$^{1}J_{PH}$ = 223 Hz, 1H, P*H*). **^{31}P{^{1}H} NMR** (162 MHz, C_6D_6) (δ, ppm): –59.5 (s, 1P). **^{31}P NMR** (162 MHz, C_6D_6) (δ, ppm) –59.5 (d, $^{1}J_{PH}$ = 223 Hz). **HRMS (MALDI):** *m*/*z* calculated for $C_{32}H_{19}P$ $[M–H]^{\bullet+}$ = 433.1141, found = 433.1149.

6.4.6 Synthesis of tri(1-pyrenyl)phosphine, $L_{4.3}$

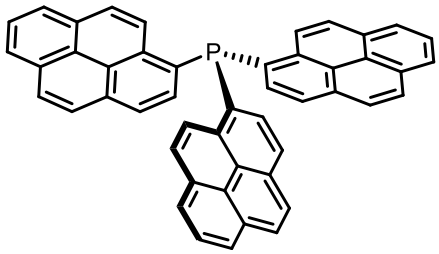

A solution of ^{n}BuLi (1.6 M in hexane, 6.0 mL, 9.0 mmol) was added to a solution of 1-bromopyrene **4.2** (2.41 g, 8.57 mmol) in Et_2O (80 mL) at –78 °C. The mixture was stirred for 1 h before PCl_3 (0.25 mL, 2.86 mmol) was added and warmed to room temperature. Volatiles were removed *in vacuo* and LiCl was extracted into MeOH. The solution was filtered, and the solvent removed *in vacuo* to give the product as a yellow solid. Yield: 1.50 g (83%). Spectroscopic data matched that previously reported.[231] **^{31}P{^{1}H} NMR** (162 MHz, $CDCl_3$) (δ, ppm): –30.6 (s, 1P).

6.4.7 Synthesis of $[RuCl_2(\eta^6\text{-}p\text{-cym})(L_{4.1})]$ complex, 4.14

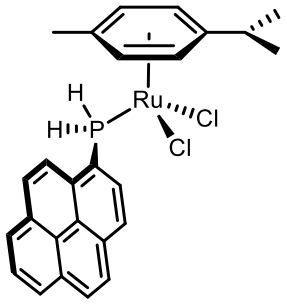

A solution of $[(\eta^6\text{-}p\text{-cymene})RuCl_2]_2$ (40 mg, 0.070 mmol) and $L_{4.1}$ (30 mg, 0.105 mmol) in CH_2Cl_2 (10 mL) was stirred at room temperature. After 1 h, the solvent was removed *in vacuo* to give the complex as a red solid. Yield: 42 mg (71%). Crystals suitable for X-ray diffraction were grown by evaporation of a CH_2Cl_2 solution of the product. **^{1}H NMR** (400 MHz, $CDCl_3$) (*δ*, ppm): 8.58 (d, $^{3}J_{HH}$ = 9.1 Hz, 1H, C*H*), 8.41 – 8.28 (m, 4H, C*H*), 8.24 (dd, $^{3}J_{HH}$ = 8.4 Hz, $^{4}J_{HH}$ = 3.3 Hz, 2H, C*H*), 8.18 – 8.09 (m, 2H, C*H*), 6.16 (d, $^{1}J_{HP}$ = 392 Hz, 2H, PH_2), 5.24 (d, $^{3}J_{HH}$ = 5.0 Hz, 2H, C*H*), 5.00 (d, $^{3}J_{HH}$ = 5.8 Hz, 2H, C*H*), 2.65 (hept, $^{3}J_{HH}$ = 7.0 Hz, 1H, C*H*$(CH_3)_2$, 2.00 (s, 3H, CH_3), 1.13 (d, $^{3}J_{HH}$ = 6.9 Hz, 6H, CH(CH_3)$_2$). **^{31}P{^{1}H} NMR** (162 MHz, $CDCl_3$) (*δ*, ppm): –26.4 (s, 1P). **^{31}P NMR** (162 MHz, $CDCl_3$) (*δ*, ppm): –26.4 (td, $^{1}J_{PH}$ = 392 Hz, $^{3}J_{PH}$ = 13 Hz). **^{13}C{^{1}H} NMR** (101 MHz, $CDCl_3$) (*δ*, ppm): 134.0, 131.3, 130.8, 129.7, 127.3, 127.0, 126.9, 126.7, 125.6, 124.8, 124.2, 87.6 (d, J_{CP} = 5.3 Hz), 86.7 (d, J_{CP} = 3.8 Hz), 30.7, 22.2, 18.6. **HRMS (ESI):** *m*/*z* calculated for $[M–Cl–HCl]^{\bullet+}$ = 469.0659, found 469.0657.

6.4.8 Synthesis of [RuCl(η^6-*p*-cym)(DPPP)] complex, 4.16

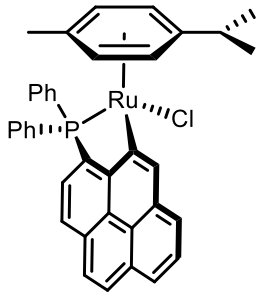

Following an adapted literature procedure.[253] A mixture of [(η^6-*p*-cymene)$RuCl_2$]$_2$ (31 mg, 0.050 mmol), DPPP (39 mg, 0.105 mmol), and NaOAc (16 mg, 0.200 mmol) in MeOH (10 mL) was stirred at room temperature for 1 h. The solvent was removed *in vacuo* and the residue was purified by silica column chromatography (50% petroleum ether/Et_2O). The yellow band was collected and concentrated *in vacuo* to give the product as a yellow solid. Yield: 46 mg (70%). **^{1}H NMR** (400 MHz, $CDCl_3$) (δ, ppm): 8.94 (s, 1H, C*H*), 8.21 – 8.11 (m, 6H, C*H*), 8.11 – 8.05 (m, 2H, C*H*), 8.02 – 7.96 (m, 1H, C*H*), 7.49 – 7.40 (m, 3H, C*H*), 7.39 – 7.28 (m, 3H, C*H*), 7.24 – 7.16 (m, 2H, C*H*), 6.03 – 5.90 (m, 2H, C*H*), 4.63 (ddt, $^3J_{HP}$ = 24.3 Hz, $^3J_{HH}$ = 6.2 Hz, $^4J_{HH}$ = 1.6 Hz, 2H, C*H*), 2.51 (hept, $^3J_{HH}$ = 7.2 Hz, 1H, C*H*(CH_3)$_2$), 1.98 (s, 3H, CH_3), 1.08 (d, $^3J_{HH}$ = 6.9 Hz, 3H, CH(CH_3)$_2$), 0.75 (d, $^3J_{HH}$ = 6.9 Hz, 3H, CH(CH_3)$_2$). **^{31}P{^{1}H} NMR** (162 MHz, $CDCl_3$) (δ, ppm): 67.1 (s, 1P). **HRMS (Nanospray):** *m*/*z* calculated for $C_{38}H_{32}PRu$ $[M–Cl]^{\bullet+}$ = 621.1285, found 621.1292.

6.4.9 Synthesis of [$RuCl_2$(η^6-*p*-cym)($L_{4.2}$)] complex, 4.17

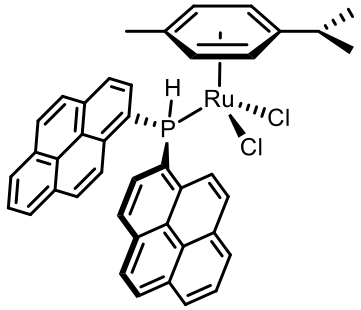

A solution of [(η^6-*p*-cymene)$RuCl_2$]$_2$ (47 mg, 0.080 mmol) and **$L_{4.2}$** (70 mg, 0.155 mmol) in CH_2Cl_2 (10 mL) was stirred at room temperature. After 1 h the solvent was removed *in vacuo* to give the complex as a red solid. Yield: 32 mg (31%). **^{1}H NMR** (400 MHz, CD_2Cl_2) (δ, ppm): 8.49 – 8.43 (m, 3H, C*H*), 8.21 (d, $^3J_{HH}$ = 7.8 Hz, 4H, C*H*), 8.16 – 8.04 (m, 6H, C*H*), 8.00 (d, $^1J_{HP}$ = 401 Hz, 1H, P*H*), 8.01 – 7.91 (m, 4H, C*H*), 5.48 (d, $^3J_{HH}$ = 5.8 Hz, 2H, C*H*), 5.39 (d, $^3J_{HH}$ = 5.8 Hz, 2H, C*H*), 2.49 (hept, $^3J_{HH}$ = 7.0 Hz, 1H, C*H*(CH_3)$_2$), 1.99 (s, 3H, CH_3), 0.80 (d, $^3J_{HH}$ = 6.9 Hz, 6H, CH(CH_3)$_2$). **^{31}P{^{1}H} NMR** (162 MHz, CD_2Cl_2) (δ, ppm): 5.2 (br. s, 1P). **^{31}P NMR** (162 MHz, CD_2Cl_2) (δ, ppm): 5.2 (d, $^1J_{PH}$ = 405 Hz). **^{13}C{^{1}H} NMR** (101 MHz, CD_2Cl_2) (δ, ppm): 134.0 (d, J_{CP} = 2.3 Hz), 133.9 (d, J_{CP} = 15.4 Hz), 132.9 (d, J_{CP} = 2.4 Hz), 131.6, 130.8, 129.8, 129.5, 127.8, 127.0, 126.8 (d, J_{CP} = 3.4 Hz), 125.5 (d, J_{CP} = 6.0 Hz), 125.4 (d, J_{CP} = 7.0 Hz), 124.9, 124.8, 124.7, 108.8, 98.7, 88.7 (d, J_{CP} = 4.8 Hz), 86.8 (d, J_{CP} = 5.2 Hz), 30.9, 21.9, 18.3. **HRMS (ESI):** *m*/*z* calculated for $C_{42}H_{32}PRu$ $[M–Cl–HCl]^{\bullet+}$ = 669.1285, found 669.1290.

6.4.10 Synthesis of [(DPPP)AuCl] complex, 4.22

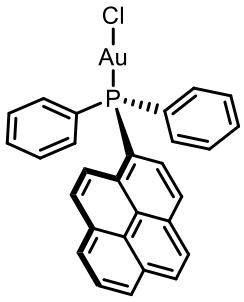

A solution of [(tht)AuCl] (32 mg, 0.110 mmol) and 1-pyrenyldiphenylphosphine, DPPP (39 mg, 0.110 mmol) in CH_2Cl_2 (10 mL) was stirred at room temperature. After 7 h, the product was precipitated from hexane, then filtered off and then dried *in vacuo*. Yield: 42 mg (68%). Spectroscopic data matched that previously reported.[312] **^{1}H NMR** (400 MHz, $CDCl_3$) (δ, ppm): 8.72 (dd, $^3J_{HH}$ = 9.2 Hz, $^4J_{HH}$ = 1.5 Hz, 1H), 8.28 (dd, $^3J_{HH}$ = 10.9 Hz, $^3J_{HH}$ = 7.6 Hz, 2H), 8.20 (t, $^3J_{HH}$ = 8.3 Hz, 2H), 8.16 – 8.04 (m, 4H), 7.69 – 7.54 (m, 5H), 7.53 – 7.41 (m, 5H). **^{31}P{^{1}H} NMR** (162 MHz, $CDCl_3$) (δ, ppm): 27.5 (s, 1P).

6.4.11 Synthesis of $Ph_2PCH_2CH_2P(Pyr)_2$, $L_{4.4}$

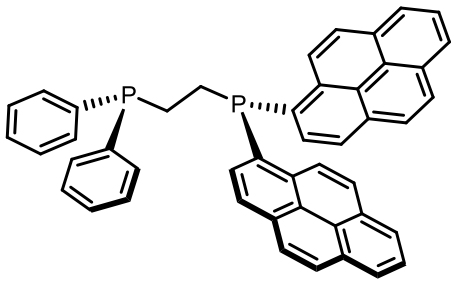

Mg turnings (54 mg, 2.2 mmol) and one crystal of I_2 were stirred under nitrogen. THF (10 mL) was added and a solution of 1-bromopyrene (562 mg, 2.00 mmol) in THF (5 mL) was added slowly to maintain reflux. The Grignard reagent was added to a solution of $Ph_2PCH_2CH_2PCl_2$ (315 mg, 1.00 mmol) in THF (10 mL) dropwise at –78 °C. The yellow suspension was warmed to room temperature and stirred for 1 h. The reaction was quenched with degassed water (5 mL), the organic layer was separated, dried over $MgSO_4$ and the product was precipitated by addition of EtOH. The product was filtered off and dried *in vacuo* to give **$L_{4.4}$** as a pale yellow solid. Yield: 170 mg (26%). **^{1}H NMR** (400 MHz, $CDCl_3$) (δ, ppm): 8.96 (dd, $^3J_{HH}$ = 9.2 Hz, $^4J_{HH}$ = 5.0 Hz, 2H), 8.18 (dt, $^3J_{HH}$ = 8.0 Hz, $^4J_{HH}$ = 4.2 Hz, 6H), 8.12 – 7.96 (m, 11H), 7.79 (dd, $^3J_{HH}$ = 7.9 Hz, $^4J_{HH}$ = 3.8 Hz, 2H), 7.35 – 7.20 (m, 7H), 2.54 (q, $^3J_{HH}$ = 8.0 Hz, 2H), 2.31 (q, $^3J_{HH}$ = 8.0 Hz, 2H).**^{31}P{^{1}H} NMR** (162 MHz, $CDCl_3$) (δ, ppm): –11.8 (d, $^3J_{PP}$ = 36 Hz), –34.4 (d, $^3J_{PP}$ = 36 Hz). **^{13}C{^{1}H} NMR** (101 MHz, $CDCl_3$) (δ, ppm): 138.2 (d, J_{CP} = 13.6 Hz), 134.4 (d, J_{CP} = 22.8 Hz), 133.0, 132.8, 131.8, 131.4, 131.0, 129.4, 128.8, 128.6, 128.5, 128.2, 127.9, 127.4, 126.1, 125.6, 125.5, 125.2, 125.0, 24.7 – 24.2 (m, CH_2), 24.2 – 23.7 (m, CH_2). **HRMS (MALDI):** *m/z* calculated for $C_{47}H_{33}P_2$ $[M+H]^{\bullet+}$ = 647.1979, found 647.1965.

6.4.12 Fluorescence quantum yield measurements, Φ_f

Quantum yields were determined relative to quinine sulfate (λ_{ex} = 350 nm) in 0.1 M H_2SO_4 as a standard (Φ_f = 0.58).[216] Absorbance measurements were recorded on an Agilent Cary 300 spectrophotometer against a solvent reference. Quantum yield measurements require the absorbance (optical density) of the solution at the absorption maxima to be < 0.1, thus appropriate sample concentrations were selected (2 – 20 μM). Limiting the absorbance to < 0.1 minimizes non-linear effects arising from inner filter (re-absorption) effects, which may otherwise skew the resulting quantum yield.[313] Fluorescence measurements were recorded on a Perkin Elmer LS-45 fluorescence spectrometer in capped quartz cuvettes in deaerated solvent.

Fluorescence quantum yields were calculated according to the following equation:

$$\Phi_{sample} = \Phi_{std} \times \left(\left(\frac{m_{sample}}{m_{std}} \right) \times \left(\frac{\eta_{sample}}{\eta_{std}} \right)^2 \right)$$

where:

m = gradient of the plot of integrated fluorescence intensity against absorbance, and

η = refractive index of the solvent, taken as 1.343 for 0.1 M H_2SO_4 and 1.424 for CH_2Cl_2.

6.5 Experimental procedures and characterising data for Chapter 5 – Non-symmetric PCP metallacycles for alkylation catalysis

6.5.1 Experimental procedures and characterising data for aminophosphines

6.5.1.1 Synthesis of 1,3-(^{t}Bu$_2$PNH)$_2$(C$_6$H$_4$), L$_{5.1}$

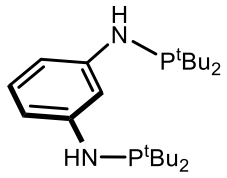

Following an adapted literature procedure.[131] A solution of 1,3-diaminobenzene (324 mg, 3.00 mmol) in THF (30 mL) was cooled to 0 °C and ^{n}BuLi (8.25 mL, 1.6 M in hexane, 6.60 mmol) was added. After stirring the mixture at room temperature for 1 h, the mixture was cooled to 0 °C and then ^{t}Bu$_2$PCl (1.25 mL, 6.60 mmol) was added. The solution was heated under reflux for 48 h, the volatiles were removed *in vacuo* and hexane was added to precipitate LiCl. The solution was then filtered, and the solvent removed *in vacuo* to give the product as an orange solid. Yield: 930 mg (78%). Spectroscopic data matched that previously reported. **^{1}H NMR** (400 MHz, CD_2Cl_2) (δ, ppm): 6.85 (t, $^3J_{HH}$ = 8.0 Hz, 1H, C*H*), 6.71 – 6.67 (m, 1H, C*H*), 6.35 – 6.30 (m, 2H, C*H*), 1.10 (d, $^3J_{HP}$ = 11.7 Hz, 36H, PC(CH_3)$_3$). **^{31}P{^{1}H} NMR** (162 MHz, CD_2Cl_2) (δ, ppm): 58.2 (s, 2P).

6.5.1.2 Synthesis of 1-(^{t}Bu$_2$PNH)-3-(^{t}Bu$_2$PNHCH$_2$)(C$_6$H$_4$), L$_{5.2}$

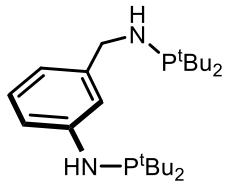

A solution of 3-aminobenzylamine (1.47 g, 12.0 mmol) in THF (150 mL) was cooled to 0 °C and ^{n}BuLi (33.0 mL, 1.6 M in hexane, 26.4 mmol) was added. After stirring the mixture at room temperature for 1 h, the mixture was cooled to 0 °C and ^{t}Bu$_2$PCl (5.01 mL, 26.4 mmol) was added. The solution was heated under reflux for 48 h, the volatiles were removed *in vacuo*, and hexane was added before filtration and evaporation. The residue was then dissolved in hot hexane, filtered and the solvent removed *in vacuo* to give the product as an orange oil. Yield: 2.55 g (52%). **^{1}H NMR** (400 MHz, $CDCl_3$) (δ, ppm): 7.10 (t, $^3J_{HH}$ = 7.7 Hz, 1H, C*H*), 7.00 (m, 1H, C*H*), 6.88 – 6.83 (m, 1H, C*H*), 6.74 (dt, $^3J_{HH}$ = 7.4 Hz, $^4J_{HH}$ = 1.3 Hz, 1H, C*H*), 4.08 (d, $^3J_{HP}$ = 6.3 Hz, 2H, CH_2), 1.13 (d, $^3J_{HP}$ = 8.7 Hz, 18H, PC(CH_3)$_3$)), 1.10 (d, $^3J_{HP}$ = 8.4 Hz, 18H, PC(CH_3)$_3$). **^{31}P{^{1}H} NMR** (162 MHz, $CDCl_3$) (δ, ppm): 81.6 (s, 1P, $CH_2NHP^tBu_2$), 59.3 (s, 1P, NHP^tBu_2). **^{13}C{^{1}H} NMR** (100 MHz, $CDCl_3$) (δ, ppm): 149.5 (d, $^2J_{CP}$ = 16.7 Hz, *C*NH), 144.0 (d, $^3J_{CP}$ = 9.6 Hz, *C*CH$_2$), 129.1 (s, *C*H), 117.6 (s, *C*H), 115.2 (d, $^3J_{CP}$ = 12.1 Hz, *C*H), 114.6 (d, $^3J_{CP}$ = 11.3 Hz, *C*H), 55.2 (d, $^2J_{CP}$ = 30.1 Hz, *C*H$_2$), 34.4 (d, $^1J_{CP}$ = 18.8 Hz, *C*(CH$_3$)$_3$), 34.3 (d, $^1J_{CP}$ = 19.4 Hz, *C*(CH$_3$)$_3$), 28.5 (d, $^2J_{CP}$ = 14.6 Hz, C(*C*H$_3$)$_3$), 28.2 (d, $^2J_{CP}$ = 15.1 Hz, C(*C*H$_3$)$_3$). **HRMS (ESI):** *m*/*z* calculated for $C_{23}H_{45}N_2P_2$ $[M+H]^{\bullet+}$ = 411.3013, found 411.3037.

6.5.1.3 Synthesis of 1,3-(^{t}Bu$_2$PNHCH$_2$)$_2$(C$_6$H$_4$), L$_{5.3}$

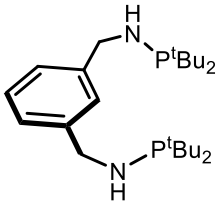

A solution of *m*-xylylenediamine (0.33 mL, 2.5 mmol) in THF (30 mL) was cooled to 0 °C and ^{n}BuLi (9.01 mL, 1.6 M in hexane, 7.25 mmol) was added. After stirring the mixture at room temperature for 3 h, the mixture was cooled to 0 °C and ^{t}Bu$_2$PCl (1.05 mL, 5.50 mmol) was added. The solution was heated under reflux for 48 h before the volatiles were removed *in vacuo* and hexane was added. The residue was then dissolved in hot hexane, filtered and the solvent removed *in vacuo* to give the product as a white solid. Yield: 670 mg (63%). **^{1}H NMR** (400 MHz, $CDCl_3$) (δ, ppm): 7.33 (s, 1H, C*H*), 7.31 – 7.21 (m, 3H, C*H*), 4.15 (t, $^3J_{HP}$ = 6.4 Hz, 4H, CH_2), 1.11 (d, $^3J_{HP}$ = 11.4 Hz, 36H, C(CH_3)$_3$). **^{31}P{^{1}H} NMR** (162 MHz, $CDCl_3$) (δ, ppm): 81.6 (s, 2P). **^{13}C{^{1}H} NMR** (100 MHz, $CDCl_3$) (δ, ppm): 143.0 (d, $^3J_{CP}$ = 10.0 Hz, *C*CH$_2$), 128.5 (s, CH), 127.0 (s, *C*H), 126.24 (s, *C*H), 55.23 (d, $^2J_{CP}$ = 29.9 Hz, *C*H$_2$), 34.42 (d, $^1J_{CP}$ = 19.0 Hz, *C*(CH$_3$)$_3$), 28.51 (d, $^2J_{CP}$ = 14.6 Hz, C(*C*H$_3$)$_3$). **HRMS (Nanospray):** *m*/*z* calculated for $C_{24}H_{47}N_2P_2$ $[M]^{\bullet+}$ = 425.3214, found 425.3226.

6.5.1.4 Synthesis of 1,3-(^{i}Pr$_2$PNH)$_2$(C$_6$H$_4$), L$_{5.4}$

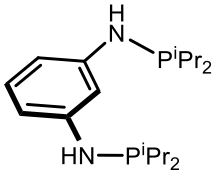

Following an adapted literature procedure.[144] A solution of 1,3-diaminobenzene (433 mg, 4.00 mmol) and DMAP (977 mg, 8.00 mmol) were combined in THF (40 mL). After stirring the mixture at room temperature for 10 min, ^{i}Pr$_2$PCl (1.27 mL, 8.00 mmol) was added. The solution immediately turned cloudy and was stirred at room temperature for 2 h, the volatiles were removed *in vacuo* and the product was extracted into toluene. The solution was then filtered through Celite, and the solvent removed *in vacuo* to give the product as a white solid. Yield: 1.23 g (90%). Spectroscopic data matched that previously reported. **^{31}P{^{1}H} NMR** (162 MHz, CD_2Cl_2) (δ, ppm): 46.0 (s, 2P).

6.5.1.5 Synthesis of 1-(^{i}Pr$_2$PNH)-3-(^{i}Pr$_2$PNHCH$_2$)(C$_6$H$_4$), L$_{5.5}$

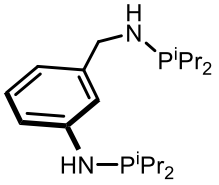

A solution of 3-aminobenzylamine (977 mg, 8.00 mmol) and DMAP (1.96 g, 16.00 mmol) were combined in THF (60 mL). After stirring the mixture at room temperature for 10 min, ^{i}Pr$_2$PCl (2.55 mL, 16.00 mmol) was added. The solution immediately turned cloudy and was stirred at room temperature for 2 h, the volatiles were removed *in vacuo* and the product was extracted into toluene. The solution was then filtered through Celite, and the solvent removed *in vacuo* to give the product as a white solid. Yield: 2.29 g (81%). **^{1}H NMR** (400 MHz, CD_2Cl_2) (δ, ppm): 7.06 (t, $^3J_{HH}$ = 7.8 Hz, 1H, C*H*), 6.98 (q, $^3J_{HH}$ = 2.1 Hz, 1H, C*H*),

6.87 – 6.79 (m, 1H, C*H*), 6.69 (d, $^3J_{HH}$ = 7.5 Hz, 1H, C*H*), 4.02 (t, $^3J_{HH}$ = 6.7 Hz, 1H, CH_2), 1.77 (hept, $^3J_{HH}$ = 7.0 Hz, 2H, PC*H*(CH_3)$_2$)), 1.66 (hept, $^3J_{HH}$ = 7.0 Hz, 2H, PC*H*(CH_3)$_2$)), 1.27 – 1.14 (m, 4H, PCH(CH_3)$_2$)), 1.13 – 1.01 (m, 20H, PCH(CH_3)$_2$)). **^{31}P{^{1}H} NMR** (162 MHz, CD_2Cl_2) (δ, ppm): 67.9 (s, 1P, $CH_2NHP^iPr_2$), 49.1 (s, 1P, NHP^iPr_2). **^{13}C{^{1}H} NMR** (100 MHz, CD_2Cl_2) (δ, ppm): 149.9 (d, $^2J_{CP}$ = 15.9 Hz, *C*NH), 144.7 (d, $^3J_{CP}$ = 7.7 Hz, *C*CH_2), 129.4 (s, *C*H), 117.9 (s, *C*H), 115.4 (d, $^3J_{CP}$ = 12.1 Hz, *C*H), 114.8 (d, $^3J_{CP}$ = 11.6 Hz, *C*H), 53.5 (d, $^2J_{CP}$ = 24.9 Hz, *C*H_2), 27.3 (dd, $^1J_{CP}$ = 12.0 Hz, *C*H(CH_3)$_2$), 19.6 (d, $^2J_{CP}$ = 20.3 Hz, CH(*C*H_3)$_2$), 19.2 (d, $^2J_{CP}$ = 20.0 Hz, CH(*C*H_3)$_2$), 17.9 (d, $^2J_{CP}$ = 7.8 Hz, CH(*C*H_3)$_2$), 17.4 (d, $^2J_{CP}$ = 7.9 Hz, CH(*C*H_3)$_2$). **HRMS (ESI):** *m*/*z* calculated for $C_{19}H_{37}N_2P_2$ $[M+H]^{\bullet+}$ = 355.2426, found 355.2442.

6.5.1.6 Synthesis of 1,3-(^{i}Pr$_2$PNHCH$_2$)$_2$(C_6H_4), $L_{5.6}$

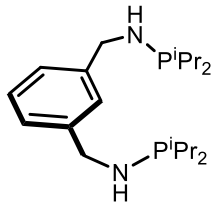

A solution of *m*-xylylenediamine (0.264 mL, 2.00 mmol) and DMAP (489 mg, 4.00 mmol) were combined in THF (20 mL). After stirring the mixture at room temperature for 10 min, ^{i}Pr$_2$PCl (0.637 mL, 4.00 mmol) was added. The solution immediately turned cloudy and was stirred at room temperature for 2 h, the volatiles were removed *in vacuo* and the product was extracted into toluene. The solution was then filtered through Celite, and the solvent removed *in vacuo* to give the product as a white solid. Yield: 580 mg (79%). **^{1}H NMR** (400 MHz, CD_2Cl_2) (δ, ppm): 7.33 – 7.30 (m, 1H, C*H*), 7.28 – 7.22 (m, 1H, C*H*), 7.22 – 7.16 (m, 2H, C*H*), 4.10 (t, $^3J_{HH}$ = 7.0 Hz, 4H, CH_2), 1.66 (hept, $^3J_{HH}$ = 7.0 Hz, 4H, PC*H*(CH_3)$_2$)), 1.13 – 0.98 (m, 24H, PCH(CH_3)$_2$)). **^{31}P{^{1}H} NMR** (162 MHz, CD_2Cl_2) (δ, ppm): 68.0 (s, 2P). **^{13}C{^{1}H} NMR** (100 MHz, CD_2Cl_2) (δ, ppm): 143.7 (d, $^3J_{CP}$ = 7.8 Hz, *C*CH_2), 128.7 (s, *C*H), 127.1 (s, *C*H), 126.4 (s, *C*H), 53.5 (d, $^2J_{CP}$ = 25.0 Hz, *C*H_2), 27.3 (d, $^1J_{CP}$ = 12.2 Hz, *C*H(CH_3)$_2$), 19.6 (d, $^2J_{CP}$ = 20.1 Hz, CH(*C*H_3)$_2$), 17.9 (d, $^2J_{CP}$ = 7.9 Hz, CH(*C*H_3)$_2$). **HRMS (ESI):** *m*/*z* calculated for $C_{20}H_{39}N_2P_2$ $[M+H]^{\bullet+}$ = 369.2595, found 369.2595.

6.5.1.7 Synthesis of 1,3-(Ph_2PNH)$_2$(C_6H_4), $L_{5.7}$

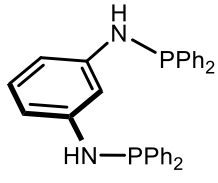

Following an adapted literature procedure.[144] A solution of 1,3-diaminobenzene (433 mg, 4.00 mmol) and DMAP (977 mg, 8.00 mmol) were combined in THF (40 mL). After stirring the mixture at room temperature for 10 min, Ph_2PCl (1.43 mL, 8.00 mmol) was added. The solution immediately turned cloudy and was stirred at room temperature for 2 h, the volatiles were removed *in vacuo* and the product was extracted into toluene. The solution was then filtered through Celite, and the solvent removed *in vacuo* to give the

product as a white solid. Yield: 1.55 g (82%). Spectroscopic data matched that previously reported. **^{31}P{^{1}H} NMR** (162 MHz, CD_2Cl_2) (δ, ppm): 24.8 (s, 2P).

6.5.1.8 Synthesis of 1-(Ph_2PNH)-3-(Ph_2PNHCH_2)(C_6H_4), $L_{5.8}$

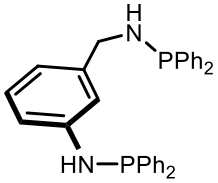

A solution of 3-aminobenzylamine (733 mg, 6.00 mmol) and DMAP (1.47 g, 12.00 mmol) were combined in THF (60 mL). After stirring the mixture at room temperature for 10 min Ph_2PCl (2.15 mL, 12.00 mmol) was added. The solution immediately turned cloudy and was stirred at room temperature for 2 h, the volatiles were removed *in vacuo* and the product was extracted into toluene. The solution was then filtered through Celite, and the solvent removed *in vacuo* to give the product as a white solid. Yield: 2.47 g (84%). **^{1}H NMR** (400 MHz, CD_2Cl_2) (δ, ppm): 7.50 – 7.41 (m, 8H, P*Ph*$_2$), 7.41 – 7.36 (m, 6H, P*Ph*$_2$), 7.36 – 7.30 (m, 6H, P*Ph*$_2$), 7.11 (t, $^{3}J_{HH}$ = 7.8 Hz, 1H, C*H*), 6.96 (q, $^{3}J_{HH}$ = 2.1 Hz, 1H, C*H*), 6.89 (dt, $^{3}J_{HH}$ = 8.0 Hz, $^{5}J_{HH}$ = 2.2 Hz, 1H, C*H*), 6.73 (dt, $^{3}J_{HH}$ = 7.6 Hz, $^{5}J_{HH}$ = 1.3 Hz, 1H, C*H*), 4.01 (app. t, $^{3}J_{HH}$ = 8.1 Hz, 2H, C*H*$_2$). **^{31}P{^{1}H} NMR** (162 MHz, CD_2Cl_2) (δ, ppm): 42.7 (s, 1P, CH_2NHPPh_2), 27.9 (s, 1P, $NHPPh_2$). **^{13}C{^{1}H} NMR** (101 MHz, CD_2Cl_2) (δ, ppm): 142.1 (d, $^{2}J_{CP}$ = 13.1 Hz, *C*NH), 140.8 (d, $^{2}J_{CP}$ = 12.2 Hz, *C*CH$_2$), 132.0 (s, *C*H), 131.8 (d, J_{CP} = 1.7 Hz, *C*H), 131.5 (s, *C*H), 129.7 (s, *C*H), 129.2 – 128.9 (m, P*Ph*$_2$), 128.9 – 128.6 (m, P*Ph*$_2$), 119.0 (s, *C*H), 115.5 (d, J_{CP} = 13.0 Hz, *C*H), 115.0 (d, J_{CP} = 13.2 Hz, *C*H), 50.7 (d, $^{2}J_{CP}$ = 15.6 Hz, *C*H$_2$). **HRMS (ESI):** *m*/*z* calculated for $C_{31}H_{29}N_2P_2$ $[M+H]^{\bullet+}$ = 491.1800, found 491.1790.

6.5.1.9 Synthesis of 1,3-(Ph_2PNHCH_2)$_2$(C_6H_4), $L_{5.9}$

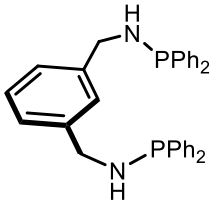

A solution of *m*-xylylenediamine (0.264 mL, 2.00 mmol) and DMAP (489 mg, 4.00 mmol) were combined in THF (20 mL). After stirring the mixture at room temperature for 10 min, Ph_2PCl (0.718 mL, 4.00 mmol) was added. The solution immediately turned cloudy and was stirred at room temperature for 2 h, the volatiles were removed *in vacuo* and the product was extracted into toluene. The solution was then filtered through Celite, and the solvent removed *in vacuo* to give the product as a white solid. Yield: 550 mg (55%). **^{1}H NMR** (400 MHz, CD_2Cl_2) (δ, ppm): 7.49 – 7.40 (m, 8H, PPh_2), 7.39 – 7.30 (m, 12H, PPh_2), 7.24 – 7.19 (m, 1H, CH), 7.17 – 7.10 (m, 3H, CH), 4.12 – 3.97 (m, 4H, CH_2). **^{31}P{^{1}H} NMR** (162 MHz, CD_2Cl_2) (δ, ppm): 42.7 (s, 2P). **^{13}C{^{1}H} NMR** (100 MHz, CD_2Cl_2) (δ, ppm): 142.5 (d, $^{3}J_{CP}$ = 6.5 Hz, *C*CH$_2$), 142.1 (d, $^{3}J_{CP}$ = 13.1 Hz, *C*CH$_2$), 131.9 (d, $^{1}J_{CP}$ = 19.7 Hz, P*Ph*$_2$), 129.0 (s, *C*H), 128.9 (s, *C*H), 128.8 (d, $^{3}J_{CP}$ = 6.3 Hz, *C*H), 127.3 (s, *C*H), 126.6 (s,

*C*H), 50.7 (d, $^2J_{CP}$ = 15.7 Hz, *C*H$_2$). **HRMS (ESI):** *m*/*z* calculated for $C_{32}H_{31}N_2P_2$ $[M+H]^{\bullet+}$ = 505.1962, found 505.1971.

6.5.2 Experimental procedures and characterising data for PCP coordination compounds

6.5.2.1 Synthesis of [($L_{5.1}$)PdCl] complex, 5.8

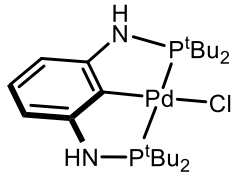

A solution of **$L_{5.1}$** (150 mg, 0.40 mmol) and [PdCl$_2$(cod)] (86 mg, 0.30 mmol) in toluene (15 mL) was heated under reflux for 18 h. After *in situ* $^{31}P\{^1H\}$ NMR showed complete conversion to the target complex, the mixture was cooled, and volatiles removed *in vacuo* to give the product as a yellow solid. Yield: 156 mg (97%). Spectroscopic data matched that previously reported.[314] **^{1}H NMR** (400 MHz, $CDCl_3$) (δ, ppm): 6.71 (tt, $^3J_{HH}$ = 7.7 Hz, $^5J_{HH}$ = 1.4 Hz, 1H, C*H*), 6.11 (d, $^3J_{HH}$ = 7.7 Hz, 2H, C*H*), 4.16 (s, 2H, N*H*), 1.41 (app. t, $^3J_{HP}$ = 7.3 Hz, 36H, C(CH_3)$_3$). **^{31}P{^{1}H} NMR** (162 MHz, $CDCl_3$) (δ, ppm): 119.5 (s, 2P). **HRMS (ESI):** *m*/*z* calculated for $C_{22}H_{41}N_2P_2Pd$ $[M–Cl]^{\bullet+}$ = 501.1780, found 501.1781.

6.5.2.2 Synthesis of [($L_{5.2}$)PdCl] complex, 5.9

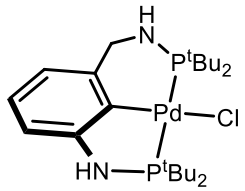

A solution of **$L_{5.2}$** (111 mg, 0.27 mmol) and [PdCl$_2$(NCPh)$_2$] (58 mg, 0.15 mmol) in CH_2Cl_2 (10 mL) was stirred for 1 h at room temperature. After *in situ* $^{31}P\{^1H\}$ NMR showed complete conversion to the target complex, hexane was added, the mixture was filtered, and the volatiles removed *in vacuo* to give the product as a yellow solid. Yield: 70 mg (84%). Crystals suitable for X-ray diffraction were grown by evaporation of a CH_2Cl_2 solution of the product. **^{1}H NMR** (400 MHz, $CDCl_3$) (δ, ppm): 6.79 (t, $^3J_{HH}$ = 7.5 Hz, 1H, C*H*), 6.52 (d, $^3J_{HH}$ = 7.8 Hz, 1H, C*H*), 6.40 (d, $^3J_{HH}$ = 7.2 Hz, 1H, C*H*), 4.09 (s, 1H, N*H*), 3.94 (d, $^3J_{HP}$ = 19.4 Hz, 2H, CH_2), 1.40 (app. t, $^3J_{HP}$ = 14.6 Hz, 36H, C(CH_3)$_3$). **^{31}P{^{1}H} NMR** (162 MHz, $CDCl_3$) (δ, ppm): 122.2 (d, $^2J_{PP}$ = 406 Hz, NHP^{t}Bu$_2$), 89.7 (d, $^2J_{PP}$ = 406 Hz, CH$_2$NHP^{t}Bu$_2$). **^{13}C{^{1}H} NMR** (100 MHz, $CDCl_3$) (δ, ppm): 142.0 (d, $^3J_{CP}$ = 8.0 Hz, quat. *C*), 127.6 (s, quat. *C*), 126.1 (s, *C*H), 118.4 (s, *C*H), 109.4 (d, $^3J_{CP}$ = 14.3 Hz, *C*H), 57.1 (d, $^2J_{CP}$ = 10.1 Hz, *C*H$_2$), 38.7 (dd, $^1J_{CP}$ = 10.9 Hz, $^3J_{CP}$ = 4.7 Hz, *C*(CH$_3$)$_3$), 38.3 (dd, $^1J_{CP}$ = 15.7 Hz, $^3J_{CP}$ = 4.8 Hz, *C*(CH$_3$)$_3$), 30.0 (d, $^2J_{CP}$ = 5.1 Hz, C(*C*H$_3$)$_3$), 28.9 (d, $^2J_{CP}$ = 5.2 Hz, C(*C*H$_3$)$_3$). **HRMS (ESI):** *m*/*z* calculated for $C_{23}H_{44}N_2P_2ClPd$ $[M+H]^{\bullet+}$ = 551.1703, found 551.1709.

6.5.2.3 Synthesis of [($L_{5.3}$)PdCl] complex, 5.10

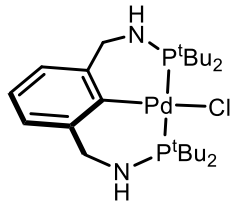

A solution of $\mathbf{L_{5.3}}$ (212 mg, 0.50 mmol) and $[PdCl_2(cod)_2]$ (143 mg, 0.50 mmol) in toluene (10 mL) was stirred for 18 h at 100 °C. After *in situ* $^{31}P\{^1H\}$ NMR showed complete conversion to the target complex, the solvent was removed *in vacuo* and the complex extracted into hexane. The hexane solution was then concentrated *in vacuo* and the precipitate was filtered off and dried to give the product as a pale-yellow solid. Yield: 142 mg (50%). Crystals suitable for X-ray diffraction were grown by evaporation of a hexane solution of the product. **^{1}H NMR** (500 MHz, CD_2Cl_2) (δ, ppm): 6.87 (m, 1H, C*H*), 6.78 (d, $^3J_{HH}$ = 7.2 Hz, 2H, C*H*), 4.13 – 3.99 (m, 4H, CH_2), 1.60 (t, $^3J_{HP}$ = 6.9 Hz, 18H, C(CH_3)$_3$), 0.98 (t, $^3J_{HP}$ = 7.0 Hz, 18H, C(CH_3)$_3$). **^{31}P{^{1}H} NMR** (162 MHz, CD_2Cl_2) (δ, ppm): 89.9 (s, 2P). **^{13}C{^{1}H} NMR** (100 MHz, CD_2Cl_2) (δ, ppm): 144.5 (t, $^2J_{CP}$ = 5.2 Hz, quat. *C*), 129.5 (quat. *C*), 124.7 (*C*H), 124.7 (*C*H), 59.3 (t, $^2J_{CP}$ = 6.0 Hz, *C*H_2), 29.9 (br. s, *C*(CH$_3$)$_3$), 29.6 (t, $^2J_{CP}$ = 3.7 Hz, C(*C*H$_3$)$_3$). **HRMS (ESI):** *m/z* calculated for $C_{24}H_{44}N_2P_2ClPd$ $[M–H]^{\bullet+}$ = 563.1703, found 563.1713.

6.5.2.4 Synthesis of [($L_{5.1}$)Pd(TFA)] complex, 5.17

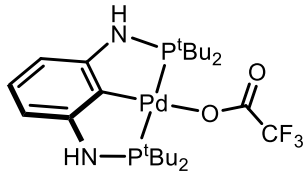

A solution of $\mathbf{L_{5.1}}$ (119 mg, 0.30 mmol) and $[Pd(TFA)_2]$ (100 mg, 0.30 mmol) in THF (10 mL) was stirred for 4 h at room temperature. After *in situ* $^{31}P\{^1H\}$ NMR showed complete conversion to the target complex, the solvent was removed *in vacuo* and the complex extracted into hexane. The hexane solution was concentrated *in vacuo* and the precipitate was filtered off and dried to give the product as a yellow solid. Yield: 65 mg (35%). Spectroscopic data matched that previously reported.[314] **^{1}H NMR** (400 MHz, CD_2Cl_2) (δ, ppm): 6.73 (tt, $^3J_{HH}$ = 7.8 Hz, $^5J_{HH}$ = 1.4 Hz, 1H, C*H*), 6.09 (d, $^3J_{HH}$ = 7.8 Hz, 2H, C*H*), 4.15 (s, 2H, N*H*), 1.40 – 1.32 (m, 36H, C(CH_3)$_3$). **^{31}P{^{1}H} NMR** (162 MHz, CD_2Cl_2) (δ, ppm): 119.9 (s, 2P). **HRMS (Nanospray):** *m/z* calculated for $C_{24}H_{42}F_3N_2O_2P_2Pd$ $[M+H]^{\bullet+}$ = 615.1708, found 615.1713.

6.5.2.5 Synthesis of [($L_{5.2}$)Pd(TFA)] complex, 5.18

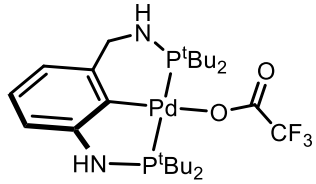

A solution of $\mathbf{L_{5.2}}$ (124 mg, 0.30 mmol) and $[Pd(TFA)_2]$ (100 mg, 0.30 mmol) in THF (10 mL) was stirred for 4 h at room temperature. After *in situ* $^{31}P\{^1H\}$ NMR showed complete conversion to the target complex, the solvent was removed *in vacuo* and the complex extracted into hexane. The hexane solution was concentrated *in*

vacuo and the precipitate was filtered off and dried to give the product as a grey solid. Yield: 142 mg (76%). **^{1}H NMR** (400 MHz, CD_2Cl_2) (δ, ppm): 6.84 – 6.76 (m, 1H, C*H*), 6.49 (dd, $^{3}J_{HH}$ = 7.7 Hz, $^{5}J_{HH}$ = 1.4 Hz, 1H, C*H*), 6.42 (ddd, $^{3}J_{HH}$ = 7.3 Hz, $^{4}J_{HH}$ = 2.3, $^{5}J_{HH}$ = 1.4 Hz, 1H, C*H*), 3.95 (d, $^{3}J_{HP}$ = 19.8 Hz, 2H, CH_2), 1.34 (d, $^{3}J_{HP}$ = 14.1 Hz, 18H, C(CH_3)$_3$), 1.27 (d, $^{3}J_{HP}$ = 13.7 Hz, 18H, C(CH_3)$_3$). **^{31}P{^{1}H} NMR** (162 MHz, CD_2Cl_2) (δ, ppm): 125.9 (d, $^{2}J_{PP}$ = 367 Hz, NHP^{i}Pr$_2$), 92.7 (d, $^{2}J_{PP}$ = 367 Hz, CH$_2$NHP^{i}Pr$_2$). **^{13}C{^{1}H} NMR** (101 MHz, CD_2Cl_2) (δ, ppm): 159.0 (app. d, $^{2}J_{CP}$ = 23.5 Hz), 142.9 (d, $^{3}J_{CP}$ = 8.4 Hz, quat. *C*), 127.6 (s, quat. *C*), 126.6 (s, *C*H), 118.7 (s, *C*H), 109.4 (d, $^{3}J_{CP}$ = 14.3 Hz, *C*H), 57.4 (d, $^{2}J_{CP}$ = 10.8 Hz, *C*H$_2$), 38.7 (dd, $^{1}J_{CP}$ = 10.9 Hz, $^{3}J_{CP}$ = 4.7 Hz, *C*(CH$_3$)$_3$), 38.3 (dd, $^{1}J_{CP}$ = 15.7 Hz, $^{3}J_{CP}$ = 4.8 Hz, *C*(CH$_3$)$_3$), 29.2 (d, $^{2}J_{CP}$ = 5.7 Hz, C(*C*H$_3$)$_3$), 28.6 (d, $^{2}J_{CP}$ = 6.1 Hz, C(*C*H$_3$)$_3$). **HRMS (Nanospray):** *m*/*z* calculated for $C_{25}H_{42}F_3N_2O_2P_2Pd$ [M–H]$^{\bullet+}$ = 627.1708, found 627.1703. *m*/*z* calculated for $C_{24}H_{43}N_2P_2Pd$ [M–TFA]$^{\bullet+}$ = 515.1936, found 515.1991.

6.5.2.6 Synthesis of [($L_{5.3}$)Pd(TFA)] complex, 5.19

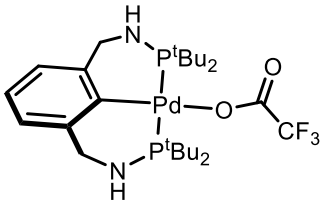

A solution of **$L_{5.3}$** (127 mg, 0.30 mmol) and [Pd(TFA)$_2$] (100 mg, 0.30 mmol) in THF (10 mL) was stirred for 4 h at room temperature. After *in situ* ^{31}P{^{1}H} NMR showed complete conversion to the target complex, the solvent was removed *in vacuo* and the complex extracted into hexane. The hexane solution was concentrated *in vacuo* and the precipitate was filtered off and dried to give the product as a yellow solid. Yield: 95 mg (49%). **^{1}H NMR** (400 MHz, CD_2Cl_2) (δ, ppm): 6.90 (dd, $^{3}J_{HP}$ = 7.7 Hz, $^{3}J_{HP}$ = 6.7 Hz, 1H, C*H*), 6.78 (d, $^{3}J_{HP}$ = 7.2 Hz, 2H, C*H*), 4.25 – 4.04 (m, 4H, CH_2), 1.37 (app. t (1:1:1), 18H, C(CH_3)$_3$), 0.92 (app. t (1:1:1), 18H, C(CH_3)$_3$). **^{31}P{^{1}H} NMR** (162 MHz, CD_2Cl_2) (δ, ppm): 92.7 (s, 2P). **^{13}C{^{1}H} NMR** (100 MHz, CD_2Cl_2) (δ, ppm): 144.5 (t, $^{2}J_{CP}$ = 5.2 Hz, quat. *C*), 129.5 (quat. *C*), 124.7 (*C*H), 124.7 (*C*H), 59.3 (t, $^{2}J_{CP}$ = 6.0 Hz, *C*H$_2$), 29.9 (br. s, *C*(CH$_3$)$_3$), 29.6 (t, $^{2}J_{CP}$ = 3.7 Hz, C(*C*H$_3$)$_3$). **HRMS (Nanospray):** *m*/*z* calculated for $C_{24}H_{45}N_2P_2Pd$ [M–TFA]$^{\bullet+}$ = 529.2093, found 529.2096.

6.5.2.7 Synthesis of [($L_{5.5}$)Pd(TFA)] complex, 5.21

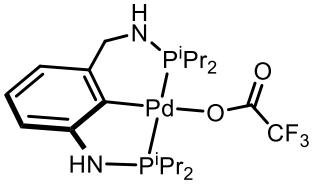

A solution of **$L_{5.5}$** (106 mg, 0.30 mmol) in THF (2.5 mL) was added to a suspension of [Pd(TFA)$_2$] (100 mg, 0.30 mmol) in THF (2.5 mL) and stirred for 20 min at room temperature. After *in situ* ^{31}P{^{1}H} NMR showed complete conversion to the target complex, the solvent was removed *in vacuo* and the complex extracted into

hexane. The hexane solution was concentrated *in vacuo* and the precipitate was filtered off and dried to give the product as a yellow solid. Yield: 115 mg (67%). **^{1}H NMR** (400 MHz, CD_2Cl_2) (δ, ppm): 6.80 (td, $^{3}J_{HH}$ = 7.5 Hz, $^{5}J_{HH}$ = 1.9 Hz, 1H, C*H*), 6.53 (dd, $^{3}J_{HH}$ = 7.7 Hz, $^{5}J_{HH}$ = 1.4 Hz, 1H, C*H*), 6.44 (dt, $^{3}J_{HH}$ = 7.3 Hz, $^{5}J_{HH}$ = 1.9 Hz, 1H, C*H*), 3.91 (d, $^{3}J_{HP}$ = 19.9 Hz, 2H, CH_2), 2.38 – 2.27 (m, 2H, C*H*(CH_3)$_2$), 2.16 – 2.05 (m, 2H, C*H*(CH_3)$_2$), 1.34 – 1.13 (m, 20H, CH(CH_3)$_2$), 1.04 (m, 4H, CH(CH_3)$_2$). **^{31}P{^{1}H} NMR** (162 MHz, CD_2Cl_2) (δ, ppm): 118.5 (d, $^{2}J_{PP}$ = 388 Hz, NHP^{i}Pr$_2$), 89.4 (d, $^{2}J_{PP}$ = 388 Hz, CH$_2$NHP^{i}Pr$_2$). **^{13}C{^{1}H} NMR** (100 MHz, CD_2Cl_2) (δ, ppm): 160.8 (q, J_{CF} = 34.9 Hz, *C*O), 158.9 (d, J_{CP} = 26.0 Hz, quat. *C*), 142.1 (dd, J_{CP} = 11.5, 1.4 Hz, quat. *C*), 126.0 (s, *C*H), 118.4 (d, J_{CP} = 1.2 Hz, *C*H), 109.2 (d, J_{CP} = 15.0 Hz, *C*H), 56.7 (d, $^{2}J_{CP}$ = 11.4 Hz, *C*H$_2$), 27.9 (dd, J_{CP} = 19.9, 4.5 Hz, *C*H(CH_3)$_2$), 25.8 (dd, J_{CP} = 24.5, 4.4 Hz, *C*H(CH_3)$_2$), 17.8 (dd, J_{CP} = 11.0, 6.7 Hz, CH(*C*H$_3$)$_2$), 16.8 (dt, J_{CP} = 20.4, 1.5 Hz, CH(*C*H$_3$)$_2$). **HRMS (Nanospray):** *m*/*z* calculated for $C_{21}H_{34}N_2O_2F_3P_2Pd$ [M–H]$^{\bullet+}$ = 571.1082, found 571.1075.

6.5.2.8 Synthesis of [($L_{5.8}$)Pd(TFA)] complex, 5.24

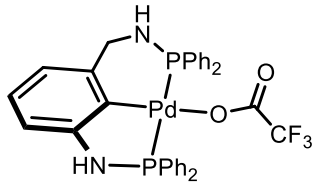

A solution of **$L_{5.8}$** (147 mg, 0.30 mmol) in THF (2.5 mL) was added to a suspension of [Pd(TFA)$_2$] (100 mg, 0.30 mmol) in THF (2.5 mL) and stirred for 20 min at room temperature. After *in situ* ^{31}P{^{1}H} NMR showed complete conversion to the target complex, the solvent was removed *in vacuo* and the complex precipitated by addition of hexane. The precipitate was filtered off and dried to give the product as an orange solid. Yield: 188 mg (88%). **^{1}H NMR** (500 MHz, CD_2Cl_2) (δ, ppm): 7.58 – 7.30 (m, 20H, P*Ph*$_2$), 6.91 (td, $^{3}J_{HH}$ = 7.5 Hz, $^{5}J_{HH}$ = 2.1 Hz, 1H, C*H*), 6.69 – 6.61 (m, 2H, C*H*), 4.10 (d, $^{3}J_{HP}$ = 24.1 Hz, 2H, CH_2). **^{31}P{^{1}H} NMR** (162 MHz, CD_2Cl_2) (δ, ppm): 88.5 (d, $^{2}J_{PP}$ = 447 Hz, NHPPh$_2$), 63.2 (d, $^{2}J_{PP}$ = 447 Hz, CH$_2$NHPPh$_2$). **^{13}C{^{1}H} NMR** (126 MHz, CD_2Cl_2) (δ, ppm): 133.0 (d, J_{CP} = 1.6 Hz, quat. *C*), 132.9 (quat *C*.), 131.6 (d, J_{CP} = 2.5 Hz, quat *C*.), 129.1 (dd, J_{CP} = 10.6 Hz, J_{CP} = 5.7 Hz, *C*H), 111.1 (d, J_{CP} = 16.6 Hz, *C*H), 107.7 (s, *C*H), 54.8 (d, J_{CP} = 12.7 Hz, *C*H$_2$). **HRMS (Nanospray):** *m*/*z* calculated for $C_{31}H_{27}N_2P_2Pd$ [M–TFA]$^{\bullet+}$ = 595.0684, found 595.0685.

6.5.2.9 Reaction of $L_{5.5}$-$L_{5.6}$ and $L_{5.8}$-$L_{5.9}$ with [$PdCl_2$(cod)] or [$PdCl_2$(NCPh)$_2$]

A solution of aminophosphine ligand (0.30 mmol) in THF (2.5 mL) was added to a solution of [$PdCl_2$(cod)] or [$PdCl_2$(NCPh)$_2$] (0.30 mmol) in THF (2.5 mL) and heated under reflux. The mixtures quickly produced a highly insoluble orange precipitate. An *in situ* ^{31}P{^{1}H} NMR analysis of the soluble material did show formation of traces of the

target complexes, however pure materials could not be isolated. The Pd–Cl containing polymeric materials were not used further.

6.5.3 Experimental procedure for allylic alkylation catalysis

To a suspension of NaH (26 mg, 1.1 mmol) in THF (5 mL) was added dimethyl malonate (114 μL, 1.00 mmol). The mixture was stirred for 10 min and then transferred to a Schlenk tube with a stir bar containing the preformed Pd catalyst (0.03 mmol, 5 mol%) and cinnamyl acetate (83 μL, 0.50 mmol) in THF (5 mL). The tube was then stirred for the prescribed time at the temperature indicated. An aliquot was quenched by filtration through a silica plug and analysed by GC-MS using dodecane as an internal standard.

6.5.4 Experimental procedures and characterising data for all-carbon pincer ligands and precursors

6.5.4.1 Synthesis of 1,3-$(CH_2CH_2OH)_2(C_6H_4)$, 5.5

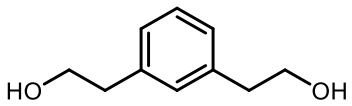

Following an adapted literature procedure. A slurry of $LiAlH_4$ (2.93 g, 77.3 mmol) in THF (50 mL) was heated under reflux for 30 mins. A solution of 1,3-$C_6H_4(CH_2CO_2H)_2$ **5.4** (5.00 g, 25.8 mmol) in THF (200 mL) was slowly added to the $LiAlH_4$ mixture to maintain reflux. After 3 h, the mixture was quenched by the slow addition of ice-cold water (50 mL). The mixture was extracted with EtOAc (3 × 100 mL) and the combined organics were washed with water and then brine, then dried ($MgSO_4$), filtered and concentrated *in vacuo*. Purification by silica column chromatography (0–50% EtOAc/hexane) to give the product as a white solid. Yield: 3.75 g (88%). Spectroscopic data matched that previously reported. **^{1}H NMR** (400 MHz, CD_3OD) (δ, ppm): 7.20 (dd, $^3J_{HH}$ = 8.1 Hz, $^4J_{HH}$ = 6.9 Hz, 1H, C*H*), 7.12 – 7.08 (m, 1H, C*H*), 7.06 (dd, $^3J_{HH}$ = 7.5 Hz, $^4J_{HH}$ = 1.8 Hz, 2H, C*H*), 3.74 (t, $^3J_{HH}$ = 7.1 Hz, 4H, CH_2), 2.79 (t, $^3J_{HH}$ = 7.1 Hz, 4H, CH_2).

6.5.4.2 Synthesis of 1,3-$(CH_2CH_2OTs)_2(C_6H_4)$, 5.6

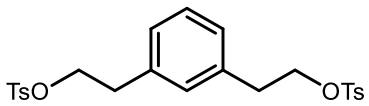

Following an adapted literature procedure.[315] To a solution of TsCl (629 mg, 3.30 mmol), DMAP (37 mg, 0.30 mmol) and NEt_3 (0.84 mL, 6.00 mmol) in CH_2Cl_2 (20 mL) at 0 °C was added a solution of **5.5** (250 mg, 1.50 mmol) in CH_2Cl_2 (8 mL). The mixture was warmed to room temperature and stirred for 18 h. The solution was then washed with sat. aq. $NaHCO_3$ and water. The combined aqueous layers were extracted with CH_2Cl_2, dried (Na_2SO_4), filtered and concentrated *in vacuo*. Purification by silica column chromatography (20%

EtOAc/hexane) to give the product as a pale-yellow oil. Yield: 472 mg (66%). **^{1}H NMR** (400 MHz, $CDCl_3$) (δ, ppm): 7.76 – 7.64 (m, 4H, C*H*), 7.33 – 7.27 (m, 4H, C*H*), 7.15 (t, $^{3}J_{HH}$ = 7.6 Hz, 1H, C*H*), 6.98 (dd, $^{3}J_{HH}$ = 7.5 Hz, $^{4}J_{HH}$ = 1.8 Hz, 2H, C*H*), 6.85 (s, 1H, C*H*), 4.18 (t, $^{3}J_{HH}$ = 7.0 Hz, 4H, CH_2), 2.89 (t, $^{3}J_{HH}$ = 7.1 Hz, 4H, CH_2O), 2.43 (s, 6H, CH_3). **^{13}C{^{1}H} NMR** (100 MHz, $CDCl_3$) (δ, ppm): 144.9 (s, *C*H), 136.7 (s, *C*H), 133.1 (s, *C*H), 130.0 (s, *C*H), 129.6 (s, *C*H), 129.0 (s, *C*H), 128.0 (s, *C*H), 127.6 (s, *C*H), 70.5 (s, $C_6H_4CH_2$), 35.3 (s, *C*H_2O), 21.8 (s, *C*H_3).

6.5.4.3 Synthesis of 1,3-($CH_2CH_2P^tBu_2(BH_3)$)$_2$(C_6H_4), 5.7

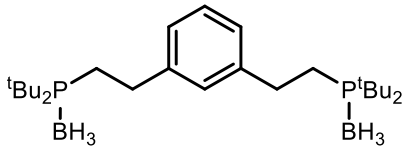

A solution of ^{n}BuLi (0.82 mL, 1.6 M in hexane, 1.30 mmol) was added to $^{t}Bu_2PH(BH_3)$ (160 mg, 1.00 mmol) in THF (20 mL) at –78 °C. After 30 min at room temperature the mixture was cooled to –78 °C and a solution of **5.6** (237 mg, 0.50 mmol) in THF (5 mL) was added and the mixture was heated under reflux for 1 h. After *in situ* ^{31}P{^{1}H} NMR showed complete conversion to the borane protected product, the mixture was then filtered through a small pad of Celite in air. The volatiles were removed *in vacuo* to give the product as a white solid. Yield: 210 mg (93%). **^{1}H NMR** (400 MHz, $CDCl_3$) (δ, ppm): 7.74 – 7.64 (m, 1H, C*H*), 7.12 – 7.03 (m, 2H, C*H*), 7.01 – 6.93 (m, 1H, C*H*), 3.03 – 2.82 (m, 4H, CH_2), 2.00 – 1.77 (m, 4H, CH_2), 1.30 (d, $^{3}J_{HP}$ = 12.4 Hz, 36H, C(CH_3)$_3$). **^{31}P{^{1}H} NMR** (162 MHz, $CDCl_3$) (δ, ppm): 44.5 (br. s, 2P). **HRMS (ESI):** *m*/*z* calculated for $C_{26}H_{54}B_2P_2$ $[M]^{\bullet+}$ =450.3887, found 456.3267.

6.5.4.4 Attempted synthesis of 1,3-($CH_2CH_2P^tBu_2$)$_2$(C_6H_4), $L_{5.10}$

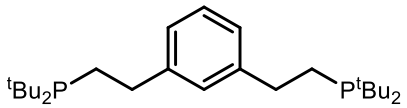

A solution of **5.7** (45 mg, 0.10 mmol) and DABCO (112 mg, 1.00 mmol) in hexane (10 mL) was heated under reflux for 18 h. After *in situ* ^{31}P{^{1}H} NMR showed complete conversion to the deprotected phosphine, the mixture was then filtered to remove the DABCO·BH_3 precipitate. The volatiles were removed *in vacuo* to give the product as a white solid. Yield: 194 mg (93%). **^{31}P{^{1}H} NMR** (162 MHz, $CDCl_3$) (δ, ppm): 29.5 (s, 2P).

6.6 Computational details

Calculations were performed using the Gaussian 09 (D.01) software package.[264] Structures **$L_{4.1}$-$L_{4.3}$**, **4.5**, **4.14**, and **4.17** were optimised in the gas phase at the B3LYP/6-31G(d)/LANL2DZ level of theory.[269] TD-DFT was used to calculate the UV-visible absorption properties the CAM-B3LYP/6-31G(d)/LANL2DZ level of theory using a polarisable continuum model for CH_2Cl_2 (ε = 9.1) as solvent.[271]

6.7 X-ray crystallography

The X-ray data presented in this thesis were collected by Dr Hazel Sparkes or Dr Natalie Pridmore at 100 K on a Bruker APEX II CCD diffractometer using Mo-Kα radiation (λ = 0.71073 Å). Intensities were integrated in SAINT[316] and absorption corrections based on equivalent reflections were applied using SADABS.[317] The structure was solved using ShelXT[318] all of the structures were refined by full matrix least squares against F^2 in ShelXL[318,319] using Olex2[320]. Crystal structure and refinement data are given in Table 6.1.

Table 6.1. Crystal data.

Identification code	$\mathbf{L_{2.11}}$	**[2.18]PF_6**	**[2.20]Cl**
Empirical formula	$C_{36}H_{26}P_2S_3$	$C_{38}H_{39}ClF_6N_5P_3Ru$	$C_{32}H_{44}Cl_2N_4O_2P_2Ru$
Formula weight	616.69	909.17	750.62
Temperature/K	100(2)	100(2)	100(2)
Crystal system	monoclinic	monoclinic	orthorhombic
Space group	$P2_1/c$	$P2_1/n$	$Pbca$
a/Å	13.4695(7)	13.9014(6)	18.9394(4)
b/Å	15.2008(9)	19.6282(9)	17.9554(4)
c/Å	15.1890(9)	14.2188(6)	19.7240(4)
α/°	90	90	90
β/°	105.8130(10)	98.3870(10)	90
γ/°	90	90	90
Volume/Å^3	2992.2(3)	3838.2(3)	6707.4(2)
Z	4	4	8
ϱ_{calc}g/cm^3	1.369	1.573	1.487
μ/mm^{-1}	0.380	0.669	0.758
F(000)	1280.0	1848.0	3104.0
Crystal size/mm^3	0.406 × 0.269 × 0.192	0.392 × 0.288 × 0.14	0.414 × 0.367 × 0.134
Radiation	MoKα (λ = 0.71073)	MoKα (λ = 0.71073)	MoKα (λ = 0.71073)
2θ range for data collection/°	3.866 to 56.04	3.562 to 55.748	3.746 to 55.962
Index ranges	-11 ≤ h ≤ 17, -19 ≤ k ≤ 20, -20 ≤ l ≤ 19	-16 ≤ h ≤ 18, -25 ≤ k ≤ 25, -18 ≤ l ≤ 11	-24 ≤ h ≤ 24, -22 ≤ k ≤ 23, -26 ≤ l ≤ 26
Reflections collected	27175	34855	56675
R_{int} / R_{sigma}	7201 [R_{int} = 0.0617, R_{sigma} = 0.0603]	0.0518 / 0.0516	8062 [R_{int} = 0.0770, R_{sigma} = 0.0469]
Data/restraints/parameters	7201/90/383	9143/132/560	8062/30/434
Goodness-of-fit on F^2	1.014	1.015	1.001
Final R indexes [I>=2σ (I)]	R_1 = 0.0427, wR_2 = 0.0854	R_1 = 0.0350, wR_2 = 0.0695	R_1 = 0.0337, wR_2 = 0.0676
Final R indexes [all data]	R_1 = 0.0725, wR_2 = 0.0970	R_1 = 0.0534, wR_2 = 0.0762	R_1 = 0.0606, wR_2 = 0.0771
Largest diff. peak/hole / e Å^{-3}	0.43/-0.38	0.49/-0.55	0.83/-0.61

Table 6.1. Crystal data (cont.).

Identification code	**2.21**	**2.22**	**4.14**
Empirical formula	$C_{32}H_{24}Cl_2N_2P_2Pt$	$C_{42}H_{32}Cl_6N_2P_2Pt$	$C_{27}H_{25}Cl_4PRu$
Formula weight	764.46	1034.42	623.31
Temperature/K	100(2)	100(2)	100(2)
Crystal system	monoclinic	monoclinic	triclinic
Space group	$P2_1/c$	$C2/c$	P-1
a/Å	10.4297(5)	17.4468(2)	11.5602(5)
b/Å	14.3210(8)	14.3479(2)	16.3474(9)
c/Å	19.6325(12)	17.6226(2)	16.9829(9)
α/°	90	90	63.114(3)
β/°	101.369(3)	114.3260(10)	71.058(3)
γ/°	90	90	70.557(3)
Volume/Å^3	2874.8(3)	4019.72(9)	2640.8(2)
Z	4	4	4
ϱ_{calc}g/cm^3	1.766	1.709	1.568
μ/mm^{-1}	5.204	4.003	1.074
F(000)	1488.0	2032.0	1256.0
Crystal size/mm^3	0.394 × 0.297 × 0.166	0.367 × 0.269 × 0.169	0.408 × 0.262 × 0.087
Radiation	MoKα (λ = 0.71073)	MoKα (λ = 0.71073)	MoKα (λ = 0.71073)
2θ range for data collection/°	4.232 to 55.908	3.824 to 55.782	2.748 to 50.7
Index ranges	-13 ≤ h ≤ 13, -18 ≤ k ≤ 18, -23 ≤ l ≤ 25	-22 ≤ h ≤ 17, -18 ≤ k ≤ 18, -23 ≤ l ≤ 23	-13 ≤ h ≤ 13, -19 ≤ k ≤ 18, -20 ≤ l ≤ 20
Reflections collected	25595	18355	40153
R_{int} / R_{sigma}	6884 [R_{int} = 0.0261, R_{sigma} = 0.0243]	4799 [R_{int} = 0.0301, R_{sigma} = 0.0298]	9664 [R_{int} = 0.0966, R_{sigma} = 0.0921]
Data/restraints/parameters	6884/0/352	4799/0/240	9664/1790/901
Goodness-of-fit on F^2	1.041	1.048	1.010
Final R indexes [I>=2σ (I)]	R_1 = 0.0183, wR_2 = 0.0381	R_1 = 0.0216, wR_2 = 0.0442	R_1 = 0.0546, wR_2 = 0.1170
Final R indexes [all data]	R_1 = 0.0217, wR_2 = 0.0389	R_1 = 0.0291, wR_2 = 0.0466	R_1 = 0.1044, wR_2 = 0.1385
Largest diff. peak/hole / e Å^{-3}	0.53/-0.59	0.83/-0.77	0.82/-1.15

Table 6.1. Crystal data (cont.).

Identification code	**5.9**	**5.10**
Empirical formula	$C_{23}H_{43}ClN_2P_2Pd$	$C_{24}H_{45}ClN_2P_2Pd$
Formula weight	551.38	565.41
Temperature/K	100.0	99.89
Crystal system	trigonal	monoclinic
Space group	*P*-3	$P2_1/c$
a/Å	20.4582(5)	14.8440(3)
b/Å	20.4582(5)	16.4594(4)
c/Å	11.8658(3)	11.1260(3)
α/°	90	90
β/°	90	100.759(2)
γ/°	120	90
Volume/Å^3	4300.9(2)	2670.56(11)
Z	6	4
ϱ_{calc}g/cm^3	1.277	1.406
μ/mm^{-1}	0.863	0.929
F(000)	1728.0	1184.0
Crystal size/mm^3	0.422 × 0.34 × 0.114	0.384 × 0.227 × 0.076
Radiation	MoKα (λ = 0.71073)	MoKα (λ = 0.71073)
2θ range for data collection/°	3.432 to 60.282	3.732 to 54.898
Index ranges	-24 ≤ h ≤ 28, -28 ≤ k ≤ 28, -16 ≤ l ≤ 16	-19 ≤ h ≤ 19, -21 ≤ k ≤ 16, -14 ≤ l ≤ 14
Reflections collected	97401	45241
R_{int} / R_{sigma}	8483 [R_{int} = 0.0425, R_{sigma} = 0.0193]	6097 [R_{int} = 0.0532, R_{sigma} = 0.0314]
Data/restraints/parameters	8483/0/393	6097/0/291
Goodness-of-fit on F^2	1.028	1.033
Final R indexes [I>=2σ (I)]	R_1 = 0.0225, wR_2 = 0.0576	R_1 = 0.0250, wR_2 = 0.0508
Final R indexes [all data]	R_1 = 0.0266, wR_2 = 0.0593	R_1 = 0.0370, wR_2 = 0.0542
Largest diff. peak/hole / e Å^{-3}	0.91/-0.51	0.43/-0.46

References

(1) CRUK cases, https://www.cancerresearchuk.org/health-professional/cancer-statistics/worldwide-cancer, (accessed 10 December 2020).

(2) Ohkuma, T.; Ooka, H.; Yamakawa, M.; Ikariya, T.; Noyori, R., *J. Org. Chem.*, **1996**, 61, 4872–4873.

(3) Scholl, M.; Ding, S.; Lee, C. W.; Grubbs, R. H., *Org. Lett.*, **1999**, 1, 953–956.

(4) Teng, X.; Cefalo, D. R.; Schrock, R. R.; Hoveyda, A. H., *J. Am. Chem. Soc.*, **2002**, 124, 10779–10784.

(5) Miyaura, N.; Suzuki, A., *J. Chem. Soc., Chem. Commun.*, **1979**, 866–867.

(6) Dieck, H. A.; Heck, R. F., *J. Org. Chem.*, **1975**, 40, 1083–1090.

(7) Koumura, N.; Zijlstra, R. W.; van Delden, R.; Harada, N.; Feringa, B. L., *Nature*, **1999**, 401, 152–155.

(8) Balzani, V.; Credi, A.; Raymo, F. M.; Stoddart, J. F., *Angew. Chem., Int. Ed.*, **2000**, 39, 3348–3391.

(9) Mjos, K. D.; Orvig, C., *Chem. Rev.*, **2014**, 114, 4540–4563.

(10) Macpherson, D. S.; Fung, K.; Cook, B. E.; Francesconi, L. C.; Zeglis, B. M., *Dalton Trans.*, **2019**, 48, 14547–14565.

(11) Kim, J. H.; Reeder, E.; Parkin, S.; Awuah, S. G., *Sci. Rep.*, **2019**, 9, 1–18.

(12) Rosenberg, B., *Platin. Met. Rev.*, **1971**, 15, 42–51.

(13) Kenny, R. G.; Marmion, C. J., in *RSC Metallobiology*, Royal Society of Chemistry, **2019**, pp. 3–30.

(14) Hucke, A.; Park, G. Y.; Bauer, O. B.; Beyer, G.; Köppen, C.; Zeeh, D.; Wehe, C. A.; Sperling, M.; Schröter, R.; Kantauskaitè, M.; Hagos, Y.; Karst, U.; Lippard, S. J.; Ciarimboli, G., *Front. Chem.*, **2018**, 6, 180.

(15) Park, G. Y.; Wilson, J. J.; Song, Y.; Lippard, S. J., *Proc. Natl. Acad. Sci. U. S. A.*, **2012**, 109, 11987–11992.

(16) Wilson, J. J.; Lippard, S. J., *Chem. Rev.*, **2014**, 114, 4470–4495.

(17) Galanski, M.; Jakupec, M.; Keppler, B., *Curr. Med. Chem.*, **2005**, 12, 2075–2094.

(18) Bergamo, A.; Dyson, P. J.; Sava, G., *Coord. Chem. Rev.*, **2018**, 360, 17–33.

(19) Oun, R.; Moussa, Y. E.; Wheate, N. J., *Dalton Trans.*, **2018**, 47, 6645–6653.

(20) Breglio, A. M.; Rusheen, A. E.; Shide, E. D.; Fernandez, K. A.; Spielbauer, K. K.; McLachlin, K. M.; Hall, M. D.; Amable, L.; Cunningham, L. L., *Nat. Commun.*, **2017**, 8, 1–9.

(21) Todd, R. C.; Lippard, S. J., *Metallomics*, **2009**, 1, 280–291.

(22) Jamieson, E. R.; Lippard, S. J., *Chem. Rev.*, **1999**, 99, 2467–2498.

(23) Berners-Price, S. J.; Frenkiel, T. A.; Frey, U.; Ranford, J. D.; Sadler, P. J., *J. Chem. Soc., Chem. Commun.*, **1992**, 789–791.

(24) Takahara, P. M.; Frederick, C. A.; Lippard, S. J., *J. Am. Chem. Soc.*, **1996**, 118, 12309–12321.

(25) Urruticoechea, A.; Alemany, R.; Balart, J.; Villanueva, A.; Vinals, F.; Capella, G., *Curr. Pharm. Des.*, **2010**, 16, 3–10.

(26) Monro, S.; Colón, K. L.; Yin, H.; Roque, J.; Konda, P.; Gujar, S.; Thummel, R. P.; Lilge, L.; Cameron, C. G.; McFarland, S. A., *Chem. Rev.*, **2019**, 119, 797–828.

(27) de Almeida, A.; Bonsignore, R., *Bioorganic Med. Chem. Lett.*, **2020**, 30, 127219.

(28) Clarke, M. J.; Bitler, S.; Rennert, D.; Buchbinder, M.; Kelman, A. D., *J. Inorg. Biochem.*, **1980**, 12, 79–87.

(29) Clarke, M. J.; Zhu, F.; Frasca, D. R., *Chem. Rev.*, **1999**, 99, 2511–2533.

(30) Leijen, S.; Burgers, S. A.; Baas, P.; Pluim, D.; Tibben, M.; van Werkhoven, E.; Alessio, E.; Sava, G.; Beijnen, J. H.; Schellens, J. H. M., *Invest. New Drugs*, **2015**, 33, 201–214.

(31) Trondl, R.; Heffeter, P.; Kowol, C. R.; Jakupec, M. A.; Berger, W.; Keppler, B. K.; Bendell, J. C.; Ogden, A.; Hoff, D. D. Von; Jaehde, U.; Stoika, R.; Zaichenko, A.; Berger, W., *Chem. Sci.*, **2014**, 5, 2925–2932.

(32) Hartinger, C. G.; Zorbas-Seifried, S.; Jakupec, M. A.; Kynast, B.; Zorbas, H.; Keppler, B. K., *J. Inorg. Biochem.*, **2006**, 100, 891–904.

(33) Wee, H. A.; Dyson, P. J., *Eur. J. Inorg. Chem.*, **2006**, 20, 4003–4018.

(34) Bergamo, A.; Sava, G.; Arion, V. B.; Hartinger, C. G.; Keppler, B. K.; Fuchs, J.; Armeanu-Ebinger, S.; Marian, B.; Jodrell, D. I.; Meggers, E.; Herlyn, M.; Pfeffer, M.; Loeffler, J. P.; Gaiddon, C.; Russo, A.; Gebbia, N.; Iacobelli, S.; Marchetti, P.; Ficorella, C., *Dalton Trans.*, **2011**, 40, 7817.

(35) Zeng, L.; Gupta, P.; Chen, Y.; Wang, E.; Ji, L.; Chao, H.; Chen, Z.-S., *Chem. Soc. Rev.*, **2017**, 46, 5771–5804.

(36) Rodríguez-Bárzano, A.; Lord, R. M.; Basri, A. M.; Phillips, R. M.; Blacker, A. J.; McGowan, P. C., *Dalton Trans.*, **2015**, 44, 3265–3270.

(37) Allardyce, C. S.; Dyson, P. J.; Ellis, D. J.; Heath, S. L., *Chem. Commun.*, **2001**, 15, 1396–1397.

(38) Kilpin, K. J.; Cammack, S. M.; Clavel, C. M.; Dyson, P. J., *Dalton Trans.*, **2013**, 42, 2008–2014.

(39) Renfrew, A. K.; Karges, J.; Scopelliti, R.; Bobbink, F. D.; Nowak-Sliwinska, P.; Gasser, G.; Dyson, P. J., *ChemBioChem*, **2019**, 20, 2876–2882.

(40) Morris, R. E.; Aird, R. E.; Del, P.; Murdoch, S.; Chen, H.; Cummings, J.; Hughes, N. D.; Parsons, S.; Parkin, A.; Boyd, G.; Jodrell, D. I.; Sadler, P. J., *J. Med. Chem*, **2001**, 44, 3616–3621.

(41) Chen, H.; Parkinson, J. A.; Parsons, S.; Coxall, R. A.; Gould, R. O.; Sadler, P. J., *J. Am. Chem. Soc.*, **2002**, 124, 3064–3082.

(42) Dorcier, A.; Dyson, P. J.; Gossens, C.; Rothlisberger, U.; Scopelliti, R.; Tavernelli, I., *Organometallics*, **2005**, 24, 2114–2123.

(43) Murray, B. S.; Babak, M. V.; Hartinger, C. G.; Dyson, P. J., *Coord. Chem. Rev.*, **2016**, 306, 86–114.

(44) Scolaro, C.; Chaplin, A. B.; Hartinger, C. G.; Bergamo, A.; Cocchietto, M.; Keppler, B. K.; Sava, G.; Dyson, P. J., *Dalton Trans.*, **2007**, 5065–5072.

(45) Nowak-Sliwinska, P.; Van Beijnum, J. R.; Casini, A.; Nazarov, A. A.; Wagnières, G.; Van Den Bergh, H.; Dyson, P. J.; Griffioen, A. W., *J. Med. Chem.*, **2011**, 54, 3895–3902.

(46) Simonetti, M.; Cannas, D. M.; Just-Baringo, X.; Vitorica-Yrezabal, I. J.; Larrosa, I., *Nat. Chem.*, **2018**, 10, 724–731.

(47) Serli, B.; Zangrando, E.; Gianferrara, T.; Scolaro, C.; Dyson, P. J.; Bergamo, A.; Alessio, E., *Eur. J. Inorg. Chem.*, **2005**, 17, 3423–3434.

(48) Bratsos, I.; Mitri, E.; Ravalico, F.; Zangrando, E.; Gianferrara, T.; Bergamo, A.; Alessio, E., *Dalton Trans.*, **2012**, 41, 7358–7371.

(49) Gill, M. R.; Thomas, J. A., *Chem. Soc. Rev.*, **2012**, 41, 3179–3192.

(50) Rilak Simović, A.; Masnikosa, R.; Bratsos, I.; Alessio, E., *Coord. Chem. Rev.*, **2019**, 398, 113011.

(51) Gill, M. R.; Thomas, J. A., *Chem. Soc. Rev.*, **2012**, 41, 3179–3192.

(52) Miller, S. E.; House, D. A., *Inorganica Chim. Acta*, **1991**, 187, 125–132.

(53) Amouyal, E.; Homsi, A.; Chambron, J.; Sauvage, J., *J. Chem. Soc. Dalton Trans.*, **1990**, 1841–1845.

(54) Friedman, A. E.; Kumar, C. V; Turro, N. J.; Barton, J. K., *Nucleic Acids Res.*, **1991**, 19, 2595–602.

(55) Barton, J. K.; Dervan, E. E.; Olmon, E. D.; McConnell, A. J.; Song, H.; Lim, M. H., *Inorg. Chem.*, **2012**, 51, 12511–12520.

(56) Hartshorn, R. M.; Barton, J. K., *J. Am. Chem. Soc.*, **1992**, 114, 5919–5925.

(57) Friedman, A. E.; Chambron, J.-C.; Sauvage, J.-P.; Turro, N.; Barton, J., *J. Am. Chem. Soc.*, **1990**, 112, 4960–4962.

(58) Yin, H.; Stephenson, M.; Gibson, J.; Sampson, E.; Shi, G.; Sainuddin, T.; Monro, S.; McFarland, S. A., *Inorg. Chem.*, **2014**, 53, 4548–4559.

(59) McKenzie, L. K.; Bryant, H. E.; Weinstein, J. A., *Coord. Chem. Rev.*, **2019**, 379, 2–29.

(60) Ramu, V.; Aute, S.; Taye, N.; Guha, R.; Walker, M. G.; Mogare, D.; Parulekar, A.; Thomas, J. A.; Chattopadhyay, S.; Das, A., *Dalton Trans.*, **2017**, 46, 6634–6644.

(61) Liu, J.; Zhang, C.; Rees, T. W.; Ke, L.; Ji, L.; Chao, H., *Coord. Chem. Rev.*, **2018**, 363, 17–28.

(62) Karges, J.; Heinemann, F.; Jakubaszek, M.; Maschietto, F.; Subecz, C.; Dotou, M.; Vinck, R.; Blacque, O.; Tharaud, M.; Goud, B.; Viñuelas ZahÍnos, E.; Spingler, B.; Ciofini, I.; Gasser, G., *J. Am. Chem. Soc.*, **2020**, 142, 6578–6587.

(63) Ko, C. N.; Li, G.; Leung, C. H.; Ma, D. L., *Coord. Chem. Rev.*, **2019**, 381, 79–103.

(64) Theralase Phase II, https://www.accesswire.com/617881/Theralase-Granted-FDA-Fast-Track-Designation-for-NMIBC-Phase-II-Clinical-Study, (accessed 4 January 2021).

(65) Theralase, https://theralase.com/theralase-technology-demonstrates-high-kill-rate-of-coronavirus-bsl-2/, (accessed 4 January 2021).

(66) Bowen, T.; Planalp, R. P.; Brechbiel, M. W., *Bioorg. Med. Chem. Lett.*, **1996**, 6, 807–810.

(67) Cronin, L.; Foxon, S. P.; Lusby, P. J.; Walton, P. H., *J. Biol. Inorg. Chem.*, **2001**, 6, 367–377.

(68) Lovering, F.; Bikker, J.; Humblet, C., *J. Med. Chem.*, **2009**, 52, 6752–6756.

(69) Morrison, C. N.; Prosser, K. E.; Stokes, R. W.; Cordes, A.; Metzler-Nolte, N.; Cohen, S. M., *Chem. Sci.*, **2020**, 11, 1216–1225.

(70) Kumar, P.; Gorai, S.; Santra, M. K.; Mondal, B.; Manna, D., *Dalton Trans.*, **2012**, 41, 7573–7581.

(71) Dhanaraj, C. J.; Johnson, J., *Appl. Organomet. Chem.*, **2016**, 30, 860–871.

(72) Urbach, F. L.; Sarneski, J. E.; Turner, L. J.; Busch, D. H., *Inorg. Chem.*, **1968**, 7, 2169–2171.

(73) Erickson, L. E.; Cook, D. J.; Evans, G. D.; Sarneski, J. E.; Okarma, P. J.; Sabatelli, A. D., *Inorg. Chem.*, **1990**, 29, 1958–1967.

(74) Ebrahimpour, P.; Haddow, M. F.; Wass, D. F., *Inorg. Chem.*, **2013**, 52, 3765–3771.

(75) Greener, B.; Moore, M. H.; Walton, P. H., *Chem. Commun.*, **1996**, 27–28.

(76) Thibault, M.-H. H.; Lucier, B. E. G.; Schurko, R. W.; Fontaine, F. G., *J. Chem. Soc., Dalton Trans.*, **2009**, 7701–7716.

(77) Torti, B. S. V; Torti, F. M.; Whitman, S. P.; Brechbiel, M. W.; Park, G.; Planalp, R. P., *Blood*, **2015**, 92, 1384–1389.

(78) Ye, N.; Park, G.; Przyborowska, A. M.; Sloan, P. E.; Clifford, T.; Bauer, C. B.; Broker, G. A.; Rogers, R. D.; Ma, R.; Torti, S. V.; Brechbiel, M. W.; Planalp, R. P., *Dalton Trans.*, **2004**, 4, 1304–1311.

(79) Samuni, A. M.; Krishna, M. C.; DeGraff, W.; Russo, A.; Planalp, R. P.; Brechbiel, M. W.; Mitchell, J. B., *Biochim. Biophys. Acta.*, **2002**, 1571, 211–8.

(80) Park, G.; Lu, F. H.; Ye, N.; Brechbiel, M. W.; Torti, S. V.; Torti, F. M.; Planalp, R. P., *J. Biol. Inorg. Chem.*, **1998**, 3, 449–457.

(81) Greener, B.; Cronin, L.; Wilson, G. D.; Walton, P. H., *J. Chem. Soc. Dalton Trans.*, **1996**, 401–403.

(82) Gamble, A. J.; Lynam, J. M.; Thatcher, R. J.; Walton, P. H.; Whitwood, A. C., *Inorg. Chem.*, **2013**, 52, 4517–4527.

(83) Kobayashi, T.; Tobita, S.; Kobayashi, M.; Imajyo, T.; Chikira, M.; Yashiro, M.; Fujii, Y., *J. Inorg. Biochem.*, **2007**, 101, 348–361.

(84) Gamble, A. J., PhD Thesis, University of York, **2012**.

(85) Wise, D. E.; Gamble, A. J.; Arkawazi, S. W.; Walton, P. H.; Galan, M. C.; O'Hagan, M. P.; Hogg, K. G.; Marrison, J. L.; O'Toole, P. J.; Sparkes, H. A.; Lynam, J. M.; Pringle, P. G., *Dalton Trans.*, **2020**, 49, 15219–15230.

(86) Hanahan, D.; Weinberg, R. A., *Cell*, **2011**, 144, 646–674.

(87) Kenny, R. G.; Marmion, C. J., *Chem. Rev.*, **2019**, 119, 1058–1137.

(88) Huang, H.; Banerjee, S.; Qiu, K.; Zhang, P.; Blacque, O.; Malcomson, T.; Paterson, M. J.; Clarkson, G. J.; Staniforth, M.; Stavros, V. G.; Gasser, G.; Chao, H.; Sadler, P. J., *Nat. Chem.*, **2019**, 11, 1041–1048.

(89) Annunziata, A.; Cucciolito, M. E.; Esposito, R.; Imbimbo, P.; Petruk, G.; Ferraro, G.; Pinto, V.; Tuzi, A.; Monti, D. M.; Merlino, A.; Ruffo, F., *Dalton Trans.*, **2019**, 48, 7794–7800.

(90) Galochkina, T.; Ng Fuk Chong, M.; Challali, L.; Abbar, S.; Etchebest, C., *Sci. Rep.*, **2019**, 9, 998.

(91) Ma, L.; Lin, X.; Li, C.; Xu, Z.; Chan, C.-Y.; Tse, M.-K.; Shi, P.; Zhu, G., *Inorg. Chem.*, **2018**, 57, 39.

(92) Jin, S.; Hao, Y.; Zhu, Z.; Muhammad, N.; Zhang, Z.; Wang, K.; Guo, Y.; Guo, Z.; Wang, X., *Inorg. Chem.*, **2018**, 57, 11135–11145.

(93) Kastner, A.; Poetsch, I.; Mayr, J.; Burda, J. V.; Roller, A.; Heffeter, P.; Keppler, B. K.; Kowol, C. R., *Angew. Chem., Int. Ed.*, **2019**, 58, 7464–7469.

(94) Meggers, E., *Curr. Opin. Chem. Biol.*, **2007**, 11, 287–292.

(95) Schmid, W. F.; Zorbas-Seifried, S.; John, R. O.; Arion, V. B.; Jakupec, M. A.; Roller, A.; Galanski, M.; Chiorescu, I.; Zorbas, H.; Keppler, B. K., *Inorg. Chem.*, **2007**, 46, 3645–3656.

(96) Thota, S.; Rodrigues, D. A.; Crans, D. C.; Barreiro, E. J., *J. Med. Chem.*, **2018**, 61, 5805–5821.

(97) Battistin, F.; Siegmund, D.; Balducci, G.; Alessio, E.; Metzler-Nolte, N., *Dalton Trans.*, **2019**, 48, 400–414.

(98) Oliveira, G. D. F. S.; Gouveia, F. S.; Pinheiro, A. D. A.; Do Nascimento Neto, L. G.; De Vasconcelos, M. A.; Teixeira, E. H.; Gondim, A. C. S.; Lopes, L. G. D. F.; De Carvalho, I. M. M.; Sousa, E. H. S., *New J. Chem.*, **2020**, 44, 6610–6622.

(99) Nazarov, A. A.; Risse, J.; Ang, W. H.; Schmitt, F.; Zava, O.; Ruggi, A.; Groessl, M.; Scopelitti, R.; Juillerat-Jeanneret, L.; Hartinger, C. G.; Dyson, P. J., *Inorg. Chem.*, **2012**, 51, 3633–3639.

(100) Lakowicz, J. R., *Principles of fluorescence spectroscopy*, Springer, 3rd Ed., **2006**.

(101) Valeur, B., *Molecular Fluorescence: Principles and Applications*, Wiley, 2nd Ed., **2012**.

(102) Fritzsche, M.; Mandenius, C. F., *Anal. Bioanal. Chem.*, **2010**, 398, 181–191.

(103) Roussakis, E.; Li, Z.; Nichols, A. J.; Evans, C. L., *Angew. Chem., Int. Ed.*, **2015**, 54, 8340–8362.

(104) Lu, Y.; Conway-Kenny, R.; Wang, J.; Cui, X.; Zhao, J.; Draper, S. M., *Dalton Trans.*, **2018**, 47, 8585–8589.

(105) Soh, N.; Sakawaki, O.; Makihara, K.; Odo, Y.; Fukaminato, T.; Kawai, T.; Irie, M.; Imato, T., *Bioorganic Med. Chem.*, **2005**, 13, 1131–1139.

(106) Onoda, M.; Uchiyama, S.; Endo, A.; Tokuyama, H.; Santa, T.; Imai, K., *Org. Lett.*, **2003**, 5, 1459–1461.

(107) Clot, O.; Wolf, M. O.; Yap, G. P. A.; Patrick, B. O., *J. Chem. Soc., Dalton Trans.*, **2000**, 2729–2737.

(108) Sirajuddin, M.; Ali, S.; Badshah, A., *J. Photochem. Photobiol. B Biol.*, **2013**, 124, 1–19.

(109) Howe-Grant, M.; Lippard, S. J.; Wu, K. C.; Bauer, W. R., *Biochemistry*, **1976**, 15, 4339–4346.

(110) Banerjee, A.; Singh, J.; Dasgupta, D., *J. Fluoresc.*, **2013**, 23, 745–752.

(111) Wenger, O. S., *Nat. Chem.*, **2020**, 12, 323–324.

(112) Saeed, H. K.; Sreedharan, S.; Jarman, P. J.; Archer, S. A.; Fairbanks, S. D.; Foxon, S. P.; Auty, A. J.; Chekulaev, D.; Keane, T.; Meijer, A. J. H. M.; Weinstein, J. A.; Smythe, C. G. W.; Bernardino De La Serna, J.; Thomas, J. A., *J. Am. Chem. Soc.*, **2020**, 142, 1101–1111.

(113) Cardoso, C. R.; Lima, M. V. S.; Cheleski, J.; Peterson, E. J.; Venâncio, T.; Farrell, N. P.; Carlos, R. M., *J. Med. Chem.*, **2014**, 57, 4906–4915.

(114) Cai, S.; Lu, Y.; He, S.; Wei, F.; Zhaoa, L.; Zeng, X., *Chem. Commun.*, **2013**, 49, 822–824.

(115) Davies, L. H.; Stewart, B.; Harrington, R. W.; Clegg, W.; Higham, L. J., *Angew. Chem., Int. Ed.*, **2012**, 51, 4921–4924.

(116) Goze, C.; Ali, M.; Jacquemin, D.; Bettaieb, A.; Le Gendre, P.; Escudero, D.; Bodio, E.; Denat, F.; Richard, P.; Dondaine, L.; Paul, C., *Eur. J. Inorg. Chem.*, **2016**, 2016, 545–553.

(117) Bange, C. A.; Mucha, N. T.; Cousins, M. E.; Gehsmann, A. C.; Singer, A.; Truax, T.; Higham, L. J.; Waterman, R., *Inorganics*, **2016**, 4, 26.

(118) Davies, L. H.; Wallis, J. F.; Probert, M. R.; Higham, L. J., *Synthesis*, **2014**, 46, 2622–2628.

(119) Christianson, A. M.; Gabbaï, F. P., *Inorg. Chem.*, **2016**, 55, 5828–5835.

(120) Okimoto, Y.; Watanabe, A.; Niki, E.; Yamashita, T.; Noguchi, N., *FEBS Lett.*, **2000**, 474, 137–140.

(121) ThermoFisher Fluorescence Spectra Viewer, https://www.thermofisher.com/uk/en/home/life-science/cell-analysis/labeling-chemistry/fluorescence-spectraviewer, (accessed 20 August 2020).

(122) Fang, Y.; Good, G. N.; Zhou, X.; Stains, C. I., *Chem. Commun.*, **2019**, 55, 5962–5965.

(123) Cerfontaine, S.; Troian-Gautier, L.; Wehlin, S. A. M.; Loiseau, F.; Cauët, E.; Elias, B., *Dalton Trans.*, **2020**, 49, 8096–8106.

(124) Peris, E.; Crabtree, R. H., *Chem. Soc. Rev.*, **2018**, 47, 1959–1968.

(125) González-Sebastián, L.; Morales-Morales, D., *J. Organomet. Chem.*, **2019**, 893, 39–

51.

(126) Asay, M.; Morales-Morales, D., *Dalton Trans.*, **2015**, 44, 17432–17447.

(127) González-Sebastián, L.; Canseco-González, D.; Morales-Morales, D., *Pincer Compd. Chem. Appl.*, **2018**, 4, 467–490.

(128) Gibbons, S. K.; Xu, Z.; Hughes, R. P.; Glueck, D. S.; Rheingold, A. L., *Organometallics*, **2018**, 37, 2159–2166.

(129) Holz, J.; Zayas, O.; Jiao, H.; Baumann, W.; Spannenberg, A.; Monsees, A.; Riermeier, T. H.; Almena, J.; Kadyrov, R.; Börner, A., *Chem. Eur. J.*, **2006**, 12, 5001–5013.

(130) Liu, J. K.; Gong, J. F.; Song, M. P., *Org. Biomol. Chem.*, **2019**, 17, 6069–6098.

(131) Leveson-Gower, R. B.; Webb, P. B.; Cordes, D. B.; Slawin, A. M. Z.; Smith, D. M.; Tooze, R. P.; Liu, J., *Organometallics*, **2018**, 37, 30–39.

(132) Bolliger, J. L.; Blacque, O.; Frech, C. M., *Angew. Chem., Int. Ed.*, **2007**, 46, 6514–6517.

(133) Benito-Garagorri, D.; Bocokić, V.; Mereiter, K.; Kirchner, K., *Organometallics*, **2006**, 25, 3817–3823.

(134) Ding, Y.; Ma, Q. Q.; Kang, J.; Zhang, J.; Li, S.; Chen, X., *Dalton Trans.*, **2019**, 48, 17633–17643.

(135) Eberhard, M. R., *Org. Lett.*, **2004**, 6, 2125–2128.

(136) Feng, J.; Cai, C., *J. Fluor. Chem.*, **2013**, 146, 6–10.

(137) Naghipour, A.; Sabounchei, S. J.; Morales-Morales, D.; Canseco-González, D.; Jensen, C. M., *Polyhedron*, **2007**, 26, 1445–1448.

(138) Moore, J. N.; Laskay, N. M.; Duque, K. S.; Kelley, S. P.; Rogers, R. D.; Shaughnessy, K. H., *J. Organomet. Chem.*, **2015**, 777, 16–24.

(139) Yen Wong, E. H.; Jia, Y. X.; Li, Y.; Pullarkat, S. A.; Leung, P. H., *J. Organomet. Chem.*, **2018**, 862, 22–27.

(140) Lagaditis, P. O.; Sues, P. E.; Sonnenberg, J. F.; Wan, K. Y.; Lough, A. J.; Morris, R. H., *J. Am. Chem. Soc.*, **2014**, 136, 1367–1380.

(141) Xiang, Y.; Ge, Q.; Wu, S.; Zheng, X.; Yang, Z., *RSC Adv.*, **2020**, 10, 9563–9578.

(142) Tsuji, J.; Takahashi, H.; Morikawa, M., *Tetrahedron Lett.*, **1965**, 6, 4387–4388.

(143) Trost, B. M.; Van Vranken, D. L., *Chem. Rev.*, **1996**, 96, 395–422.

(144) Wang, Z.; Eberhard, M. R.; Jensen, C. M.; Matsukawa, S.; Yamamoto, Y., *J. Organomet. Chem.*, **2003**, 681, 189–195.

(145) Selander, N.; Szabó, K. J., *Chem. Rev.*, **2011**, 111, 2048–2076.

(146) Aydin, J.; Larsson, J. M.; Selander, N.; Szabó, K. J., *Org. Lett.*, **2009**, 11, 2852–2854.

(147) Pilarski, L. T.; Selander, N.; Böse, D.; Szabó, K. J., *Org. Lett.*, **2009**, 11, 5518–5521.

(148) Alessio, E., *Eur. J. Inorg. Chem.*, **2017**, 1549–1560.

(149) Bijelic, A.; Theiner, S.; Keppler, B. K.; Rompel, A., *J. Med. Chem.*, **2016**, 59, 5894–5903.

(150) Hartinger, C. G.; Jakupec, M. A.; Zorbas-Seifried, S.; Groessl, M.; Egger, A.; Berger, W.; Zorbas, H.; Dyson, P. J.; Keppler, B. K., *Chem. Biodivers.*, **2008**, 5, 2140–2155.

(151) Morris, R. E.; Aird, R. E.; Del Socorro Murdoch, P.; Chen, H.; Cummings, J.; Hughes, N. D.; Parsons, S.; Parkin, A.; Boyd, G.; Jodrell, D. I.; Sadler, P. J., *J. Med. Chem.*, **2001**, 44, 3616–3621.

(152) Fernández, R.; Melchart, M.; Habtemariam, A.; Parsons, S.; Sadler, P. J., *Chem. Eur. J.*, **2004**, 10, 5173–5179.

(153) Habtemariam, A.; Melchart, M.; Fernández, R.; Parsons, S.; Oswald, I. D. H.; Parkin, A.; Fabbiani, F. P. A.; Davidson, J. E.; Dawson, A.; Aird, R. E.; Jodrell, D. I.; Sadler, P. J., *J. Med. Chem.*, **2006**, 49, 6858–6868.

(154) Peacock, A. F. A.; Melchart, M.; Deeth, R. J.; Habtemariam, A.; Parsons, S.; Sadler, P. J., *Chem. Eur. J.*, **2007**, 13, 2601–2613.

(155) Wu, Q.; Liu, L.-Y.; Li, S.; Wang, F.-X.; Li, J.; Qian, Y.; Su, Z.; Mao, Z.-W.; Sadler, P. J.; Liu, H.-K., *J. Inorg. Biochem.*, **2018**, 189, 30–39.

(156) Scolaro, C.; Bergamo, A.; Brescacin, L.; Delfino, R.; Cocchietto, M.; Laurenczy, G.; Geldbach, T. J.; Sava, G.; Dyson, P. J., *J. Med. Chem.*, **2005**, 48, 4161–4171.

(157) Adhireksan, Z.; Davey, G. E.; Campomanes, P.; Groessl, M.; Clavel, C. M.; Yu, H.; Nazarov, A. A.; Yeo, C. H. F.; Ang, W. H.; Dröge, P.; Rothlisberger, U.; Dyson, P. J.; Davey, C. A., *Nat. Commun.*, **2014**, 5, 3462.

(158) Guichard, S. M.; Else, R.; Reid, E.; Zeitlin, B.; Aird, R.; Muir, M.; Dodds, M.; Fiebig, H.; Sadler, P. J.; Jodrell, D. I., *Biochem. Pharmacol.*, **2006**, 71, 408–415.

(159) Howerton, B. S.; Heidary, D. K.; Glazer, E. C., *J. Am. Chem. Soc.*, **2012**, 134, 8324–8327.

(160) Walker, J. M.; McEwan, A.; Pycko, R.; Tassotto, M. L.; Gottardo, C.; Th'ng, J.; Wang, R.; Spivak, G. J., *Eur. J. Inorg. Chem.*, **2009**, 4629–4633.

(161) Haghdoost, M. M.; Golbaghi, G.; Létourneau, M.; Patten, S. A.; Castonguay, A., *Eur. J. Med. Chem.*, **2017**, 132, 282–293.

(162) Wang, F.; Chen, H.; Parsons, S.; Oswald, I. D. H.; Davidson, J. E.; Sadler, P. J., *Chem. Eur. J.*, **2003**, 9, 5810–5820.

(163) Huang, H.; Zhang, P.; Chen, Y.; Ji, L.; Chao, H., *Dalton Trans.*, **2015**, 44, 15602–15610.

(164) Greener, B.; Foxon, S. P.; Walton, P. H., *New J. Chem.*, **2000**, 24, 269–273.

(165) Erickson, L. E.; Cook, D. J.; Evans, G. D.; Sarneski, J. E.; Okarma, P. J.; Sabatelli, A. D., *Inorg. Chem.*, **1990**, 29, 1958–1967.

(166) Moodley, K. G., *Der Pharma Chem.*, **2019**, 11, 1–19.

(167) Nagura, K.; Saito, S.; Yusa, H.; Yamawaki, H.; Fujihisa, H.; Sato, H.; Shimoikeda, Y.; Yamaguchi, S., *J. Am. Chem. Soc.*, **2013**, 135, 10322–10325.

(168) Hunt, S. W.; Yang, L.; Wang, X.; Richmond, M. G., *J. Organomet. Chem.*, **2011**, 696,

1432–1440.

(169) Miura, Y.; Chiba, H.; Katoono, R.; Kawai, H.; Fujiwara, K.; Suzuki, S.; Okada, K.; Suzuki, T., *Tetrahedron Lett.*, **2012**, 53, 6561–6564.

(170) Habtemariam, A.; Melchart, M.; Fernández, R.; Parsons, S.; Oswald, I. D. H.; Parkin, A.; Fabbiani, F. P. A.; Davidson, J. E.; Dawson, A.; Aird, R. E.; Jodrell, D. I.; Sadler, P. J., *J. Med. Chem.*, **2006**, 49, 6858–6868.

(171) Dyson, P. J.; Marchetti, F., *Dalton Trans.*, **2017**, 46, 11973–12366.

(172) Zhao, J.; Zhang, D.; Hua, W.; Li, W.; Xu, G.; Gou, S., *Organometallics*, **2018**, 37, 441–447.

(173) Topală, T.; Bodoki, A.; Oprean, L.; Oprean, R., *Farmacia*, **2014**, 62, 1049–1061.

(174) Kumar, C. V; Asuncion, E. H., *J. Am. Chem. Soc.*, **1993**, 115, 8547–8553.

(175) Wu, Q.; Liu, L. Y.; Li, S.; Wang, F. X.; Li, J.; Qian, Y.; Su, Z.; Mao, Z. W.; Sadler, P. J.; Liu, H. K., *J. Inorg. Biochem.*, **2018**, 189, 30–39.

(176) O'Hagan, M.; Morales, J. C.; Galan, M. C., *Eur. J. Org. Chem.*, **2019**, 4995–5017.

(177) Neidle, S., *J. Med. Chem.*, **2016**, 59, 5987–6011.

(178) Asamitsu, S.; Obata, S.; Yu, Z.; Bando, T.; Sugiyama, H., *Molecules*, **2019**, 24, 429.

(179) Balasubramanian, S.; Hurley, L. H.; Neidle, S., *Nat. Rev. Drug Discov.*, **2011**, 10, 261–275.

(180) Kypr, J.; Kejnovská, I.; Renčiuk, D.; Vorlíčková, M., *Nucleic Acids Res.*, **2009**, 37, 1713–1725.

(181) Dai, J.; Carver, M.; Yang, D., *Biochimie*, **2008**, 90, 1172–1183.

(182) De Cian, A.; DeLemos, E.; Mergny, J. L.; Teulade-Fichou, M. P.; Monchaud, D., *J. Am. Chem. Soc.*, **2007**, 129, 1856–1857.

(183) Rajput, C.; Rutkaite, R.; Swanson, L.; Haq, I.; Thomas, J. A., *Chem. Eur. J.*, **2006**, 12, 4611–4619.

(184) Yu, Q.; Liu, Y.; Zhang, J.; Yang, F.; Sun, D.; Liu, D.; Zhou, Y.; Liu, J., *Metallomics*, **2013**, 5, 222–231.

(185) Yu, Q.; Liu, Y.; Wang, C.; Sun, D.; Yang, X.; Liu, Y.; Liu, J., *PLoS One*, **2012**, 7, 1–13.

(186) O'Hagan, M. P.; Haldar, S.; Duchi, M.; Oliver, T. A. A.; Mulholland, A. J.; Morales, J. C.; Galan, M. C., *Angew. Chem., Int. Ed.*, **2019**, 58, 4334–4338.

(187) Georgiades, S. N.; Abd Karim, N. H.; Suntharalingam, K.; Vilar, R., *Angew. Chem., Int. Ed.*, **2010**, 49, 4020–4034.

(188) De Cian, A.; Guittat, L.; Kaiser, M.; Saccà, B.; Amrane, S.; Bourdoncle, A.; Alberti, P.; Teulade-Fichou, M. P.; Lacroix, L.; Mergny, J. L., *Methods*, **2007**, 42, 183–195.

(189) Wang, Y.; Patel, D. J., *Structure*, **1993**, 1, 263–282.

(190) Luu, K. N.; Phan, A. T.; Kuryavyi, V.; Lacroix, L.; Patel, D. J., *J. Am. Chem. Soc.*, **2006**, 128, 9963–9970.

(191) Marrison, J.; Räty, L.; Marriott, P.; O'Toole, P., *Sci. Rep.*, **2013**, 3, 1–7.

(192) Kasprowicz, R.; Suman, R.; O'Toole, P., *Int. J. Biochem. Cell Biol.*, **2017**, 84, 89–95.

(193) Puckett, C. A.; Barton, J. K., *J. Am. Chem. Soc.*, **2009**, 131, 8738–8739.

(194) Burke, C. S.; Byrne, A.; Keyes, T. E., *Angew. Chem., Int. Ed.*, **2018**, 57, 12420–12424.

(195) Matkovich, K. M.; Thorne, L. M.; Wolf, M. O.; Pace, T. C. S.; Bohne, C.; Patrick, B. O., *Inorg. Chem.*, **2006**, 45, 4610–4618.

(196) Jeon, Y. M.; Kim, D.; Mirkin, C. A.; Golen, J. A.; Rheingold, A. L., *Tetrahedron*, **2008**, 64, 8428–8434.

(197) Elsegood, M. R. J.; Lake, A. J.; Elliott, C. L.; Smith, M. B.; Weaver, G. W., *Phosphorus, Sulfur, and Silicon*, **2008**, 183, 435–439.

(198) Bays, J. T.; Priyadarshani, N.; Jeletic, M. S.; Hulley, E. B.; Miller, D. L.; Linehan, J. C.; Shaw, W. J., *ACS Catal.*, **2014**, 4, 3663–3670.

(199) Reetz, M. T.; Lohmer, G.; Schwickardi, R., *Angew. Chem., Int. Ed.*, **1997**, 36, 1526–1529.

(200) Durran, S. E.; Elsegood, M. R. J.; Hawkins, N.; Smith, M. B.; Talib, S., *Tetrahedron Lett.*, **2003**, 44, 5255–5257.

(201) Priyadarshani, N.; Ginovska, B.; Bays, J. T.; Linehan, J. C.; Shaw, W. J., *Dalton Trans.*, **2015**, 44, 14854–14864.

(202) Nickita, N.; Gasser, G.; Pearson, P.; Belousoff, M. J.; Goh, L. Y.; Bond, A. M.; Deacon, G. B.; Spiccia, L., *Inorg. Chem.*, **2009**, 48, 68–81.

(203) Cheng, Q.; Cui, Y.; Xiao, N.; Lu, J.; Fang, C. J., *Molecules*, **2018**, 23, 1–10.

(204) Lu, X. X.; Tang, H. S.; Ko, C. C.; Wong, J. K. Y.; Zhu, N.; Yam, V. W. W., *Chem. Commun.*, **2005**, 1572–1574.

(205) Parveen, S.; Hanif, M.; Movassaghi, S.; Sullivan, M. P.; Kubanik, M.; Shaheen, M. A.; Söhnel, T.; Jamieson, S. M. F.; Hartinger, C. G., *Eur. J. Inorg. Chem.*, **2017**, 2017, 1721–1727.

(206) Castonguay, A.; Doucet, C.; Juhas, M.; Maysinger, D., *J. Med. Chem.*, **2012**, 55, 8799–8806.

(207) Renfrew, A. K.; Scopelliti, R.; Dyson, P. J., *Inorg. Chem.*, **2010**, 49, 2239–2246.

(208) Păunescu, E.; McArthur, S.; Soudani, M.; Scopelliti, R.; Dyson, P. J., *Inorg. Chem.*, **2016**, 55, 1788–1808.

(209) Stíbal, D.; Therrien, B.; Süss-Fink, G.; Nowak-Sliwinska, P.; Dyson, P. J.; Čermáková, E.; Řezáčová, M.; Tomšík, P., *J. Biol. Inorg. Chem.*, **2016**, 21, 443–452.

(210) Biancalana, L.; Gruchała, M.; Batchelor, L. K.; Błauż, A.; Monti, A.; Pampaloni, G.; Rychlik, B.; Dyson, P. J.; Marchetti, F., *Eur. J. Inorg. Chem.*, **2020**, 1061–1072.

(211) Angurell, I.; Turrin, C. O.; Laurent, R.; Maraval, V.; Servin, P.; Rossell, O.; Seco, M.; Caminade, A. M.; Majoral, J. P., *J. Organomet. Chem.*, **2007**, 692, 1928–1939.

(212) Vonlanthen, M.; Cevallos-Vallejo, A.; Aguilar-Ortíz, E.; Ruiu, A.; Porcu, P.; Rivera, E., *Polymer*, **2016**, 99, 13–20.

(213) Chua, C. J.; Ren, Y.; Baumgartner, T., *Organometallics*, **2012**, 31, 2425–2436.

(214) Zhao, J.; Zhang, D.; Hua, W.; Li, W.; Xu, G.; Gou, S., *Organometallics*, **2018**, 37, 441–447.

(215) Reynolds, G. A.; Drexhage, K. H., *Optics Commun.*, **1975**, 13, 222–225.

(216) Taniguchi, M.; Lindsey, J. S., *Photochem. Photobiol.*, **2018**, 94, 290–327.

(217) Turnbull, W. L.; Murrell, E.; Bulcan-Gnirss, M.; Majeed, M.; Milne, M.; Luyt, L. G., *Dalton Trans.*, **2019**, 48, 14077–14084.

(218) Bodapati, R.; Sahoo, C.; Gudem, M.; Das, S. K., *Inorg. Chem.*, **2019**, 58, 11470–11479.

(219) Li, G.; Xu, Y.; Zhuang, W.; Wang, Y., *RSC Adv.*, **2016**, 6, 84787–84793.

(220) Jagodinsky, J. C.; Sulima, A.; Cao, Y.; Poprawski, J. E.; Blackman, B. N.; Lloyd, J. R.; Swenson, R. E.; Gottesman, M. M.; Hall, M. D., *J. Biol. Inorg. Chem.*, **2015**, 20, 1081–1095.

(221) Stewart, B.; Harriman, A.; Higham, L. J., *Organometallics*, **2011**, 30, 5338–5343.

(222) Wu, S.; Deligonal, N.; Protasiewicz, J. D., *Dalton Trans.*, **2013**, 42, 14866–14874.

(223) Ficks, A.; Clegg, W.; Harrington, R. W.; Higham, L. J., *Organometallics*, **2014**, 33, 6319–6329.

(224) Randić, M., *Chem. Rev.*, **2003**, 103, 3449–3605.

(225) Akasaka, K.; Suzuki, T.; Ohrui, H.; Meguro, H., *Anal. Lett.*, **1987**, 20, 797–807.

(226) Shioji, K.; Oyama, Y.; Okuma, K.; Nakagawa, H., *Bioorganic Med. Chem. Lett.*, **2010**, 20, 3911–3915.

(227) Wilkins, L. C.; Kim, Y.; Litle, E. D.; Gabbaï, F. P., *Angew. Chem., Int. Ed.*, **2019**, 58, 18266–18270.

(228) Davies, L. H.; Harrington, R. W.; Clegg, W.; Higham, L. J., *Dalton Trans.*, **2014**, 43, 13485–13499.

(229) Davies, L. H.; Wallis, J. F.; Harrington, R. W.; Waddell, P. G.; Higham, L. J., *J. Coord. Chem.*, **2016**, 69, 2069–2080.

(230) Huang, W.; Qian, Y.; Qian, S. Y.; Fang, Q.; Li, J.; Li, S.; Duan, R.; Wang, S.; Yi, Y.; Guo, X.; Yang, G., *Chem. Commun.*, **2017**, 53, 5702–5705.

(231) Behm, K.; Essner, J. B.; Barnes, C. L.; Baker, G. A.; Walensky, J. R., *Dalton Trans.*, **2017**, 46, 10867–10875.

(232) Blake, A. J.; Champness, N. R.; Forder, R. J.; Frampton, C. S.; Frost, C. A.; Reid, G.; Simpson, R. H., *J. Chem. Soc., Dalton Trans.*, **1994**, 3377–3382.

(233) Forder, R. J.; Reid, G., *Polyhedron*, **1996**, 15, 3249–3255.

(234) Moldes, I.; De La Encarnación, E.; Ros, J.; Alvarez-Larena, Á.; Piniella, J. F., *J. Organomet. Chem.*, **1998**, 566, 165–174.

(235) Termaten, A. T.; Nijbacker, T.; Schakel, M.; Lutz, M.; Spek, A. L.; Lammertsma, K., *Chem. Eur. J.*, **2003**, 9, 2200–2208.

(236) Goodwin, N. J.; Henderson, W.; Nicholson, B. K.; Fawcett, J.; Russell, D. R., *J. Chem. Soc., Dalton Trans.*, **1999**, 1785–1793.

(237) Downard, A. J.; Goodwin, N. J.; Henderson, W., *J. Organomet. Chem.*, **2003**, 676, 62–72.

(238) Paris, S. I. M.; Lemke, F. R.; Sommer, R.; Lönnecke, P.; Hey-Hawkins, E., *J. Organomet. Chem.*, **2005**, 690, 1807–1813.

(239) Paris, S. I. M.; Petersen, J. L.; Hey-Hawkins, E.; Jensen, M. P., *Inorg. Chem.*, **2006**, 45, 5561–5567.

(240) Brissos, R. F.; Clavero, P.; Gallen, A.; Grabulosa, A.; Barrios, L. A.; Caballero, A. B.; Korrodi-Gregório, L.; Pérez-Tomás, R.; Muller, G.; Soto-Cerrato, V.; Gamez, P., *Inorg. Chem.*, **2018**, 57, 14786–14797.

(241) Rafols, L.; Torrente, S.; Aguilà, D.; Soto-Cerrato, V.; Pérez-Tomás, R.; Gamez, P.; Grabulosa, A., *Organometallics*, **2020**, 39, 2959–2971.

(242) Hu, J.; Yip, J. H. K.; Ma, D. L.; Wong, K. Y.; Chung, W. H., *Organometallics*, **2009**, 28, 51–59.

(243) Crawford, A. G.; Liu, Z.; Mkhalid, I. A. I.; Thibault, M. H.; Schwarz, N.; Alcaraz, G.; Steffen, A.; Collings, J. C.; Batsanov, A. S.; Howard, J. A. K.; Marder, T. B., *Chem. Eur. J.*, **2012**, 18, 5022–5035.

(244) Qiu, L.; Hu, W.; Wu, D.; Duan, Z.; Mathey, F., *Org. Lett.*, **2018**, 20, 7821–7824.

(245) He, C.; He, Q.; Chen, Q.; Shi, L.; Cao, H.; Cheng, J.; Deng, C.; Lin, T., *Tetrahedron Lett.*, **2010**, 51, 1317–1321.

(246) Yip, H. L.; Ma, H.; Jen, A. K. Y.; Dong, J.; Parviz, B. A., *J. Am. Chem. Soc.*, **2006**, 128, 5672–5679.

(247) Dordević, L.; Milano, D.; Demitri, N.; Bonifazi, D., *Org. Lett.*, **2020**, 22, 4283–4288.

(248) Ji, L.; Edkins, R. M.; Lorbach, A.; Krummenacher, I.; Brückner, C.; Eichhorn, A.; Braunschweig, H.; Engels, B.; Low, P. J.; Marder, T. B., *J. Am. Chem. Soc.*, **2015**, 137, 6750–6753.

(249) Merz, J.; Fink, J.; Friedrich, A.; Krummenacher, I.; Al Mamari, H. H.; Lorenzen, S.; Haehnel, M.; Eichhorn, A.; Moos, M.; Holzapfel, M.; Braunschweig, H.; Lambert, C.; Steffen, A.; Ji, L.; Marder, T. B., *Chem. Eur. J.*, **2017**, 23, 13164–13180.

(250) Kalio, R.; Lönnecke, P.; Hey-Hawkins, E., *J. Organomet. Chem.*, **2008**, 693, 590–600.

(251) Johnpeter, J. P.; Therrien, B., *Inorganica Chim. Acta*, **2013**, 405, 437–443.

(252) Wrona-Piotrowicz, A.; Zakrzewski, J.; Métivier, R.; Brosseau, A.; Makal, A.; Woźniak, K., *RSC Adv.*, **2014**, 4, 56003–56012.

(253) Sun, R.; Chu, X.; Zhang, S.; Li, T.; Wang, Z.; Zhu, B., *Eur. J. Inorg. Chem.*, **2017**, 2017, 3174–3183.

(254) Geeson, M. B.; Jupp, A. R.; McGrady, J. E.; Goicoechea, J. M., *Chem. Commun.*, **2014**, 50, 12281–12284.

(255) Navrátil, M.; Faria, E. N.; Panahy, G.; Císařová, I.; Goicoechea, J. M.; Štěpnička, P., *Dalton Trans.*, **2020**, 49, 8645–8651.

(256) Bent, H. A., *Chem. Rev.*, **1961**, 61, 275–311.

(257) Kourkine, I. V; Maslennikov, S. V; Ditchfield, R.; Glueck, D. S.; Yap, G. P. A.; Liable-Sands, L. M.; Rheingold, A. L., *Inorg. Chem.*, **1996**, 35, 6708–6716.

(258) Muller, T. E.; Green, J. C.; Mingos, D. M. P.; Mcpartlin, C. M., *J. Organomet. Chem.*, **1998**, 551, 313–330.

(259) Price, G. A.; Brisdon, A. K.; Flower, K. R.; Pritchard, R. G.; Quayle, P., *Tetrahedron Lett.*, **2014**, 55, 151–154.

(260) Irmler, P.; Gogesch, F. S.; Larsen, C. B.; Wenger, O. S.; Winter, R. F., *Dalton Trans.*, **2019**, 48, 1171–1174.

(261) Berberan-Santos, M. N., *PhysChemComm*, **2000**, 3, 5–10.

(262) Wilson, G. J.; Launikonis, A.; Sasse, W. H. F.; Mau, A. W. H., *J. Phys. Chem. A*, **1998**, 102, 5150–5156.

(263) Dawson, W. R.; Windsor, M. W., *J. Phys. Chem.*, **1968**, 72, 3251–3260.

(264) *Gaussian 09, Revision D.01*, Gaussian, Inc., Wallingford CT, **2016**.

(265) Vosko, S. H.; Wilk, L.; Nusair, M., *Can. J. Phys.*, **1980**, 58, 1200–1211.

(266) Lee, C.; Yang, W.; Parr, R. G., *Phys. Rev. B*, **1988**, 37, 785–789.

(267) Becke, A. D., *J. Chem. Phys.*, **1993**, 98, 5648–5652.

(268) Stephens, P. J.; Devlin, F. J.; Chabalowski, C. F.; Frisch, M. J., *J. Phys. Chem.*, **1994**, 98, 11623–11627.

(269) Wadt, W. R.; Hay, P. J., *J. Chem. Phys.*, **1985**, 82, 284–298.

(270) Yanai, T.; Tew, D. P.; Handy, N. C., *Chem. Phys. Lett.*, **2004**, 393, 51–57.

(271) Tomasi, J.; Mennucci, B.; Cammi, R., *Chem. Rev.*, **2005**, 105, 2999–3093.

(272) Buckley, L. E. R.; Coe, B. J.; Rusanova, D.; Sánchez, S.; Jirásek, M.; Joshi, V. D.; Vávra, J.; Khobragade, D.; Pospíšil, L.; Ramešová, Š.; Císařová, I.; Šaman, D.; Pohl, R.; Clays, K.; Van Steerteghem, N.; Brunschwig, B. S.; Teplý, F., *Dalton Trans.*, **2017**, 46, 1052–1064.

(273) Fey, N.; Papadouli, S.; Pringle, P. G.; Ficks, A.; Fleming, J. T.; Higham, L. J.; Wallis, J. F.; Carmichael, D.; Mézailles, N.; Müller, C., *Phosphorus, Sulfur, and Silicon*, **2015**, 190, 706–714.

(274) Hiney, R. M.; Higham, L. J.; Müller-Bunz, H.; Gilheany, D. G., *Angew. Chem., Int. Ed.*, **2006**, 45, 7248–7251.

(275) Fleming, J. T.; Higham, L. J., *Coord. Chem. Rev.*, **2015**, 297–298, 127–145.

(276) Moulton, C. J.; Shaw, B. L., *J. Chem. Soc., Dalton Trans.*, **1976**, 918, 1020–1024.

(277) Van Koten, G.; Timmer, K.; Noltes, J.; Spek, A. L., *J. Chem. Soc. Dalton Trans.*, **1978**, 45, 250–252.

(278) Younus, H. A.; Ahmad, N.; Su, W.; Verpoort, F., *Coord. Chem. Rev.*, **2014**, 276, 112–152.

(279) Eberhard, M. R.; Matsukawa, S.; Yamamoto, Y.; Jensen, C. M., *J. Organomet. Chem.*,

2003, 687, 185–189.

(280) Zhu, G.; Terry, M.; Zhang, X., *Tetrahedron Lett.*, **1996**, 37, 4475–4478.

(281) Zhu, G.; Terry, M.; Zhang, X., *J. Organomet. Chem.*, **1997**, 547, 97–101.

(282) Tabrizi, L.; Chiniforoshan, H., *Dalton Trans.*, **2017**, 46, 14164–14173.

(283) Churusova, S. G.; Aleksanyan, D. V.; Rybalkina, E. Y.; Susova, O. Y.; Brunova, V. V.; Aysin, R. R.; Nelyubina, Y. V.; Peregudov, A. S.; Gutsul, E. I.; Klemenkova, Z. S.; Kozlov, V. A., *Inorg. Chem.*, **2017**, 56, 9834–9850.

(284) Poverenov, E.; Gandelman, M.; Shimon, L. J. W.; Rozenberg, H.; Ben-David, Y.; Milstein, D., *Chem. Eur. J.*, **2004**, 10, 4673–4684.

(285) Poverenov, E.; Gandelman, M.; Shimon, L. J. W.; Rozenberg, H.; Ben-David, Y.; Milstein, D., *Organometallics*, **2005**, 24, 1082–1090.

(286) Kranenburg, M.; Kamer, P. C. J.; Van Leeuwen, P. W. N. M., *Eur. J. Inorg. Chem.*, **1998**, 25–27.

(287) Van Haaren, R. J.; Oevering, H.; Coussens, B. B.; Van Strijdonck, G. P. F.; Reek, J. N. H.; Kamer, P. C. J.; Van Leeuwen, P. W. N. M., *Eur. J. Inorg. Chem.*, **1999**, 1237–1241.

(288) Van Leeuwen, P. W. N. M.; Kamer, P. C. J.; Reek, J. N. H.; Dierkes, P., *Chem. Rev.*, **2000**, 100, 2741–2769.

(289) Van Haaren, R. J.; Druijven, C. J. M.; Van Strijdonck, G. P. F.; Oevering, H.; Reek, J. N. H.; Kamer, P. C. J.; Van Leeuwen, P. W. N. M., *J. Chem. Soc., Dalton Trans.*, **2000**, 1549–1554.

(290) Van Haaren, R. J.; Goubitz, K.; Fraanje, J.; Van Strijdonck, G. P. F.; Oevering, H.; Coussens, B.; Reek, J. N. H.; Kamer, P. C. J.; Van Leeuwen, P. W. N. M., *Inorg. Chem.*, **2001**, 40, 3363–3372.

(291) Czauderna, C. F.; Jarvis, A. G.; Heutz, F. J. L.; Cordes, D. B.; Slawin, A. M. Z.; Van Der Vlugt, J. I.; Kamer, P. C. J., *Organometallics*, **2015**, 34, 1608–1618.

(292) Al-Salem, N. A.; Empsall, H. D.; Markham, R.; Shaw, B. L.; Weeks, B., *J. Chem. Soc., Dalton Trans.*, **1979**, 1972–1982.

(293) Baber, R. A.; Bedford, R. B.; Betham, M.; Blake, M. E.; Coles, S. J.; Haddow, M. F.; Hursthouse, M. B.; Orpen, A. G.; Pilarski, L. T.; Pringle, P. G.; Wingad, R. L., *Chem. Commun.*, **2006**, 3880–3882.

(294) Mesganaw, T.; Im, G. Y. J.; Garg, N. K., *J. Org. Chem.*, **2013**, 78, 3391–3393.

(295) Ballatore, C.; Soper, J. H.; Piscitelli, F.; James, M.; Huang, L.; Atasoylu, O.; Huryn, D. M.; Trojanowski, J. Q.; Lee, V. M. Y.; Brunden, K. R.; Smith, A. B., *J. Med. Chem.*, **2011**, 54, 6969–6983.

(296) Mann, S.; Melero, C. P.; Hawksley, D.; Leeper, F. J., *Org. Biomol. Chem.*, **2004**, 2, 1732–1741.

(297) Lloyd-Jones, G. C.; Taylor, N. P., *Chem. Eur. J.*, **2015**, 21, 5423–5428.

(298) Solin, N.; Kjellgren, J.; Szabó, K. J., *J. Am. Chem. Soc.*, **2004**, 126, 7026–7033.

(299) Guo, R.; Portscheller, J. L.; Day, V. W.; Malinakova, H. C., *Organometallics*, **2007**,

26, 3874–3883.

(300) Evans, I. P.; Spencer, A.; Wilkinson, G., *J. Chem. Soc. D*, **1973**, 204–209.

(301) Dhara, S. C., *Indian J. Chem*, **1970**, 8, 193.

(302) Bassan, R.; Bryars, K. H.; Judd, L.; Platt, A. W. G.; Pringle, P. G., *Inorganica Chim. Acta*, **1986**, 121, 41–42.

(303) McDermott, J. X.; White, J. F.; Whitesides, G. M., *J. Am. Chem. Soc.*, **1976**, 98, 6521–6528.

(304) Hunt, S. W.; Yang, L.; Wang, X.; Richmond, M. G., *J. Organomet. Chem.*, **2011**, 696, 1432–1440.

(305) Johnson, B. J.; Lindeman, S. V; Mankad, N. P., *Inorg. Chem.*, **2014**, 53, 10611–10619.

(306) Ji, W.; Li, N.; Chen, D.; Qi, X.; Sha, W.; Jiao, Y.; Xu, Q.; Lu, J., *J. Mater. Chem. B*, **2013**, 1, 5942–5949.

(307) He, C.; He, Q.; Chen, Q.; Shi, L.; Cao, H.; Cheng, J.; Deng, C.; Lin, T., *Tetrahedron Lett.*, **2010**, 51, 1317–1321.

(308) Bresien, J.; Faust, K.; Schulz, A.; Villinger, A., *Angew. Chem., Int. Ed.*, **2015**, 54, 6926–6930.

(309) Wiedermann, J.; Mereiter, K.; Kirchner, K., *J. Mol. Catal. A Chem.*, **2006**, 257, 67–72.

(310) Wu, L. P.; Suenaga, Y.; Kuroda-Sowa, T.; Maekawa, M.; Furuichi, K.; Munakata, M., *Inorganica Chim. Acta*, **1996**, 248, 147–152.

(311) Clifton, J., PhD Thesis, University of Bristol, **2016**.

(312) Hu, J.; Nguyen, M. H.; Yip, J. H. K., *Inorg. Chem.*, **2011**, 50, 7429–7439.

(313) Dhami, S.; Mello, A. J. D.; Rumbles, G.; Bishop, S. M.; Phillips, D.; Beeby, A., *Photochem. Photobiol.*, **1995**, 61, 341–346.

(314) Benito-Garagorri, D.; Becker, E.; Wiedermann, J.; Lackner, W.; Pollak, M.; Mereiter, K.; Kisala, J.; Kirchner, K., *Organometallics*, **2006**, 25, 1900–1913.

(315) Stokes, B. J.; Opra, S. M.; Sigman, M. S., *J. Am. Chem. Soc.*, **2012**, 134, 11408–11411.

(316) Bruker, SAINT+ v8.38A Integration Engine.

(317) Bruker, SADABS, Bruker AXS area detector.

(318) Sheldrick, G. M., *Acta Crystallogr. Sect. C Struct. Chem.*, **2015**, 71, 3–8.

(319) Sheldrick, G. M., *Acta Crystallogr. Sect. A Found. Crystallogr.*, **2007**, 64, 112–122.

(320) Dolomanov, O. V.; Bourhis, L. J.; Gildea, R. J.; Howard, J. A. K.; Puschmann, H., *J. Appl. Crystallogr.*, **2009**, 42, 339–341.